The Growth of the First Galaxies

Kenneth James Duncan

Thesis submitted to the University of Nottingham
for the degree of Doctor of Philosophy, April 2015

"We all have a thirst for wonder. It's a deeply human quality. Science and religion are both bound up with it. What I'm saying is, you don't have to make stories up, you don't have to exaggerate. There's wonder and awe enough in the real world. Nature's a lot better at inventing wonders than we are.

– Carl Sagan, Contact

"He had a suspicion of plausible answers; they were so often wrong.

– Arthur C. Clarke, Rendezvous with Rama

Supervisor:	Prof. Christopher J. Conselice
Examiners:	Dr. Meghan Gray Dr. Elizabeth Stanway
Submitted:	April 10th, 2015
Examined:	June 8th, 2015

Abstract

This thesis explores the growth of galaxies during the first few billion years of galaxy formation and their potential role as the sources which powered the process of reionization. The data used throughout the thesis is taken from the Cosmic Assembly Near-infrared Extragalactic Legacy Survey (CANDELS).

First, we measure new estimates for the galaxy stellar mass function and star formation rates for samples of galaxies at $z \sim 4,\ 5,\ 6$ & 7 using data in the CANDELS GOODS South field. The deep near-infrared observations allow us to construct the stellar mass function at $z \geq 6$ directly for the first time. We estimate stellar masses for our sample by fitting the observed spectral energy distributions with synthetic stellar populations, including the contributions from nebular line and continuum emission. The observed UV luminosity functions for the samples are consistent with previous observations, however we find that the observed M_{UV} - M_* relation has a shallow slope more consistent with a constant mass to light ratio and a normalisation which evolves with redshift.

We observe stellar mass functions which have steep low-mass slopes ($\alpha \approx -1.9$), steeper than previously observed at these redshifts and closer to that of the UV luminosity function. Integrating our new mass functions, we find the observed stellar mass density evolves from $\log_{10} \rho_* = 6.64^{+0.58}_{-0.89}$ at $z \sim 7$ to 7.36 ± 0.06 $\mathrm{M}_\odot\mathrm{Mpc}^{-3}$ at $z \sim 4$. Combining the measured UV continuum slopes (β) with their rest-frame UV luminosities, we calculate dust corrected star-formation rates (SFR) for our sample. We find the specific star-formation rate for a fixed stellar mass increases with redshift whilst the global SFR density falls rapidly over this period. Our new SFR density estimates are higher than previously observed at this redshift.

Next, we utilise the same dataset to test a new method for estimating the merger fraction of galaxies in photometric surveys. Using a probabilistic method for estimating close galaxy pairs using photometric redshift probability distributions, we estimate the merger fraction of galaxies at $z \geq 2$. For projected separations of $5 \leq r_{\rm p} \leq 20$ kpc and $5 \leq r_{\rm p} \leq 30$ kpc we measure the merger fraction for mass selected samples of $\log_{10}(\mathrm{M}_{\star}/\mathrm{M}_{\odot}) > 9.5$ and $\log_{10}(\mathrm{M}_{\star}/\mathrm{M}_{\odot}) > 10$ and merger ratios of 1:4 or less (major mergers).

For assumed merger timescales based on hydrodynamical simulations, we estimate the average time between mergers per galaxy (Γ, Gyr) and the comoving merger rate ($\mathcal{R}$, Gyr^{-1} Mpc^{-3}). Over the redshift range $2 \lesssim z \lesssim 4$ we find that the average time between mergers per galaxy is approximately constant at ≈ 4 Gyr ($\log_{10}(\mathrm{M}_{\star}/\mathrm{M}_{\odot}) > 9.5$) or ≈ 8 Gyr ($\log_{10}(\mathrm{M}_{\star}/\mathrm{M}_{\odot}) > 10$). Compared to the star-formation rates measured for galaxies at these masses, we conclude that star-formation is the dominant form of growth (by a factor $\approx 10\times$) during this epoch. Although we find that the methodology performs well at $z \lesssim 4$, more data is required to make robust estimations of the merger fraction at $z \sim 5$ or $z \sim 6$. Similarly, tighter constraints on the observed stellar mass functions are required before we can draw meaningful conclusions from the observed comoving merger rates.

Finally, we present a new analysis of the ionizing emissivity ($\dot{N}_{\rm ion}$, s^{-1} Mpc^{-3}) for galaxies during the epoch of reionization and their potential for completing and maintaining reionization. We use extensive SED modelling – incorporating two plausible mechanisms for the escape of Lyman continuum photon – to explore the range and evolution of ionizing efficiencies consistent with new results on galaxy colours (β) during this epoch. We estimate $\dot{N}_{\rm ion}$ for the latest observations of the luminosity and star-formation rate density at $z < 10$, outlining the range of emissivity histories consistent with our new model.

Given the growing observational evidence for a UV colour-magnitude relation in high-redshift galaxies, we find that for any plausible evolution in galaxy properties, red (brighter) galaxies are less efficient at producing ionizing photons than their blue (fainter) counterparts. The assumption of a redshift and luminosity

evolution in β leads to two important conclusions. Firstly, the ionizing efficiency of galaxies naturally increases with redshift. Secondly, for a luminosity dependent ionizing efficiency, we find that galaxies down to a rest-frame magnitude of $M_{\rm UV} \approx -15$ alone can potentially produce sufficient numbers of ionizing photons to maintain reionization as early as $z \sim 8$ for a clumping factor of $C_{\rm HII} \leq 3$.

Published Work

Much of the work described in this thesis has been presented in the following papers:

I Duncan, K.; Conselice, C. J.; Mortlock, A.; Hartley, W. G.; Guo, Y.; Ferguson, H. C.; Dav, R.; Lu, Y.; Ownsworth, J.; Ashby, M. L. N.; Dekel, A.; Dickinson, M.; Faber, S.; Giavalisco, M.; Grogin, N.; Kocevski, D.; Koekemoer, A.; Somerville, R. S.; White, C. E., *"The mass evolution of the first galaxies: stellar mass functions and star formation rates at* $4 < z < 7$ *in the CANDELS GOODS-South field"*, Monthly Notices of the Royal Astronomical Society (2014), Volume 444, Issue 3, p.2960-2984

II Duncan, K.; Conselice, C. J.; Mundy, C. J.; Lu, Y.; Guo, Y.; Ferguson, H. C. and the CANDELS collaboration, *"Towards a complete history of galaxy assembly: Major merger rates at* $2 \leq z \leq 6$ *in the CANDELS fields"*, in preparation.

III Kenneth Duncan and Christopher J Conselice, *"Powering reionization: assessing the galaxy ionizing photon budget at* $z < 10$*"*, Monthly Notices of the Royal Astronomical Society (2015), Volume 451, Issue 2, p.2030-2049

Paper I contains the work presented in Chapter 2 of this thesis. Chapter 3 presents a subset of the analysis in Paper II which is currently a work in progress. Finally, Paper III presents the work described in Chapter 4.

The vast majority of the work presented in this thesis is the sole work of the author. This includes all photometric redshift, stellar mass estimation, SED modelling and completeness simulations. Exceptions to this are clearly outlined in the

relevant sections and predominantly include the production of the photometric catalogs and semi-analytical models used in Chapters 2 and 3. The methodology for the merger analysis presented in Chapter 3 has been implemented in an equal collaborative effort with Carl J Mundy.

Acknowledgements

My foremost acknowledgements go to Chris Conselice for guiding and supporting the research in this thesis from start to finish. I am grateful for the freedom i've had to explore my own ideas as well as the fantastic discussion, help and feedback throughout my PhD. I would also like to thank all of the staff within the department, all of whom have contributed with advice or help in at least some small way to the work in this thesis.

This work couldn't have been done without my collaborators and colleagues both near and far. From Nottingham, a special thanks goes to Will Hartley, Alice Mortlock, Jamie Ownsworth and Carl Mundy. From farther afield, i'd like to thank Harry Ferguson for immeasurable help and advice as well as those who offered help or advice, including but not by no means limited to Romeel Davë, Brant Robertson, Mark Dickinson, Yu Lu and Matt Ashby.

A big thank you to my officemates through the years, I couldn't have asked for a nicer set of people to keep me company every day. To the friends I made in Nottingham, your company, humour, alcohol and sugary baked goods meant more to me than you realise or would ever have been admitted to in person. Thank you all for a fantastic four years. A special mention however should go to Emma Bradshaw, who I credit with helping to bring me to Nottingham and for being a great friend and colleague while there as well.

Finally and most importantly, I wouldn't have gotten to where I am without the love and support of my family. This thesis is dedicated to you.

Contents

List of Figures

List of Tables

The Growth of the First Galaxies

Chapter 1

Introduction

One of the most remarkable achievements in physical sciences over the last few decades is the precision to which cosmologists have been able measure the initial conditions of our Universe. We know very well how it all began 13.8 billion years ago and what the starting ingredients were. From the panoply of planets, stars and galaxies we see around us today, we also have a good grasp on what those ingredients eventually became. The challenge facing Astronomy is to fill in the gaps in that long history and shed light upon the underlying physics which shaped the formation and evolution of these celestial objects.

1.1 The Early Universe

What makes the measurements of the initial conditions in our Universe possible is the detailed observation of the cosmic microwave background (CMB). Famously discovered accidentally by Arno Penzias and Robert Wilson in 1964 (Penzias & Wilson, 1965) but independently postulated several times in the preceding decades, the CMB represents the oldest light in the Universe. For the first $\sim 373,000$ years after the Big Bang all baryonic matter in the Universe – including free electrons, protons and neutrons – was coupled together in a hot, uniform, radiation-filled hydrogen plasma. As the Universe expanded and cooled, the electrons and protons eventually cooled enough to form neutral atoms ('recombination') shortly before cooling far enough to allow the radiation field to

decouple from the baryons and the photons to stream freely through space ('decoupling'). It is those primordial photons that have been propagating through space and slowly cooling until this date to produce the cosmic microwave background we observe today.

Since the initial measurements of the CMB 50 years ago, a succession of ground-based, balloon-borne and space-based telescopes have measured the CMB with increasing precision. Despite initially appearing uniform in all directions, in 1992 data from the Cosmic Background Explorer (COBE) satellite indicated minute variations in the temperature of the CMB on small scales[1]. These anisotropies have since been measured to exquisite precision by the Wilkinson Microwave Anisotropy Probe (WMAP) and Planck experiments, leading to strong support for the currently favoured model of Λ-Cold Dark Matter (ΛCDM) cosmology. Figure 1.1 illustrates just how much each new generation of space-based CMB laboratory has improved our picture of the microwave background.

Imprinted by primordial quantum fluctuations that have grown and stretched with the expansion of the Universe, the observed anisotropies carry a wealth of information and any candidate cosmological model must be able to explain their properties. The current 'standard' ΛCDM cosmology (constrained by the Planck measurements) tells us that the present Universe is one consisting of precisely $30.89 \pm 0.62\%$ matter with the rest ($69.11 \pm 0.62\%$) comprised of an unknown 'dark energy', denoted 'Λ' (Planck Collaboration et al., 2015). Of that $\sim 30\%$ matter, only a modest $\sim 5\%$ is baryonic matter, visible as stars, dust and gas in the inter-stellar and intergalactic medium (ISM and IGM respectively). The remaining $\sim 25\%$ of matter is cold dark matter (CDM), itself still very much a mystery.

In the ΛCDM model, the primordial fluctuations that gave rise to the CMB anisotropy and cold dark matter also play a crucial role in the formation of structure in the Universe. Before recombination occurred, the primordial ele-

[1]Re-analysis of data from the Soviet RELIKT-1 anisotropy experiment did in fact lead to publication of anisotropy results several months before the COBE announcement (re-published in Strukov et al. 1992). However it was the COBE results for which the Nobel prize was later awarded.

ments which formed through big bang nucleosynthesis (BBN; Burles et al. 2001) were coupled to the electromagnetic radiation field through Thomson scattering; smoothing out any inhomogeneities. However, the non-baryonic dark matter was completely decoupled from the electromagnetic radiation and able to form small over-densities around the tiny density fluctuations. Under the force of their own gravity, these small over-densities were able to collapse into larger halos. Meanwhile, because of the radiation pressure on the coupled baryon-photon plasma the 'ordinary' matter was prevented from collapsing. It was not until recombination and the baryon-photon decoupling occurred that the baryons were able to fall

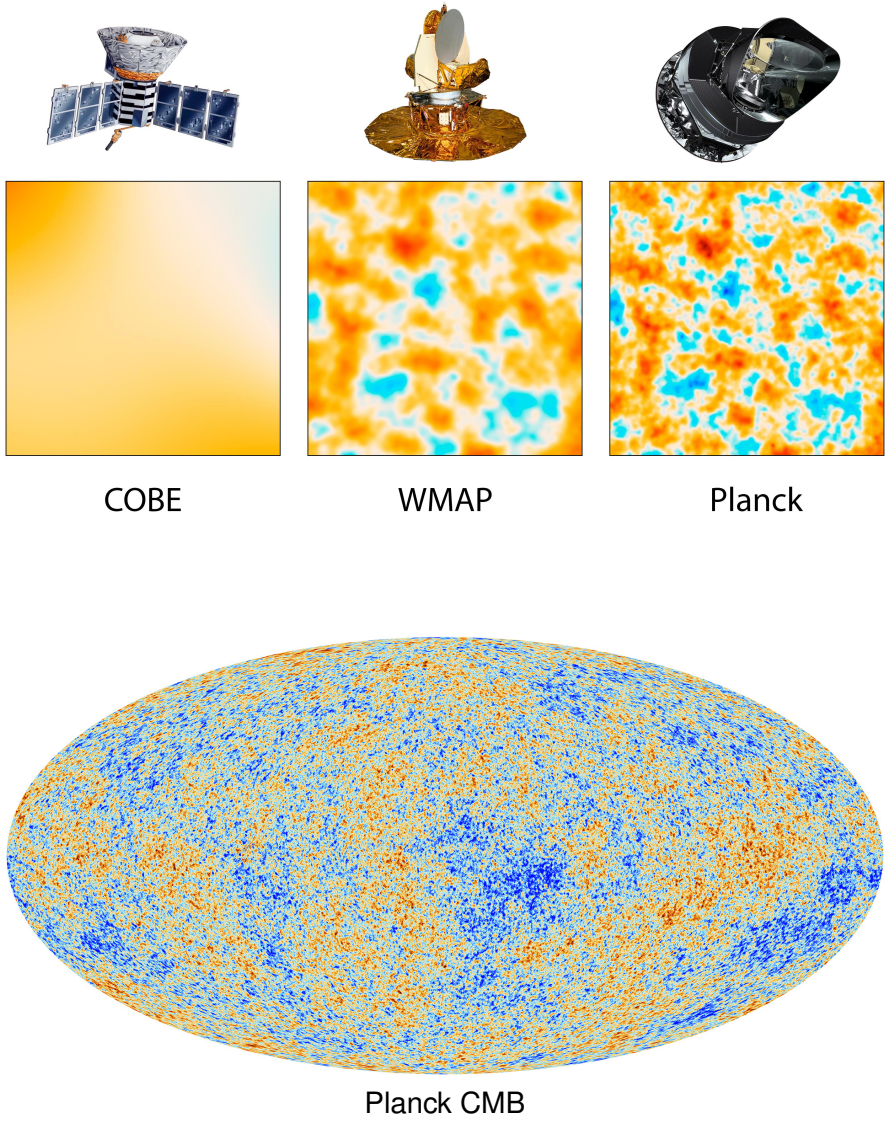

Figure 1.1: Top: Illustration of the increase in angular resolution offered by successive generation of CMB observatories, Credit – NASA/JPL-Caltech/ESA. Bottom: The all-sky map of the cosmic microwave background anisotropies as measured by the Planck satellite, Credit – ESA and the Planck Collaboration.

into the gravitational potentials created by the collapsed dark-matter halos.

Over the following few hundred million years these over-densities continued to grow in a so-called hierarchical way, whereby the first halos to collapse were small and larger halos were built up through many mergers of smaller halos. Eventually, the baryonic matter in the centre of the deepest gravitational potentials reached a high enough density and the neutral gas reached such high temperatures and pressures that the molecular hydrogen was able to radiate energy away. By radiatively cooling, the dense baryonic potentials could collapse further and reach high enough pressures and temperatures for nuclear fusion to commence; forming the first stars. The exact process of how these first stars formed is not well known and represents one of the true frontiers of modern astronomy (Bromm, 2013). However, what is for sure is that these first stars signalled the end of the so-called 'dark ages'.

With the formation of the first stars and their emission of energetic photons into the surrounding medium, the previously neutral hydrogen of IGM began to ionize into the predominantly ionized medium we see around us today. This era is known as the epoch of reionization (EoR). By using the imprinted polarisation on the CMB, WMAP and now Planck have been able to measure the total optical depth to the surface of last scattering, revealing that the start of the process of reionization (averaged across the Universe) began around 560 million years after the Big Bang (Planck Collaboration et al., 2015).

However, the details of the epoch of reionization remain something of a mystery and have been important drivers in both the study of cosmology and galaxy evolution. For example, which were the sources that powered reionization? What form did the transition take, was it a longer drawn out process or did it occur in one (or more) rapid transition? Were there enough galaxies to provide the required number of ionizing photons, or were quasars or exotic stellar populations required?

1.2 Galaxy Formation

If the CMB represents constraints of the initial conditions on the time evolution of galaxies, observations of the local evolved galaxy population are effectively the corresponding boundary condition at late times. Any theory or description of galaxy formation and evolution must have as its goal the ability to explain both the wide range of galaxy properties that exist and the correlations and links between many of those properties.

The most obvious and earliest property to be categorised and studied was the morphology of galaxies – their visual appearance. The morphology of local galaxies falls broadly into two categories: ellipticals and spirals, famously first visually classified by Edwin Hubble (Hubble, 1926). Elliptical galaxies as the name suggests are ellipsoidal and supported predominantly by the random motions of their stars (dispersion dominated). In contrast, spiral galaxies are flatter disc-like structures, supported mainly by their rotation and usually containing one or more visible spiral arms (hence the term 'spirals') which themselves may or may not include a barred structure. The majority of local galaxies sit somewhere between these two types, with the elliptical component commonly referred to as the 'bulge' and the flat rotational structure known as the 'disc'. In Hubble's eponymous 'tuning fork' diagram, galaxies lie on a sequence from entirely bulge-dominated elliptical galaxies through to pure discs with a mixture of the two components in between.

However, not all galaxies can be placed neatly along the Hubble sequence (or other such updated scheme, de Vaucouleurs 1959). Firstly, there are peculiar or irregular galaxies, which resemble neither ellipsoids nor discs due to the presence of features such as multiple subcomponents, long tail-like features and distorted structures. Many of these peculiar features have been associated with interactions or mergers with other nearby galaxies, suggesting that these interactions perhaps play a role in transforming one morphology into another. Secondly, a subset of irregular galaxies are those known as dwarf irregulars, galaxies that have low masses and large amounts of gas and on-going star formation, potentially representing local analogs of the earliest galaxies.

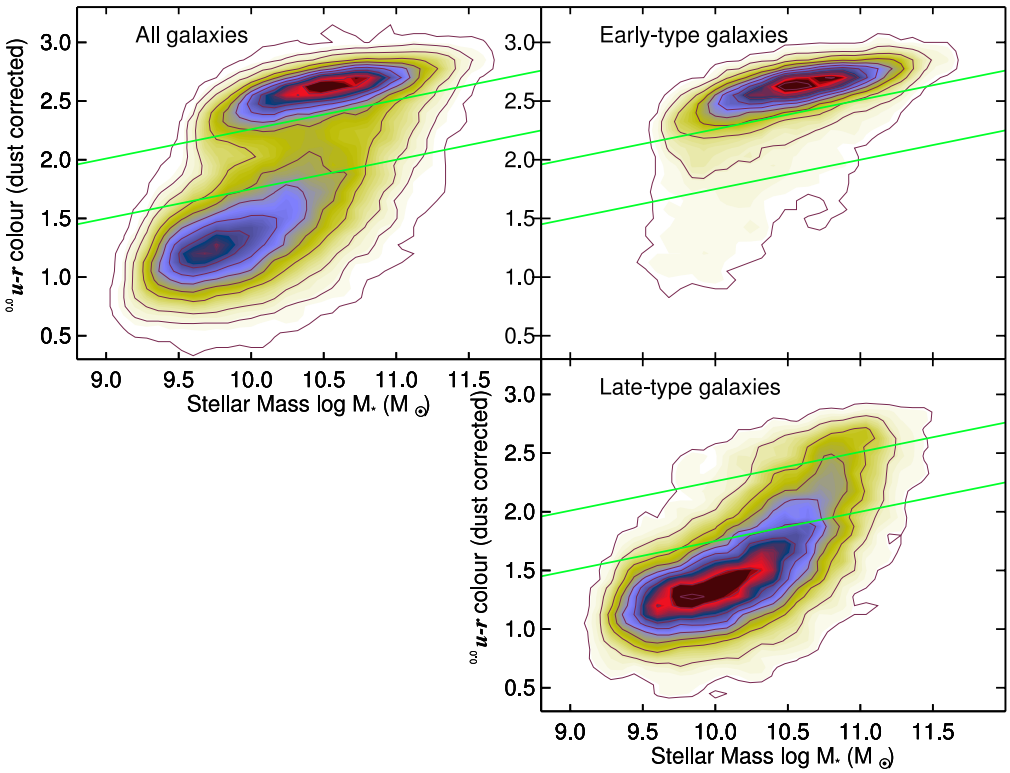

Figure 1.2: Colour ($\mathcal{U} - \mathcal{R}$) vs stellar mass for nearby galaxies from the SDSS all-sky survey, separated by visual morphological classifications done through the Galaxy Zoo project. In the left-hand panel the 'red sequence' and 'blue cloud' are clearly visible in the top and bottom concentrations of galaxies respectively. Separating the galaxy by morphological type further reveals the correlation between colour and morphology, with early-type galaxies (elliptical or bulge dominated) being red and typically more massive and late-type (spiral or disc dominated) being blue and of lower mass. Figure from Schawinski et al. (2014).

In addition to the wide diversity of galaxy morphologies, local galaxies span a wide range in luminosity and stellar mass (several orders of magnitude). Furthermore, not only do overall galaxy luminosities vary, they come in a wide range of colours (the ratio of luminosities or fluxes in two different photometric filters), which appear to be linked to the morphological type. Early-type galaxies (including ellipticals and lenticulars) generally have redder colours than late-type galaxies (spirals and irregulars), i.e. the luminosity in the longer wavelength filter is high relative to that in the shorter 'bluer' filter[2]. This bi-modality is particularly well illustrated by the galaxy colour-magnitude (or colour-mass) diagram, an example of which is shown Figure 1.2.

[2]There are caveats to this statement, in that the reddening of galaxy colours by the attenuation of dust must also be taken into account. Section 1.3 of this introduction explores in more detail the processes and difficulties of measuring galaxy properties through their colours.

Since the colour of a galaxy is intrinsically related to the age of its stellar population, the observed bi-modality is indicative of differences in the formation histories between early and late-type galaxies. More specifically, redder galaxies are generally older and/or more chemically enriched than bluer galaxies. The early-type galaxies that make up the red sequence must therefore have built up their stellar mass and ceased star-formation earlier (on average) than the late-type galaxies which make up the blue cloud. The idea that the most massive galaxies formed first and quickest is known as 'downsizing' (Cowie et al., 1996), and at first seems contrary to what would be expected in the simple hierarchical structure formation models, whereby the largest galaxies would be formed later in cosmic history through the merging and build-up of many smaller galaxies (De Lucia et al., 2006).

One of the primary aims of modern astronomy is to understand how this bi-modality was formed, and what physical processes governed the evolutionary pathways of these different galaxy types. By studying in detail the stellar populations, chemistry and kinematics of local galaxies, it is possible to work backwards to understand their histories. However, the beauty of a Universe in which light has a finite travel time is that we are able to peer back through cosmic history and see these processes in action, providing a direct view of galaxy formation and evolution at earlier times.

Observations of the star-formation rate density indicate that the star-formation history of the Universe peaked at around two to three billion years after the Big Bang at a redshift of $2 \lesssim z \lesssim 3$ (Figure 1.3), indicating that the majority of stellar mass in galaxies was formed more 6 Gyr ago. Studies of galaxy morphologies through time have also shown that the Hubble sequence began to form in the few billion years following this peak in star-formation (Mortlock et al., 2013).

In addition to extensive study of galaxy star-formation rates and stellar masses since the epoch of peak star-formation (sometimes dubbed 'Cosmic high-noon'), much work has also gone into measuring the merger history of galaxies across time. By studying the statistics of galaxies in close pairs (Patton et al., 2000; Le Fèvre et al., 2000; Bell et al., 2006; Bluck et al., 2009, 2012) and the fraction

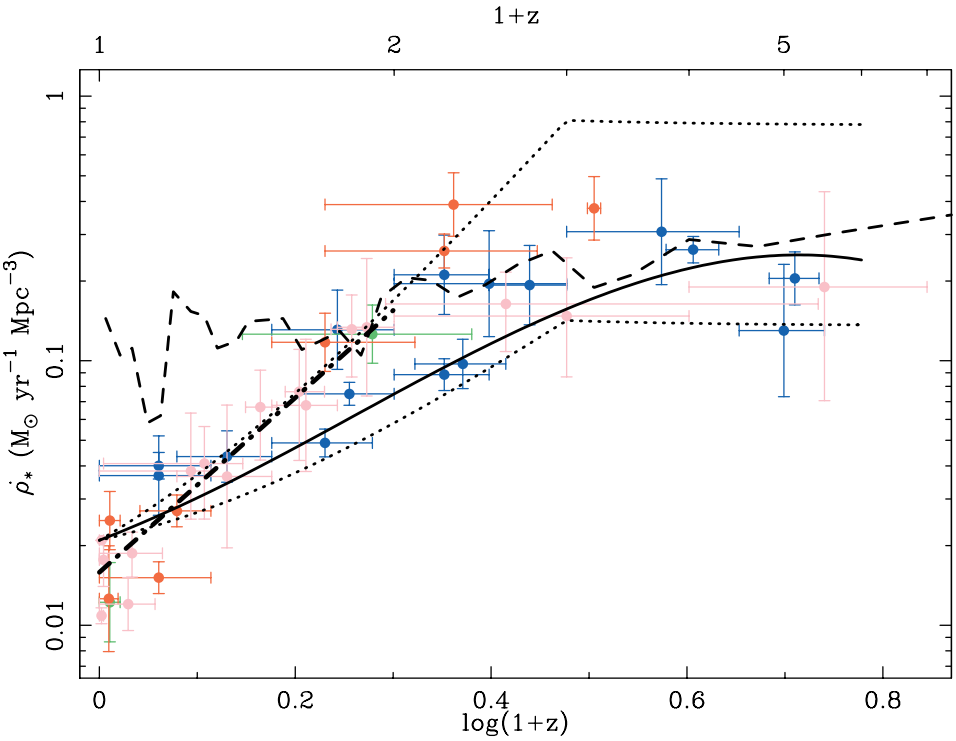

Figure 1.3: Evolution of the star-formation rate density through cosmic time. Data points are colour-coded corresponding to the star-formation rate indicator, with UV (blue), [OII] and Hα/Hβ (green and red respectively) and Xray/far-infrared/sub-millimetre and radio estimates (pink). The dot-dashed line at $z < 1$ shows the best-fitting line to the collective data. The solid and dotted lines show estimates additional radio based SFR estimates while the long-dashed line shows the 'fossil' record from local group galaxies. Figure from Hopkins (2004), see references therein for individual SFR density citations.

of galaxies which show signs of morphogical disturbance due interactions with nearby companions (Conselice et al., 2003, 2008; Lotz et al., 2011), the merger rates of galaxies have been well studied as far back as $z \sim 3$. Extending such analysis to earlier epochs and to lower mass galaxies has however proved difficult, with very few even attempting to do so (Conselice & Arnold, 2009).

As mentioned previously, one of the key predictions for structure formation in a ΛCDM universe is that mergers play a vital role in the formation and evolution of galaxies. Furthermore, mergers are also a potential driver for evolution in other galaxy properties such as their structure, kinematics and morphology (Conselice, 2014). Between the peak in the cosmic star-formation history and now, the progenitors of today's most massive galaxies grew through almost equal parts of star-formation, major mergers and minor mergers (Ownsworth et al., 2014). Understanding how those galaxies assembled before that time represents one of the current challenges in extragalactic astronomy.

It is also thought that major mergers, and in particular mergers between gas-rich galaxies, may be important in fuelling the growth of central super-massive black holes of galaxies (Springel et al., 2005; Hopkins et al., 2008b,a). Measuring the abundances of gas-rich mergers through time is therefore essential in linking them to the rise and fall of AGN and starburst activity through cosmic history.

In Chapters 2 and 3 of this thesis, we aim to better understand how those progenitors grew into what we see at $z = 3$ through studying the stellar mass growth, star-formation rates and merger histories of galaxies during the first few Gyr of galaxy formation. Until recently, the ability to find and observe galaxies as far back as the first two billion years of the Universe was just not possible. In the last two decades however, huge leaps in both the technology and observational techniques has allowed for remarkable progress in studying the first galaxies.

1.2.1 Illuminating the dark ages

The first realisation that galaxies could be observed at truly cosmological distances was made by Maarten Schmidt who measured the redshifts of five quasi-stellar objects (QSOs) out to $z \approx 2$ (Schmidt, 1965). These QSOs, or quasars, are now better understood to be the emission from accretion onto the super-massive black holes at the centre of galaxies. At the time of these measurements, their properties were still very a much a mystery.

Around this time, Partridge & Peebles (1967) made the first predictions of the potential to detect normal star-forming galaxies at early times through their bright Ly-α emission, the UV continuum emission and the Lyman absorption decrement. All UV bright galaxies exhibit a characteristic drop at 912Å (the ionization energy of neutral hydrogen) and in young star-forming galaxies rich in cold gas (and hence neutral hydrogen) this break was expected to be very strong. It was therefore hoped that such a strong spectral feature provide an excellent way of identifying high-redshift galaxies. Despite valiant attempts along the way (Meier, 1976), it would be several decades before such searches became successful.

By using a carefully selected set of optical filters, Steidel & Hamilton (1992) were

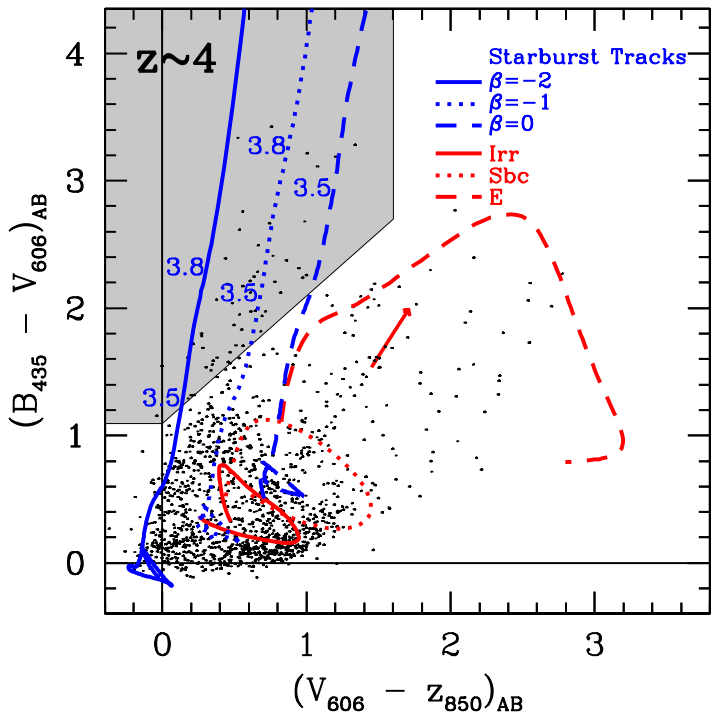

Figure 1.4: Two-colour diagram illustrating selection criteria used to select $z \sim 4$ ('B dropouts') in the Hubble Ultra Deep field by Bouwens et al. (2009). The blue solid, dotted and dashed lines illustrate the colour tracks as a function of redshift for galaxies with UV continuum slopes of $\beta = -2$, -1 and 0 respectively. The red lines show the comparable tracks for standard morphological types at lower redshift.

able to successfully select an ordinary star-forming galaxy at $z \sim 3.4$ based on the photometric colours of filters either side of the redshifted Lyman absorption decrement at $z \sim 3$. This technique, now commonly known as Lyman break selection, made it possible to easily select galaxies at high redshift with a good degree of reliability using only photometric surveys.

In contrast to the relative stagnation of the preceding two decades, the subsequent years have seen a relentless and rapid progression in the study of galaxies at high-redshift. Following the first few detections through the Lyman break technique, the *Hubble* Deep Field allowed this technique to applied further, to redshifts of $z \sim 4$ and beyond (Steidel et al., 1995; Madau et al., 1996) (see Figure 1.4 for an example of the colour criteria used to select such galaxies). Spectroscopic confirmation of the brightest $z \sim 3$ Lyman break galaxies soon followed (Steidel et al., 1996). During this time, the first successful detection of high-redshift galaxies through their Ly-α emission line were also made (Hu & McMahon, 1996; Hu, 1998; Cowie & Hu, 1998), finally confirming the predictions of Partridge &

Peebles.

Now proven successful, the availability of deep optical data from both ground and space based instruments meant that the selection of high-redshift galaxies could be extended both to fainter samples and out to even higher redshifts ($z \sim 6$) both photometrically (Steidel et al., 1999; Thompson et al., 2001; Thompson, 2003; Fontana et al., 2003; Stanway et al., 2003; Giavalisco et al., 2004b; Dickinson et al., 2004; Capak et al., 2004) and spectroscopically (Bunker et al., 2003; Stanway et al., 2004b,a). At $z \gtrsim 6.5$ the Lyman break has been redshifted out of the optical wavelengths into the near-infrared regime ($\lambda \sim 1\mu$m) where observations deep enough to make strong detections of galaxies above the break at $z \sim 7$ were much more difficult, although not impossible (Bouwens et al., 2004). There was however a limit to how far this method could be pushed with the existing ground and space-based facilities, temporarily putting the rush to ever higher redshifts into a somewhat lower gear (for now).

The installation of the Wide-field Camera 3 (WFC3) on the *Hubble Space Telescope* in spring 2009 came as a particular boon to the study of detection of galaxies at $z \sim 7$ and beyond. With a significantly more sensitive near-infrared detector, as well as an improved filter set and increased field-of-view compared to the previous NICMOS camera, the earliest data taken with the WFC3/IR camera allowed several independent groups to find robust samples of galaxies at $z \sim 7$, deep into the epoch of reionization (Bunker et al., 2010; Finkelstein et al., 2010; Grazian et al., 2011; Labbé et al., 2010; Oesch et al., 2010, 2012; Bouwens et al., 2010, 2011c). The greatly improved survey efficiency has also meant that large-scale *Hubble* projects such as CANDELS (Grogin et al., 2011) and 3D-HST (Brammer et al., 2012) are now able to make deep near-infrared surveys over far wider areas than possible with NICMOS. In Section 1.4 we present further details of the CANDELS survey and its aims.

Alongside the advances in space based near-infrared observations has also come advances in the sensitivity of ground-based telescopes. Although not able to reach the same depths as those possible with WFC3, the wider field of view means that deep ground-based surveys such as UltraVISTA (McCracken et al., 2012) or the

UKIDSS Ultra Deep Survey (Lawrence et al., 2007; Cirasuolo et al., 2007) can survey far larger areas ($> 1\mathrm{deg}^2$) than HST and allow for searches of the brightest but rarest sources at $z > 4$ (McLure et al., 2006, 2009; Castellano et al., 2010).

It is not just at the most extreme redshifts for which the addition of deep near-infrared observations have been of benefit. With an increase in the number of optical and infrared filters has also come an increase in the use of photometric redshift selection in place of the traditional colour-colour Lyman break selection (McLure et al., 2006, 2010). Photometric redshift analysis typically works by fitting a set of known template spectra (either empirical or model generated) to the full range of broadband filters available for a galaxy in order to find the redshift that minimises χ^2 (Bolzonella et al., 2000; Brammer et al., 2008) or maximises some Bayesian likelihood (Benítez, 2000)[3].

The estimation of photometric redshifts is strongly dependent on the ability of the method to identify key spectral features in the observed data, especially the main Balmer and Lyman spectral breaks. In this regard, the use of photometric redshifts to select galaxy at $z > 3$ is not far removed from Lyman break selection. However, the benefit of photometric redshift analysis is that it is able to take into account the shape of the galaxy spectrum above the break and at other points in the spectrum to discern between similar spectral features which would otherwise be degenerate in a single colour. Perhaps more importantly, photometric redshifts also make it possible to quantify the uncertainty in identifying these spectral features in a way that a binary yes-or-no colour selection cannot (e.g. Dunlop et al. 2007). In Chapter 2 of this thesis, we investigate the potential discrepancy between the two selection methods at high-redshift and illustrate the advantages of photometric redshifts when sources suffer from significant photometric scatter.

It is worth noting that the selection of high-redshift galaxies through their rest-frame UV emission is no longer the only option. Developments in detectors of all types has led to galaxies at $z > 3$ being found through their rest-frame optical and near-infrared (Franx et al., 2003; van Dokkum et al., 2003) and sub-mm/far-

[3]Other more novel approaches such as the use of artificial neural networks (Collister & Lahav, 2004) have also been applied but have not gained such widespread usage.

infrared (Walter et al., 2003; Robson et al., 2004) emissions and via gamma-ray bursts (Haislip et al., 2006; Kawai et al., 2006; Tanvir et al., 2009).

1.2.1.1 Sample contamination

While there now exist several methods for selecting high redshift galaxies from large photometric catalogs, it is also vitally important to take into account the range of other (non-) astrophysical sources which can also satisfy high redshift selection criteria. Potential contaminants for high-redshift galaxy samples can broadly be separated into types; each corresponding to a different scale within the Universe.

Firstly, there is local or instrumental contamination to contend with. When pushing the selection of galaxies to the very limits of its current detection capabilities, cosmic rays or image artefacts in *Hubble Space Telescope* (HST) photometry can have an increased effect on the generation of spurious sources in catalogs. In any single HST photometry exposure, numerous pixels within the CCD detector will be hit by cosmic rays passing through the telescope resulting in bright over saturated pixels in otherwise empty areas of the sky.

For the vast majority of circumstances, such cosmic ray hits are not a problem. Since the distribution of affected pixels is entirely random, by taking multiple exposures it is much easier to identify the effected pixels and exclude (or 'mask') them from the final reduced images. Furthermore, if such a spurious source is missed by these cosmic ray rejection algorithms (e.g. van Dokkum 2001) and results in a statistically significant detection in the resulting photometry catalog, the lack of any source detection in other photometric bands will serve to identify the source as contamination. However, if no such detection in any other photometric band is actually expected (as is precisely the case for potential $z \sim 10$ to 12 galaxies), such spurious sources pose a genuine problem and must be considered carefully (Bouwens et al., 2011b). Taking the potential detection of a $z \sim 10$ galaxy by Bouwens et al. (2011b) as an example, the non-spurious nature of the detection was determined by confirming its detection in two independent subsets of the data (i.e. exposures taken in different years). Such a confirmation

does not necessarily mean that the object in question is definitely at high redshift (Brammer et al., 2013) but it can at least rule out that source as a spurious detection.

A second major source of potential contamination is low-mass stars within the Milky Way itself (Caballero et al., 2008). For low-mass stars, the combination of a cool blackbody temperature for the underlying stellar emission and strong absorption lines within their atmospheres (e.g. TiO, H_2O, CH_4) can combine to produce broadband photometric colours which are very similar to those of galaxies at $z \gtrsim 6$ (Finkelstein, 2014; Wilkins et al., 2014). The classification of objects as stars (and their exclusion from high-redshift galaxy samples) is most difficult for ground-based observations, where the larger point-spread function makes separating compact distant galaxies from stellar point sources more difficult (Bowler et al., 2012, 2013). However, even for observations with high resolution HST photometry, it is still necessary to use additional information such as photometric colours or spectroscopy to discriminate between stellar and extragalactic sources (Stanway et al., 2008; Pirzkal et al., 2009).

Finally, other extragalactic sources can also pose problems in creating clean and robust samples of galaxies at $z > 3$. For photometric selection of high-redshift galaxies, dusty red galaxies at lower redshifts can cause significant confusion in the selection methods and can be a major source of contamination. The confusion occurs due to the similarity in colours between the Lyman break at high redshift and a Balmer/4000Å break with strong dust attenuation (at $\approx 3 - 5\times$ lower). It is precisely this confusion between spectral features which the inclusion of long wavelength *Spitzer* data in photometric redshift fitting is intended reduce (McLure et al., 2011).

A second class of potential low-redshift galaxy contaminants are extreme-emission line galaxies (EELGs) at $z > 1$ (van der Wel et al., 2011; Atek et al., 2011). Although they do not strongly affect most photometric selection methods they do pose a problem when searching for high redshift galaxies via their Lyman-α emission or when looking for Lyman break drop-outs at the very highest redshifts (Brammer et al., 2013). EELGs have been found to be low-metallicity dwarf

galaxies which are undergoing starbursts, resulting in optical emission lines (e.g. [OIII]) with extreme equivalent widths and faint continuum photometric detections similar to those expected for high redshift Lyman-α emitters. Depending on the precise redshift (and hence the position of rest-frame optical emission within the corresponding broad band filters) the photometric colours of these lower redshift interlopers can also mimic the broadband selection criteria of $z \sim 8$ galaxies (Atek et al., 2011).

1.2.2 The first billion years of galaxy evolution

With the detection of statistically significant numbers of high-redshift galaxies has come the ability to begin measuring the fundamental properties of the galaxy population in this epoch with some degree of reliability and accuracy. Of particular interest is the measurement of the galaxy luminosity function (LF) as it represents a key observable for studying the evolution of the galaxy population across time. At rest-frame ultraviolet wavelengths ($\sim$ 1500 Å), as is observed at high-redshift, the UV luminosity is also closely related to the ongoing star-formation so studying the shape and evolution of the UV luminosity are vital in understanding the physical processes which govern star-formation across history.

At low redshift, the luminosity function of galaxies is well described by the Schechter (1976) parametrisation, whereby the number density of galaxies, ϕ, at a specific magnitude, M, is given by

$$\phi(M) = 0.4 \ln(10) \phi^* \ 10^{-0.4(M-M^*)(\alpha+1)} \ \exp(-10^{-0.4(M-M^*)}) \qquad (1.1)$$

where α is the power-law slope of the faint end of the luminosity function, M^* the characteristic magnitude beyond which the number densities exponentially decline and ϕ^* the normalisation. Understanding the evolution of the faint end slope and characteristic magnitude is vital for several reasons.

Firstly, since the overall luminosity density (and hence the underlying star-formation rate density) is strongly dependent on the slope of the luminosity function, accurately measuring the UV LF during the EoR is vital to understanding how or when galaxies were able to reionize the Universe. Measurements of the

rest-frame UV luminosity function at high redshift have shown that the faint-end slope gets steeper with redshift (Bouwens et al., 2007, 2015b; Finkelstein, 2014), indicating that the star-formation rate density is increasingly dominated by faint galaxies. Chapter 4 of this thesis explores what these observations mean for the ability of galaxies to reionize the inter-galactic medium during the epoch of reionization.

Secondly, the shape of the luminosity function is governed by the nature of feedback within star-forming galaxies and thus provides a vital constraint on models of galaxy formation (Bower et al., 2006) – the slope of the luminosity function is strongly dependent on the strength of feedback resulting from supernovae and stellar winds while the exponential cut-off at the bright-end of the LF is likely caused by feedback from active galactic nuclei or some other quenching mechanism (Benson et al., 2003; Peng et al., 2010). The limitation of the UV luminosity function as a tool for studying these processes however is that it is particularly sensitive to the dust-extinction within the star-forming galaxies. In order to enable comparisons with theoretical predictions is necessary to either a) correct for the effects of dust extinction in the observations or, b) include a prescription for dust within the theoretical predictions.

If we wish to fully understand the physical processes governing star-formation in galaxies, what we really wish to measure are the fundamental galaxy properties such as stellar mass or the ages and metallicities of the stellar populations within a galaxy. In addition to providing much more information about the differences between galaxy samples, they enable direct comparison with computational or analytic models of galaxy evolution which can be used to understand the physical mechanisms behind such differences.

Out to redshifts of $z \sim 3$, current estimates of the stellar mass function (SMF) indicate that the characteristic mass or 'knee' of the SMF evolves very little for star-forming galaxies (Ilbert et al., 2013; Muzzin et al., 2013). This fixed mass has been interpreted as evidence for some sort of characteristic quenching mass, beyond which star-formation is suppressed much more strongly. If such a model is the case, it could also potentially account for the characteristic correlation be-

tween age and stellar mass of downsizing (Peng et al., 2010). If this characteristic mass is independent of redshift as the observations suggest, at earlier times in the Universe we could expect the *apparent* shape of the high mass end of the galaxy SMF to differ from the exponential cut-off of the Schechter function: as the galaxy population grows, until the most massive galaxies reach the characteristic mass and begin to be suppressed, the observed stellar mass function would exhibit a pure power-law form.

In recent observations by Bowler et al. (2013), there is evidence that the slope of the bright end of the LF begins to diverge from the exponential decline of the Schechter function, potentially indicating the onset of mass-quenching. However, because of the particular sensitivity to dust attenuation, such evolution could also be plausibly explained by the evolution of dust content in galaxies at early times. Making accurate measurements of the stellar-masses and star-formation rates of galaxies at $z > 3$ and their distributions within the galaxy population (i.e. the stellar mass or star-formation rate functions) would provide much more robust ways of discerning between the different evolutionary models. However, unravelling the fundamental properties of galaxies from their integrated light is a non-trivial task. The following section, Section 1.3, explores in greater detail the link between the optical/infrared emissions of a galaxy and its properties. We first introduce the models and simulations of galaxy formation and evolution which have become essential to understanding and interpreting the observed properties of galaxies.

1.2.3 Numerical simulations and models of galaxy formation

While great improvements have been made in measuring the properties of galaxies in the early Universe, there is still only limited amount of data available for individual high-redshift galaxies. Thus in order to improve our understanding of the processes which drive galaxy evolution it is necessary to interpret the available observations by comparing the bulk properties of galaxy samples with theoretical predictions and the results of extensive simulations. However, in order to interpret

observations through models in this way, it is necessary to understand the biases and limitations of both the observations and the models.

Within this thesis, we compare observational results to two distinct types of astrophysical model; *hydrodynamical* and *semi-analytical*. The full details of how individual models were produced or simulated and the various techniques and assumptions involved can be found within the corresponding references, whilst a broader overview can also be found in the recent review by Somerville & Davé (2014). However, the significant use of these models in Chapters 2 and 3 merits some discussion on the general features of these models and their limitations.

- Numerical hydrodynamic models:

  Hydrodynamic models represent the most involved way of modelling the formation and evolution of galaxies, solving the various equations of state (gravity, hydrodynamics and thermodynamics) for dark matter, gas and stars simultaneously. Although computationally expensive, the scale of hydrodynamic models has now grown to the point where the latest generation of models are able to simulate large cosmologically representative volumes, models such as the EAGLE (Schaye et al., 2014) and *Illustris* (Vogelsberger et al., 2014) projects.

  By modelling all three matter components concurrently (dark matter, stars and gas), it is possible to take into account their effect on each other and make predictions for the densities and kinematics of the various components as well as predictions for the temperatures and chemical evolution of the gas in galaxies through time.

  However, due to the technical limitations on the dynamic range which can be studied, many of the crucial physical processes which occur on smaller scales (star formation and the growth or feedback of black holes) must be included using so-called "sub-grid" models. Such simulations are also still subject to significant systematics due to various computational parameters and methods. Care should therefore be taken when interpreting numerical model predictions of properties like kinematics, as emergent properties and trends can be driven not just by the physics included in the modelling but

also by the effects of resolution, scale lengths or choice of algorithm.

- Semi-analytical models:

  Another class of models commonly used to simulate galaxy evolution are semi-analytical models, or "SAMs". Rather than explicitly solving the hydro- or thermodynamic equations for a set of model particles/cells, SAMs use a set of simplified analytical models built on top of a dark matter only cosmological simulation (where only gravity is taken into account).

  In comparison to hydrodynamical models, SAMs (and the underlying dark matter only simulations) are computationally much less expensive. They can therefore be used for much larger volumes as well being run with greater frequency, allowing for many different model prescriptions to be compared.

  The simplicity of the physical prescriptions included in SAMs is both a strength and a weakness when it comes to interpreting model predictions and understanding the physical process in galaxy evolution. On the one hand, the speed gained from using simple prescriptions means it is possible to explore in detail the effects of individual parameters or physical prescriptions on the properties of the model galaxy population through numerous simulation runs. On the other hand, since most of the key physics must be included manually, the model predictions and their accuracy are limited by restrictions or omissions of the physical prescriptions we put in.

Another aspect of both types of model to consider, is that they are all tuned in some capacity to a set of observations such as the $z = 0$ stellar mass function and this is often done by hand. The tuning therefore does not necessarily take into account the same properties at higher redshift and how they evolve through time, or any potential errors on the tuning parameters.

Newer generations of semi-analytic model are at least beginning to take account of these problems, using Markov Chain Monte Carlo techniques to statistically constrain parameters and their uncertainties (Lu et al., 2011; Henriques et al., 2013), and comparing to observations over large spans of cosmic history (Henriques et al., 2013). Comparing observations of high redshift galaxies with pre-

dictions from either hydrodynamical or semi-analytical models must therefore be done with caution, bearing in mind the potential limitations and drawbacks of each model individually.

1.3 The spectral energy distributions of galaxies

Using the panchromatic spectral energy distribution (SED) of a galaxy to estimate its stellar mass (or other physical property of interest) has become an increasingly prevalent and powerful technique as extensive multi-wavelength catalogs of galaxies have been built-up. At its simplest, the shape of a galaxy's SED tells us about the mass-to-light ratio, $\mathrm{M}_{\star}/L$, and its overall normalisation can be used to estimate the corresponding total stellar mass. The shape of the SED itself (and hence the $\mathrm{M}_{\star}/L$) is a product of almost every physical property of the baryonic matter in a galaxy and can tell as about both the past and present stellar, gas and dust properties.

Firstly, the age of the underlying stellar population (and by association the galaxy's star-formation history) as well its metallicity (Z) history are encoded into the stellar emission. Secondly, the initial stellar emission can then be absorbed by the surrounding gas and dust and re-emitted as atomic and molecular emission lines as well as thermal dust emission at longer wavelengths. The observed SED is therefore also a function of the inter-stellar medium and the distribution, mass and grain sizes of the dust within a galaxy. The importance of dust in particular is highlighted by the fact that of the total extragalactic background light, approximately half of the total energy is in the form of infrared radiation (~ 4 to ~ 1000 μm) emitted by dust particles heated by the stellar UV/optical emission (Hauser & Dwek, 2001).

Just what can be learned from the integrated light of a galaxy is highly dependent both on the quality of the data (including whether it is photometric or spectroscopic) and the model ingredients used to interpret that data. The physical properties of interest will inform and direct the specifics of what models are fitted and how this fitting is done, but the overall principles remain broadly

similar.

When using stellar population synthesis to interpret galaxy SEDs, the basic building blocks are simple stellar populations (SSPs) – the SED of a single stellar population formed at the same time with a single metallicity and initial mass function (IMF). SSPs are typically constructed from a combination of empirical stellar spectral libraries and stellar isochrones that relate the effective temperature ($T_{\rm eff}$), surface gravity ($\log g$) and stellar mass (M) for the desired age and metallicity. The exact details of transforming these properties into a library of SSPs are specific to each individual implementation and are often influenced by the limitations of the spectral libraries or isochrones being used (e.g. Leitherer et al. (1999); Bruzual & Charlot (2003); Maraston (2005) – see also the review by Conroy (2013) for further details on the wider issues and limitations). Crucially, since the outputs of these models is simply the flux as a function of wavelength for a given set of population parameters, they can both be easily compared with each other and used in identical ways.

With a suite of SSPs, composite stellar populations (CSPs) can be constructed to simulate more complicated star-formation and metallicity histories as well as more complicated treatments of dust attenuation and emission (for example as a function of age – Charlot & Fall 2000). In theory, SFR(t) (or SFH – the star-formation history) and $Z(t)$ can be arbitrarily complex. However, in practice this would require huge computational expense and with most data lead to minimal increase in accuracy for estimates of stellar masses over simpler model assumptions. Two such simplifications are commonly made: firstly, that for a given composite stellar population the metallicity is fixed to a single value; and secondly, the SFH can be parametrised as a simpler time dependent function with one or more parameters.

Most commonly used is a SFH which decays exponentially over some characteristic timescale, τ, such that SFR(t) $\propto \exp(-t/\tau)$. More recently, it has been shown that rising star-formation models (e.g. negative τ's) are both a better a fit to the observed photometry of high-redshift galaxies (Maraston et al., 2010) and a better representation of the theoretical predictions from simulations (Finlator et al.,

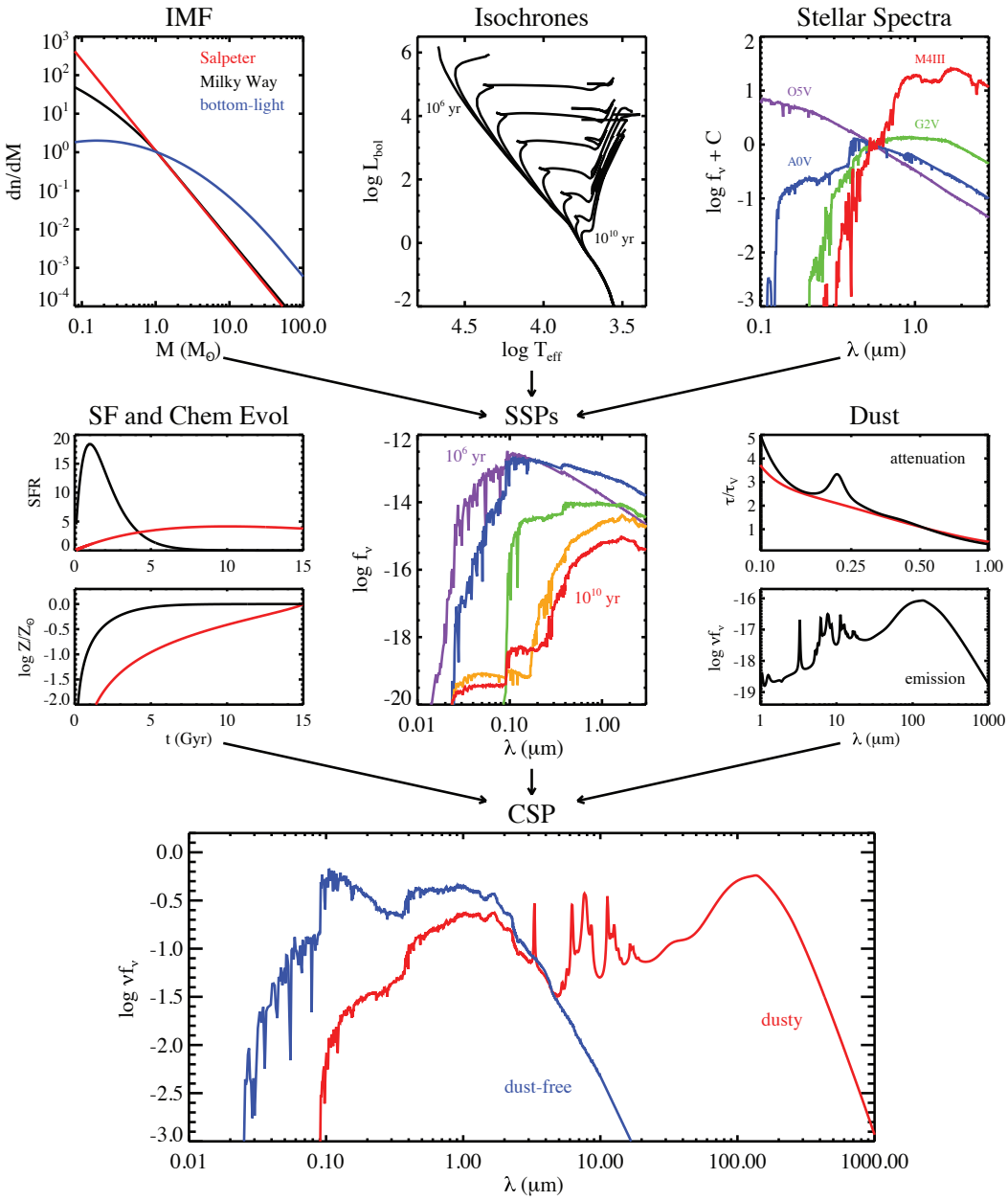

Figure 1.5: Schematic diagram of the steps in building composite stellar populations from Conroy (2013). The ingredients for simple stellar populations on the top row; the initial mass function, stellar isochrones and stellar spectra – are combined to make SSPs for different ages and metallicities. The SSPs are then combined based on a star-formation and metallicity history, before dust attenuation is applied (and the corresponding emissions then modelled) to make composite stellar populations. In the bottom plot, the blue spectrum represents the intrinsic stellar emission for the CSP while the red line shows how this spectrum changes due to dust.

2011; Dayal et al., 2013). Other simple single parametrisations have also been applied such as the 'delayed' model ($\propto \frac{t}{\tau^2}\exp(-t/\tau)$). At high-redshift, there is also now evidence that the average SFH is best-fit by an increasing power-law form (Papovich et al., 2011; Salmon et al., 2015) rather than previously assumed exponential form. Another novel approach to constructing plausible and accurate star-formation and metallicity history is that of Pacifici et al. (2012), whereby a large number of SFR and Z histories from semi-analytic models are used to construct a more set of realistic CSPs for fitting.

However the SFR and metallicity histories of models are parametrised, what is most important is that the chosen models can accurately represent the full dynamic range of observed galaxy photometry and give un-biased estimates of the stellar population properties we are interested in measuring. At $z > 3$, when the Universe is less than $\sim$ 2 Gyr old, the upper limits on the possible stellar ages means that degeneracies introduced into SED fitting from the SFH alone are somewhat reduced (Schaerer et al., 2013).

Another critical assumption in the use of SPS modelling is the choice of initial mass function. Unfortunately, it is not possible to constrain the IMF from the integrated light of galaxies alone. There exist just too many degeneracies to make any useful constraints except for the most special circumstances. Without direct measurements of the IMF in distant galaxies, we are limited to the assumption of a fixed and universal IMF based on measurements of the local IMF such as the canonical Salpeter (1955) or Chabrier (2003) and Kroupa (2001) functions.

While the optical and near-infrared filters of *Hubble Space Telescope* are ideally suited for selecting galaxies at high-redshift due to the position of the redshifted Lyman break at $4 < z < 7$, they are not well-suited for deriving accurate stellar population properties such as stellar mass. This is because the rest-frame UV continuum probed by these filters is predominantly produced by young stars so is dominated by recent star-formation and (as mentioned in Section 1.2.2) is particularly sensitive to dust attenuation. Mid-infrared observations from the IRAC camera (Fazio et al., 2004) aboard the *Spitzer Space Telescope* have been essential to making reliable estimations of galaxy properties at high-redshift, especially the

deep observations at 3.6 and 4.5 μm made during *Spitzer's* post-cryogenic mission (e.g. Ashby et al. 2013). By extending the observations to mid-infrared wavelengths, it means constraints on the rest-frame optical emission of (brighter) high-redshift galaxies out to $z \geq 7$ are now possible.

Probing the rest-frame optical emission however comes with its own potential pitfalls. At $z \geq 4$ the bright nebular emission lines (such as Hα, [OIII] and [OII]) are redshifted into the 3.6 and 4.5 μm IRAC bandpasses, potentially contaminating the broadband fluxes and systematically biasing the SED fitting. Early studies of galaxy SEDs at high redshift suggested that the measured stellar masses and ages may be systematically over-estimated because of such contamination (Schaerer & de Barros, 2009, 2010; Ono et al., 2010). Accounting for the effects of nebular emission in SED fits is therefore vital in making un-biased measurements of galaxy properties at high-redshift.

At the onset of the work undertaken in this thesis, constraints on galaxy stellar masses at $z \geq 4$ were limited either by the small samples (González et al., 2011) with WFC3 observations, or the limiting depth of ground-based near-infrared observations (Stark et al., 2007) available at the time. However, a new generation of deep near-infrared surveys means that it may now be possible to make robust studies of galaxy stellar mass evolution over the first few billion years of galaxy evolution.

1.4 The CANDELS survey

Regions of the sky that have been well studied by the *Hubble Space Telescope*, such as the GOODS fields (Giavalisco et al., 2004a), have become increasingly valuable resources for studying the evolution of galaxies (and the growth and activity of super-massive black holes) through cosmic time. This advance is thanks to the ever-growing wealth of observations across the whole electromagnetic spectrum, regularly reaching the most extreme depth observed at any particular wavelength. However, the deep fields such as GOODS North and South cover only very small areas of the sky ($\sim$ 320 arcmin^2 combined for Hubble data) and the extremely

deep *Hubble* Ultra Deep Field extending to only a small fraction of this. Such small fields can lead to large uncertainties in galaxy counts due to cosmic variance and also makes them poor for studying the brightest and most massive objects.

While the deep optical coverage from *Hubble's* Advanced Camera for Surveys (ACS) has allowed the Lyman break selection of galaxies out to $z \sim 6$ and provided rest-frame optical morphologies of lower redshift galaxies, in order to extend this analysis to greater redshifts requires near-infrared observations of comparable depth to those existing at shorter wavelengths. Near-infrared surveys reaching to depths of $H_{160} \gtrsim 26$ *were* possible with the NICMOS camera, but were severely limited by the survey efficiency of the instrument with respect to its optical counter-part, ACS. The GOODS NICMOS Survey (GNS, Conselice et al. 2011) observed parts of the GOODS North and South fields to a depth of $H_{160} \sim 26.5$ (cf. $V_{606} = 27.8$, Giavalisco et al. 2004a). Surveying 45 arcmin^2 to this depth in just one single filter required 180 orbits of Hubble observations. Clearly, extending such a survey to more filters and significantly greater areas was not feasible with the existing facilities. Furthermore, using ground-based facilities, the depths required to detect all but the brightest sources are just not possible, even with the largest 8m+ telescopes.

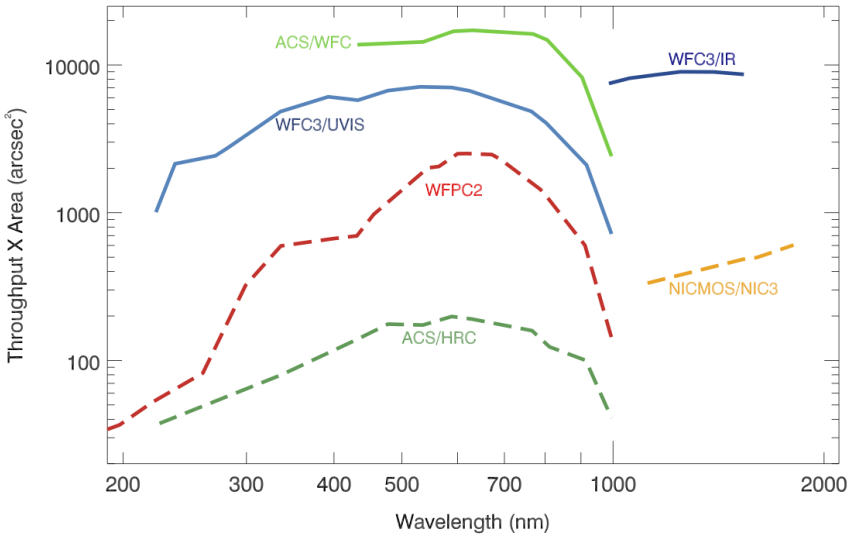

Figure 1.6: Discovery efficiency (defined as the field of view area multiplied by the system throughput) of the Hubble Space Telescope detectors. The order of magnitude increase in efficiency at near-IR wavelengths from NICMOS (orange dashed line) to WFC3 (solid dark blue line) is well illustrated. Credit: STScI/Space Telescope Science Institute

Thankfully, the greatly improved capabilities of the Wide Field Camera 3 (WFC3), installed in *Hubble* as part of the final service mission, such a task was made considerably more feasible. The stark increase in efficiency at infrared wavelengths is illustrated in Figure 1.6. Furthermore, for equivalent exposures and signal-to-noise, the limiting magnitude of the WFC3/IR is up to ~ 1 magnitude fainter than that of NICMOS.

The CANDELS project (Cosmic Assembly Near-infrared Deep Extra-galactic Legacy Survey) leverages the new infrared capabilities to make observations which are both deeper and more extensive than previously available for the key legacy fields. Awarded 902 orbits of *Hubble* time, CANDELS represents the largest HST project in its history. The final survey program involved observations of five key extra-galactic survey fields – GOODS South, GOODS North, the extended Groth strip (EGS), the UKIDSS Ultra Deep Survey (UDS) and the COSMOS field – with observations of these fields split into two distinct tiers.

The first (and deepest) of these tiers, hereafter CANDELS/Deep, is primarily comprised of observations over parts of the GOODS North and South (totalling 120 arcmin^2) to a depth of ~ 13 Hubble orbits. The second shallower tier (CANDELS/Wide) consists of observations over all five fields with $\sim 2-3$ orbits per tile and covering 668 arcmin^2 to a depth comparable or greater than that in the GNS.

The first deep field completed was the GOODS South field and is the basis for the majority of the analysis undertaken throughout this thesis. Full details of this dataset can be found in Guo et al. (2013), including the data reduction and homogenisation of the respective space and ground-based ancillary data.

In the context of the many outstanding questions in galaxy formation and evolution, the CANDELS survey set out with a wide range of primary scientific goals in four key areas:

1. *Cosmic Dawn*: the formation and early evolution of galaxies ($z > 4$)
2. *Cosmic High Noon*: the peak of star-formation and AGN activity ($1 < z < 3$)

3. Ultraviolet Observations: Hot stars at $1 < z < 3.5$

4. Supernovae: Standardizable candles beyond $z \sim 1$

It is the first of these areas in which the goals of this thesis lie.

1.5 Thesis Outline

The aim of this thesis is to improve our understanding of the growth of galaxies during the first few billion years of cosmic history through studying their stellar mass, star-formation and merger history in details not previously possible at this epoch. Alongside this, we also aim to better understand the role that galaxies played in the epoch of reionization and place new constraints on their ability to power reionization.

Chapter 2 makes use of the deep multi-wavelength data of the CANDELS GOODS South field to investigate the evolution of the stellar mass function at redshift $z \sim 4$ and above. In addition to the stellar masses we make estimates of the galaxies' star-formation rates to study the evolution of the specific star-formation rates and star-formation rate function with redshift. As part of this chapter we also undertake extensive tests to explore the reliability of photometric selection for galaxies at high-redshift in comparison to a more traditional Lyman-break selection.

Chapter 3 then investigates the major merger rates of galaxies at $z > 2$ in the GOODS South field. We study the photometric close-pair statistics using a new approach which corrects for chance line-of-sight pairs using the photometric redshift probability distributions. By applying this method to a sub-sample of the available CANDELS data, we aim to show that it is now possible to study the merger properties of mass selected galaxies as far back as $z \sim 6$.

In both Chapters 2 and 3 we make use of semi-analytical and hydrodynamical models to compare our new observations with the predictions of theoretical models at high-redshift.

Chapter 4 studies the current constraints on the potential for galaxies to provide sufficient numbers of ionizing photons to power reionization. Using the latest observations of the galaxy rest-frame UV luminosity and stellar mass functions at high redshift (including the results of Chapter 2) and their UV continuum colours, we use extensive SED modelling to make new estimates of the ionizing emissivity during the epoch of reionization.

In the final chapter we discuss the conclusions drawn from the work done in this thesis and explore how future work can build on these results.

Chapter 2

The mass evolution of the first galaxies: stellar mass functions and star formation rates at $4 < z < 7$ in the CANDELS GOODS-South field

2.1 Introduction

Thanks to the unprecedented sensitivity of the latest extragalactic surveys, the last decade has seen a revolution in the observation of galaxies in the high-redshift universe. It is now possible to study the beginnings of the mechanisms and processes that formed the diverse array of galaxies we find in the local universe today. Since the first successful detections through the Lyman break technique, via the characteristic 'break' induced by blanketing hydrogen absorption of the UV continuum (Guhathakurta et al., 1990; Steidel & Hamilton, 1992), the study of high-redshift galaxies has progressed rapidly. With the introduction of the Wide-field Camera 3 (WFC3) in 2009 and the unprecedented depth in the near-infrared it provides, the study of galaxies out to redshifts of $z > 6$ has become

commonplace.

The numerous measurements of the UV luminosity function of high-redshift galaxies spanning the redshift range $4 \leq z \leq 9$ (Bouwens et al., 2007; McLure et al., 2009; Oesch et al., 2009; Bouwens et al., 2010; Grazian et al., 2011; Lorenzoni et al., 2011; McLure et al., 2013; Schenker et al., 2013a) are not only giving an insight into the processes of galaxy formation, they are also helping us to understand the role those galaxies played in the ionization of the intergalactic medium during the epoch of reionization (EoR). These surveys have put strong constraints on the contribution of star-forming galaxies to reionization, requiring a significant contribution from faint galaxies below the current detection limits to complete reionization within the observed redshift.

Because they represent the time integral of all past star-formation, the stellar masses of galaxies provide additional independent constraints on their contribution to reionization through the observed stellar mass density (Robertson et al., 2010). Successful models of galaxy evolution and reionization must therefore be able to reconcile both the star-formation observed directly, and the record of past star-formation contained in the observed stellar masses. The galaxy stellar mass function (SMF) and its integral the stellar mass density (SMD), are therefore important tools in the study of galaxy evolution.

However, accurately measuring the stellar masses of galaxies at high-redshift is very difficult for a number of fundamental reasons. These reasons stem from the fact that the rest-frame wavelengths probed by optical/near-infrared surveys extend only to the UV continuum, requiring mid-infrared observations to extend past $\lambda_{rest} = 4000$Å. Even when rest-frame optical measurements are available through deep *Spitzer* 3.6 and 4.5 μm observations, e.g. Stark et al. (2009); Labbé et al. (2010); González et al. (2011); Yan et al. (2012), the degeneracies between dust extinction, age and metallicity are large (see Dunlop 2013 for a detailed discussion).

More recently it has also been shown that the spectral energy distributions (SEDs) of high-redshift galaxies, for both photometrically selected (Schaerer & de Barros, 2009, 2010; Ono et al., 2010; McLure et al., 2011; Lorenzoni et al., 2011; González

et al., 2012) and smaller spectroscopically confirmed samples (Shim et al., 2011; Curtis-Lake et al., 2013; Stark et al., 2013), can exhibit colours that are best fit by the inclusion of nebular emission lines when measuring galaxy properties such as mass and age. The inclusion of these lines results in fitted ages that are significantly younger compared to fits without nebular emission, as well as being of lower stellar mass. Another consequence of the degeneracies in SED fitting at high-redshift is the increased importance in the assumed star formation history (SFH) of the models being fit. Observational studies of the mass growth of galaxies at a constant number density (Papovich et al. 2011, Salmon et al. 2015) and hydrodynamical simulations (Finlator et al., 2011) imply that the star formation histories for galaxies at $z > 3$ are smoothly rising. This increase is in contrast to the smoothly falling or constant SFH commonly used at low-redshift (see Conroy 2013 for a review). In Maraston et al. (2010), it is also shown that exponentially rising star-formation histories can provide improved fits to both simulated and observed SEDs of high redshift galaxies.

González et al. (2011) were amongst the first to make use of the capabilities offered by the WFC3/IR data, using data from the Early Release Science (ERS; Windhorst et al. 2011) to measure the stellar mass to UV luminosity ratio for a sample of dropout galaxies and applying it to the observed luminosity functions to measure the stellar mass function out to $z \sim 7$. In contrast to the steep faint-end slope of the UV luminosity function ($\alpha = -2$ to -1.7) at high-redshifts, this work observed a notably shallower mass function ($\alpha = -1.6$ to -1.4). Subsequent work by Lee et al. (2012) with much greater sample sizes from ground-based near-infrared found a similarly shallow slope at $z \sim 4$ and 5. In contrast, observations by Caputi et al. (2011) and Santini et al. (2012) observe a significantly steeper low-mass slope at $z > 3$.

In González et al. (2011), the shallow low-mass slope arises due to the observed evolution of the mass-to-light ratio with UV luminosity. Similarly, Lee et al. (2012) infer an evolving mass-to-light in order to reconcile the luminosity and mass function slopes observed. The primary physical explanation for this evolving mass-to-light ratio is luminosity dependent dust-extinction. However, obser-

vations of the stellar populations of high-redshift galaxies have produced conflicting results on the existence and strength of any luminosity dependence. When measuring the UV continuum slope, β (Calzetti et al., 1994), for samples of high-redshift galaxies, Wilkins et al. (2011), Bouwens et al. (2011d) and Bouwens et al. (2014) find evidence for a strong UV luminosity dependence across all redshifts at $z > 3$. In contrast, similar studies by Dunlop et al. (2011), Finkelstein et al. (2011) and Rogers et al. (2013) find no clear evidence for a luminosity dependence on β. Several of these studies outline the importance of the selection of high redshift galaxies (through either Lyman break or photometric redshift selection) and the treatment of their biases. To this end, more recent analyses (Bouwens et al., 2014; Rogers et al., 2014), which increase sample sizes and minimise biases in the sample selection and β measurements, are in good agreement, with both studies finding a clear luminosity dependence.

The deep near-infrared observations of the GOODS South field made as part of the Cosmic Assembly Near-infrared Deep Extragalactic Survey (CANDELS; Co-PIs: Faber & Ferguson; Grogin et al. 2011; Koekemoer et al. 2011), combined with the extensive existing optical observations make it a data set ideally suited to the study of galaxy evolution at the so-called 'cosmic dawn'. Covering an area approximately 200% larger than the WFC3 ERS observations alone (Windhorst et al., 2011), and incorporating the even deeper UDF observations, the CANDELS data combines the high sensitivity of the WFC3 observations with high-redshift samples large enough to attempt the first direct derivation of the completeness corrected stellar mass function at $z \geq 6$ and build upon the existing work at $z \sim 4$ and $z \sim 5$. In this chapter, we make use of this comprehensive data set to study galaxy stellar masses across the redshift range $z \sim 4$ to $z \sim 7$. In particular, we aim to estimate stellar masses for a large and robust sample of high-redshift galaxies, investigating how the inclusion of nebular emission and increasing star-formation histories affect the observed stellar mass - UV luminosity relation and the shape of the stellar mass function. For this same sample, we also aim to measure the dust-corrected star-formation rates, which will combine to make a detailed census of the stellar mass growth of high-redshift galaxies.

The structure of this chapter is as follows. In Section 2.2, we describe the properties of the optical and near-IR data sets used in this study as well as the methods of photometry extraction used. In Section 2.3, we describe the photometric redshift analysis and the selection criteria used to construct the high-redshift samples used in our analysis. Section 2.4 then investigates how the use of photometric redshift criteria compares with colour selection and test the robustness of this method. The SED fitting method used to estimate the stellar masses for our sample is outlined in Section 2.5. Section 2.5.6 then describes the simulations undertaken to account for the effects of completeness and sample selection. In Section 2.6 we present the results of this work and our analyses. Finally, Section 2.7 presents our summary and conclusions of the work in this chapter. Throughout this chapter all magnitudes are quoted in the AB system (Oke & Gunn, 1983) and we assume a ΛCDM cosmology with $H_0 = 70$ kms^{-1}Mpc^{-1}, $\Omega_m = 0.3$ and $\Omega_\Lambda = 0.7$. Quoted observables are expressed as actual values assuming this cosmology.

2.2 The Data

The photometry used throughout this work is taken from the catalog of Guo et al. (2013), a UV to mid-infrared multi-wavelength catalog in the CANDELS GOODS South field based on the CANDELS WFC3/IR observations combined with existing public data.

2.2.1 Imaging Data

The near-infrared WFC3/IR data combines observations from the CANDELS survey (Grogin et al., 2011; Koekemoer et al., 2011) with the WFC3 Early Release Science (ERS; Windhorst et al. 2011) and Hubble Ultra Deep Field (HUDF; PI Illingworth; Bouwens et al. 2010) surveys. The southern two thirds of the field (incorporating the CANDELS 'DEEP' and 'WIDE' regions and the UDF) were observed in the F105W, F125W and F160W bands. The northern-most third, comprising the ERS region, was observed in F098M, F125W and F160W. In

addition to the initial CANDELS observations, the GOODS South field was also observed in the alternative J band filter, F140W, as part of the 3D-HST survey (Brammer et al. 2012).

The optical HST images from the Advanced Camera for Surveys (ACS) images are version v3.0 of the mosaicked images from the GOODS HST/ACS Treasury Program, combining the data of Giavalisco et al. (2004a) with the subsequent observations obtained by Beckwith et al. (2006) and (Koekemoer et al., 2011). The field was observed in the F435W, F606W, F775W, F814W and F850LP bands. Throughout the chapter, we will refer to the HST filters F435W, F606W, F775W, F814W, F850LP, F098M, F105W, F125W, F160W as B_{435}, V_{606}, i_{775}, I_{814}, z_{850}, Y_{098}, Y_{105}, J_{125}, H_{160} respectively.

The *Spitzer*/IRAC (Fazio et al., 2004) 3.6 and 4.5μm images were taken from the Spitzer Extended Deep Survey (PI: G. Fazio, Ashby et al. 2013) incorporating the pre-existing cryogenic observations from the GOODS Spitzer Legacy project (PI: M. Dickinson). Complementary to the space based imaging of HST and Spitzer is the ground-based imaging of the CTIO U band, VLT/VIMOS U band (Nonino et al., 2009), VLT/ISAAC K_s (Retzlaff et al., 2010) and VLT/HAWK-I K_s (Fontana et al. *in prep.*) bands.

2.2.2 Source photometry and deconfusion

The full details on how the source photometry was obtained are outlined in Guo et al. (2013), however we provide a brief summary of the method used for reference here. Photometry for the HST bands was done using SExtractor's dual image mode, using the WFC3 H band mosaic as the detection image and the respective ACS/WFC3 mosaics as the measurement image after matching of the point-spread function (PSF).

For the ground-based (VIMOS and CTIO U band and ISAAC and Hawk-I Ks) and Spitzer IRAC bands, deconvolution and photometry was done using template fitting photometry (TFIT). We refer the reader to Laidler et al. (2007), Lee et al. (2012) and the citations within for further details of the TFIT process and the

improvements gained on mixed wavelength photometry.

2.3 Photometric Redshifts and Sample Selection

Photometric redshifts for the entire source catalog were calculated using the EAZY photometric redshift software (Brammer et al., 2008). The fitting was done to all available bands using the default reduced template set based on the PEGASE spectral models of Fioc & Rocca-Volmerange (1997) with an additional template based on the spectrum of Erb et al. (2010). The additional template exhibits features expected in young galaxy populations such as strong optical emission lines and a high Lyman-α equivalent width.

For each galaxy we construct the full redshift probability distribution function (PDF), $P(z) \propto exp(-\chi_z^2/2)$, using the χ^2-distribution returned by EAZY. Although EAZY allows the inclusion of a magnitude based prior when calculating redshifts, none was included in the fitting due to the large uncertainties still present in the H-band (our photometry selection band) luminosity function at high-redshifts (Henriques et al., 2012).

2.3.1 Selection Criteria

To investigate how the SMF evolves from z = 4-7, we wish to construct a sample of galaxies in the redshift range $3.5 < z < 7.5$. To select a robust sample suitable for SED fitting, we apply a set of additional criteria based on the full redshift probability distribution for each galaxy to construct the different redshift samples, similar to those used in previous high-redshift sample selections (McLure et al., 2011; Finkelstein et al., 2012). We then apply the following criteria:

$$\int_{z_{\rm sample}-0.5}^{z_{\rm sample}+0.5} P(z)\ dz > 0.4 \tag{2.1}$$

$$\int_{z_{\rm peak}-0.5}^{z_{\rm peak}+0.5} P(z)\ dz > 0.6 \tag{2.2}$$

$$(\chi^2_{min}/N_{\rm filters} - 1) < 3 \tag{2.3}$$

where z_{sample} = 4, 5, 6 and 7 for the respective bins and z_{peak} is the redshift at the peak of the probability distribution (i.e. minimum χ^2).

The first criterion (Equation 2.1) requires that a significant amount of the probability distribution lies within the redshift range we are examining. The second criterion (Equation 2.2) requires that the bulk of the PDF lies close to the peak of the distribution, i.e. that the primary solution is a dominant one. Finally, we require that EAZY provides a reasonable fit to the data (Equation 2.3).

A signal-to-noise (S/N) cut is placed on the J and H bands, requiring S/N(J_{125}) > 3.5 and S/N(H_{160}) > 5. Known AGN, stars and sources with photometry flagged as effected by artefacts are removed. We also visually inspect each galaxy across all the HST bands, excluding sources which were caused or strongly affected by artefacts such as diffraction spikes, bright stars and image edges that were not excluded by any of the other criteria.

Of the initial 34930 objects in the CANDELS GOODS South catalog, 3164 objects satisfy our first criterion. Of those objects, 256 are excluded by the second criterion and a further 167 are rejected based on their χ^2. The signal-to-noise criteria exclude a further 274 sources and the remaining criteria exclude a further 204 sources. The resulting final sample comprises 2263 galaxies.

By construction, the secondary redshift solutions for our sample make up a maximum of $\sim$ 40% of the integrated probability distribution. In practice, the addition of other criteria results in secondary redshift solutions which make up $<$ 5 to 10% of the integrated probability distribution for all but the faintest galaxies. As mentioned at the beginning of this section, a Bayesian luminosity prior is sometimes included in the estimation of photometric redshift PDFs to improve the redshift accuracy. The application of such a prior could significantly effect the relative strength of the secondary redshift solutions for the sources in our

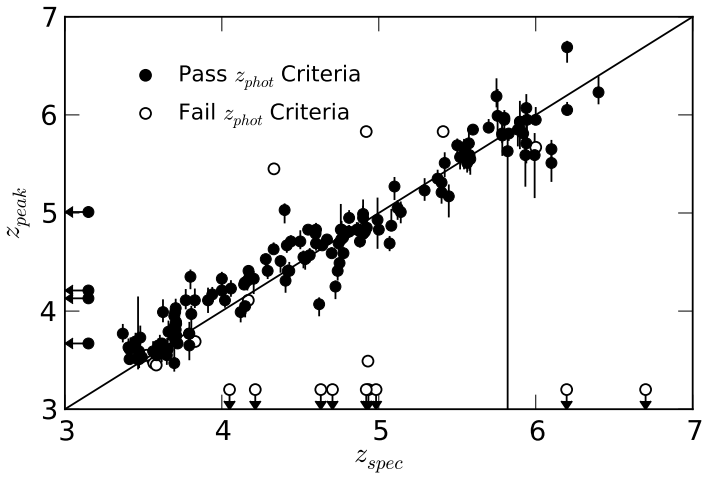

Figure 2.1: Comparison between spectroscopic and photometric redshift for the galaxies in our sample with available spectroscopy and spectroscopic redshift quality of 'Good" or better. Filled circles show sources that pass our selection criteria (including interlopers), empty circles show spectroscopically confirmed high-redshift sources that do not pass the selection criteria. The photometric redshift shown is the peak of the probability distribution (χ^2 minimum) with 1-σ lower and upper limits.

samples. However, existing galaxy evolution models are not yet well constrained at these redshifts, so there is no suitably well motivated distribution upon which to base a prior. Furthermore, at the faintest magnitudes where priors are most needed, the prior distributions are typically very broad (Brammer et al., 2008) and have minimal effect.

Figure 2.1 compares the available spectroscopic redshifts for the galaxies in our sample with the corresponding best-fit photometric redshift (minimum χ^2) as found by EAZY. In total, there are 151 spectroscopic redshift matches for galaxies that pass our selection criteria and are therefore included in our samples. In addition, there are a further 21 galaxies with spectroscopic redshifts of $z > 3.5$ that pass the signal-to-noise, AGN criteria but do not pass the photometric redshift criteria. Of these 21 galaxies, 12 are correctly identified as high redshift galaxies but are excluded due to poor fits (11) or have a redshift very close to the $z = 3.5$ limit but photometric scatter pushes the photometric redshift to below the criteria (1). The remaining 9 spectroscopically confirmed high-redshift sources have best-fit photometric redshifts of $z_{peak} < 3$. The simulations undertaken to correct for selection completeness are outlined in Section 2.5.6.1.

For the matched galaxies that pass our selection criteria, we find that our redshift accuracy is very good, with a scatter of just $\sigma_{z,O} = rms(\Delta z/1 + z_{\rm spec}) = 0.037$

when outliers are excluded, where $\Delta z = (z_{\rm spec} - z_{\rm phot})$ (Dahlen et al., 2013). We define outliers as $|\Delta z| / (1 + z_{\rm spec}) > 0.15$, and find an outlier fraction of 2.65% (4 galaxies). This compares with Finkelstein et al. (2011) who find a scatter of $\sigma_z/(1 + z) = 0.044$ at $z > 3$ after excluding outliers (defined more strictly as $|\Delta z| > 0.5$) in the same CANDELS field. We also find that there is very little bias in our photometric redshifts, with $median(\Delta z) = -0.04$. Of the 4 galaxies classed as outliers, all lie at redshifts of $z < 3$ and are low-redshift interlopers that our selection criteria have not been able to exclude.

Dahlen et al. (2013) have recently shown that by combining the results from multiple photometric redshift codes, the scatter and outlier fraction in photometric redshifts can be significantly reduced compared to the results of any single code. For the same set of 151 spectroscopic redshift sources, the photometric redshifts produced through the Bayesian combination outlined in Dahlen et al. (2013) have $\sigma_{z,O} = 0.033$ with an outlier fraction of 3.98% and $median(\Delta z) = 0.01$.

Although utilising the photometric redshifts for the CANDELS GOODS-S field produced by this method would result in a small gain in photometric accuracy, we would no longer be able to reproduce the full selection method when running simulations. Given this small improvement, we are confident that the use of photometric redshifts produced by a single code will not adversely affect the overall accuracy of the results.

The matched spectroscopic redshifts are from the following surveys: Le Fèvre et al. (2004); Stanway et al. (2004a); Vanzella et al. (2008); Hathi et al. (2008); Popesso et al. (2009); Wuyts et al. (2009); Rhoads et al. (2009); Vanzella et al. (2009); Balestra et al. (2010); Kurk et al. (2012). The high-redshift spectroscopic sources within these surveys all derive from initial target selections of predominantly bright Lyman Break galaxy candidates. The measured photometric redshift accuracies are therefore likely biased to a better scatter than the full high-redshift galaxy population. Furthermore, the galaxies at high-redshift for which spectroscopic redshifts can be successfully measured will be biased towards those with strong Lyman alpha emission lines (Lyman alpha emitters; LAEs), and therefore undergoing strong star-formation (or AGN activity). Spectroscopic red-

shifts will not be measurable for more quiescent galaxies, or those with strong dust absorption.

However, examining the redshift accuracy of the mock galaxy catalog used for our selection comparisons in Section 2.4, we find that the photometric redshift accuracy remains good down to the lowest masses probed in this survey (for galaxies of varying star-formation properties). For example, for galaxies of $M_* \approx 10^{8.5} M_\odot$, we find a scatter excluding outliers of $\sigma_{z,O} = 0.053$ and $median(\Delta z) = 0.025$ before any $P(z)$ criteria are applied.

To investigate how the SMF evolves from z = 4-7, we then constructed four redshift samples in bins across this redshift range: $z \sim 4$ ($3.5 \leq z < 4.5$), $z \sim 5$ ($4.5 \leq z < 5.5$), $z \sim 6$ ($5.5 \leq z < 6.5$) and $z \sim 7$ ($6.5 \leq z < 7.5$).

2.3.2 Monte Carlo Samples

Although we find that our photometric redshifts do well when compared with the matched spectroscopic redshifts, the group of outliers are indicative of the difficulties that exist in correctly distinguishing between the Lyman break of high-redshift galaxies at $z > 3$ and strong Balmer break galaxies at more moderate redshifts $z \approx 0.5 - 2.5$ in low S/N data. Pirzkal et al. (2012, 2013) have shown that it is very difficult to categorically classify sources as high-redshift galaxies and not low-redshift interlopers using photo-z's or S/N criteria on the dropout bands.

Previous work using photometric redshifts has dealt with this problem by making use of the full redshift PDF when calculating luminosity functions (Dahlen et al., 2005; McLure et al., 2009, 2013), thereby incorporating the uncertainty in the analysis. Due to the nature of the SED fitting code used for this work (described in Section 2.5), the computational effort required to fit the mass at each redshift in order to integrate over the full PDF becomes impractical. As such, we chose to account for these problems in a different manner whilst still dealing with them in a straight-forward way.

Rather than using only the best-fit redshift from our photometric analysis when

Table 2.1: Average sample size and variance for each redshift bin for the 500 Monte Carlo samples generated, see text for details.

Redshift Bin	Mean Sample Size	Variance on sample size
4	1235	180
5	416	63
6	169	25
7	42	9

selecting our sample, we instead draw the redshift for each galaxy randomly from its full PDF before placing it in the appropriate redshift sample. Where secure spectroscopic redshifts are available, we fix the redshift to that value for all samples (known interlopers are therefore excluded in all samples). This process was repeated 500 times to produce a set of samples to which we then apply the rest of the analysis described in the chapter separately. We then average over the results from each sample, using the mean of this full set as our 'true' value along with the 1-σ upper and lower limits around this mean.

The resulting sample sizes for each redshift bin are shown in Table 2.1. The varying samples account for both scattering between redshift bins for objects at the boundaries as well as objects moved out of the sample into secondary low-redshift solutions. The effect of this scattering into and out of the samples can be seen when comparing the combined mean samples sizes (1862) to our full high-redshift sample of 2263.

The strength of using photometric redshifts for sample selection over colour cuts (especially when redshifts would still need to be calculated for a colour-cut sample in order to do SED fitting) is that the method can automatically make use of all available photometry. This is important because although photometric redshifts are still fitting primarily to the characteristic break at Lyman-α targeted by the colour selections, the filters long-ward of the break are useful in excluding low-redshift interlopers (McLure et al., 2011). Additionally, the large errors in colour possible due to low signal-to-noise and possible non-detections in the filter just short of the Lyman break means that likely high-redshift candidates can be scattered well outside the selection region when using colour cuts. In contrast, because the photometric redshift code used in this analysis fits to the observed fluxes in linear flux space it is able to fully take into account any (/all) non-

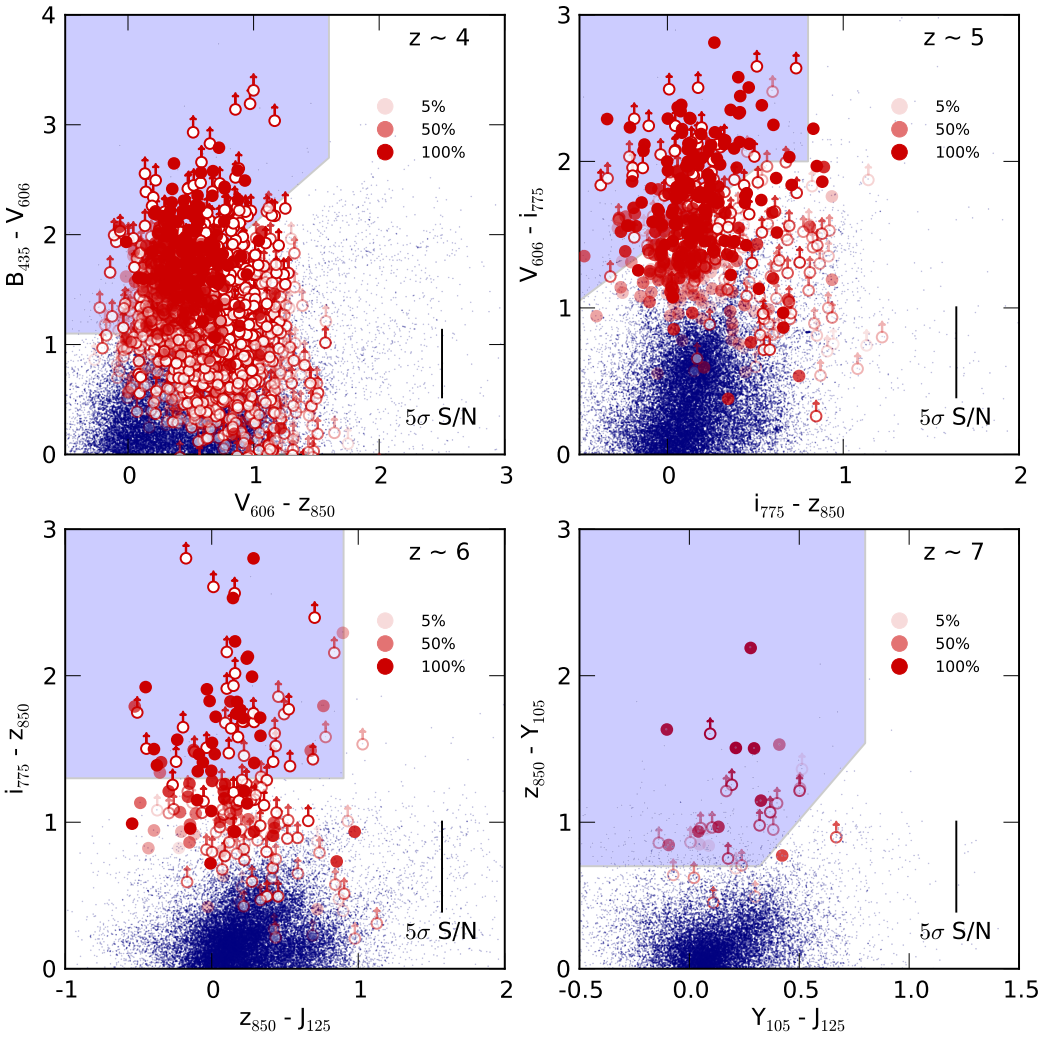

Figure 2.2: The colours of our photometric redshift selected samples in relation to the two-colour cuts typically used to select Lyman break galaxies. Non-detections in a filter are converted to 2-σ upper limits when calculating the colours. The shaded blue regions show the region in colour space used to select dropout galaxies in that redshift bin as described in Bouwens et al. (2007) and Bouwens et al. (2011d). The blue points show the colours for the full GOODS-S photometric catalog from which we select our high redshift samples. Red symbols represent galaxies selected in our sample by our selection criteria, where the transparency of the symbols is determined by the number of Monte Carlo samples in which it is selected i.e. the fainter the symbol, the smaller the fraction of MC samples that galaxy is selected in. The legend in each plot illustrates this transparency for galaxies selected in 5, 50 and 100% of Monte Carlo samples. Colours that make use of 2-σ upper limits are plotted with open circles, while objects with 2-σ detections or better in all bands are plotted with filled circles. Example error bars corresponding to 5-σ detections (for both filters in a given colour) are shown for each of the corresponding drop-out colours.

detections and negative fluxes (Brammer et al., 2008). Sources that have SEDs consistent with those of high-redshift galaxies (within error) will therefore not be erroneously excluded from the potential sample.

Figure 2.2 shows the positions of our galaxy samples on the colour-colour planes commonly used to select dropout samples. It is obvious that many of the galaxies selected with photometric redshifts lie outside the selection regions (as taken from Bouwens et al. 2007), especially those galaxies where colours must be calculated using an upper limit. To test whether the discrepancy between the observed colours and those required for Lyman break selection can be explained solely by photometric scatter, in the following section we perform an extensive range of tests on a mock catalogs from semi-analytic models.

2.4 Selection method comparison

Traditionally, (star-forming) galaxies at high-redshift have been selected using the Lyman break technique, whereby galaxies are selected based on the observed colours across the redshifted Lyman break in their spectra.

When the observed colours of our photometric redshift selected galaxies are plotted in the same way, the selected galaxies span a range of colours far wider than those encompassed by the Lyman break galaxy (LBG) selection criteria. Many of the galaxies have colours which would place them in the locus spanned by low-redshift galaxies, according to the Lyman break criteria. This has been observed before by Dahlen et al. (2010), who find a similar range of colours for galaxies with photometric redshifts at $z \sim 4$ and 5.

This raises the question as to whether this discrepancy is solely due to photometric scatter in the relevant colours, if they have stellar populations different from those expected for the Lyman break criteria, or if in fact those galaxies outside the selection criteria are low-redshift interlopers or catastrophic failures in the photometric redshift estimation.

To answer these questions, we have taken a sample of mock galaxies from the

CANDELS semi-analytic models of Somerville et al. (2008) and Somerville et al. (2012) across all redshifts. From the full SAM catalog of galaxies from $z = 0$ to $z > 8$, we have included all galaxies at $z > 3$ and a randomly selected sample of a quarter of the galaxies at $z = 3$ and below (subsequent calculations of the interloper fraction fully correct for this reduced number density at $z < 3$). The resulting sample of $\sim 260,000$ galaxies consists of approximately equal numbers of high-redshift galaxies and a fully representative sample of low-redshift galaxies across their corresponding luminosity and colour distributions. For full details of the mock galaxy properties as a function of redshift we refer the reader to Somerville et al. (2008) and Lu et al. (2014).

We then assign photometric errors to the intrinsic fluxes in each band based on the observed errors in the original catalog and then perturb the flux by those errors. The resulting colours should then indicate the effects of photometric scattering on the intrinsic colours. We have assumed the errors are gaussian (the fluxes are perturbed by a value drawn from a gaussian where σ = Flux Error) and have applied the errors based on the measured flux errors of objects with equivalent fluxes in the UDF, DEEP and WIDE regions.

To further illustrate this process we also select an example galaxy from our mocks that we can follow through the individual steps. The photometric properties of the galaxy and the corresponding photometric errors are outlined in Table 2.2. The galaxy has a redshift of $z = 5.01$, a stellar mass of $\approx 8 \times 10^8 M_\odot$ and a UV-continuum slope of $\beta = -2.1$.

Table 2.2: Intrinsic magnitudes, fluxes and typical observation errors for the example galaxy and the CANDELS GOODS South region. The first row outlines the true intrinsic fluxes F_{true} in the key filters at $z \sim 5$. In the second row we show the measured 5-σ limiting magnitudes (or fluxes) for the DEEP region estimated in Guo et al. (2013) for the photometry used in this chapter. The third row shows the average and standard deviation flux error for objects in the photometric catalog (Guo et al., 2013) with fluxes within 0.1 dex of the intrinsic flux for our example galaxy (i.e. the distribution from which our assigned photometric error is drawn). The final row shows the 'observed' fluxes (F_{obs}) for our example galaxy after assigning a flux error σ_F and perturbing the intrinsic flux by a value drawn from a gaussian with width $\sigma = \sigma_F$.

	V_{606}		i_{775}		z_{850}		H_{160}	
	AB	μJy	AB	μJy	AB	μJy	AB	μJy
Intrinsic Flux - F_{true}	29.35	0.0066	27.14	0.0506	26.83	0.0673	26.91	0.0625
DEEP 5-σ limit	29.35	0.0066	28.55	0.0138	28.55	0.0138	27.36	0.0413
Mean Error $\pm$1 SD	-	0.0054 ± 0.0028	-	0.0111 ± 0.0057		0.0145 ± 0.0113	-	0.0099 ± 0.0074
'Observed' Flux - F_{obs}	> 27.82	0.009 ± 0.009	27.07	0.054 ± 0.010	26.85	0.066 ± 0.013	27.01	0.057 ± 0.006

The intrinsic colours of the mock galaxies at $z \sim 5$ ($4.5 \leq z < 5.5$) are shown in Figure 2.3. It is clear that the colours spanned by the galaxies lie well within the Lyman break selection criteria of Bouwens et al. (2007), with only a small fraction of galaxies redder than the criteria in the colour above the break or bluer across the Lyman break. Our input population therefore closely matches the colours for which the colour-colour criteria have been designed. The same is true across all redshift bins.

The lower panel of Figure 2.3 shows the colours of our mock galaxy catalog after being perturbed by errors drawn from the CANDELS DEEP region. Only galaxies with $S/N(H_{160}) > 5$ are shown, matching the selection criteria for our high-redshift samples, resulting in a sample of 5673 galaxies with $4.5 < z_{\rm true} < 5.5$. As for our observed objects in Figure 2.2, 2-σ upper-limits are used to derive magnitudes for non-detections ($S/N < 2$) and objects with negative fluxes.

It is immediately clear that photometric scatter pushes the colour spanning the Lyman break to values much lower in $V_{606} - i_{775}$ than the range covered by the selection criteria. However, the main locus of galaxies still resides either within or within the typical error of the Lyman break selection region. In addition, the majority of mock galaxies with 'observed' $V_{606} - i_{775} < 1$ are those with a non-detection in V_{606} and hence represent a lower limit. The same effect occurs across all regions, with the lower photometric errors in deeper GOODS South region resulting only in a fainter magnitude for an equivalent signal-to-noise in the optical bands.

The systematic shift towards lower values of $V_{606} - i_{775}$ once photometric scatter is included can be explained by the relative signal-to-noise ratios in the filters above and below the Lyman break. Given the depth of each filter (see Table 2.2), objects with relatively faint apparent magnitudes above the break and intrinsic colours $> 1-2$ will always have a significantly lower signal-to-noise in the filter below the break. In this scenario, V_{606} fluxes that are scattered to higher values will result in a brighter more robust magnitude. Conversely, objects that are scattered to fainter magnitudes are more likely to result in non-detections, requiring the use of upper limits which will push the observed colours down.

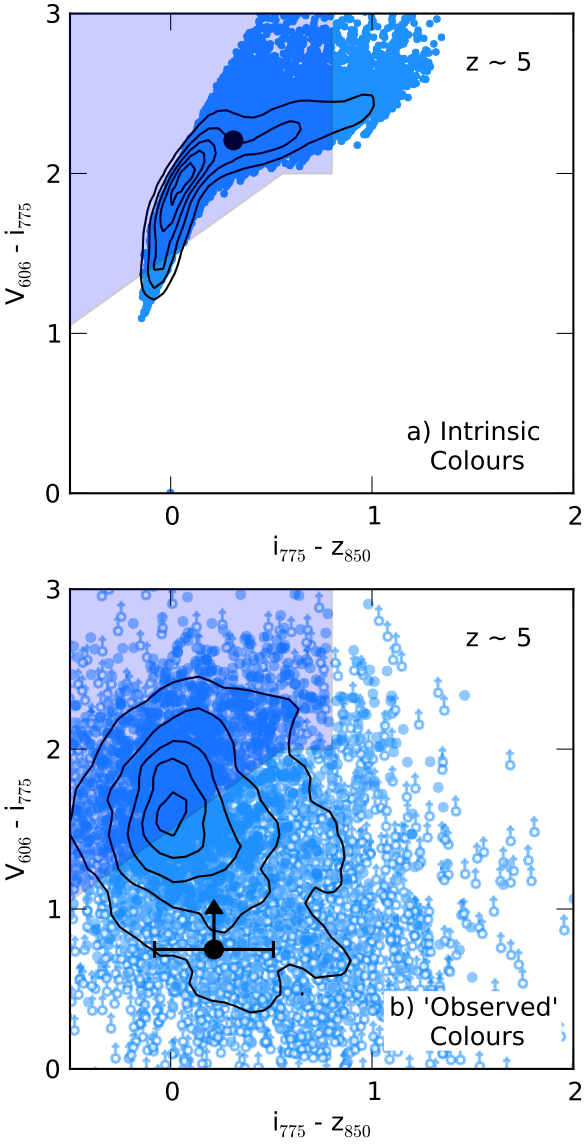

Figure 2.3: a) Intrinsic colours of galaxies at $4.5 < z < 5.5$ from the CANDELS semi-analytic mock catalog. Also shown are contours representing the density of points, with the innermost contour corresponding to five times the density of the outermost contour. The larger black point shows the intrinsic colour of the galaxy from the example outlined in the text. b) Observed colours of galaxies at $4.5 < z < 5.5$ from SAM mock sample after the photometry has been perturbed by flux errors proportional to the observed flux errors in the CANDELS DEEP region of observed photometry. Open circles represent colours constructed from 2-σ upper limits. As in a), the innermost contour corresponds to five times the density of points of the outermost contour.

These simulations show that high-redshift galaxies can exhibit colours across the Lyman break well outside the traditional selection criteria. However, it is also important to show that the galaxies selected by photometric redshift with colours outside the colour criteria are indeed these high-redshift galaxies rather than lower redshift galaxies in the same colour space.

To address this, we next calculate photometric redshifts for the SAM mock galaxy sample incorporating the photometric errors using the same method as described in Section 2 and apply our sample selection criteria. By applying additional cuts based on the full $P(z)$ distribution, the number of interlopers can be reduced at the expense of excluding some real sources. How strict the selection criteria are is a balance between minimising the contamination from interlopers and scatter at the bin edges and maximising the number of real high-redshift galaxies in the sample. In Figure 2.4 we show the colours of galaxies that pass our high-redshift selection criteria. The top panel of Figure 2.4 shows those galaxies with $4.5 < z_{\rm true} < 5.5$, these galaxies span the full range of colours traced by the error perturbed colours of input high-redshift galaxies shown in the previous plots. In the case of the Table 2.2 example galaxy, the best-fitting photometric redshift is $z = 5.0^{+0.2}_{-0.5}, 5.2 \pm 0.1$ and $4.86^{+0.27}_{-0.15}$ for the DEEP, UDF and WIDE errors respectively.

In the bottom panel of Figure 2.4, we show the selected galaxies that have true redshifts outside of the desired redshift range. At $z \sim 5$, the majority of low-redshift ($z < 3$) interlopers which are selected to be $z \sim 5$ by the photometric redshift selection exhibit colours which lie outside of the Lyman break colour criteria. The fraction of low-redshift interlopers is very small compared to the number of 'real' high-redshift galaxies in this colour space. However, as redshift increases, the fraction of low-redshift interlopers increases such that at $z \sim 7$ based on the best-fitting z_{peak} alone, the fraction of outliers equals ~ 0.60, 0.51 and 0.72 for DEEP, UDF and WIDE respectively. Clearly, basing high-redshift samples on the best-fitting photometric redshift alone would produce highly biased samples. Further S/N or photometric criteria such as those used in this work are clearly required to produce a reliable sample.

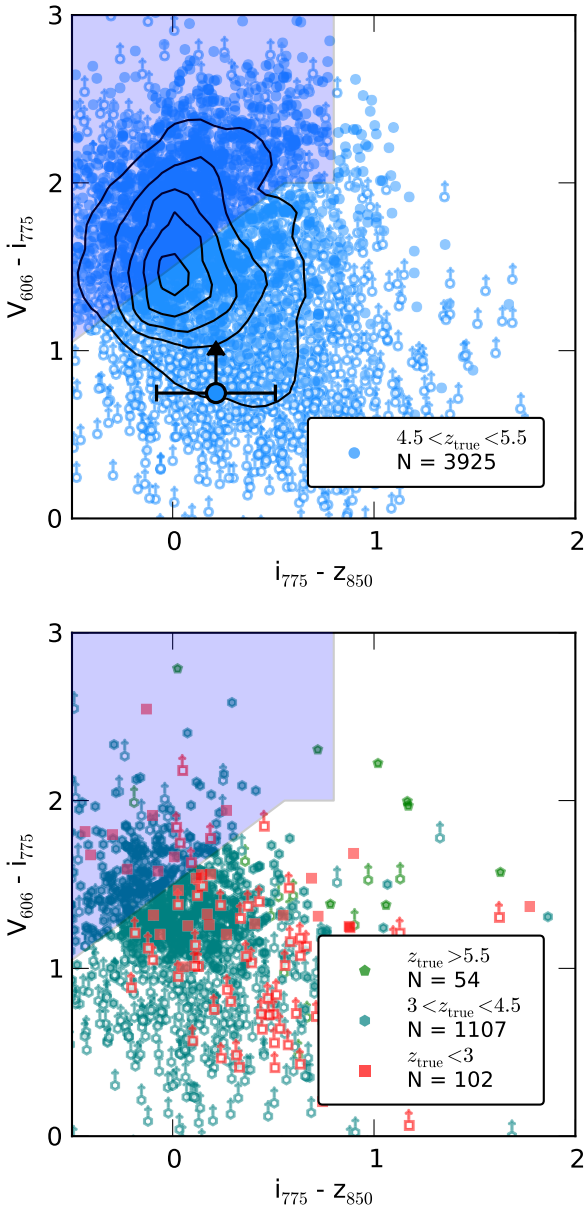

Figure 2.4: *Top:* Observed colours of galaxies from the SAM mock sample that pass our photometric redshift selection criteria, have best-fitting photometric redshifts in the range $4.5 < z_{\rm phot} < 5.5$ and have true redshifts in the range $4.5 < z_{\rm true} < 5.5$. As in Figure 2.3, the innermost contour corresponds to five times the density of points of the outermost contour. Open circles with arrows represent colours constructed from 2-σ upper-limits. The separately marked large blue circle corresponds to the the example galaxy which is correctly estimated to be $z \sim 5$. *Bottom:* Observed colours of galaxies from the SAM mock sample that pass our photometric redshift selection criteria and have best-fitting photometric redshifts in the range $4.5 < z_{\rm phot} < 5.5$ but have true redshifts outside of the desired redshift bin. As in the top panel, open symbols with arrows represent colours constructed from 2-σ upper-limits. In both panels, N is the number of galaxies in the corresponding sample. As outlined in the text, the number of $z_{\rm true} < 3$ galaxies shown represents a quarter of those expected in a fully representative sample. Using the best-fitting photometric redshift and our selection criteria, the low-redshift interloper fraction for this sample $= (102 \times 4)/(54 + (102 \times 4) + 1107 + 3925) = 0.07$. This low-redshift interloper fraction is reduced to ≈ 0.06 when we generate our Monte Carlo samples.

Applying the selection criteria and generating Monte Carlo samples as outlined in Section 2.3.1, the low-redshift interloper fractions for our mock samples are reduced to an estimated 0.008, 0.06, 0.15 and 0.22 for $z \sim 4$, 5, 6 and 7 respectively. This was estimated by combining the fractions calculated for each field (assuming the ERS region to have interloper fractions comparable to the DEEP region) proportional to the number of high-redshift galaxies selected from each region of the field.

The lower panel of Figure 2.4 also highlights the importance of fully incorporating the photometric redshift errors when creating high-redshift galaxy samples. Approximately 20% of the galaxies selected as $z \sim 5$ have true redshifts below the desired range. However upon closer inspection, we find that the median true redshift for the $3 < z_{\rm true} < 4.5$ points (turquoise hexagons) is 4.4 whilst the median best-fitting photometric redshift for the same sample is 4.6 with average 1-σ errors of $^{+0.18}_{-0.35}$.

By making use of the full $P(z)$ distribution estimated by the photometric redshift code as we do in this work (see Section 2.3.2), galaxies with $P(z)$ that span the redshift boundaries will be scattered between and contribute to both adjacent redshifts bins between different MC samples (or scattered out of the sample e.g. $z < 3.5$ or $z > 7.5$). Throughout this work, the errors resulting from this photometric redshift uncertainty are incorporated in the analysis and errors presented.

To compare the low-redshift interloper fractions and the robustness of our photometric redshift selection, we also run the SAM mock catalog through a Lyman break selection process. Our Lyman break selection criteria are based on the V_{606}-dropout criteria of Bouwens et al. (2011d) and we exclude sources with $S/N > 2$ in any of the bands blueward of the dropout bands ($U_{\rm CTIO}$, $U_{\rm VIMOS}$ and B_{435}). We also require $S/N(i_{775}) > 5.5$, comparable with other Lyman break selections at this redshift, e.g. Giavalisco et al. (2004b) and Beckwith et al. (2006). However we note that by choosing a stricter optical S/N requirement, the purity of the sample can always be improved at the expense of total sample size. For consistency with other LBG selections, when making the colour cuts, we use the observed magnitudes for detections above 1-σ and the 1-σ upper limit below this.

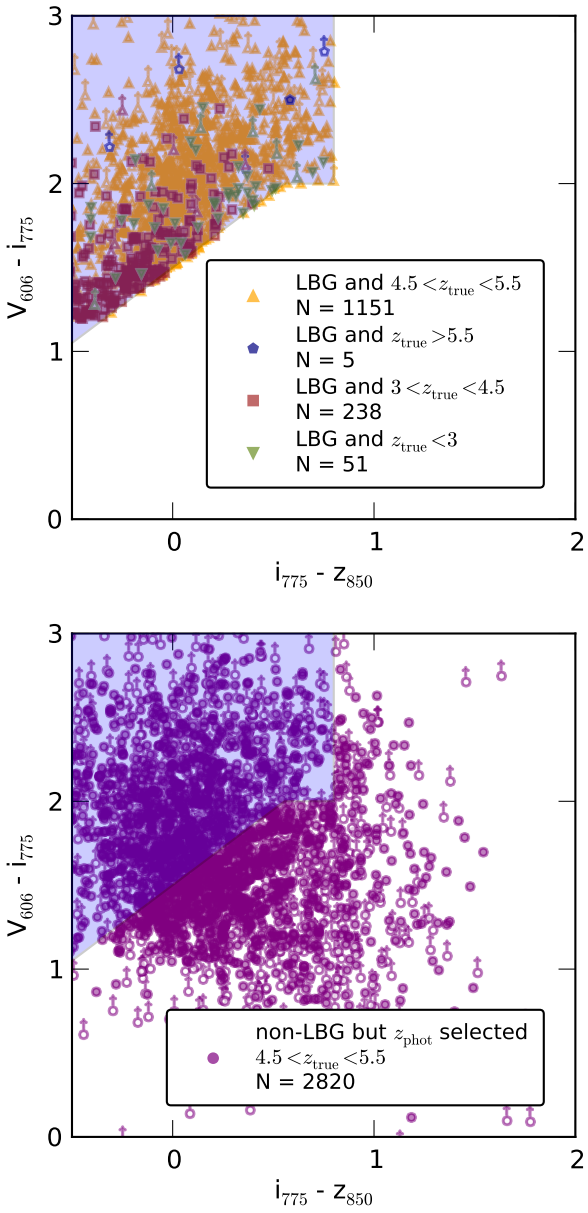

Figure 2.5: *Top:* Observed colours of galaxies from the SAM mock sample that pass the Lyman break selection criteria outlined in the text, separated into bins of intrinsic redshifts. In contrast to previous plots and in keeping with common LBG selection techniques, when calculating colours the measured magnitude is used down to a $S/N = 1$ and the 1-σ upper limit is used below this. The same is true for colours plotted in the bottom panel. As outlined in the text, the number of $z_{\rm true} < 3$ galaxies shown represents a quarter of those expected in a fully representative sample. The low-redshift interloper fraction for this sample $= (4*51)/(5+(51\times4)+238+1151) = 0.13$. *Bottom:* Observed colours of galaxies from the SAM mock sample with $4.5 < z_{\rm true} < 5.5$ that fail the Lyman break selection criteria outlined in the text but are correctly selected as $z \sim 5$ galaxies by the photometric redshift selection used in this work.

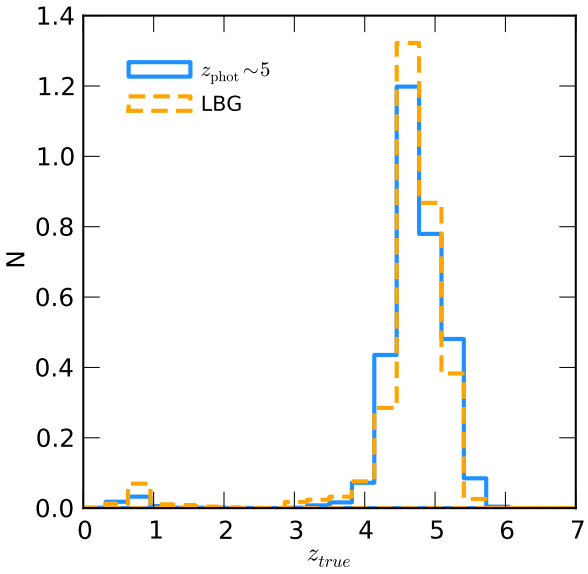

Figure 2.6: Normalised number densities as a function of true redshift for the photometric redshift and Lyman break galaxy samples generated for our SAM mock galaxy catalog.

We caution that since the mock photometric catalog in this section is designed to replicate the H_{160} selection of the observational data used in this chapter, the detection criteria for our Lyman break sample will differ from those in the literature based solely on the optical (e.g. Bouwens et al. 2007). Therefore, the selection efficiencies and low-redshift interloper fractions calculated here represent only the Lyman break technique as applied to the CANDELS data in this chapter specifically. As such, we do not make any claims regarding the low-redshift interloper fraction of Lyman break selection elsewhere in the literature.

In the upper panel of Figure 2.5, we show the colour distribution and sample sizes for our LBG sample. For this sample, we find a low-redshift interloper fraction comparable to that of the photometric redshift selection. In the lower panel of Figure 2.5, we show galaxies which have true redshifts in the range $4.5 < z_{\rm true} < 5.5$ and do not satisfy all of the LBG criteria but do pass the photometric redshift selection criteria. Although many of these galaxies have colours outside the LBG colour criteria, photometric redshifts are also able to select galaxies which fail the non-detection or optical S/N criteria. In Figure 2.6, we also compare the intrinsic redshift distribution of the two selection methods. Both the low-redshift contaminants and scatter at bin extremities are clearly visible for both samples.

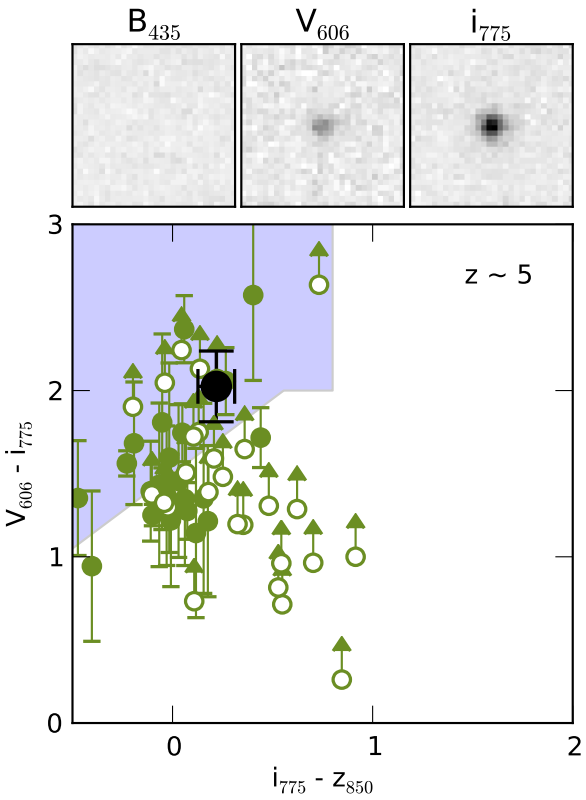

Figure 2.7: *Top panels*: 1.8×1.8 arcsec^2 postage-stamp images of the median stacked faint sources in the B_{435}, V_{606} and i_{775} filters. *Main panel*: The observed colours of the individual faint sources are shown by the smaller green circles. Open circles represent sources where the V_{606} has been calculated from the 2σ flux upper limit. The large black circle shows the measured colour for the stacked images.

As a further step to demonstrate the difference in the observed Lyman break colours can be explained solely by photometric scatter, we examine the photometry for a median stack of the 50 candidate $z \sim 5$ galaxies in the CANDELS DEEP region with the lowest $S/N(H_{160})$. Stacking the photometry of a large enough number of sources should cancel out most of the photometric noise, with the resulting images closely reproducing the average intrinsic colours of the input galaxies. In Figure 2.7, we show the initial observed colours (or lower limits) for each of the faint $z \sim 5$ candidates along with the observed colours of the stacked sources. Although the majority of the input galaxies have colours outside the Lyman break selection, the combined stack has a colour which places it more than 1-σ inside the desired region and fully consistent with the expected $z \sim 5$ colours.

Also shown in Figure 2.7 are the median stacked images in the 3 filters from below to above the Lyman break. Crucially, for any high-redshift candidate galaxy, the

filters at wavelengths lower than the Lyman selection colours should contain zero flux due to the complete absorption by inter-galactic Hydrogen. The median stack in B_{435} for our faint sample contains no trace of flux, with a 2-σ upper limit of 29.48 within a 0.6" diameter aperture.

While the tests presented in this section cannot account for objects with peculiar intrinsic colours (i.e. significantly different from those predicted by semi-analytic or synthetic stellar population models), they demonstrate that the observed colour distribution can be fully accounted for by the photometric scattering of the expected intrinsic colours. We also conclude that photometric redshift selection can be much less sensitive to photometric scatter than the Lyman break selection criteria for the same redshift range. Furthermore, that it is also able to correctly select high-redshift galaxies that are not identified by the traditional Lyman break selection techniques. In addition, the samples produced by both methods contain similar fractions of low-redshift galaxy contamination when criteria of comparable strictness are applied.

2.5 Mass Fitting

Stellar masses were estimated for our samples using a custom template fitting code with SEDs derived from the synthetic stellar population models of Bruzual & Charlot (2003) (BC03 hereafter). In comparison to subsequently released stellar population models (e.g. Charlot & Bruzual (2007) or Maraston 2005), the BC03 models include a weaker contribution due to thermally-pulsating asymptotic giant branch (TP-AGB) stars. However, due to the relatively young ages of the stellar populations (as constrained by the age of the Universe at the redshifts involved), the effects of TP-AGB stars on resulting SEDs are minimal, e.g. Stark et al. (2009). To illustrate this, in Figure 2.8 we show a comparison of SEDs produced by the BC03 models and the later 2007 models with increased TP-AGB contribution for a galaxy at $z = 4$.

It is apparent that the increased emission from TP-AGB stars occurs predominantly in the rest-frame near-infrared (at wavelengths of $\gtrapprox 1$ μm). For galaxies at

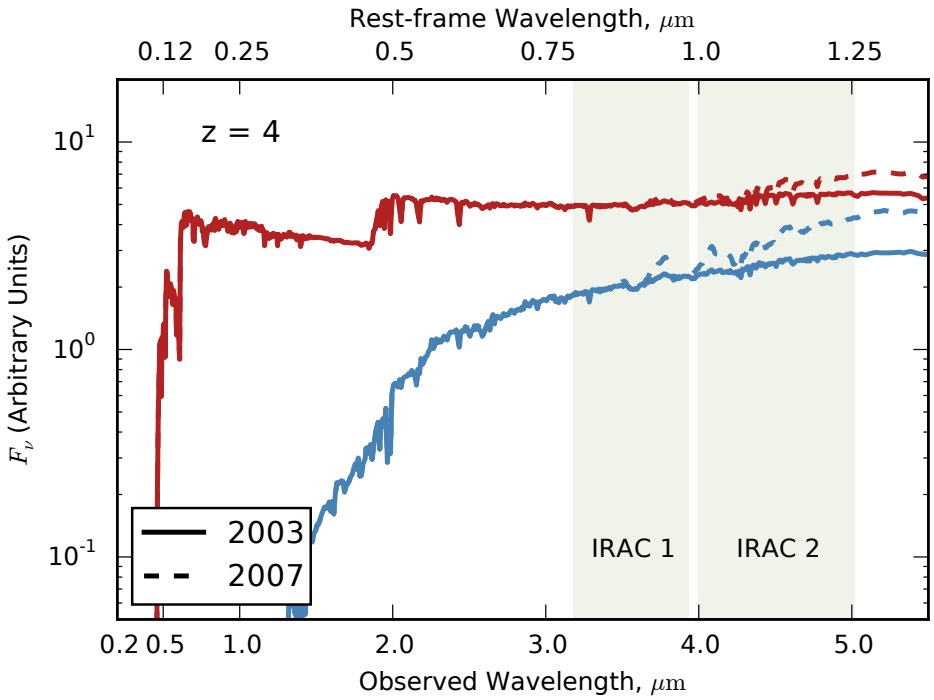

Figure 2.8: Two examples effect of increased TP-AGB star contribution to the SEDs of galaxies at $z = 4$ for the two sets of Bruzual & Charlot models, from 2003 and 2007. In red we show the redshifted SEDs for an old stellar population (1.5 Gyr) with a short declining star-formation history. In blue we show the SEDs for a younger (0.5 Gyr) stellar population with a constant star-formation history. Both sets of stellar populations assume a solar metallicity and zero dust attenuation.

$z > 3$, this results in only the two reddest filters being affected by these changes: the IRAC 3.6 and 4.5 μm bands. For the 1.5 Gyr old quiescent stellar population (blue lines) in which their effect should be greatest, the increased TP-AGB contribution results in IRAC fluxes which are ≈ 4 and 30% higher for the same stellar population. For the more realistic younger star-forming population (500 gyr, red lines) the effects are much lower, with IRAC 1 and 2 fluxes increased by ≈ 1 and 12% respectively. The shorter wavelength WFC3 IR filters are almost entirely unchanged. Furthermore, at $z \approx 5$ and above, the affected wavelengths are redshifted beyond even the IRAC 4.5μm filter.

Given the small change in apparent SEDs at high redshift when incorporating the stronger TP-AGB contributions and the continuing debate over which models are the most accurate (Kriek et al., 2010), we chose not to use the updated SSP models. However, we are confident that the use of Charlot & Bruzual (2007) or Maraston (2005) in place of BC03 should have no result on the conclusions found in this work.

2.5.1 Model SEDs

First, model SEDs are generated from the single stellar populations of Bruzual & Charlot for a range of population ages, metallicities and star-formation histories (SFHs). For our models and throughout this work we use the initial mass function (IMF) of Chabrier (2003). Each template is then normalised such that the total stellar mass equals 1 $M_{\odot}$. Nebular emission lines are added to the pure stellar component following the method outlined in Section 2.5.2. Internal dust extinction is applied following the extinction law of Calzetti et al. (2000) for the desired range of extinction magnitude A_V.

When applying dust extinction to the nebular emission, we assume the differential dust extinction between stellar and nebular emissions to be fixed as $E(B-V)_{\rm stellar} = E(B-V)_{\rm nebular}$, in contrast to the ratio of $E(B-V)_{\rm stellar} = 0.44E(B-V)_{\rm nebular}$ derived by Calzetti et al. (2000). This choice was motivated by the conflicting evidence for the relative extinction of the two emission sources at $z \sim 2$ (Erb et al., 2006; Förster Schreiber et al., 2009) and that in the context of these models specifically, the assumed differential extinction ratio and escape fraction are degenerate.

The absolute magnitude at 1500 Å (M_{UV}) is measured for each template by integrating the flux within a 100 Å-wide flat bandpass centered on 1500 Å. Similarly, the UV-continuum slope β is calculated by fitting a simple power-law to the integrated template fluxes in the windows described in Calzetti et al. (1994). The accuracy of this method in calculating β is explored in Finkelstein et al. (2012) and Rogers et al. (2013).

Next, each model SED is redshifted in the range $0 \leq z < 9$ in steps of $\Delta z = 0.02$, and attenuation by intergalactic neutral hydrogen is applied following the prescription of Madau (1995). The resulting grid of SEDs is then integrated through the response filter for each of the observed bands, dimmed by the corresponding distance modulus for each redshift.

2.5.2 Nebular Emission

Nebular emission lines and continuum are added to the templates following a method similar to previous high-redshift fitting methods, e.g. Ono et al. (2010); Schaerer & de Barros (2010); McLure et al. (2011), Salmon et al. (2015). Line strength ratios relative to Hβ for the major Balmer, Paschen and Brackett recombination lines are taken from Osterbrock & Ferland (2006), with the total Hβ line luminosity (in erg s^{-1}) given by

$$L(\mathrm{H}\beta) = 4.78 \times 10^{-13}(1 - f_{\mathrm{esc}})N_{\mathrm{LyC}} \tag{2.4}$$

from Krueger et al. (1995), where f_{esc} is the continuum escape fraction and the number of Lyman continuum photons N_{LyC} is calculated from each template. The strength of the nebular emission is therefore directly proportional to the number of ionizing photons (Lyman continuum) in the HII region. Since the Lyman continuum emission is dominated by young massive stars, the relative contribution of nebular emission to the total SED is highly dependent on the age of the stellar population and the amount of recent star-formation.

Line ratios for the common metal lines relative to Hβ were taken from the empirical measurements of Anders & Alvensleben (2003) for each of the input template metallicities, assuming gas metallicity is equal to the stellar metallicity. Similarly, the nebular continuum emission luminosity is given by

$$L_\nu = \frac{\gamma_\nu^{(total)}}{\alpha_B}(1 - f_{\mathrm{esc}})N_{\mathrm{LyC}}, \tag{2.5}$$

where α_B is the case B recombination coefficient for hydrogen and $\gamma_\nu^{(total)}$ is the continuum emission coefficient given by

$$\gamma_\nu^{(total)} = \gamma_\nu^{(HI)} + \gamma_\nu^{(2q)} + \gamma_\nu^{(HeI)}\frac{n(He^+)}{n(H^+)} + \gamma_\nu^{(HeII)}\frac{n(He^{++})}{n(H^+)}. \tag{2.6}$$

$\gamma_\nu^{(HI)}$, $\gamma_\nu^{(HeI)}$, $\gamma_\nu^{(HeII)}$ and $\gamma_\nu^{(2q)}$ are the continuum emission coefficients for free-free and free-bound emission by Hydrogen, neutral Helium, singly ionized Helium and two-photon emission for Hydrogen respectively, where the values are taken from Osterbrock & Ferland (2006). The coefficients and constants used assume an electron temperature $T = 10^4$ K, electron density $n_e = 10^2$ cm^{-3} and the

abundance ratios are set to be $\frac{n(He^+)}{n(H^+)} = 0.1$ and $\frac{n(He^{++})}{n(H^+)} = 0$ (Krueger et al., 1995).

2.5.3 SED Fitting

The fitting of our SEDs to the observed photometry is done using a Bayesian-like approach, whereby the normalised likelihood $\mathcal{L}(M,t)$ for a given stellar mass, M, and template type, t, is given by

$$\mathcal{L}(M,t) = \frac{\exp(-\frac{1}{2}\chi^2(M,t))}{\sum_{t'}\int dM' \ \exp(-\frac{1}{2}\chi^2(M',t'))}. \tag{2.7}$$

The χ^2 value is given by where $F_j(t)$, F_j^{obs} and σ_j are the template flux, observed flux and the observed flux error in the jth filter respectively. The template types, t, and their associated fluxes correspond to the full range of galaxy parameters (age, star-formation history, dust extinction and metallicity) at the closest matching redshift in the model SED grid.

Because we fit all templates simultaneously, it is therefore straight-forward to calculate the stellar mass probability distribution function (PDF), i.e.

$$P(M) \propto \sum_t \mathcal{L}(M,t), \tag{2.8}$$

marginalised over all other template galaxy properties (assuming a flat prior). Similarly, PDFs for other parameters such as β or M_{UV} ($M_{1500\text{A}^\circ}$) can be constructed by summing the likelihoods at a fixed parameter value. Estimating the galaxy parameters in such a way allows us to fully account for errors due to both degeneracies between galaxies properties and errors in the scaling due to the photometric errors.

For our mass fitting, model ages are allowed to vary from 5 Myr to the age of the Universe at a given redshift, dust attenuation is allowed to vary in the range $0 \leq A_V \leq 2$ and metallicities of 0.02, 0.2 and 1 $Z_\odot$. Due to the difficulty in obtaining spectroscopy at $z > 3$, the metallicity at high-redshift is not currently well known. Observations of samples at $z \sim 3$ and above (Shapley et al., 2003; Maiolino et al., 2008a; Sommariva et al., 2012; Jones et al., 2012) show that the average metallicity is likely to be mildly sub-solar, however there is a large scatter.

Sommariva et al. (2012) also find that the gas-phase and stellar metallicities are consistent within errors. As such, we choose to fix the metallicity for the nebular emission equal to stellar metallicity.

The star formation histories follow the exponential form $SFR \propto e^{-t/\tau}$ with characteristic timescales of τ = 0.05, 0.25, 0.5, 1, 2.5, 5, 10, -0.25, -0.5, -1, -2.5, -5, -10 and 1000 (effectively constant SFR) Gyrs. Negative τ values represent exponentially increasing histories. Fitting is done to the templates both with and without the inclusion of nebular emission. When nebular emission is included in the templates, we assume a moderate escape fraction $f_{\rm esc} = 0.2$, consistent with the observational constraints on reionization and with simulations (Yajima et al., 2010; Fernandez & Shull, 2011; Finkelstein et al., 2012; Robertson et al., 2013).

2.5.4 Star Formation Rates

In order to calculate UV star-formation rates, the rest frame absolute magnitudes (M_{1500}) measured from the SED fitting are first corrected for dust extinction using the Meurer et al. (1999) relation

$$A_{1600} = 4.43 + 1.99\beta, \tag{2.9}$$

which links the observed UV continuum slope β as measured by the SED fitting code (see Section 2.5.1) and the extinction at 1600Å, A_{1600}. For measured $\beta < -2.23$, where the above relation would imply a negative extinction, the UV extinction was set to 0. UV star-formation rates are calculated using:

$$\mathrm{SFR}(M_{\odot}\mathrm{yr}^{-1}) = \frac{L_{UV}(\mathrm{erg\ s^{-1}Hz^{-1}})}{13.9 \times 10^{27}}, \tag{2.10}$$

where the L_{UV} conversion factor of Madau et al. (1998) and Kennicutt (1998) corrected to the Chabrier IMF is used (-0.24 dex).

In addition to the the star formation rate obtained by this method ($\mathrm{SFR_{Madau}}$ hereafter), from our SED fitting code we also obtain the instantaneous star formation rate of the best-fitting template for each galaxy ($\mathrm{SFR_{Template}}$). We find that the two measures agree well at all SFRs with a median($\log_{10}(\mathrm{SFR_{Madau}}) -$

$\log_{10}(\mathrm{SFR_{Template}})) < 0.1$. With the exception of the few galaxies with the highest $\mathrm{SFR_{Madau}}$, typically $\mathrm{SFR_{Madau}} > 100$ $\mathrm{M_{\odot}yr^{-1}}$. These galaxies are red, such that the best-fitting template is an older quiescent stellar population. The Meurer relation however assumes an actively star-forming population with high dust extinction.

We also find that the scatter around the 1:1 relation correlates strongly with the age of the best-fitting SED template, such that younger populations have higher $\mathrm{SFR_{Template}}$. As we will show in the next section however, individual stellar population parameters such as age and dust extinction are very degenerate in SED fits of high-redshift galaxies. Because of these factors, and for consistency with previous works, we primarily use $\mathrm{SFR_{Madau}}$ throughout this work. The net effect of the differences in the two star-formation rate estimates can be seen in our observed SFR functions in Section 2.5.4.

2.5.5 Observed UV continuum slopes

As one of the key observables that it is possible to accurately measure for high-redshift galaxies using photometry, the UV continuum slope (β) has been well studied but with initally conflicting results (Dunlop et al., 2011; Wilkins et al., 2011; Bouwens et al., 2011d; Finkelstein et al., 2012; Rogers et al., 2013; Bouwens et al., 2014). The method used in this work to measure β follows a similar procedure to that outlined in Finkelstein et al. (2012). The relative accuracy of the different methods and the effects of differing sample criteria are explored in depth by Rogers et al. (2013), however from our simulations (Section 2.5.6) we can test the accuracy of our fitting directly. Figure 2.9 shows the difference between the input and measured β as a function of $\mathrm{H_{160}}$ magnitude for all regions of the GOODS-S field combined.

In Rogers et al. (2013), it was shown that the SED fitting method for measuring β suffers from a red bias when measuring the average slope. This is a result of limits placed on the measured β by the bluest template available in the fitting, artificially clipping the measurement to values above that limit. The problem is most severe for the faintest galaxies or those that have the least secure photometric

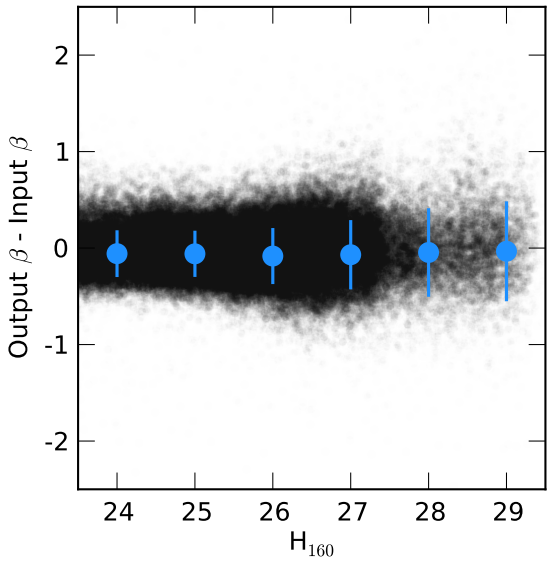

Figure 2.9: Recovered β - input β as a function of apparent H_{160} magnitude. The blue circles show the mean β_{out} - β_{in} in bins with width = 1 magnitude. The bias ($|median(\beta_{out} - \beta_{in})|$ is less than 0.1 for all magnitudes, whilst the standard deviation increases from = 0.24 at $H_{160} = 24$ to = 0.44 at $H_{160} = 28$

redshifts. In Figure 2.10, we show the measured β as a function of UV magnitude for one of our Monte Carlo samples alongside the M_{UV} binned bi-weight means and other values from the literature. We do not see a strong piling up of sources at the bluest templates (≈ -2.69 when nebular emission is included) suggesting our observations are not strongly affected by this potential bias. However, it may have a small effect on the average β for a fixed M_{UV} (see Figure 2.11).

Because we apply the dust correction to each galaxy based on its own measured β, rather than an observed average, our dust corrections will be unaffected by any such bias if it does exist. For any galaxy bluer than $\beta = -2.23$, the applied extinction based on the relation of Meurer et al. (1999) is 0. We note that it is now expected that the intrinsic UV slopes of high-redshift galaxies are significantly steeper (Castellano et al., 2014; Schaerer et al., 2015) and that the Meurer et al. (1999) may therefore no longer be valid. However, a full investigation of UV dust corrections at high redshift is beyond the scope of this thesis. The use of the Meurer et al. (1999) relation (and its implied intrinsic UV slope of $\beta = -2.23$) is used throughout this work in order to allow direct comparison with other dust corrections performed at high redshift (Smit et al., 2012).

For the measured βs in our high-redshift galaxy samples, we find that the observed

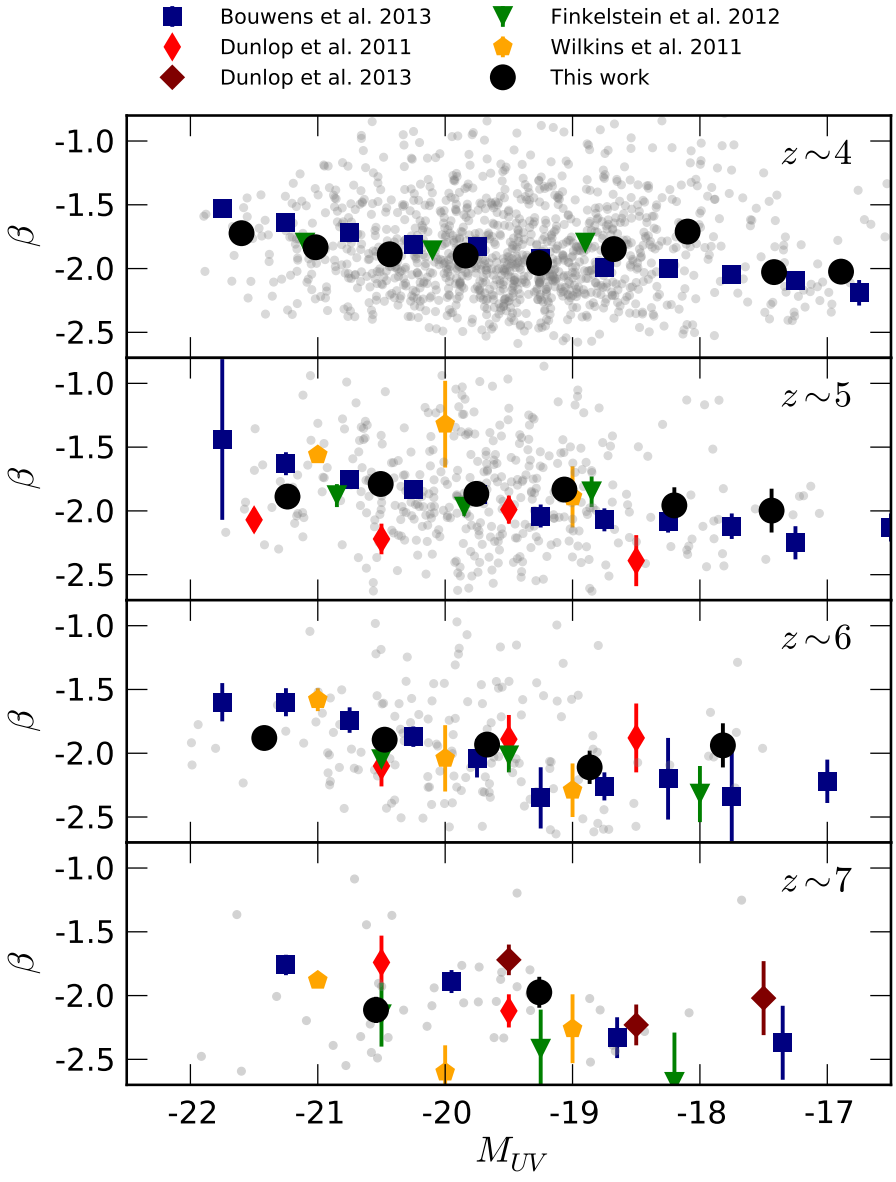

Figure 2.10: Measured UV continuum slope as a function of UV magnitude for this work and previous studies as of August 2014. The background grey circles show the individual points for one of the Monte Carlo samples used in our work. The black circles show the biweight mean β and corresponding standard error on the mean as a function of M_{UV} averaged over 100 of our Monte Carlo samples. Also shown are the equivalent M_{UV} binned means available from the literature.

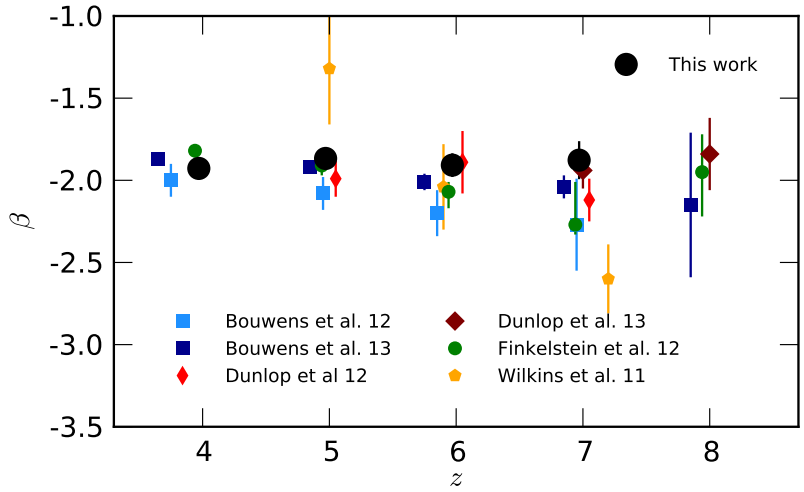

Figure 2.11: UV continuum slope as a function of redshift for a fixed UV magnitude. The points from (Finkelstein et al., 2011) are for a fixed $M_{UV} \sim 20$, all other data points are for $M_{UV} \sim 19.5$.

magnitude evolution in β (as a function of redshift of UV luminosity) is smaller than the estimated measurement errors for any individual galaxy (Figure 2.9). If the underlying intrinsic scatter is directly comparable to the measurement uncertainties, the use of average β values to make corrections for dust could systematically bias the inferred star-formation rate. However, as noted above, in this work we make use of the individually measured β values rather than the average values. We therefore do not perform any additional analysis in order to estimate the underlying true intrinsic scatter (e.g. for galaxies at a given UV luminosity). We note that through extensive tests on the observed M_{UV}-β relation at $z \sim 5$, Rogers et al. (2014) find that intrinsic scatter is significant, ranging from $\Delta\beta \approx 0.1$ to 0.5 for faint to bright galaxies respectively.

2.5.6 Image and Detection Simulations

By their nature, high-redshift galaxies are small and extremely faint objects. Lying close to the limiting depth in some (or even all) of the observed filters, noise and systematic effects can have a significant effect on the detection and completeness of high-redshift galaxy samples as well as the accurate estimation of their properties. The completeness of our galaxy sample can be separated into two distinct factors: firstly, the inclusion of an object in the initial catalog as a function of the detection image depth, and secondly, the selection of an object in

a given sample (e.g $z \approx 4$ based on its estimated redshift), which is a function of the overall SED shape and accompanying errors. In this section, we outline a set of detailed simulations undertaken to measure and correct for these effects.

2.5.6.1 Completeness Simulations

The detection completeness across the field was estimated by inserting thousands of mock galaxies into the detection image (H-band) used for the photometry and recovering them with the same SExtractor parameters and method used for the original sample catalog. The synthetic galaxies were first convolved with the CANDELS WFC3 H-band PSF before being placed randomly across the field with appropriate Poisson noise. The resulting image was then run through the same SExtractor procedure as the initial source detection and the process repeated until a total of $\approx 10^5$ input galaxies had been recovered across the entire field.

Galaxy sizes were drawn from a log-normal distribution of mean = 0.15″and $\sigma = 0.075$, motivated by existing observations of the size evolution of Lyman break galaxies (Ferguson et al., 2004; Oesch et al., 2010; Grazian et al., 2011; Huang et al., 2013) whilst the galaxies profiles were drawn from a distribution of Sérsic indices centred around $n = 1.5$ in the range $0.5 \leq n \leq 4.0$. Although the precise distribution of morphological profiles for high-redshift galaxies is not well known, studies of lower redshift analogues and stacked samples of LBGs suggests that they are predominantly disk-like ($n < 2$) (Ravindranath et al., 2006; Hathi et al., 2007). Our chosen distribution reflects this, with $\sim 80\%$ of input galaxies with $n \leq 2$.

Figure 2.12 shows the resulting completeness curves for each of the image regions. In Guo et al. (2013), the H_{160} 50% completeness limit is estimated using the differential number density to be 25.9, 26.6 and 28.1 for the WIDE, DEEP+ERS and UDF regions respectively. When compared to the results of a set of detection simulations similar to those undertaken in our work, Guo et al. (2013) find a good agreement between the two estimates. For the UDF and DEEP+ERS regions, our 50% completeness limits are in good agreement with those of Guo et al. (2013). However, in the WIDE region we find a 50% completeness limit ≈ 0.5 mag deeper

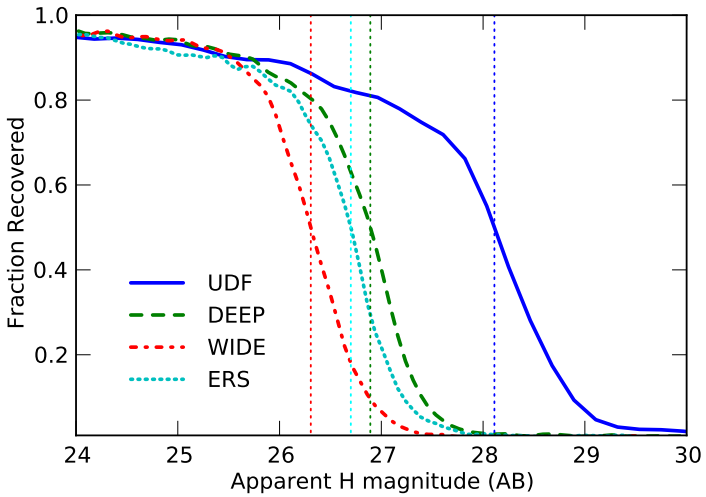

Figure 2.12: Completeness as a function of H_{160} magnitude for each region of the GOODS South field. The vertical dashed lines show the magnitude at which the recovery fraction equals 0.5 for each region of the field.

for our input galaxy population.

Grazian et al. (2011) demonstrated the significant effect that sizes and morphologies can have on the completeness simulations of high-redshift galaxies. Differences due to the distribution of sizes and slightly differing galaxy profiles used are to be expected. For all regions, the effects of confusion and blending with nearby sources results in a small fraction of input galaxies that are not recovered by the photometry, even at brighter magnitudes. We note that the surface density of mock sources input into the image was ≈ 30 arcmin^{-2}, significantly lower than the surface density of detected sources in the initial photometry catalog (≈ 200 arcmin^{-2}). The overall surface density of sources within the images was therefore not significantly increased by the mock sources and we are confident that the effects of confusion have not been unduly biased by these input sources.

2.5.6.2 Sample Selection

To estimate the selection functions for each of the redshift bins, a mock photometry catalog of high-redshift galaxies was created and put through the same photometric redshift and sample selection criteria as our real sample. This catalog was constructed by first creating a sample of SEDs drawn randomly from the template sets used for fitting (both with and without nebular emission) with a distribution of β centred at ≈ -1.8 to -2, but extending out to $\beta > 1$. Redshifts

were allowed to vary in the range $2.5 < z < 9$ and the templates were scaled to H_{160} band magnitudes in the range $22 < H_{160} < 30$, with the corresponding magnitudes in the other filters determined by the shape of each SED.

We produced a catalog in this way, rather than using the mock photometry of semi analytic models as used in Section 2.4, in order to allow the inclusion of nebular emission in subsequent tests on the stellar mass fitting and ensure good number statistics across all input magnitudes.

In order to assign photometric errors to the mock photometry (or non-observations where appropriate), each simulated galaxy was assigned a position in the field drawn from the same set of input coordinates as used in the completeness simulations. Photometric errors were then assigned to each photometric band based on the observed flux errors of objects in the original catalog, specific to the region in which it resides (e.g. CANDELS Deep). The flux values for each SED were then perturbed by a gaussian of width equal to the photometric error.

This process does not precisely mirror the method used to produce the observed photometry as it does not include the source extraction for each band individually. However, the resulting catalog is a very close approximation with a catalog of SEDs that have realistic photometric errors and filter coverage across the field, e.g. Y_{098} observations in the ERS region alone.

To measure the selection efficiency for our high-redshift samples, 100 simulated Monte Carlo samples were created from the template-based mock galaxy catalog (as described in this section) using the method outlined in Section 2.3.1. From these samples, we measured the fraction of simulated galaxies that pass the selection criteria for any of the high-redshift samples as a function of input redshift and magnitude.

Figure 2.13 shows the measured selection efficiencies for the deepest region of the field, the UDF. The selection probabilities (as indicated by the colour scale) do not include the effects of completeness as measured in Section 2.5.6.1, therefore the lower probabilities measured at faint magnitude are a result of photometric redshift errors due to poor constraints from faint photometry.

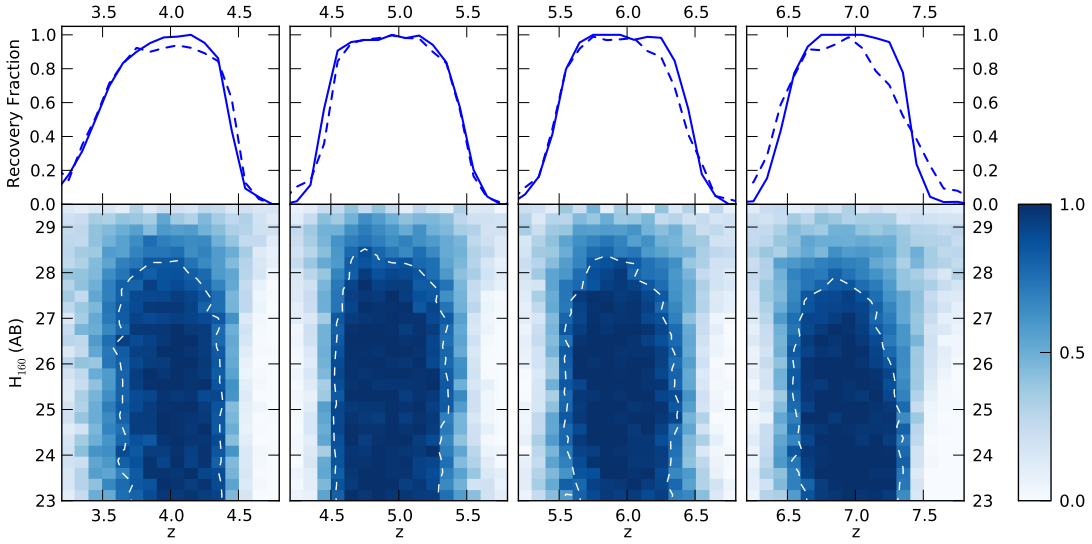

Figure 2.13: Example selection efficiencies for the Ultra Deep Field region of the CANDELS field. The colour scale represents the fraction of input galaxies which pass the $P(z)$ criteria for a given redshift bin as a function of input redshift and apparent magnitude. The dashed white line in the lower sections of the figure shows the 80% contour in the fraction of recovered galaxies. The upper panels show the recovery fraction as a function of redshift at a fixed input magnitude, $H_{160} = 25$ (continuous) and $H_{160} = 27$ (dashed).

For $z \sim 4$ and 5, where the semi-analytic mock catalog used in Section 2.4 has good number statistics across a wide magnitude range, we reproduce the selection function in the same manner as above and find that the shape of the resulting selection functions are unchanged. We are therefore confident that the photometric selection of our samples is robust to variations in the exact shape of the input SEDs and the limiting factor in selection is the photometric noise.

2.5.6.3 Uncertainties in measuring galaxy parameters

The ability of SED fitting codes to recover the properties of dropout galaxies was well explored by Lee et al. (2010), who found that stellar mass was the most reliably measured parameter (in comparison to star formation rate and age) and the most robust to assumptions in star-formation history. However this analysis was limited to input and fitted SED models that did not include the effects of nebular emission. The degeneracies in measuring age, dust extinction and star-formation histories from SED fitting have also been well examined e.g. Schaerer & de Barros (2010). Despite these degeneracies, it has been shown that one can reliably measure the UV continuum slope, β (Finkelstein et al., 2011; Rogers et al., 2013). Given assumptions about the age and metallicity, i.e. the underlying

intrinsic β, it is then possible to estimate the dust extinction using observations of β.

For the $\sim 10^5$ galaxies in our simulated catalog that pass the selection criteria, we ran them through the SED fitting code using the same fitting parameters as for our observed data. From these results we are able to test how well the input stellar masses are recovered for our simulated galaxies. In addition, we can also test the accuracy in recovering the other properties of the input stellar populations.

Figure 2.14 illustrates how well the SED code is able to recover the stellar masses, ages and dust extinction. As expected, stellar mass is the most robust of the parameters with age and dust extinction showing a very large scatter and bias due to the degeneracy in fitting. The recovery of the input dust extinction in particular is very poor, with the extinction in very dusty galaxies systematically underestimated by a factor of $\approx \times 2A_V$. For input templates with low to moderate dust extinction (0 to $0.5A_V$), as the majority of high-redshift galaxies are expected to be, the error in the best-fit dust extinction becomes dominated by the very large scatter. Despite these degeneracies in the single best-fitting templates, when calculating the marginalised β over all template likelihoods the resulting estimate of β is un-biased and well constrained. We show the estimated accuracy of our β measurements from these simulations in Section 2.5.5.

For input galaxies with masses $\approx 10^9 \mathrm{M}_\odot$, the median$(\log_{10}(\mathrm{M_{out}}) - \log_{10}(\mathrm{M_{in}}))$ = 0.02, with a standard deviation of 0.4 when input SEDs including nebular emission are fitted with comparable templates. For input masses $\approx 10^{8.5}\mathrm{M}_\odot$ and below, both the bias (+0.22 dex at $\approx 10^{8.5}\mathrm{M}_\odot$) and scatter increase. When mock galaxies with pure stellar SEDs are fitted with pure stellar templates, both the scatter and bias are reduced at all mass ranges. The increased bias and scatter for galaxies with nebular emission is a result of confusion between an older stellar population with a 4000Å break and a young star-forming galaxy with strong nebular emission (Schaerer & de Barros, 2009; Curtis-Lake et al., 2013).

Finally, we find that the recovered value for M_{UV} is extremely robust across the full dynamic range of our data, with a scatter of < 0.2 dex and negligible bias

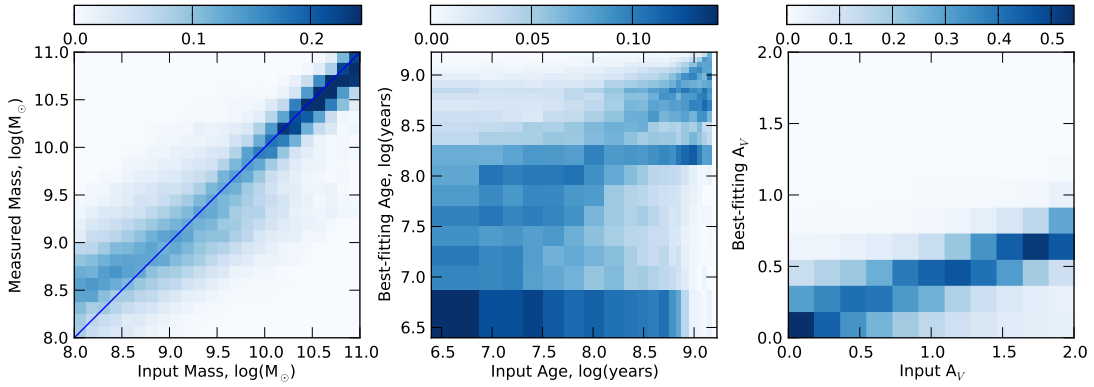

Figure 2.14: 2D histograms showing the recovered SED parameters for a set of input SEDs incorporating nebular emission when fitted with nebular emission. The values for the age (centre) and dust (right) are those corresponding to the single best-fitting model whilst the measured mass (left) is taken as $\int MP(M)dM$ for the mass likelihood distribution marginalised over all other parameters. Each histogram is normalised by the number of input galaxies in each bin and the colour scale corresponds to the fraction of input galaxies at the observed mass (/age/dust extinction).

across all redshift out to the limits of our completeness as shown in Figure 2.15. From these simulations, we determine that M_{UV} is robust to $M_{UV} \approx$ -17 at $z \approx 4$, reducing to -18 at $z \approx 7$.

2.6 Results

2.6.1 The $1/V_{\rm max}$ estimator

To compute our luminosity and mass functions we use an extension of the $1/V_{\rm max}$ method of Schmidt (1968), treating each of our high-redshift samples as a "coherent' sample comprised of the individual GOODS South regions with corresponding depths as outlined by Avni & Bahcall (1980); Eales (1993); Ilbert et al. (2005). The maximum comoving volume in which a galaxy can be observed and remain in the sample is given by

$$V_{\rm max,i} = \sum_{k}^{N_{regions}} \int_{z_{1,k}}^{z_{2,k}} \frac{dV}{dz} dz \; d\Omega_k \tag{2.11}$$

where the sum, k, is over each of the sub-regions in the field with their corresponding solid angle, $d\Omega_k$, integration limits $z_{1,k}$, $z_{2,k}$ and dV/dz is the comoving volume element in Mpc^3 at redshift z. The integration limits are given by $z_{1,k} = z_{min}$ and $z_{2,k} = min\left\{z_{max}, z(z_j, m_j, m_{max,k})\right\}$ where z_{min} and z_{max} are the lower and upper

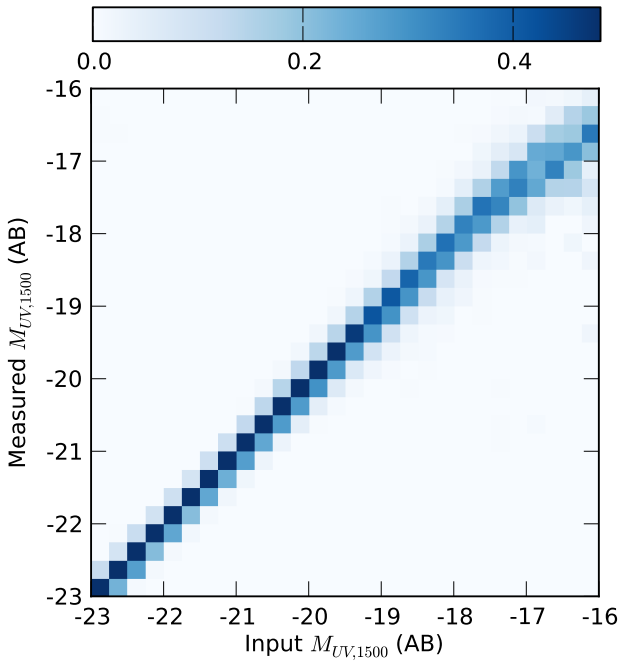

Figure 2.15: Comparison of the recovered versus input M_{UV} for the full mock galaxy sample. As in Figure 2.14, the histogram is normalised by the number of input galaxies in each bin and the colour scale corresponds to the fraction of input galaxies at the observed M_{UV}.

boundaries respectively for the given redshift bin, e.g. $z_{min} = 4.5$ and $z_{max} = 5.5$ for the $z \approx 5$ sample. The function, $z(z_j, m_j, m_{max,k})$, returns the maximum redshift at which an object of apparent magnitude m_j, observed redshift z_j, could still be observed given the magnitude limit $m_{max,k}$ of the region.

The mass (or luminosity) function ϕ_k for discrete bins of mass (/magnitude) k is then:

$$\phi_k dM = \sum_{i}^{N_{gal}} \frac{w_i}{V_{\mathrm{max},i}} W(M_k - M_i), \tag{2.12}$$

where the weighting term, w_i, incorporates corrections for incompleteness and the selection function of the redshift bin as calculated in Section 2.5.6. The window function W is defined as

$$W(x) = \begin{cases} 1 \text{ if } -dM/2 \leq x < dM/2 \\ 0 \text{ otherwise} \end{cases} \tag{2.13}$$

and N_{gal} is the number of galaxies in the sample.

To incorporate the large error in the stellar masses, where the mass likelihood function for an individual galaxy can span a range much larger than the desired bin widths, we make amendments to Equation 2.12, such that the mass function evaluated for the mass bin $M_1 < M_k < M_2$ is given by

$$\phi(M)dM = \sum_{i}^{N_{gal}} \frac{w_i}{V_{max,i}} \int_{M_1}^{M_2} P_i(M)dM \tag{2.14}$$

where $P_i(M)$ is the probability of galaxy i having stellar mass, M, as calculated from the SED fitting at the fixed redshift for that specific Monte Carlo sample.

2.6.2 UV Luminosity functions

As a more robust observable (relative to the stellar mass, Section 2.5.6) with many previous observations, the rest-frame UV luminosity function provides a useful comparison for the method and completeness corrections used in this chapter. To ensure that the shapes of our observed mass functions are not affected by biases in our $1/V_{\rm max}$ or completeness correction methods we reproduce the luminosity function (LF) for each of our redshift bins, which we can compare to previous work. Figure 2.16 shows the discretized luminosity functions calculated using the method outlined in Equation 2.12. In comparison with previous measurements of the luminosity function at high-redshift we find overall a very good agreement in the general shape of the luminosity functions for our $1/V_{\rm max}$ data points.

The data points for this work were also fit through χ^2-minimisation with the Schechter (1976) parameterization

$$\phi(M) = \phi^* \tfrac{\log(10)}{2.5} 10^{-0.4(M-M^*)(\alpha+1)} \exp\left(-10^{-0.4(M-M^*)}\right), \tag{2.15}$$

where M is the rest-frame UV magnitude and ϕ^*, α and M^* are the normalisation, faint-end slope and characteristic UV magnitude as standard. The resulting best-fitting parameters shown in Table 2.3 along with the corresponding parameters from the selected literature observations shown in Figure 2.16. At all redshifts, the faint end slope is steep ($\alpha < -1.6$) and shows a tentative steepening towards

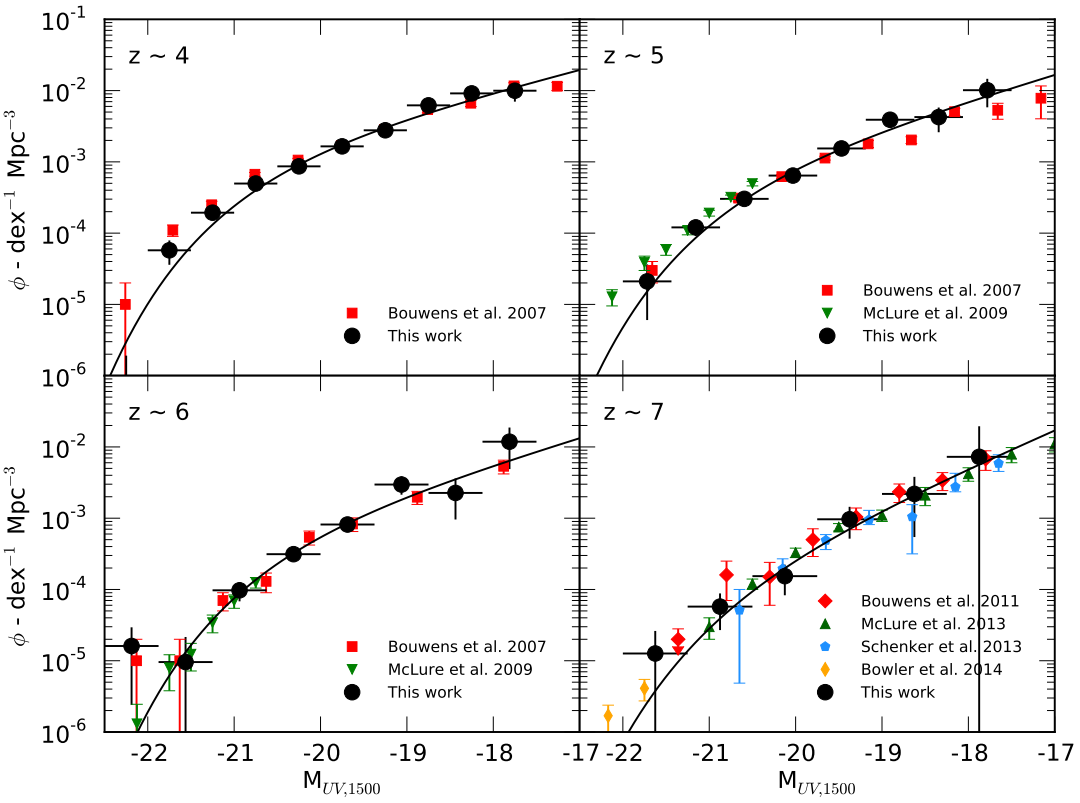

Figure 2.16: A comparison of our $1/V_{\rm max}$ luminosity function estimates with those in the literature. We show the results of Bouwens et al. (2007) at $z \approx 4, 5$ & 6 (red squares) derived from deep HST observations as well as the ground-based estimates of the bright end of the $z \approx 5$ and 6 luminosity functions by McLure et al. (2009)(green downward triangles). For the $z \approx 7$ LF, we show the estimate of Bouwens et al. (2011c) as well as the recent results of McLure et al. (2013) and Schenker et al. (2013a) which make use of the deeper UDF12 observations (Koekemoer et al., 2013) to probe fainter M_{UV} than we are able to.

$z \sim 7$. However, the poor constraints on the faint end slope towards the highest redshifts make it difficult to comment on any evolution of the slope that might occur over this redshift range. At all redshifts, the slope is consistent with a fixed slope of $\alpha = -1.7$ (Bouwens et al., 2011c).

At $z \sim 4$, our measured M^*_{UV} of -20.47±0.21 is significantly fainter than that observed by Bouwens et al. (2007), who find $M^*_{UV} = -21.06 \pm 0.1$. We find a closer agreement with the fainter M^*_{UV} observed by Huang et al. (2013) of $-20.60^{+0.13}_{-0.17}$. At the bright end of the $z \sim 4$ luminosity function, our fit is strongly affected by the very low number density at $M_{UV} \approx -22.25$. Given the relatively small area of our survey field, the numbers of galaxies contributing to the brightest bins is very small ($\approx 1-3$). Differences in the measured (or assumed) redshift when calculating the rest-frame magnitude can therefore have a large effect, e.g.

Table 2.3: Schechter (1976) function parameters for χ^2 fits to the $1/V_{\rm max}$ luminosity functions. The quoted errors represent the 1-σ limits, but do not account for systematic error due to cosmic variance.

Redshift	M^*_{UV}	α	ϕ^* (10^{-3} Mpc^{-3})
z $\sim$ 4			
This work	-20.47 $\pm$0.21	-1.77 $\pm$0.18	$1.90^{+0.79}_{-0.65}$
Bouwens et al. 2007	-21.06 $\pm$ 0.1	-1.76 $\pm$ 0.05	1.1 $\pm$ 0.2
z $\sim$ 5			
This work	-20.47 $^{+0.26}$	$-1.90^{+0.21}_{-0.16}$	$1.07^{+0.59}_{-0.14}$
Bouwens et al. 2007	-20.69 $\pm$ 0.13	-1.66 $\pm$ 0.09	0.9 $^{+0.3}_{-0.2}$
McLure et al. 2009	-20.73 $\pm$ 0.11	-1.66 $\pm$ 0.06	0.94 $\pm$0.19
Bouwens et al. 2012	-20.60 $\pm$ 0.23	-1.79 $\pm$ 0.12	1.4 $^{+0.7}_{-0.5}$
z $\sim$ 6			
This work	$-20.31^{+0.84}_{-1.59}$	$-1.91^{+0.91}_{-0.59}$	$0.95^{+2.21}_{-0.91}$
Bouwens et al. 2007	-20.29 $\pm$ 0.19	-1.77 $\pm$ 0.16	1.2 $^{+0.6}_{-0.4}$
McLure et al. 2009	-20.04 $\pm$ 0.12	-1.71 $\pm$ 0.11	1.8 $\pm$0.5
Bouwens et al. 2012	-20.37 $\pm$ 0.3	-1.73 $\pm$ 0.20	1.4 $^{+1.1}_{-0.6}$
z $\sim$ 7			
This work	$-20.47^{+1.43}$	$-2.31^{+1.31}_{-0.19}$	$0.29^{+2.87}_{-0.13}$
Bouwens et al. 2011	-20.14 $\pm$ 0.26	-2.01 $^{+0.14}_{-0.15}$	$0.86^{+0.70}_{-0.39}$
McLure et al. 2013	-19.90 $^{+0.23}_{-0.28}$	-1.9 $^{+0.14}_{-0.15}$	$1.10^{+0.56}_{-0.45}$
Schenker et al. 2013	-20.14 $^{+0.36}_{-0.48}$	-1.87 $^{+0.18}_{-0.17}$	$0.64^{+0.56}_{-0.27}$

the difference in the distance modulus between $z = 3.5$ and $z = 4$ is ≈ 0.35. As such, the characteristic cut-off in our Schecter function parameterisation is not well constrained, and the discrepancy is not significant.

2.6.3 Observed mass-to-light ratios

In the past, the relationship between a galaxy's stellar mass and its UV luminosity (or $\log_{10}(\mathrm{M}_*)$ and M_{UV}) has been used as both a diagnostic of galaxy formation histories (Stark et al., 2009) and as a tool for estimating the galaxy stellar mass function at high-redshift (González et al., 2011). In a scenario where galaxies form their stars continuously, a strong $\log_{10}(\mathrm{M}_*)$-M_{UV} relation should form, whereas more stochastic bursty star formation modes could result in a relation with wider scatter and a weaker trend.

Using the stellar mass and M_{UV} probability distributions produced by our SED fitting code, we plot the observed mass-to-light ratios for each of our redshift bins in Figure 2.17. For a given Monte Carlo sample (see Section 2.3.1), the

2D $\log_{10}(\mathrm{M}_*)$-M_{UV} probability distributions of each galaxy in the redshift bin are summed. The resulting PDFs of each sample are then summed to create a combined PDF in each redshift bin across all Monte Carlo samples. Finally, we normalise such that the probability at each value of M_{UV} integrates to unity. By plotting the observed $\log_{10}(\mathrm{M}_*)$-M_{UV} in this way, we take into account the full redshift and fitting errors. However, this representation is still subject to the effects of small number statistics for the brightest and faintest galaxies.

As such, we also show the biweight mean $\log_{10}(\mathrm{M}_*)$ for bins of M_{UV} within the range of reliably measurable M_{UV}. For $z \geq 5$, each bin contains a minimum of 5 galaxies by design, whilst for the $z \sim 4$ sample each bin contains a minimum of 10 galaxies. To these means, we fit linear functions with intercept $\log_{10} \mathrm{M}_{*(M_{UV}=-19.5)}$ and slope $d \log_{10} \mathrm{M}_*/dM_{UV}$. The best-fit values for each redshift sample are shown in Table 2.4 for stellar mass estimates both with and without the inclusion of nebular emission.

As has been seen in many previous studies, we observe a clear 'main-sequence' trend of increasing mass with increasing UV luminosity, and a large scatter about this trend. For the bright galaxies ($\mathrm{M}_{UV} < -21$), our results agree well with those of Stark et al. (2009), González et al. (2011) and Lee et al. (2012). Over the full range of UV luminosity, we find a shallower trend with M_{UV} than González et al. (2011). We also find that this trend evolves in normalisation between redshift $z \sim 4$ and 7.

The change in the observed normalisation of the $\log_{10}(\mathrm{M}_*)$-M_{UV} relation with redshift as a consequence of the inclusion of nebular emission has been examined before (Shim et al., 2011; Schenker et al., 2013b; Stark et al., 2013; de Barros et al., 2014). However, we find that although this trend for decreasing normalisation with redshift is enhanced when nebular emission is included in the mass fitting, the trend still exists when fitting with pure stellar templates (see Table 2.4).

In Figure 2.17, the effect of including nebular emission in the stellar mass estimate can be seen clearly in the bottom panel. At all redshifts, the average stellar mass for a given M_{UV} is lower when nebular emission is included. Salmon et al. (2015) also consider the effects of adding nebular emission lines to the SED models for

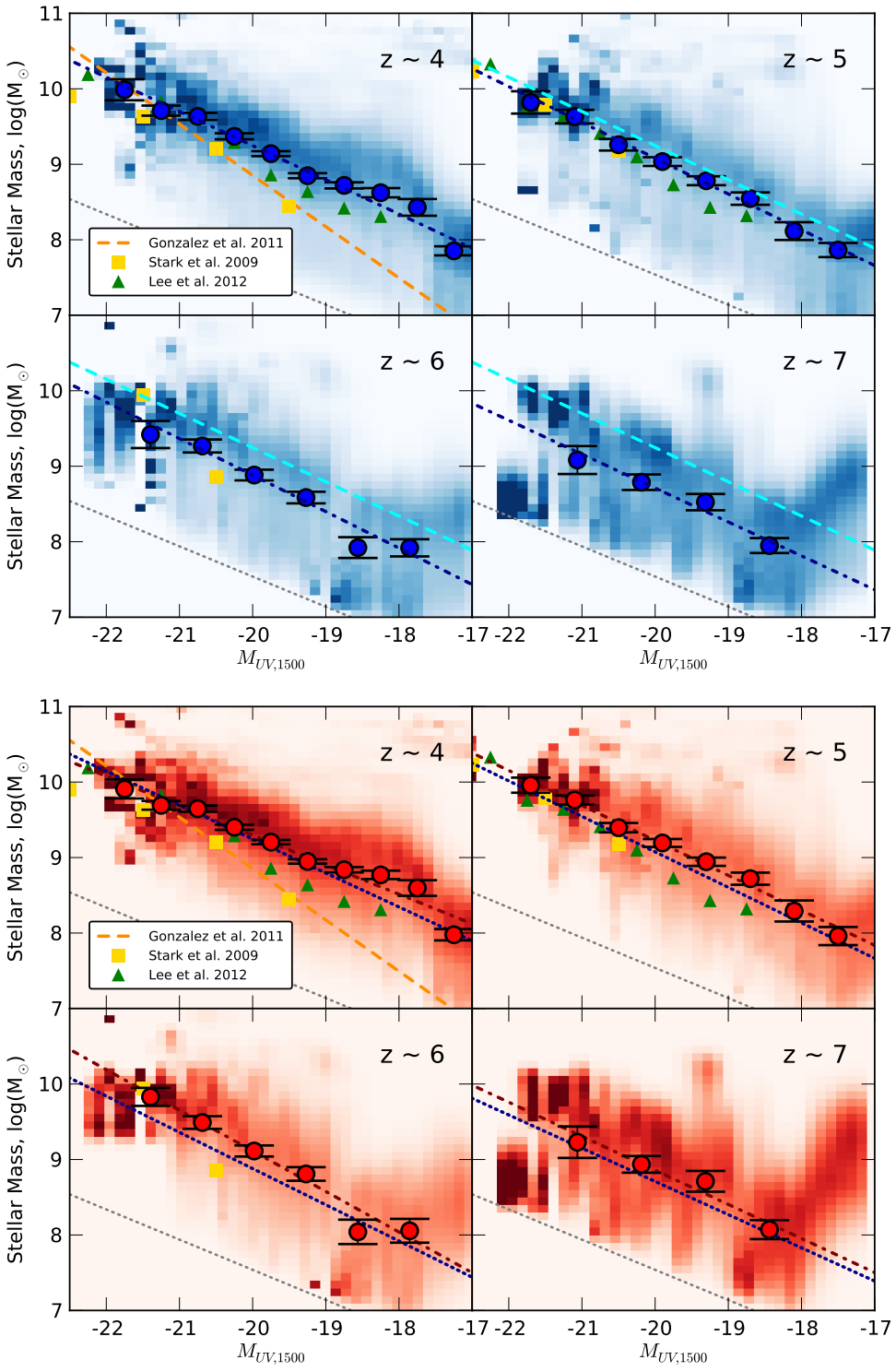

Figure 2.17: Top: Probability distribution of the mass-to-light ratios observed when nebular emission is included in the fitting, stacked across all of the Monte Carlo samples. The values are normalised such that the probability at each value of M_{UV} integrates to unity The blue dot-dashed line represents the average of the best-fitting line to robust means in each of the Monte Carlo samples, with the corresponding average means and their errors shown by the blue circles. The $z \sim 4$ relation is shown for reference at high-redshifts (cyan dotted line). Bottom: The corresponding probability distributions, bi-weight means and best-fitting relation (red dot-dashed line) when nebular emission is excluded from the SED fitting. The blue dotted line shows the best-fitting relation from the top panel (including nebular emission) for each sample. In both panels, the orange dashed line shows the mass-to-light ratio observed by González et al. (2011), measured for their $z \approx 4$ sample and applied across all bins. The green triangles and yellow squares show the average stellar mass in M_{UV} bins as calculated by Lee et al. (2012) and Stark et al. (2009) respectively, all stellar masses have been converted to the same Chabrier IMF. The grey dotted line represents the template in our SED fitting parameters with the lowest mass to light ratio.

galaxies in the same redshift range, and they find similar changes to the derived masses as we do here. In addition, the median stellar masses they observe for UV faint galaxies are higher than those of González et al. (2011) and Lee et al. (2012), consistent with our observations.

Because in our SED fitting on the mass, we restrict the age of the templates to be less than the age of the universe at that redshift, the range of $\log_{10}(\mathrm{M}_*)$-M_{UV} ratios available in the fitting does vary with redshift, i.e. a galaxy at $z = 7$ can never have as old as a stellar population as a galaxy at $z = 4$. If the fits to galaxies at $z \sim 6$ and 7 were being restricted by this upper limit, the limits set by the template set could create an artificial evolution in the scaling of the $\log_{10}(\mathrm{M}_*)$-M_{UV} relation with redshift. However, examining the best-fitting SED parameters across all of the Monte Carlo samples, we find that at all redshifts and M_{UV} values the highest best-fitting mass lies well below the maximum mass allowed by the template set. From this, we conclude that the observed scaling is therefore physical and not a result of systematics in our analysis.

The slopes of our fitted $\log_{10}(\mathrm{M}_*)$-M_{UV} relations are all close to that of a constant mass to light ratio ($\mathrm{M}_* \propto -0.4\ M_{UV}$) across the full range in luminosity. This implies there is no strong evolution of the mass to light ratio with luminosity. Lee et al. (2012) suggested the source of the change in their observed $\log_{10}(\mathrm{M}_*)$-M_{UV} ratio could be due to a luminosity dependent extinction, a result which had also been implied by the evolution of β with M_{UV} seen by Bouwens et al. (2011d). Subsequent observations by Dunlop et al. (2011) and Finkelstein et al. (2011) have found no obvious luminosity dependence. However, recent studies by Bouwens et al. (2014) and (Rogers et al., 2014) with greatly increased sample sizes and greater dynamic range confirm an unambiguous colour-magnitude relation. While measurements of β for our sample do not exhibit strong evidence for such a strong luminosity dependent extinction at any redshift (see Section 2.5.5), our sample does not contain a statistically significant number of the brightest and faintest galaxies to rule out such evolution given the large scatter and error on β.

Due to the increasing uncertainty in stellar mass measurements for galaxies below $10^9\mathrm{M}_\odot$, the average mass-to-light ratios for the faintest galaxies could become

Table 2.4: The best-fitting slope and intercepts of the $\log_{10}(\mathrm{M}_*)$-M_{UV} mass-to-light relation, averaged across all Monte Carlo samples. At $z \sim 4$ and 5, we also show in parentheses the best-fitting values when the fits are restricted to only the brightest galaxies ($M_{UV} < -19.5$).

z	$\log_{10}\mathrm{M}_{*\ (M_{UV}=-19.5)}$	$d\log_{10}\mathrm{M}_*/dM_{UV}$
	With Nebular Em.	
4	9.02 ± 0.02	-0.45 ± 0.02
	(9.06 ± 0.05)	(-0.42 ± 0.06)
5	8.84 ± 0.04	-0.47 ± 0.04
	(8.85 ± 0.12)	(-0.46 ± 0.11)
6	8.64 ± 0.06	-0.48 ± 0.07
7	8.49 ± 0.09	-0.44 ± 0.12
	Without Nebular Em.	
4	9.10 ± 0.02	-0.39 ± 0.02
	(9.12 ± 0.05)	(-0.37 ± 0.05)
5	9.00 ± 0.04	-0.46 ± 0.04
	(9.00 ± 0.09)	(-0.45 ± 0.08)
6	8.84 ± 0.07	-0.54 ± 0.07
7	8.63 ± 0.11	-0.45 ± 0.13

increasingly biased towards fainter UV luminosities. As such, we cannot rule out a change in the $\log_{10}(\mathrm{M}_*)$-M_{UV} slope at faint luminosities like that inferred by Lee et al. (2012). To better constrain the average mass-to-light ratio for faint galaxies, detailed stacking across the full SEDs as a function of M_{UV} would be required. Restricting our analysis to the brightest galaxies ($M_{UV} < -19.5$) at $z \sim 4$ and 5 where the potential biases are minimised, we find no significant change in the fitted $\log_{10}(\mathrm{M}_*)$-M_{UV} slopes.

In hydrodynamical simulations of galaxies at $z > 5$, Wilkins et al. (2013) found a relationship between the intrinsic L_{1500} (excluding dust absorption) and M/L_{1500} which is roughly constant. This relationship is also seen to evolve, with the normalisation decreasing with increasing redshift. When dust extinction was applied to the intrinsic model luminosities based on the β observations of Bouwens et al. (2011d), the observed $\log_{10}(\mathrm{M}_*)$-M_{UV} exhibited a much stronger correlation comparable to that observed by González et al. (2011).

2.6.4 Stellar mass functions at high redshift

Following the method outlined in Section 2.6.1, specifically using the $1/V_{\rm max}$ method in Equation 2.14, we construct the stellar mass function for each of our high-redshift samples. The resulting stellar mass functions are shown in Figure 2.18. Our data points and errors take into account the stellar mass errors, Poisson errors and the errors due to the photometric redshift uncertainty.

The black lines in Figure 2.18 show the best-fitting Schechter (1976) functions from χ^2 minimisation to the the $1/V_{\rm max}$ data above our chosen mass completeness limits (black points). We perform two sets of fits to our data. Firstly, we allow all 3 parameters to vary (solid line, $z \sim 4, 5$ and 6) and secondly, we fix the characteristic mass such that $\rm M^* = M^*_{z\sim4}$ (dashed line, $z \sim 5, 6$ and 7). The parameters for these fits are shown in Table 2.5.

Because there exists such a large scatter in the observed mass-to-light ratios for the high-redshift galaxies, accurately estimating the mass completeness limit is non-trivial. For a given mass near the completeness limit, there could exist a significant contribution from galaxies below the luminosity limit proportional to how large the actual intrinsic scatter is. However, it is not known how much of the observed scatter is due to photometric error (and therefore photometric redshift estimates and parameters from SED fitting) and how much is intrinsic. Rather than trying to correct for galaxies lost through incompleteness down to the lowest observed masses, we instead restrict our analysis to masses unaffected by this scatter. We calculate this mass limit by taking the 95% mass percentile of the observed galaxies within 0.5 dex of our H_{160} magnitude limit, finding it to be $\approx 10^{8.5}$ $\rm M_\odot$. Under the reasonable assumption that the intrinsic scatter in the mass-to-light ratio does not rapidly increase below our detection limit, the contribution to masses above $\approx 10^{8.5}$ from galaxies below the limit will be negligible.

Additionally, as shown in Section 2.5.6, the accuracy of stellar mass estimates begins to deteriorate at lower masses with an increasing bias which could lead to biased slopes. Taking these factors into account, the limits chosen when fitting the stellar mass functions were $\log_{10}(\rm M_\odot) = 8.55$, 8.85, 8.85 and 9.15 for $z \sim 4$,

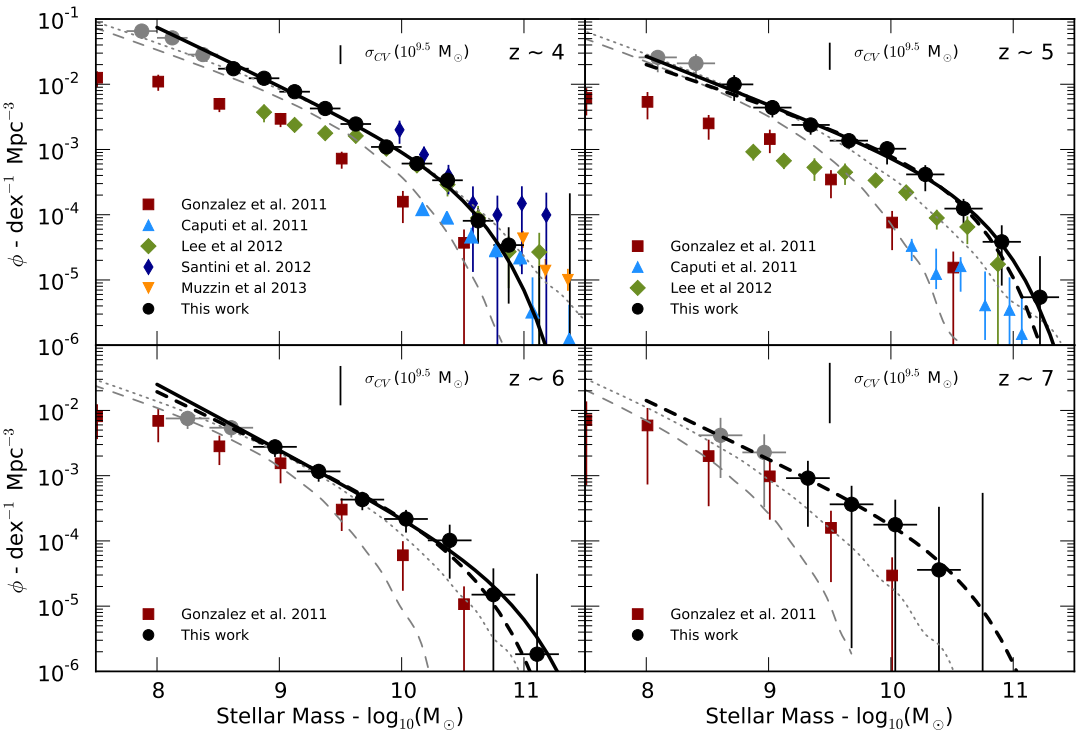

Figure 2.18: The $1/V_{\rm max}$ stellar mass functions for the high-redshift samples. Error bars take into account random Poisson noise as well as the scatter between the Monte Carlo samples due to photometric redshift uncertainty. The black circles show the mass bins included in the χ^2 fitting to the Schechter (1976) functions based on the stellar mass limits described in the text. The dashed and dotted lines show the stellar mass functions calculated by applying the best-fitting mass-to-light ratio (including nebular emission, see Table 2.4) to the literature luminosity functions at each redshift with a scatter of 0.2 (dashed) and 0.5 (dotted) dex. For the $z \sim 4$ bin, the Schecter fit of Bouwens et al. (2007) was used, whilst at $z \sim 5$ & 6 and $z \sim 7$ the fits of Bouwens et al. (2012) and McLure et al. (2013) respectively were used to generate the luminosity distribution. We also show using the error bars at the top of each panel the cosmic variance expected for galaxies of stellar mass $\approx 10^{9.5}$ M$_\odot$, as predicted by the method outlined in Moster et al. (2011).

5, 6 and 7 respectively.

Inspecting the observed mass functions in Figure 2.18, it can be seen that the exact limit should have little effect on the measured slope within reasonable bounds at $z \sim 4-6$. Choosing limits ± 0.5 dex would not affect our conclusion that the mass function is steep.

Due to the small sample size at $z \sim 7$ and the large errors in estimating the stellar mass (from both the photometric redshift and fitting errors), the mass function is very poorly constrained. The range of acceptable values for α cover an extremely wide range but are consistent with the slope of $\alpha \approx -1.9$ found for the lower redshift bins and the slope of the corresponding luminosity function. Over the redshift range examined by this work, the errors in α are too large to infer any

Table 2.5: Schechter (1976) function parameters for χ^2 fits to the $1/V_{\rm max}$ mass functions. For the $z \sim 5$, 6 and 7 samples, we do two fits, one in which $\log_{10}(\mathrm{M}^*)$ is allowed to vary, and one in which it is fixed to the best-fitting value for the $z \sim 4$ sample. The quoted errors represent the 1-σ errors from fitting marginalised over the remaining parameters but do not account for any systematic errors due to cosmic variance.

z	$\log_{10}(\mathrm{M}^*)$	α	ϕ^* (10^{-4} Mpc^{-3})
4	$10.51^{+0.36}_{-0.32}$	$-1.89^{+0.15}_{-0.13}$	$1.89^{+3.46}_{-1.32}$
5	$10.68^{+0.98}_{-0.46}$	$-1.74^{+0.41}_{-0.29}$	$1.24^{+4.77}_{-1.19}$
	10.51	$-1.64^{+0.15}_{-0.17}$	$2.21^{+0.80}_{-0.76}$
6	$10.87^{+1.13}_{-1.06}$	$-2.00^{+0.57}_{-0.40}$	$0.14^{+4.11}_{-0.14}$
	10.51	$-1.90^{+0.27}_{-0.31}$	$0.46^{+0.36}_{-0.26}$
7	10.51	$-1.89^{+1.39}_{-0.61}$	$0.36^{+3.01}_{-0.35}$

evolution in slope with redshift.

As we are observing only a single field, we are unable to estimate the cosmic variance in the number densities by comparing the field to field variation. We use the updated QuickCV code of Moster et al. (2011) (see also Newman & Davis 2002) to estimate the cosmic variance as a function of mass in each of our redshift bins for a survey field with the dimensions of CANDELS GOODS South. In Figure 2.18 we show the estimated error on the counts for galaxies of mass $\approx 10^{9.5}$ $\mathrm{M}_\odot$. For stellar mass $\approx 10^{10}$ $\mathrm{M}_\odot$ and above, the cosmic variance predicted by this method exceeds $> 100\%$ at $z \sim 6$ and 7. However, due to the lack of constraints on the galaxy bias at high-redshift, there is a large uncertainty on these estimates. When compared to the field-to-field variation observed by Lee et al. (2012), our estimates represent a conservative assessment of the likely cosmic variance. With the full CANDELS imaging now complete, future analysis incorporating all five of the separate survey fields should allow much more robust measures on the true cosmic variance at high-redshift.

In addition to the $1/V_{\rm max}$ estimates, we also estimate the stellar mass function using a method analogous to that of González et al. (2011). For each sample, 10^6 UV magnitudes in the range $-23 < M_{UV,1500} < -13$ are drawn from the observed luminosity functions from the literature at each redshift (Bouwens et al., 2007, 2012; McLure et al., 2013). The $M_{UV,1500}$ are then converted to stellar masses

using the best-fitting relations from Table 2.4 for each redshift sample and a scatter of 0.2 (dashed lines) or 0.5 dex (dotted lines).

At $z \sim 4$, the $1/V_{\rm max}$ data shows a good agreement with the mass functions generated by this method. At higher redshifts however, luminosity based mass functions increasingly underpredict the number density at high masses for the same fixed scatter in the $\log_{10}(\mathrm{M}_*)$-M_{UV} relation. To increase the number densities at high mass to match those observed, either a more strongly evolving $\log_{10}(\mathrm{M}_*)$-M_{UV} relation (in direct disagreement with that observed) or a significantly greater scatter in the intrinsic $\log_{10}(\mathrm{M}_*)$-M_{UV} ratios is required.

2.6.4.1 Comparison with the literature

Caputi et al. (2011) studied the massive end of the stellar mass function at $3 \leq z \leq 5$ over a wide area in the UKIDSS Ultra Deep Survey (UDS), using photometric redshifts for a sample of $4.5\mu m$ selected galaxies. Our observed number densities show a broad agreement at $z \sim 4$ ($3.5 \leq z < 4.25$ for Caputi et al.) for $\log_{10} \mathrm{M}_* > 10.5$ but are significantly higher at lower masses. The same is also true across all masses at $z > 4$ ($4.25 \leq z < 5.0$). However for both redshift samples, Caputi et al. (2011) find a very steep low-mass slope when parameterised with a Schechter (1976) fit, in agreement with our results. At the massive end of the $z \sim 4$ galaxy SMF, our results agree with those of Muzzin et al. (2013) over the limited mass range covered by both works.

Covering a significantly smaller area than those observations but probing to lower masses are the $1/V_{\rm max}$ observations of Santini et al. (2012). We find a good agreement with these results, however due to the small number statistics at the high mass end of the SMF, the errors on both sets of observations are large.

Another measurement of the stellar mass function at $z \sim 4-5$ is that of Lee et al. (2012), who study the SMF for a Lyman break selected sample in the GOODS North and South fields (Giavalisco et al., 2004a). At $z \sim 4$, for stellar masses $\log_{10} \mathrm{M}_* > 9.5$ the two results are in excellent agreement. Below this mass range, the significantly steeper low-mass slope measured in this work results in a higher number densities than those found by Lee et al. (2012). At $z \sim 5$, we again find

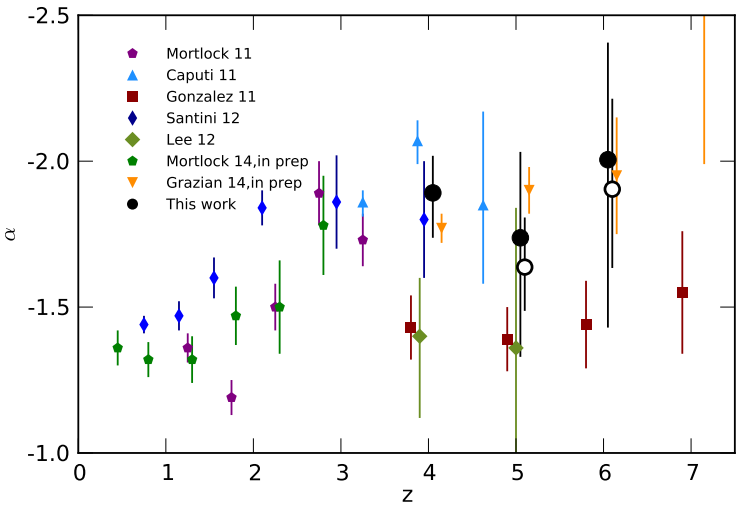

Figure 2.19: Evolution of the low-mass slope from $z = 0$ to $z \sim 7$. We show the best-fitting α for both the freely varying (filled circles) and fixed M_* (empty circles) fits. The fits for $z \sim 7$ were excluded due to the poor constraints. We show results from the recent literature for the stellar mass function at lower redshifts and at $z > 3$. Shown are the α quoted for single Schechter (1976) fits to the observed data where α has been left as a free parameter in the fitting or has been estimated analytically (González et al., 2011).

higher number densities although there is some agreement at the highest masses.

González et al. (2011) provides the only previous observation that covers the full redshift range and is also the only work that does not construct the galaxy stellar mass function from the galaxy masses directly. Instead, González et al. (2011) measure the $\log_{10}(M_*)$-M_{UV} relation at $z \sim 4$ (testing for consistency with the smaller samples at $z \sim 5$ and 6). The mass-to-light ratio is then applied to the observed UV luminosity function for each redshift bin, allowing the estimation of the SMF to lower masses and higher redshift than would otherwise have been possible. Because their $\log_{10}(M_*)$-M_{UV} ratio is fixed at all redshifts, there is less evolution in the SMF than we observe. The slope of the $\log_{10}(M_*)$-M_{UV} relation observed by González et al. (2011) also results in a low-mass slope which is shallow across all redshift bins.

When placed in the context of low-redshift observations of the stellar mass function, our results at $z \sim 4$ are a continuation of the trend of increasing α with redshift. In Figure 2.19, we show recent observations of the low-mass slope of the SMF from $z = 0$ out to $z \sim 7$. We include only results where α has been fitted as a free parameter and the values of α quoted are from the single Schecter function parameterisations of the SMF.

At $z \sim 3$, there is a broad agreement in the estimations of the low-mass slope at $\alpha \approx -1.8$. By $z \sim 4$, there is a much larger disagreement between observed value spread across $\alpha \sim -2$ to -1.4. It is important to note that the observations with a shallower low-mass slope, González et al. (2011); Lee et al. (2012), are those with galaxies selected using the Lyman break technique colour cuts and source detection using optical bands (typically z_{850}). In contrast, those with steep slopes, Caputi et al. (2011), Santini et al. (2012) and this work, use photometric redshift selection as well as near- or mid-infrared band for source detection. The best-fitting α of this work are also in good agreement with the maximum-likelihood estimates of Grazian et al. *in prep*, an independent analysis of the combined CANDELS GOODS and UDS (UKIDSS Ultra Deep Survey) fields.

2.6.4.2 Comparison with theory

In Figure 2.20, we compare our measurements of the observed stellar mass function with the predictions of both smoothed particle hydrodynamic (SPH) and semi-analytic models. The SPH predictions are taken from the hybrid energy/momentum-driven wind (ezw) model of Davé et al. (2013). We also show the predictions of three semi-analytic models (SAM), from Croton et al. (2006), Lu et al. (2011) and Somerville et al. (2008) (see also Somerville et al. 2012). Details of the three models and an in-depth comparison between the model predictions across all redshifts can be found in Lu et al. (2014). The number densities have been renormalised to the comoving volume of the cosmology used throughout our chapter ($H_0 = 70$ kms^{-1}Mpc^{-1}, $\Omega_0 = 0.3$ and $\Omega_\Lambda = 0.7$). Analysis is restricted to $z \leq 6$ due to limits on the robustness of simulations at higher redshifts from the numerical resolution of the simulations.

Inspecting the mass functions at $z \sim 4$, there is excellent agreement between the observations and the models of Davé et al. (2013), Croton et al. (2006) and to a lesser extent Lu et al. (2011). Of the three SAM predictions, Somerville et al. (2008) shows the least agreement at $z \sim 4$ due to the over-abundance of higher mass galaxies. However, at higher redshifts the reverse is true, with the Somerville et al. (2008) models providing the best match to the observed $z \sim 5$

and 6 mass functions.

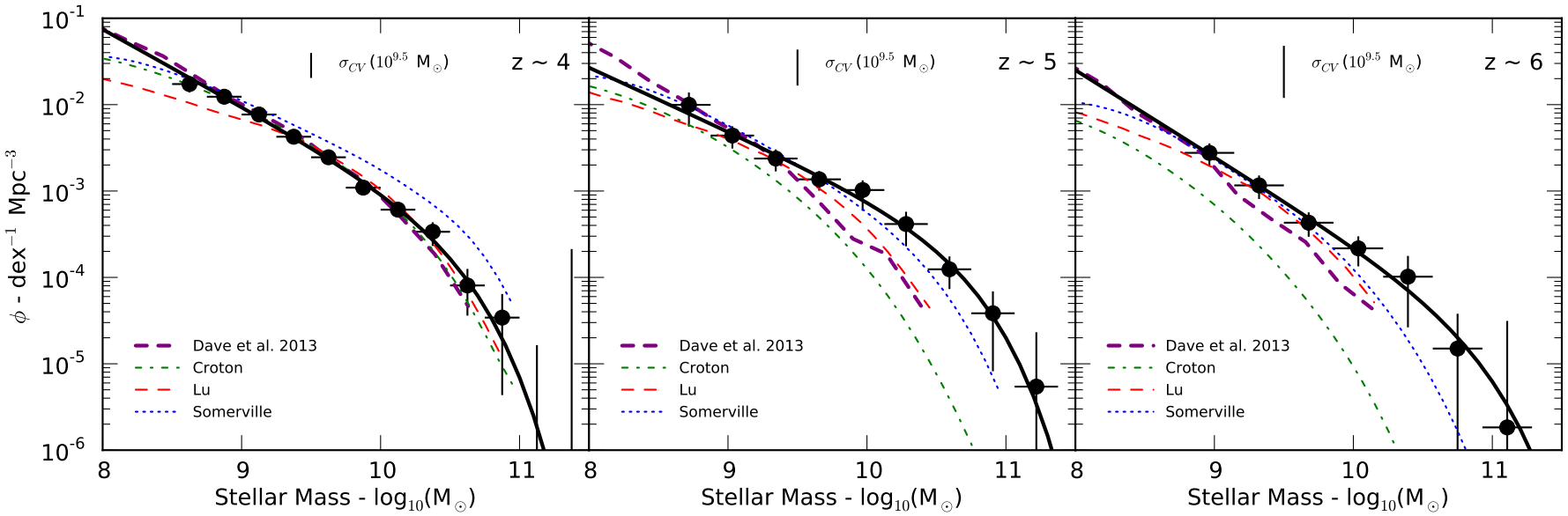

Figure 2.20: Comparison of the observed galaxy stellar mass functions in this work with theoretical model predictions at $z \sim 4$, 5 and 6. We show the semi-analytic models of Croton et al. (2006), Somerville et al. (2008) and Lu et al. (2011), using the error convolved stellar mass functions as outlined in Lu et al. (2014). The dashed purple line shows the results from the hydrodynamical simulations of Davé et al. (2013).

Of the four model predictions presented here, the SPH simulations of Davé et al. (2013) exhibit the steepest low-mass slopes and the closest agreement with our observations. The steepening of the low-mass slope in this model (from $z \sim 0$ to $z > 3$) is a result of decreasing contribution from wind recycling at high-redshifts. The resulting feedback at high-redshift has a smaller mass dependence than other models. This can be seen when compared to the SAM model of Lu et al. (2011) which has feedback with a much stronger mass dependence owing to increasingly strong (or efficient) feedback in low-mass haloes.

The SPH predictions, along with those of the Lu et al. (2011) SAM, most closely match the evolution in the overall normalisation of the number densities across the observed redshift range. The other semi-analytic models undergo a much stronger evolution in the number density of the most massive galaxies. It is important to take into account the fact that all 3 of the semi-analytic models are tuned to match only the $z = 0$ stellar mass function. The range of acceptable parameters at $z = 0$ found by Lu et al. (2011) results in a broad distribution of predicted stellar mass functions at high-redshift. Nevertheless, it is clear that our new observations of the high-redshift SMF can be used to further constrain our best models of galaxy evolution.

The observed steepening of the low-mass slope with redshift, or in more physical terms its flattening as a function of time, has implications for how galaxies at a given mass grow at different points during cosmic history. The exact physical causes for the flattening of α with time is still uncertain, however it is informative to study the stellar mass function at low redshift when galaxies have been decomposed into star-forming and quiescent components.

As shown by Muzzin et al. (2013), Ilbert et al. (2013) and Mortlock et al. (2014), the evolution in the shape of the overall total galaxy SMF is largely driven by an increase in number density of quiescent galaxies at the massive end of the SMF. The shape of the SMF for star-forming galaxies remains comparatively unchanged, with a steeper measured low-mass slope than the corresponding total SMF at all redshifts (Mortlock et al., 2014). However, as the normalisation of the passive galaxy population SMF grows with time relative to that of star-forming

galaxies, the mass at which quiescent galaxies (with their corresponding shallower SMF shape) dominate the observed number densities decreases with time.

While this qualitative picture may give more detail to how precisely the SMF shape is changing, it does not tell us what are the physical processes responsible for the suppression of star-formation in high mass galaxies and the build up of quiescent galaxy population. At lower redshifts, the suppression of star-forming galaxies and the build of quiescent galaxies could driven by the process of galaxy mergers, which play an increasingly significant role in massive galaxy formation at low redshift (Ownsworth et al., 2014). Equally, it may be caused by other physical processes such a quenching due to halo mass (Peng et al., 2010) or AGN activity (Henriques et al., 2015).

Understanding the exact physical causes of the change in the observed SMF requires additional work to link the observed galaxies at different epochs to their host dark matter halos through clustering measurements, allowing much more to learned from comparison with models such as those discussed above. Additionally, better understanding of the merger histories and star-formation rate duty cycles of galaxies at $z > 2$ will be crucial in unravelling the underlying physical processes driving these changes.

2.6.5 Stellar Mass Density

We compute the total stellar mass density (SMD) by integrating the fitted Schechter (1976) function from $M_* = 10^8$ to $10^{13} M_\odot$, with 1-σ errors estimated from the minimum and maximum SMD within the 1-σ contours for the fit parameters (see Table 2.6). For the $z \sim 5$, 6 and 7 samples, we use the best-fitting parameters with $M^* = M^*_{z\sim4}$. The results are shown in Figure 2.21 as the solid black points. We also show results from the literature across all redshift ranges, converted to the same cosmology and IMF (Chabrier/Kroupa).

Our observations show the continuation of the rapid decline in global stellar mass density towards high-redshifts, falling by a factor of between ~ 4 and 40 in the ~ 1 Gyr between $z \sim 4$ and 7. This rate of stellar mass growth observed is

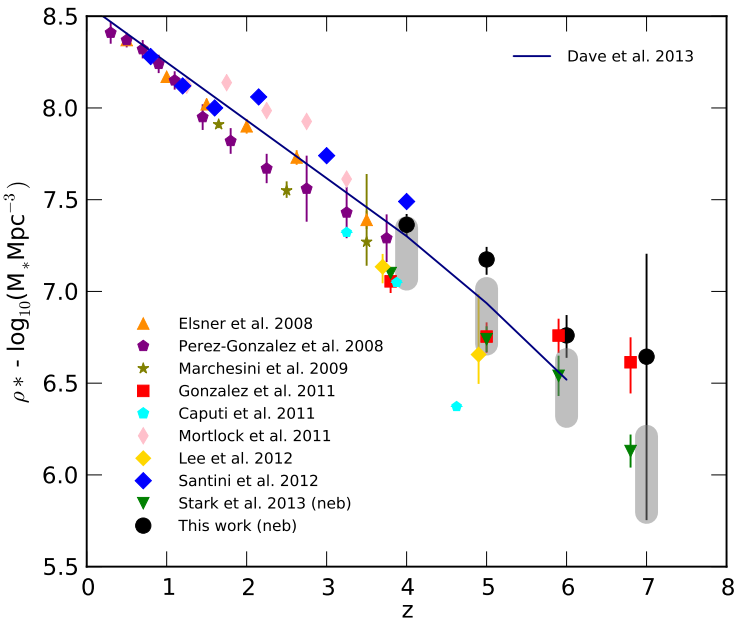

Figure 2.21: Observed stellar mass densities (for M $> 10^8$ $M_\odot$). All literature values have been converted to a Chabrier/Kroupa IMF as appropriate. The grey regions at $z \sim 4$, 5, 6 and 7 show the range in stellar mass density traced by the luminosity function-based mass functions described in Section 2.6.4, the lower and upper limits correspond to 0.2 and 0.5 dex of scatter in the applied mass-to-light ratios respectively.

Table 2.6: Stellar mass densities integrated from the Schecter parameters in Table 2.5 for M $> 10^8 M_\odot$. Error bars correspond to the minimum and maximum stellar mass densities within the 1 σ contours of the mass function fits.

z	$\rho_*(\log_{10}\ M_\odot Mpc^{-3})$
4	7.36 ± 0.06
5	$7.17^{+0.07}_{-0.08}$
6	$6.76^{+0.11}_{-0.12}$
7	$6.64^{+0.56}_{-0.89}$

higher than observed by González et al. (2011) over the same time period but comparable to that found by Stark et al. (2013) when the large uncertainty in the $z \sim 7$ SMD is taken into account.

At $z \sim 4$, our results lie within the range of past stellar mass density measurements at this redshift. Although larger than the results of the Lyman break selected samples (González et al., 2011; Lee et al., 2012; Stark et al., 2013), we find a SMD less than that of Santini et al. (2012) and comparable to that of some of the other photometric redshift selected samples (Pérez González et al., 2008; Marchesini et al., 2009). As could be inferred from the stellar mass functions, the stellar mass densities of Davé et al. (2013) underpredict observed SMD at $z \sim 5$ and $z \sim 6$ but shows a good agreement at $z \sim 4$. Similarly, the range of densities

covered by our luminosity based mass functions (grey regions) are significantly lower than the directly observed SMD in all redshift bins apart from $z \sim 4$.

2.6.6 Star Formation Rates

2.6.6.1 Specific star formation rates

Earlier observations of the sSFR evolution at $z > 3$, with mass estimates excluding the effects of nebular emission, showed the sSFR at a fixed mass remained roughly constant at ~ 2 Gyr^{-1} with increasing redshift (Stark et al., 2009; González et al., 2010; Bouwens et al., 2011d). Such a plateau in the sSFR evolution was at odds with most plausible models of galaxy evolution (as explored by Weinmann et al. 2011).

However, it has since been shown that the inclusion of nebular emission in stellar mass estimates at high-redshift has a significant effect on the redshift evolution of the specific star formation rate (sSFR) (Schaerer & de Barros, 2009, 2010; Stark et al., 2013; González et al., 2014). By lowering the measured mass for a fixed star formation rate, the inclusion of nebular emission results in a higher sSFR proportional to the strength (or effect on the estimated stellar mass) of the emission lines.

In Figure 2.22, we show our results for the sSFR (when using $\mathrm{SFR_{Madau}}$) in a stellar mass bin at $\log_{10}(\mathrm{M/M_{\odot}}) = 9.7 \pm 0.3$ alongside previous observations at $z > 2$. We find an average sSFR of 2.32 ± 0.08, 2.94 ± 0.20, 4.21 ± 0.54 and 6.2 ± 2.5 Gyr^{-1} for $z \sim 4$, 5, 6 and 7 respectively. Our observations show a clear trend in increasing sSFR with redshift in the redshift range $4 \leq z \leq 7$. The observed sSFR are in very good agreement with those of González et al. (2014) but are systematically lower than those of Stark et al. (2013) over the same redshift range. However, as noted in Stark et al. (2013), the introduction of 0.5 dex of intrinsic scatter to the $log_{10}\mathrm{M}_* - M_{UV}$ used when estimating their sSFR would result in a reduction of 2.8$\times$ at $z \sim 4$. Such a large intrinsic scatter would be fully consistent with the $log_{10}\mathrm{M}_* - M_{UV}$ relations and stellar mass functions observed in this chapter. Taking this offset into account, the increasing consensus

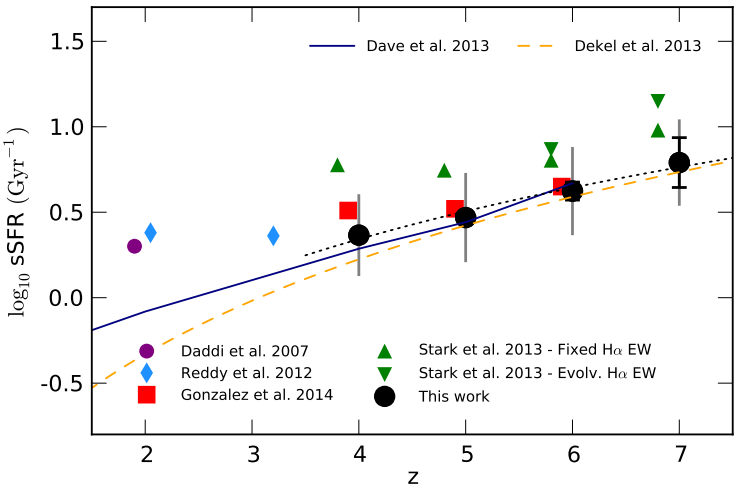

Figure 2.22: Biweight mean specific star-formation rates (sSFR) and error on the mean for galaxies of mass $M_* = 5 \times 10^9 M_\odot$ as a function of redshift for this work (black circles). We find the scatter in sSFR, taken as the biweight scale of the distributions (grey error bars), to be ≈ 0.25 dex across all redshifts. The dashed yellow line shows the evolution of the specific accretion rate, $\propto (1+z)^{2.5}$, as outlined in Dekel et al. (2013). The blue line shows the sSFR predicted by Davé et al. (2013), the model which most closely matches the observed stellar mass function (see Section 2.6.4.2). The black dotted line shows the best-fitting power law to the results in this chapter from $z \sim 4$ to 7 ($\propto (1+z)^{2.06 \pm 0.25}$).

in the observed sSFR at high redshift is encouraging.

Performing a simple best fit to our observed sSFR across all four redshift bins, weighted to the measured scatter, gives sSFR $\propto (1+z)^{2.06 \pm 0.25}$ (black dotted line). This trend is much more consistent with theoretical expectations of the sSFR evolution than a plateau at ~ 2 Gyr^{-1}, whereby the increased accretion of cold gas onto haloes results in higher specific star formation rates in the early universe. This can be seen in the evolution of the specific accretion rate (Neistein & Dekel, 2007; Dekel et al., 2013), $\propto (1+z)^{2.5}$, shown as the orange dashed line in Figure 2.22. Also shown in Figure 2.22 are the simulation predictions of Davé et al. (2013) which are in good agreement with both our observations and the the specific accretion rate model at $z > 3$.

Although we find a strong agreement with the zero-th order specific accretion rate model over the redshift range covered in this work, such a comparison should not be made in isolation from the previous observations of the sSFR at lower redshift. By $z \sim 4$ and below, the observed sSFR begins to diverge strongly from that predicted by the specific accretion rate and the SPH models of Davé et al. (2013). If we include the additional observations of Daddi et al. (2007)

and Reddy et al. (2012) we find a best-fit of sSFR $\propto (1+z)^{0.9\pm0.2}$, consistent with that found by González et al. (2014). However, restricting the power law fit previously calculated to only $z \sim 5$, 6 and 7, we find sSFR $\propto (1+z)^{2.6\pm0.4}$.

Given the large degeneracies and assumptions inherent to the stellar mass and star formation estimates (de Barros et al., 2014; Schaerer et al., 2013), there may still be significant systematic errors in the observed sSFR at high redshift. For example, Salmon et al. (2015) find that the use of an SMC-like extinction curve instead of Calzetti et al. (2000) results in systematically lower sSFR for their sample at $z \sim 4$ to $z \sim 6$ using the same CANDELS data as our work. Similarly, the poor constraints on the properties of nebular emission and the escape fraction at high redshift allows for a wide range of plausible scenarios which could affect the measured stellar mass and SFR significantly. This is especially important at $z \sim 6$ and 7 where the impact of nebular emission is strongest (Stark et al., 2013; Smit et al., 2014; González et al., 2014). Although the previous tension between theory and observations at $z > 4$ has been largely resolved, improved constraints on the stellar populations and star formation rates of high-redshift galaxies are still required before robust comparisons can be made.

2.6.6.2 Star formation rate functions and the cosmic star formation rate density

To measure the evolution of the star-formation rate (SFR) density for across our observed redshift bins, we use the previously calculated $1/V_{\rm max}$ values for each galaxy to construct a SFR function analogous to the mass or luminosity function for the same data, such that

$$\phi_{SFR,k} d\epsilon = \sum_{i}^{N_{gal}} \frac{w_i}{V_{max,i}} W(\epsilon_k - \epsilon_i), \tag{2.16}$$

where $\epsilon = \log_{10}(\mathrm{SFR}_{UV})$. The SFR functions for our high-redshift samples are shown in Figure 2.23 for both the dust corrected UV star-formation rates ($\mathrm{SFR}_{\rm Madau}$) and the SED star-formation rates as outlined in Section 2.5. At low to moderate star-formation rates ($\log_{10}(SFR_{UV}) \leq 1.5$), the two SFR estimates are in good agreement across all redshifts as was seen when the two estimates for

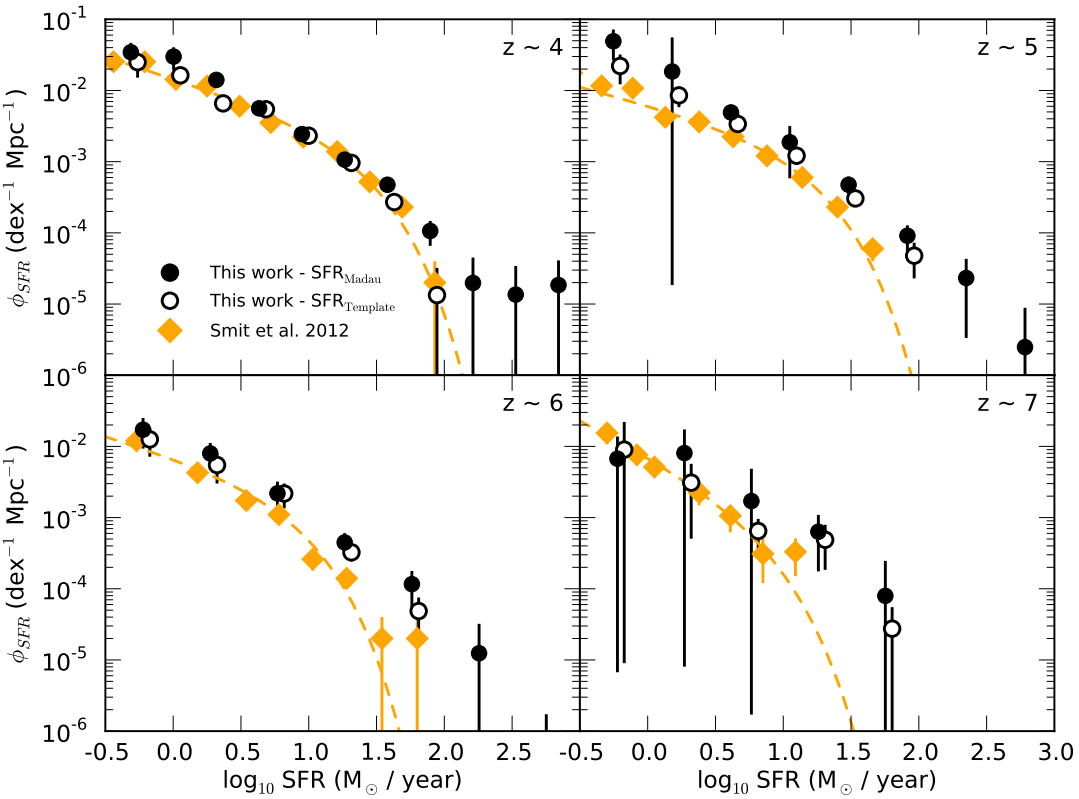

Figure 2.23: Star-formation rate functions calculated using the $1/V_{\rm max}$ estimator as outlined in Equation 2.16. The filled black circles correspond to star-formation rates estimated from the dust corrected UV luminosity whilst the open black circles correspond to the best-fitting star-formation rate from the SED fitting, see Section 2.5.4. The SFR-functions of Smit et al. (2012) converted to a Chabrier IMF are shown by the yellow diamonds.

individual galaxies were compared.

The SFR function estimates of Smit et al. (2012) (converted to the same IMF used in this work) exhibit lower star-formation rates than we observe at all redshifts, with the exception of the SFR$_{\rm template}$ based estimate at $z \sim 4$ which shows excellent agreement across the full SFR range. Smit et al. (2012) correct the observed UV luminosity functions (Bouwens et al., 2007, 2012) to intrinsic magnitudes using the same Meurer et al. (1999) relation as outlined in Section 2.5. Since the underlying UV luminosity functions for both observations show a good agreement, this discrepancy can be attributed solely to the β values and methodology when correcting extinction. The Bouwens et al. (2011d) $M_{UV} - \beta$ relations used to correct for dust extinction in Smit et al. (2012) exhibit a stronger UV luminosity dependence as well as a bluer average colour than that observed in our work (see Section 2.5.5).

Integrating the SFR function across a suitable range gives the global SFR density.

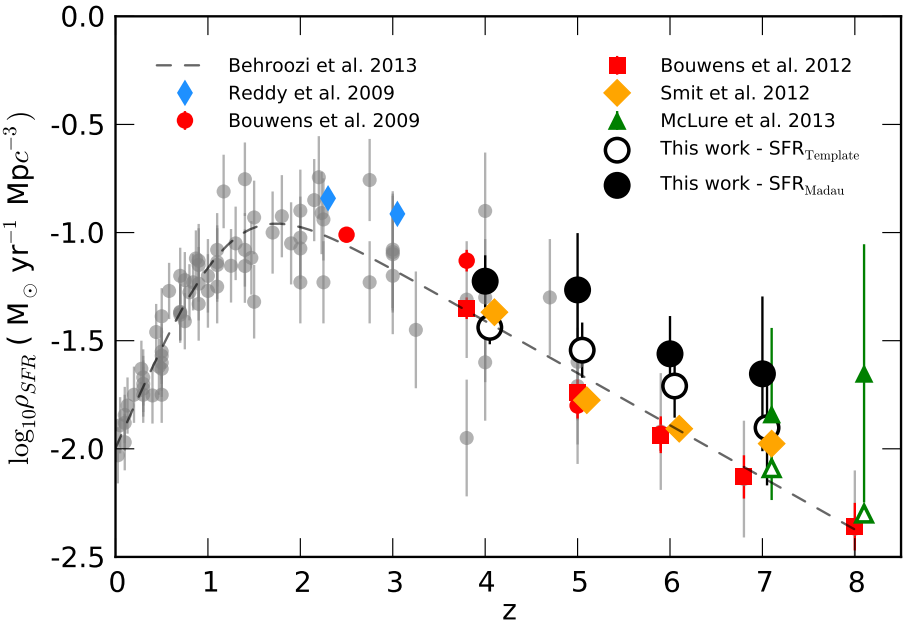

Figure 2.24: Evolution of the SFR density as estimated from the SFR functions in Figure 2.23. The black filled circles show the SFR density calculated by integrating under the observed data directly using $\mathrm{SFR}_{\mathrm{Madau}}$. The empty black circles show the corresponding estimates using $\mathrm{SFR}_{\mathrm{Template}}$, these points have been offset by $+0.05z$ for clarity. We show the recent compilation of SFR density observations (grey circles) and the fitted functional form from Behroozi et al. (2013). Shown separately are the dust-corrected UV SFR estimates of Reddy & Steidel (2009), Bouwens et al. (2009), Bouwens et al. (2011d), Smit et al. (2012) and McLure et al. (2013). The Smit et al. (2012) values were calculated by integrating the analytic SFR functions presented in their work from $\log_{10}(SFR_{UV}) = -0.47$ and above, in line with the limits used in other observations (see text). For the UV SFR density observations of McLure et al. (2013) (open triangles), we apply a dust correction based on the observed β slopes of the same survey as measured by Dunlop et al. (2013) (filled triangles). We assume a fixed average extinction (with respect to M_{UV}) consistent with their observations, using $\langle\beta\rangle = -2.1 \pm 0.2$ for $z \sim 7$ and $\langle\beta\rangle = -1.9 \pm 0.3$ for $z \sim 8$.

For consistency with other UV SFR density measurements, the lower bound in the integration of the SFR function was chosen to be $\log_{10}(SFR_{UV}) = -0.47$, equivalent to $0.03L^*_{z=3}$, and the data points were integrated directly in steps. The evolution of the cosmic star formation rate density is shown in Figure 2.24. Alongside our new estimates of the SFR density at high-redshift we show the compilation of observed cosmic SFR from $z = 0$ to $z = 8$ from Behroozi et al. (2013) and their fitted functional form to the same data. Our observations show a clear rise in the cosmic SFR over the ~ 1 Gyr between $z \sim 7$ and $z \sim 4$ with an increase of ≈ 0.5 dex over this period.

As expected from the inspection of the SFR functions, the integrated SFR densities predicted by Smit et al. (2012) are lower than those observed in this work. The same is true for the cosmic SFR observed by Bouwens et al. (2011d) which

makes use of the same $M_{UV} - \beta$ relations. Due to the steep UV luminosity functions, the cosmic SFR is dominated by the faint galaxy population. The difference in dust correction resulting from the redder observed UV continua in this work therefore has a large effect on the observed dust corrected SFR density.

In the recent β observations of Bouwens et al. (2014), the authors find systematically redder β's than for Bouwens et al. (2011d). They find that for a fixed redshift and rest-frame UV luminosity, $\Delta\beta \sim 0.13 - 0.19$ for $z = 4 - 6$ and $\Delta\beta \sim 0.22$ at $z \sim 7$. Following the the Meurer et al. (1999) relation, we estimate that the corresponding difference in dust corrections would be $\Delta A_{1500} \sim 0.26 - 0.38$ for $z = 4 - 6$ and $\Delta A_{1500} \sim 0.44$ at $z \sim 7$. An increase in the Smit et al. (2012) star-formation rates of this magnitude would bring the two dust-corrected UV SFR-function estimates into greater agreement (and hence the corresponding SFR densities). However, such a correction is a simplification, and does not take into account the different $M_{UV} - \beta$ slopes observed and the effects of scatter. We can therefore not make a fully quantitative comparison of how SFR functions based on the β observations of Bouwens et al. (2014) would compare with those in this work.

Applying a dust correction based on the observations by Dunlop et al. (2013) to the uncorrected SFR density observed by McLure et al. (2013) (for the same sample and photometry), we find the results are in good agreement with our observations at $z \sim 7$. In Bouwens et al. (2014), the authors claim that the β observations of Dunlop et al. (2013) are biased red-ward by $\Delta\beta \sim 0.13$, our estimated dust-corrected SFR-density for McLure et al. (2013) could therefore be a factor of $0.26dex$ too high. We note that if we apply a correction to the β's observed in this work in order to match the observed $M_{UV} - \beta$ relations of Bouwens et al. (2014), our SFR density estimates would be reduced by $\Delta\rho_{SFR} \sim 0.05 - 0.1dex$.

As with our observations of the specific star formation rate, the possible systematic errors resulting from the treatment of dust could have a significant effect on the observed SFR density. The importance of this can be seen in the difference between the UV and SED-fitting SFR functions and their corresponding SFR

density estimates. The rarer red objects selected by our photometric redshift samples can contribute a significant fraction of cosmic SFR density if assumed to be dusty star-forming objects, i.e. β corrected UV star-formation rates. Although the growing availability of spectroscopic data for high redshift galaxies will help reduce the uncertainty in some of these assumptions, the independent SFR observations at $z > 3$ promised by ALMA and LOFAR will be essential for obtaining robust measures of the cosmic SFR in the early universe.

2.7 Summary

In this chapter, we make use of the deep data provided by the CANDELS survey of the GOODS South to study the stellar mass growth of galaxies in the first 2 billion years of galaxy evolution. For a photometric redshift selected sample, we present new measurements of the galaxy stellar mass function across the redshift range $z \sim 4$ to 7 along with observations of the UV star formation rate of this sample. Stellar masses for the sample are measured from SED template fitting incorporating the effects of nebular emission, previously shown to have a significant effect on the observed stellar masses at high-redshift.

Using the rest-frame UV magnitudes and UV continuum slopes measured by our SED fitting code, we also calculate dust-corrected star formation rates for our sample. From these we derive specific star formation rates and a measure of the cosmic SFR density as a function of redshift. Our primary conclusions are as follows:

- Our new observations of the stellar mass functions at $z \sim 4$ to $z \sim 7$ exhibit steep low-mass slopes across the whole redshift range. These slopes are significantly steeper than previous observations in this redshift regime and are much closer to those observed in the UV luminosity functions of these same objects and recent observations at lower redshifts.

- The observed stellar mass to UV luminosity ratio of our sample exhibits minimal evolution with luminosity, with close to a constant M/L_{UV} in all

redshift bins. The overall normalisation of the $\log_{10}(\mathrm{M}_*)$-M_{UV} undergoes a significant increase in the scaling of this relation over time.

- From our observations of the stellar mass function, we calculate the stellar mass density at $z \sim 7$ is $6.64^{+0.58}_{-0.89}$ $\log_{10}$ $\mathrm{M}_\odot\mathrm{Mpc}^{-3}$ rising to 7.36 ± 0.06 at $z \sim 4$ for galaxies M$> 10^8\mathrm{M}_\odot$ and a Chabrier IMF.

- At a fixed stellar mass ($M = 5 \times 10^9 M_\odot$), the mean specific star formation rate rises with redshift. We find sSFR $= 2.32 \pm 0.08$ Gyr^{-1} at $z \sim 4$, rising to 6.2 ± 2.5 Gyr^{-1} at $z \sim 7$. These results are in good agreement with other estimates of sSFR that incorporate nebular emission in the stellar mass estimates.

- We observe a rapid decline in the cosmic star formation rate at $z > 4$, but find star formation rate densities up to ≈ 0.5 dex higher than those of Bouwens et al. (2011d) and Smit et al. (2012) at the same redshifts. We conclude that much of this difference can be attributed to the rarest objects with large amounts of inferred dust extinction. Future spectroscopic and long-wavelength observations will be vital in better understanding star-formation rates in this epoch.

Given the wide range of data, models and assumptions used to derive the results presented in this chapter, easily comparing the relative effects of each input ingredient on the final result is not possible, especially given the correlations and covariance between some of the measured properties. However, we estimate that the most significant overall sources of error are primarily due to two factors. Firstly, the low number of high mass (or star-formation rate) objects in our sample limits the accuracy of the stellar mass, luminosity and star-formation rate functions, even at $z \sim 4$ and $z \sim 5$ where the overall number of sources is quite high and the redshift and SED fits are well constrained.

In addition to the high Poisson noise resulting from the small number of sources, the galaxies with the highest masses and star-formation rates are also subject to the greatest cosmic variance (Moster et al., 2011). The extension of the analysis performed in this chapter to the full five CANDELS fields will greatly improve

the overall number statistics of galaxies at the high mass end of the SMF and will also significantly reduce the effects of cosmic variance.

The second key source of uncertainty is the systematic uncertainty in the dust properties of galaxies at high redshift and the corresponding corrections made when estimating intrinsic star-formation rates. Irrespective of the statistical errors due to sample size and redshift uncertainty, estimates of the cosmic star-formation rate density or the star-formation rate function estimate at high redshift will only be as accurate as the dust corrections applied.

As discussed in the previous section, new observations at longer wavelengths will significantly improve our understanding of dust in high redshift galaxies, e.g. Schaerer et al. (2015). However, another critical factor in improving the estimates of dust-corrected star-formation rates and stellar mass fits will be understanding the systematic variation of dust properties within galaxies as a function of other properties at less extreme redshifts (Kriek & Conroy, 2013). On both accounts, significant progress on improving the accuracy and reliability of measurements of the star-formation and stellar mass evolution of galaxies at $z > 4$ will be possible in the coming years, using data and facilities already available.

Chapter 3

The merger history at $z \geq 2$

3.1 Introduction

Galaxies can grow their stellar mass in one of two distinct ways. Firstly, by forming new stars from cold gas which is either accreted from the surroundings or already within the galaxy. Secondly, by merging with other galaxies in their local environment. Both channels of growth have played equally important parts in the build up of the most massive galaxies over the last eleven billion years (Bundy et al., 2009; Bridge et al., 2010a; Ownsworth et al., 2014).

Measuring the in-situ star-formation is by far the easiest of the two growth mechanisms to measure and track through cosmic time. The numerous ways of observing star-formation; UV emission, optical emission lines, radio and far-infrared emissions, have allowed star-formation rates of individual galaxies to be estimated deep into the earliest epochs of galaxy formation (Hopkins & Beacom, 2006; Behroozi et al., 2013; Bouwens et al., 2015b). In contrast, measuring the merger rates of galaxies is a significantly more tricky task.

There are two main avenues for studying the galaxy merger rate. The first method relies on counting the number of galaxies that exist in close pairs (Patton et al., 2000). This assumes that for galaxies in close proximity, a galaxy pair are either in the process of merging or will do so within some characteristic timescale. The second method relies on observing the morphological disturbance that re-

sults from galaxies undergoing major mergers or have recently merged (Conselice et al., 2003). These two methods are complimentary, in that they probe different timescales within the process of a galaxy merger. However, these merger timescales represent one of the largest uncertainties in measuring the galaxy merger rate (Kitzbichler & White, 2008; Conselice, 2009; Lotz et al., 2010a,b; Hopkins et al., 2010).

The major merger rates of galaxies have been well studied out to redshifts of $z \leq 2$ but fewer studies have extended the analysis beyond this. Taking into account systematic differences due sample selection and methodology, there is strong agreement that between $z = 0$ and $z \approx 2-3$ the merger fraction increases significantly (López-Sanjuan et al., 2010; Bluck et al., 2012; Ownsworth et al., 2014). Conselice & Arnold (2009) presented the first tentative measurements of the merger fractions at redshifts as high as $4 \leq z \leq 6$, making use of both pair-count and morphological estimates of the merger rate. For both estimates, the fraction of galaxies in mergers declines past $z \sim 4$, supporting the potential peak in the galaxy merger fraction at $1 \lesssim z \lesssim 2$ reported by Conselice et al. (2008; morphology) and Ryan et al. (2008; close pairs). However, as the analysis of Conselice & Arnold (2009) was limited to only optical photometry in the very small but deep Ultra Deep Field (Beckwith et al., 2006), the results were subject to small sample sizes and a lack of robust photometric redshift and stellar mass estimates.

When studying galaxy close pair statistics, to satisfy the close pair criterion two galaxies must firstly be within some chosen radius (typically 20 to 50 kpc) in the plane of the sky and secondly within some small velocity offset along the redshift axis. The typical velocity offset required is $\Delta 500$ km s^{-1}, corresponding to a redshift offset of $\delta z/(1+z) = 0.0017$. However, this clearly leads to difficulties when studying the close pair statistics of deep photometry surveys, the scatter on even the best photometric redshift estimates is $\delta z/(1+z) \approx 0.01$ to 0.04 (Molino et al., 2014). Moreover, measuring systemic spectroscopic redshifts is increasingly difficult at high redshift due to the increased difficulty in observing multiple emission lines for systemic redshift estimates (Stark et al., 2015). The

required redshift accuracy is often beyond spectroscopy even if such data was available for all galaxies in a survey.

To estimate the merger fractions of galaxies in wide-area photometric redshift surveys or at high-redshift, we must find a methodology that allows us to overcome the limitations of redshift accuracy in these surveys and correct or account for the pairs observed in the plane of the sky that are due to chance alignments along the line-of-sight. Various approaches have been used to overcome this limitation, including the use of de-projected two-point correlation functions (Bell et al., 2006), correcting for chance pairs by searching over random positions in the sky (Kartaltepe et al., 2007), and integrating the mass or luminosity function around the target galaxy to estimate the number of expected random companions (Le Fèvre et al., 2000; Bluck et al., 2009; Bundy et al., 2009). The drawback of these methods is that they are unable to take into account the effects of the redshift uncertainty on the derived properties such as rest-frame magnitude or stellar mass, potentially affecting their selection by mass or luminosity

López-Sanjuan et al. (2015) present a new method for estimating reliable merger fractions through the photometric redshift probability distribution functions (PDFs) of galaxies. By making use of all available redshift information in a probabilistic manner, this method has been shown to produce accurate merger fractions in the absence of spectroscopic redshift measurements. In this chapter we apply this PDF close pair technique presented in López-Sanjuan et al. (2015) to the deep CANDELS (Grogin et al., 2011; Koekemoer et al., 2011) photometric survey in order to estimate the major merger rate of sub-$M^*_\star$ galaxies at $z \geq 2$. In addition to the greatly improved number statistics available due to increased volume probed by the CANDELS survey (compared to the Hubble UDF alone), this study also benefits from the use of deep *Spitzer* IRAC observations for improved photometric redshift and stellar mass estimation at high-redshift. It has been shown that sampling galaxies SEDs above the Lyman break is essential for reliably selecting galaxies at $z > 5$ (McLure et al., 2011) and estimating accurate photometric redshifts and stellar masses.

The aim of this chapter is to measure the major merger rate at $z \geq 2$ and

make the first robust estimates for mass selected samples at $z \sim 4$, 5 and 6. By applying this novel method to a subset of the available CANDELS data we hope to show its potential for helping understand the early assembly history of galaxies. If successful, this method will allow us for the first time to constrain the contribution of mergers to the progenitors of today's most massive galaxies before the peak in the cosmic star-formation history. In tandem with complimentary analysis at lower redshifts (Mundy et al. *in prep.*), it will be possible to study the merger history of massive galaxies in a consistent manner throughout the bulk of cosmic history.

The structure of this chapter is as follows: In Section 3.2 we briefly outline the photometric data used in this analysis. In Section 3.3 we describe the probabilistic pair-count method of López-Sanjuan et al. (2015) (LS15 hereafter) as implemented in this work, including how photometric redshifts, stellar masses and completeness corrections were estimated. In Section 3.4 we present the results of this work, including comparison of our observations with the predictions of numerical models of galaxy evolution and comparable studies in the literature. In Section 3.5, we discuss our results and their implications. Finally, Section 3.6 presents our summary and conclusions for the results in this chapter. Throughout this chapter all quoted magnitudes are in the AB system (Oke & Gunn, 1983) and we assume a Λ-CDM cosmology ($H_0 = 70$ kms^{-1}Mpc^{-1}, $\Omega_m = 0.3$ and $\Omega_\Lambda = 0.7$) throughout. Quoted observables are expressed as actual values assuming this cosmology unless explicitly stated otherwise. Note that luminosities and luminosity-based properties such as observed stellar masses scale as h^{-2}.

3.2 Data

In this work we make use of the CANDELS multi-wavelength photometry catalog in the GOODS South field. Details of the catalog, the space and ground-based imaging and its reduction can be found in Chapter 2 and Guo et al. (2013) and references therein.

3.3 Methodology

The primary goal of analysing the statistics of close pairs of galaxies is to estimate the fraction of that which are in the process of merging. From numerical simulations (Kitzbichler & White, 2008), it is well understood that the vast majority of galaxies within some given physical separation will eventually merge. For spectroscopic studies in the nearby Universe, a close pair is often defined by a projected separation, $r_{\rm p}$, in the plane of the sky of $r_{\rm p} < 20$ to 50 $\rm h^{-1}$ kpc and a separation in redshift or velocity space of $\Delta v \leq 500$ km $\rm s^{-1}$.

Armed with a measure of the statistics of galaxies that satisfy these criteria within a sample, we can then estimate the corresponding merger fraction, $f_{\rm m}$, defined as

$$f_{\rm m} = \frac{N_{\rm pairs}}{N_{\rm T}}, \tag{3.1}$$

where $N_{\rm pairs}$ and $N_{\rm T}$ are the number of galaxy pairs and the total number of galaxies respectively within some target sample, e.g. a volume limited sample of mass selected galaxies. Note that $N_{\rm pairs}$ is the number of galaxy pairs rather then number of galaxies *in* pairs which is a factor two higher (Patton et al., 2000).

In this work, we analyse the galaxy close pairs through the use of their photometric redshift probability density functions (PDFs). The use of photometric redshift PDF takes into account the uncertainty in galaxy redshifts in the pair selection and the effect of the redshift uncertainty on the projected distance and derived galaxy properties. In the following section we outline the method as applied in this work and how it differs to that presented in LS15 in the use of stellar mass instead of luminosity when defining the close pair selection criteria as well as our use of flux-limited samples and the corresponding corrections.

3.3.1 Selecting initial potential close pairs

Before defining a target-sample, we first clean the photometric catalog for sources that have a high likelihood of being stars or image artefacts. Stars are defined as sources that have a high SExtractor stellarity parameter (> 0.95) and/or have an SED that is consistent with being a star (as determined in the CANDELS of-

ficial photometric redshift release, Dahlen et al. (2013)). The exclusion of objects with high SExtractor stellarity parameters (i.e. more point-like sources) could potentially bias the selection by erroneously excluding very compact neighbouring galaxies instead of stars. However, the fraction of sources excluded by this criterion is very small (0.73% over the whole catalog, 0.4% of objects with photometric redshifts $z \gtrsim 2$) so should not present a significant bias in the following analysis. Sources that are flagged as artefacts or strongly affected by bright stars in the field (and their diffraction spikes) as determined by the photometry flag map (Guo et al., 2013) are also excluded.

In the following paragraph we give a brief description of our methodology with the details presented in the subseqent sections. Once an initial sample has been selected (see Section 3.3.3), we then search for projected close pairs between the target and full galaxy samples. The initial search is for close pairs which have a projected separation less than the maximum angular separation across the full redshift range of interest (corresponding to the desired physical separation). Duplicates are then removed from the initial list of close pairs (with the primary galaxy determined by the galaxy with the highest stellar mass at its corresponding best-fit photometric redshift) to create the list of galaxy pairs for PDF analysis. Because the PDF analysis makes use of all available information to determine the pair fractions, it is applied to all galaxies within the initial sample simultaneously, with the redshift and mass ranges of interest determined by the selection functions and integration limits outlined in the following sections.

3.3.2 The pair probability function

For a given projected close pair of galaxies within the full galaxy sample, the combined redshift probability function, $\mathcal{Z}(z)$, is defined as

$$\mathcal{Z}(z) = \frac{2 \times P_1(z) \times P_2(z)}{P_1(z) + P_2(z)} = \frac{P_1(z) \times P_2(z)}{N(z)} \tag{3.2}$$

where $P_1(z)$ and $P_2(z)$ are the photometric redshift probability distribution functions (PDFs) for the primary and secondary galaxies in the projected pair. The normalisation, $N(z) = (P_1(z) + P_2(z))/2$, is implicitly constructed such that

$\int_0^\infty N(z)dz = 1$ and $\mathcal{Z}(z)$ therefore represents the number of close pairs at redshift z for the projected close pairs being studied. Following Equation 3.2, when either $P_1(z)$ or $P_2(z)$ equal zero, the combined probability $\mathcal{Z}(z)$ also goes to zero. This can be seen visually for the example galaxy pairs in Figure 3.1 (black line). The total number of pairs for a given system is then given by

$$\mathcal{N}_z = \int_0^\infty \mathcal{Z}(z)dz. \tag{3.3}$$

and can range between 0 and 1. As each initial target galaxy can have more than one close companion, each potential galaxy pair is analysed separately and included in the total pair count. Note that because the initial list of projected pairs is we cleaned for duplicates before analysing the redshift PDFs, if the two galaxies in a system (with redshift PDFs of $P_1(z)$ and $P_2(z)$) both satisfy the primary galaxy selection function, the number of pairs is not doubly counted.

In Figure 3.1 we show two examples of projected pairs around a primary galaxy that sits within the Hubble Ultra Deep Field region of CANDELS GOODS South. The primary galaxy sits at $z \approx 3.0$ and has at least one galaxy with a high pair-probability (top panel) and several other companions with a non-negligible pair-probability.

As the redshift probability function takes into account the line-of-sight information for the potential galaxy pair, two additional binary redshift masks are required to enforce the additional pair selection criteria. These masks are equal to one at a given redshift when the selection criteria are satisfied and zero otherwise. As above, we follow the notation outlined in LS15 and define the angular separation mask, $\mathcal{M}^\theta(z)$, as

$$\mathcal{M}^\theta(z) = \begin{cases} 1, & \text{if } \theta_{min}(z) \leq \theta \leq \theta_{max}(z) \\ 0, & \text{otherwise,} \end{cases} \tag{3.4}$$

where the angular separation between the galaxies in a pair as a function of redshift is denoted $\theta(z)$. The angular separation is a function of the projected distance r_p and the angular diameter distance, $d_A(z)$, for a given redshift and cosmology, i.e. $\theta_{max}(z) = r_p^{max}/d_A(z)$ and $\theta_{min}(z) = r_p^{min}/d_A(z)$.

The pair selection mask, denoted $\mathcal{M}^{\text{pair}}(z)$, is where our method differs to that

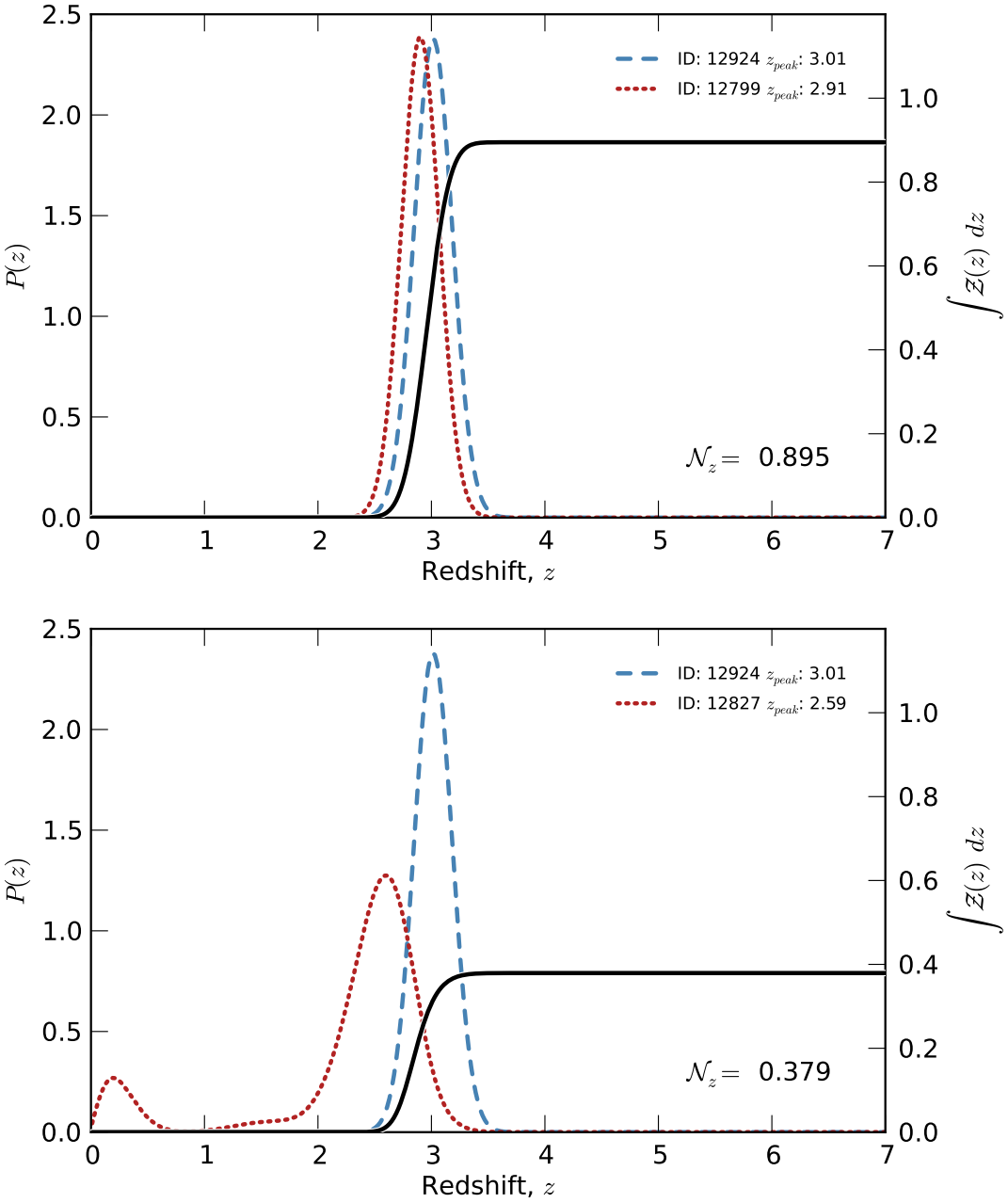

Figure 3.1: Example redshift PDFs and integrated $\mathcal{Z}(z)$ for two projected pairs around a primary galaxy at $z \approx 3.01$ in the *Hubble* Ultra Deep Field. In both panels, the blue dashed line corresponds to the redshift PDF for the primary galaxy while red the dotted line is that of the projected companion. The solid black line shows the cumulative integrated $\mathcal{Z}(z)$ for the galaxy pair.

outlined by LS15. Rather than selecting galaxy pairs based on the luminosity ratio, we instead select based on the estimated stellar mass ratio. We define our pair-selection mask as

$$\mathcal{M}^{\rm pair}(z) = \begin{cases} 1, & \text{if } \mathrm{M}_{\star}^{\rm lim,1}(z) \leq \mathrm{M}_{\star,1}(\mathrm{z}) \leq \mathrm{M}_{\star,\rm max} \\ & \text{and } \ \mathrm{M}_{\star}^{\rm lim,2}(z) \leq \mathrm{M}_{\star,2}(\mathrm{z}) \\ 0, & \text{otherwise.} \end{cases} \tag{3.5}$$

where $\mathrm{M}_{\star,1}(\mathrm{z})$ and $\mathrm{M}_{\star,2}(\mathrm{z})$ are the stellar mass as a function of redshift, details of how $\mathrm{M}_{\star}(\mathrm{z})$ is calculated for each galaxies are discussed in Section 3.3.4. The flux-limited mass cuts, $\mathrm{M}_{\star}^{\rm lim,1}(z)$ and $\mathrm{M}_{\star}^{\rm lim,2}(z)$, are given by

$$\mathrm{M}_{\star}^{\rm lim,1}(z) = max\{\mathrm{M}_{\star}^{\rm min}, \mathrm{M}_{\star}^{\rm flux}(z)\} \tag{3.6}$$

and

$$\mathrm{M}_{\star}^{\rm lim,2}(z) = max\{\mu \mathrm{M}_{\star}^{1}(z), \mathrm{M}_{\star}^{\rm flux}(z)\} \tag{3.7}$$

respectively, where $\mathrm{M}_{\star}^{\rm flux}(z)$ is the redshift-dependent mass completeness limit outlined in Section 3.3.5.1 and $\mathrm{M}_{\star}^{min}$ and $\mathrm{M}_{\star}^{max}$ are the lower and upper ranges of our target sample of interest. The mass ratio μ is typically defined as $\mu = 1/4$ for major mergers and $\mu = 1/10$ for minor mergers, throughout this work we set $\mu = 1/4$ by default unless otherwise stated. This pair selection mask ensures the following criteria are met at each redshift. Firstly, the primary galaxy is within the mass range of interest. Secondly, the mass ratio between the primary and secondary galaxy is within the desired range (e.g. for selecting major or minor mergers). And finally that both the primary and secondary galaxy are above the mass completeness limit at the corresponding redshift. We note that the first criteria of Equation 3.5 also constitutes the selection function for the primary sample, given by

$$S(z) = \begin{cases} 1, & \text{if } \mathrm{M}_{\star}^{\rm lim,1}(z) \leq \mathrm{M}_{\star,1}(\mathrm{z}) \leq \mathrm{M}_{\star,\rm max} \\ 0, & \text{otherwise.} \end{cases} \tag{3.8}$$

With these three properties in hand for each potential companion galaxy around our primary target, the pair-probability function, PPF(z), is then given by

$$\mathrm{PPF}(z) = \mathcal{Z}(z) \times \mathcal{M}^{\theta}(z) \times \mathcal{M}^{\rm pair}(z). \tag{3.9}$$

In Section 3.3.6 we outline how this pair-probability function is integrated to determine the photometric pair-probability, but first we outline how the photometric redshifts and stellar masses used in this analysis were estimated and then outline the steps taken to correct for selection effects within the data.

3.3.3 Photometric redshifts

Photometric redshifts for all sources are calculated using the EAZY photometric redshift code (Brammer et al., 2008). The redshifts were fit to all available photometric bands for each field as outlined in Section 3.2 and made use of the default EAZY reduced template set plus the addition of a young Lyα emitting galaxy template based on the spectrum of Erb et al. (2010). We construct the redshift probability distribution (PDF, $P(z)$) for each galaxy from its χ^2 distribution following $P(z) \propto \exp(-\chi^2(z)/2)$.

When calculating the galaxy PDFs we do not make use of a luminosity-dependent redshift prior as is commonly done (Brammer et al., 2008; Dahlen et al., 2013). Luminosity dependent priors such as the one implemented in EAZY rely on model lightcones which accurately reproduce the observed (apparent) luminosity function. Current semi-analytic models do agree well with observations at $z < 2$ (Henriques et al., 2012), but increasingly diverge at higher redshift.

Furthermore, the use of a prior which is only dependent on a galaxy's luminosity and not its colour or wider SED properties could significantly bias the estimation of close pairs using redshift PDFs. Consider a pair of galaxies at identical redshifts and with identical stellar population properties, where the only difference is the stellar mass of the galaxy (i.e. similar star-formation histories, differing only in normalisation). A luminosity-dependent prior will change the posterior probability distribution for each galaxy individually and could erroneously decrease the integrated pair probability. The effects of luminosity-based priors on redshift PDFs at $z < 3$ where SAMs are much better constrained are explored in further detail in Mundy et al. *in prep.*

As discussed in Hildebrandt et al. (2008) and Dahlen et al. (2013), the redshift

probability density functions output by photometric redshift codes can often be an inaccurate representation of the true photometric redshift error. This inaccuracy can be due to under- or over-estimates of photometric errors, or a result of systematic effects such as the template choices. Whatever the cause, it can result in significantly over or underestimated 1 and 2 σ errors whilst still producing good agreement with between the best-fit $z_{\rm phot}$ and corresponding $z_{\rm spec}$. Although this systematic effect may be negated when measuring the bulk properties of larger galaxies samples, the method outlined in this chapter relies on the direct comparison of individual redshift PDFs so it is essential that they accurately represent the true uncertainties.

We therefore endeavour to ensure the accuracy of our redshift PDFs before undertaking any analysis based on their PDFs. Following the method outlined in Dahlen et al. (2013), we first calculate the fraction of spectroscopic redshifts which fall inside the corresponding 68.3% photo-z confidence intervals. Based on the raw PDFs output by EAZY, we find that of 302 galaxies with high-quality spectroscopic redshifts at $z > 2$, only 35 % fall inside the corresponding 1σ PDF confidence intervals, indicating that our redshift errors are being underestimated. We therefore smooth the PDFs using a boxcar filter and recalculate the fraction of spectroscopic redshifts within the 1σ, repeating until this value reaches 68.3%.

In Figure 3.2 we compare our photometric redshifts and their corrected 1σ errors with the available faint spectroscopic redshift samples[1] ($H_{160} \geq 23.5$). Following the same metrics as in Molino et al. (2014) and LS15, we find that the quality of photometric redshifts is excellent given the high-redshifts being studied and the broadband nature of the photometry catalog. We find a normalised median absolute deviation[2] of $\sigma_{\rm NMAD} = 0.036$ and a bias of median$(z_{\rm phot} - z_{\rm spec}) = 0.03$.

As acknowledged in Chapter 2, the typically bright nature of the galaxies with high quality spectroscopic redshift may present a biased representation of the quality of the photometric redshifts. The selection of only the fainter sources with spectroscopic redshifts ($H_{160} \geq 23.5$) is designed to minimise this potential

[1]References for the compiled spectroscopic redshift sample can be found in Chapter 2.

[2]The normalised median absolute deviation is defined as $\sigma_{\rm NMAD} = 1.48 \times {\rm median}\left(\frac{|\Delta z|}{1+z_{\rm spec}}\right)$, see Dahlen et al. (2013).

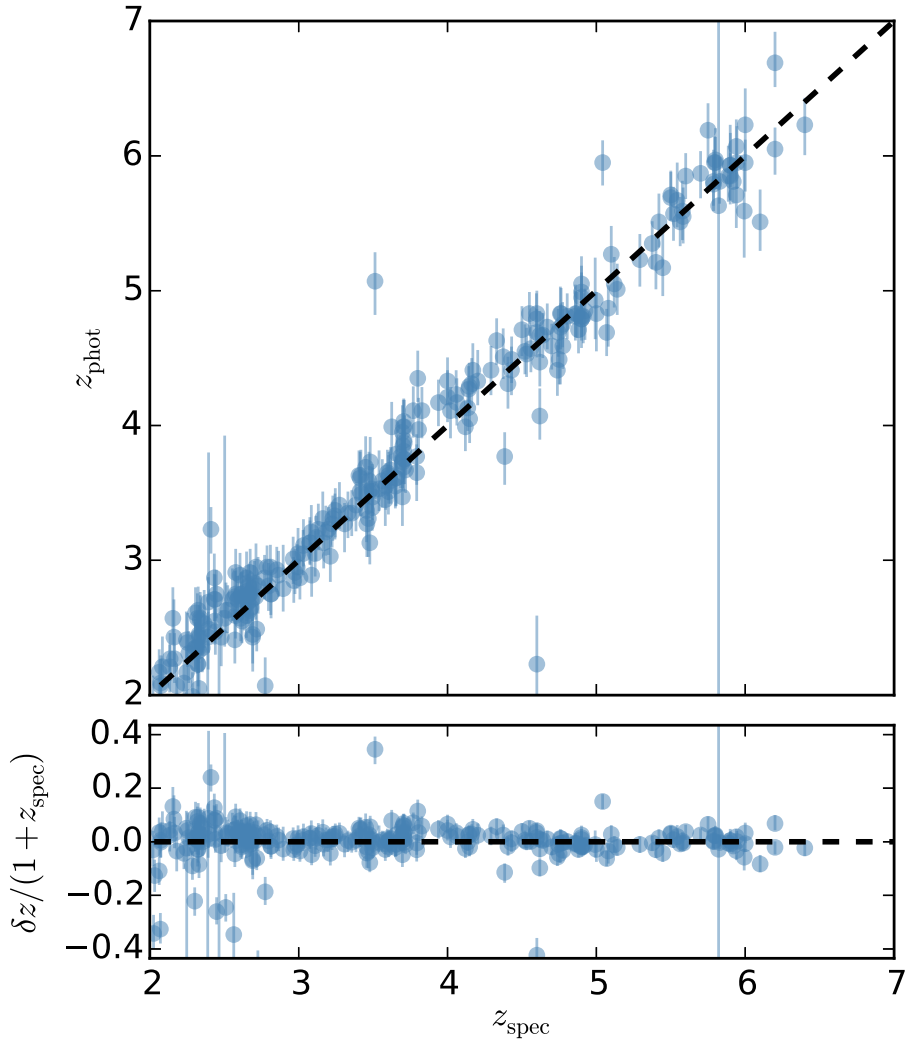

Figure 3.2: Comparison between spectroscopic and photometric redshift for the galaxies in our sample with available spectroscopy at $z \geq 2$, spectroscopic redshift quality of 'Good' or better and apparent magnitude of $H_{160} > 23.5$. The photometric redshift shown is the peak of the probability distribution (χ^2 minimum) with 1-σ lower and upper limits after smoothing of $P(z)$ outlined in the text. The bottom panel shows the normalised residuals ($\Delta z = z_{\rm phot} - z_{\rm spec}$) as a function of the measured spectroscopic redshift.

bias. We are also confident that the photometric redshift accuracy fainter galaxies remains high based on the results of the photometric redshift analysis performed on mock galaxies simulations in Chapter 2.

3.3.4 Stellar mass estimation

The stellar mass as a function of redshift, $\mathrm{M}_*(z)$, for each galaxy is estimated using a modified version of the SED code introduced in Chapter 2 to which we refer the reader for further details. Rather than estimating the best-fit mass (or mass

likelihood distribution) for a fixed input photometric or spectroscopic redshift, we instead estimate the stellar mass at all redshifts in the photometric redshift fitting range simultaneously. Specifically, we calculate the likelihood-weighted mean:

$$\mathrm{M}_*(z) = \frac{\sum_t w_t(z)\mathrm{M}_{*,t}(z)}{\sum_t w_t(z)} \tag{3.10}$$

where the sum is over all galaxy template types, t, with ages less than the age of the Universe at the redshift z and $\mathrm{M}_{\star,t}(z)$ is the optimum stellar mass for each galaxy template (Equation 3.13). The likelihood, $w_t(z)$, is determined by

$$w_t(z) = \exp(-\chi^2_t(z)/2), \tag{3.11}$$

where $\chi^2_t(z)$ is given by:

$$\chi^2_t(z) = \sum_j^{N_{filters}} \frac{(\mathrm{M}_{\star,t}(z)F_{j,t}(z) - F_j^{obs})^2}{\sigma_j^2}. \tag{3.12}$$

The sum is over j filters available for each galaxy, its observed photometric fluxes, F_j^{obs} and corresponding error, σ_j. The optimum scaling for each galaxy template type (each normalised to 1 $\mathrm{M}_\odot$), $\mathrm{M}_{\star,t}$, is calculated analytically by setting the differential of Equation 3.12 equal to 0 and rearranging to give:

$$\mathrm{M}_{\star,t}(z) = \frac{\sum_j \frac{F_{j,t}(z)F_j^{obs}}{\sigma_j^2}}{\sum_j \frac{F_{j,t}(z)^2}{\sigma_j^2}}. \tag{3.13}$$

In this work we also incorporate a so-called "template error function" to account for uncertainties caused by the limited template set and any potential systematic offsets as a function of wavelength. The template error function and method applied to our stellar mass fits is identical to that outlined in Brammer et al. (2008) and included in the initial photometric redshift analysis outlined in Section 3.3.3. Specifically, this means that the total error for any individual filter, j, is given by:

$$\sigma_j = \sqrt{\sigma^2_{j,obs} + \left(F_{j,obs}\sigma_{\mathrm{temp}}(\lambda_j)\right)^2} \tag{3.14}$$

where $\sigma_{j,obs}$ is observed photometric flux error, $F_{j,obs}$ its corresponding flux and $\sigma_{\mathrm{temp}}(\lambda_j)$ the template error function interpolated at the pivot wavelength for that filter, λ_j. We note that in addition to estimating the stellar mass, this method also provides a secondary measurement of the photometric redshift, whereby

$P(z) \propto \sum_t w_t(z)$. Our reasons for using an independently estimated redshift PDF in the pair analysis in place of those generated by the marginalised redshift likelihoods from the stellar mass fits are two-fold. Firstly, for consistency with results of Chapter 2 where the redshifts from EAZY have been well tested at high-redshift. And secondly, the fact that the accuracy and reliability offered by EAZY is greater due to its ability to fit non-negative combinations of multiple templates simultaneously (Brammer et al., 2008; Dahlen et al., 2013).

For the Bruzual & Charlot (2003) templates used in our stellar mass fitting we allow a similar range of stellar population parameters as used in Chapter 2. Model ages are allowed to vary from 10 Myr to the age of the Universe at a given redshift, metallicities of 0.02, 0.2 and 1 $Z_{\odot}$, and dust attenuation strength in the range $0 \leq A_V \leq 3$ assuming a Calzetti et al. (2000) attenuation curve. The assumed star-formation histories follow exponential τ-models ($SFR \propto e^{-t/\tau}$), both decreasing and increasing (negative τ), for characteristic timescales of $|\tau| =$ 0.25, 0.5, 1, 2.5, 5, 10, plus an additional short burst ($\tau = 0.05$) and continuous star-formation models ($\tau \gg 1/H_0$).

Nebular emission is included assuming a relatively high escape fraction $f_{\rm esc} = 0.2$ (Yajima et al., 2010; Fernandez & Shull, 2011; Finkelstein et al., 2012; Robertson et al., 2013) and hence a relatively conservative estimate on the contribution of nebular emission. As in Chapter 2, we assume for the nebular emission that the gas-phase stellar metallicities are equivalent and that stellar and nebular emission are attenuated by dust equally.

In Figure 3.3, we show the estimated stellar mass as a function of redshift for the two example projected pairs shown in Figure 3.1. For the galaxy pair shown in the top panel (with $\mathcal{N}_z = 0.895$) the pair selection criteria are all satisfied over most of the redshift range with high probability ($z \sim 3$). As this pair also satisfies the separation criteria, the pair-probability for this projected pair is $\int_0^{\infty} \mathrm{PPF}(z)dz = 0.869$. In contrast, the second potential pair (with $\mathcal{N}_z = 0.379$) does not satisfy the pair criteria at any redshift due to the low stellar mass of the secondary galaxy and therefore has a final pair-probability of $\int_0^{\infty} \mathrm{PPF}(z)dz = 0.$.

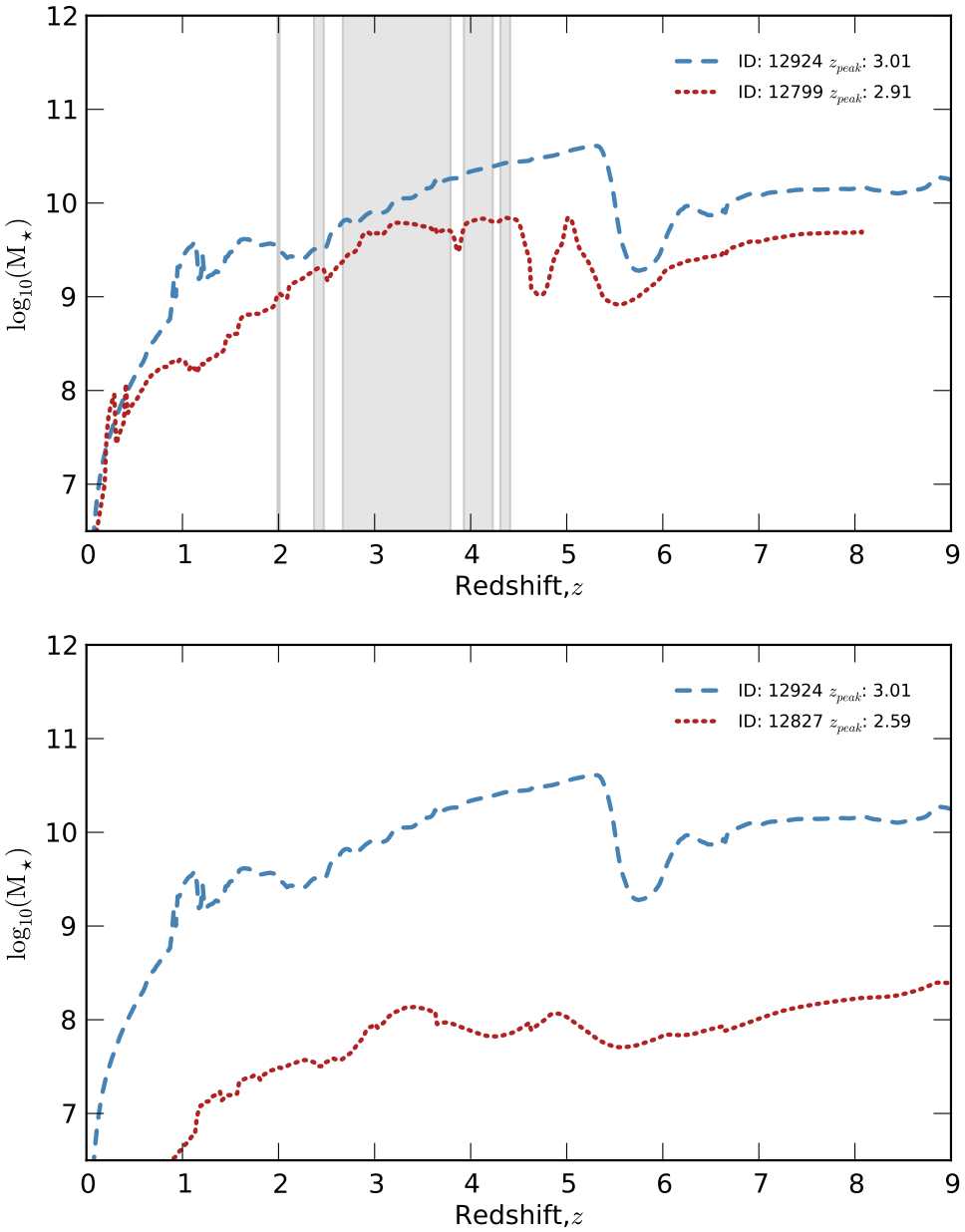

Figure 3.3: redshift-dependent stellar mass estimations for the example close pairs shown in Figure 3.1. In both panels, the blue dashed line corresponds to the stellar mass for the primary galaxy while the red dotted line is that of the projected companion. The grey shaded regions highlight the redshift ranges in which the pair-selection criteria are met (Equation 3.5), with $\log_{10}(M_\star^{min}) = 9.5$ and $\mu = 1/4$.

3.3.5 Correction for selection effects

As defined by LS15, the pair-probability function in Equation 3.9 is affected by two selection effects. Firstly, the incompleteness in search area around galaxies that are near the image boundaries or near areas affected by bright stars (Section 3.3.5.2). And secondly, the selection in photometric redshift quality (Section 3.3.5.3). Additionally, because in this work we use a flux-limited sample rather than one that is volume limited (as used by LS15), we must also include a further correction to account for this fact.

3.3.5.1 The redshift-dependent mass completeness limit

Since the photometric survey we are using includes regions of different depth and high-redshift galaxies are by their very nature quite faint, restricting our analysis to a volume-limited sample would necessitate excluding the vast majority of the available data. As such, we choose to use a redshift-dependent mass completeness limit with the limit determined by the flux limit determined by the survey.

Due to the limited number of galaxy sources available, determining the strict mass completeness as a function of redshift entirely empirically (Pozzetti et al., 2010) is not possible. Instead, we make use of a semi-empirical method based on that of Pozzetti et al. (2010), using the available observed stellar mass estimates to inform the selection of a template SED for the evolving 95% stellar mass-to-light limit. We make use of the full set of high-redshift Monte Carlo samples of Chapter 2, selecting galaxies which are within a given redshift bin, then scaling the masses of the faintest 20% such that their apparent magnitude is equal to the flux limit. The mass completeness limit for a given redshift bin is defined as the mass corresponding to the 95th percentile of the scaled mass range, the resulting mass completeness at $z > 3.5$ in bins with width $\Delta z = 0.5$ are shown in Figure 3.4 assuming a flux-limit equal to that in the GOODS South 'DEEP' region.

Based on the estimated completeness limits, we select a Bruzual & Charlot (2003) template that closely matches the observed $M_\star/L$ redshift evolution. By doing

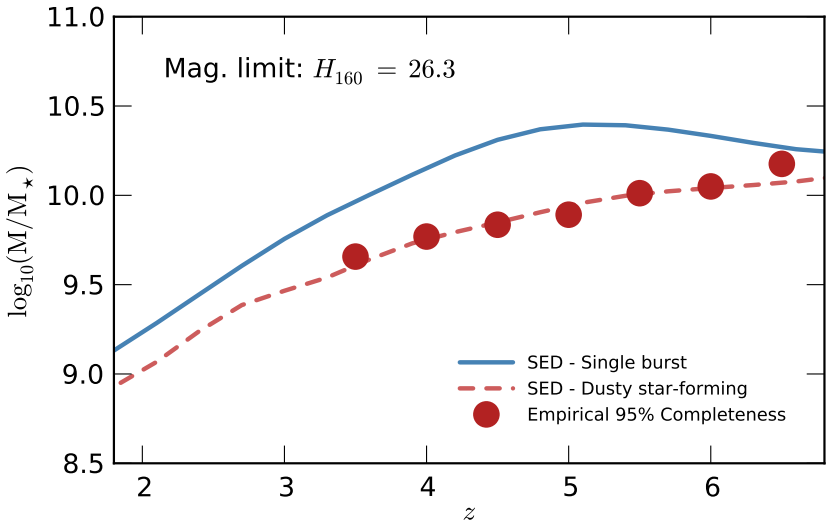

Figure 3.4: Mass completeness limit corresponding to a flux limit of $H_{160} = 26.3$, the approximate depth of the DEEP and ERS regions within CANDELS GOODS South. Red circles correspond to the 95% completeness limits derived from the stellar mass estimates of Chapter 2, the continuous blue and dashed red lines are the completeness limits corresponding to a maximally old (at a given redshift) single burst or dusty star-forming population respectively, see text for details.

so we can estimate the mass completeness as a continuous function of redshift and extend the constraints to redshifts lower than those explored in Chapter 2. A common choice of template for estimating the strict $M_\star/L$ completeness is a maximally old single burst (continuous blue line in Figure 3.4). However, since the vast majority of galaxies above $z \sim 3$ are star-forming, this assumption significantly overestimates the actual completeness limit at high-redshift. Based on plausible assumptions for galaxies at high-redshift and tuning by hand, we find a maximally old, very dusty ($A_V = 2$) star-forming galaxy with a power-law star-formation history ($\propto t^{1.4}$) provides a good fit to the empirical data (red dashed line in Figure 3.4). For both the burst and star-forming SEDs, we assume an onset of star-formation at $z = 12$, sub-solar metallicity (0.2 $Z_\odot$) and an escape fraction for nebular emission of $f_{\rm esc} = 0.2$.

While a dust extinction of $A_V = 2$ is higher than typically observed at high redshift (Schaerer et al., 2015), it is consistent with the dust extinction seen in sub-mm galaxies at $z > 2$ (Targett et al., 2013; Wiklind et al., 2014; Smolčić et al., 2015) and therefore represents a plausible limit for the highest mass-to-light ratios at high redshift. Instead of assuming a rising star-formation history and high fixed dust attenuation, we could have instead plausibly chosen a different

star-formation history and allowed dust to vary with redshift in a manner which also matched the estimated empirical completeness.

The redshift-dependent mass limit, $\mathrm{M}_{\star}^{\mathrm{flux}}(z)$, is defined as

$$\log_{10}(\mathrm{M}_{\star}^{\mathrm{flux}}(z)) = 0.4 \times (H_{\mathrm{M}_{\star}/L}(z) - H^{\mathrm{lim}}) \tag{3.15}$$

where H^{lim} is the H_{160} magnitude at the flux-completeness limit in the field or region of interest and $H_{\mathrm{M}_{\star}/L}(z)$ is the H_{160} magnitude of the dusty star-forming template normalised to 1 $\mathrm{M}_{\odot}$ and observed through the H_{160} at a given redshift (automatically taking the required k-correction into account).

For a primary galaxy with a mass close to the redshift-dependent mass-limit imposed by the selection criteria $S(z)$, the mass range within which secondary pairs can included may be reduced, i.e. $\mu\mathrm{M}_{\star}^{1}(z) < \mathrm{M}_{\star}^{\mathrm{lim}}(z) < \mathrm{M}_{\star}^{1}(z)$. To correct for the potential galaxy pairs that may be lost by the applied completeness limit, we make a statistical correction based on the stellar mass function at the redshift of interest. The flux-limit weight, $w_2^{\mathrm{flux}}(z)$, applied to every secondary galaxy found around each primary galaxy, is defined as

$$w_2^{\mathrm{flux}}(z) = \frac{1}{W_2(z)}, \tag{3.16}$$

where

$$W_2(z) = \frac{\int_{\mathrm{M}_{\star}^{\mathrm{lim}}(z)}^{\mathrm{M}_{\star}^{1}(z)} \phi(\mathrm{M}_{\star}|z) d\mathrm{M}_{\star}}{\int_{\mu\mathrm{M}_{\star}^{1}(z)}^{\mathrm{M}_{\star}^{1}(z)} \phi(\mathrm{M}_{\star}|z) d\mathrm{M}_{\star}} \tag{3.17}$$

and $\phi(\mathrm{M}_{\star}|z)$ is the stellar mass function at the corresponding redshift. The redshift-dependent mass limit is $\mathrm{M}_{\star}^{\mathrm{lim}}(z) = max\{\mu\mathrm{M}_{\star}^{1}(z), \mathrm{M}_{\star}^{\mathrm{flux}}(z)\}$, where $\mathrm{M}_{\star}^{\mathrm{flux}}(z)$ is defined in Equation 3.15). By applying this weight to all pairs associated with a primary galaxy, we get the the pair statistics corresponding to $\mu\mathrm{M}_{\star}^{1}(z) \leq \mathrm{M}_{\star}^{2}(z) \leq \mathrm{M}_{\star}^{1}(z)$ (the volume limited case). As in Patton et al. (2000), we assign additional weights to the primary sample in order to minimise the error from primary galaxies that are closer to the flux limit (i.e. PDF weighted to higher redshifts) as these galaxies will have fewer numbers of *observed* pairs. The primary flux-weight, $w_{\mathrm{flux}}^{1}(z)$ is defined as

$$w_1^{\mathrm{flux}}(z) = W_1(z) = \frac{\int_{\mathrm{M}_{\star}^{\mathrm{lim}}(z)}^{\mathrm{M}_{\star}^{\mathrm{max}}} \phi(\mathrm{M}_{\star}|z) d\mathrm{M}_{\star}}{\int_{\mathrm{M}_{\star}^{\mathrm{min}}}^{\mathrm{M}_{\star}^{\mathrm{max}}} \phi(\mathrm{M}_{\star}|z) d\mathrm{M}_{\star}} \tag{3.18}$$

where $\mathrm{M}_{\star}^{\mathrm{min}}$ and $\mathrm{M}_{\star}^{\mathrm{max}}$ are the lower and upper limits of the mass range of interest for the primary galaxy sample, the redshift-dependent lower limit is defined as $\mathrm{M}_{\star}^{\mathrm{lim}}(z) = max\{\mathrm{M}_{\star}^{\mathrm{min}}, \mathrm{M}_{\star}^{\mathrm{flux}}(z)\}$, and the remaining parameters are as outlined above. In the case of a volume-limited sample (where $\mathrm{M}_{\star}^{\mathrm{flux}}(z) < \mu \mathrm{M}_{\star}^{1}(z)$ at all redshifts) both of the flux-limit weights are equal to unity.

The stellar mass functions (SMF) parametrisations as a function of redshift, $\phi(\mathrm{M}_{\star}|z)$, are taken from Mortlock et al. (2014) at $z \leq 3$, Santini et al. (2012) at $3 < z < 3.5$ and Chapter 2 at $z \geq 3.5$. When selecting redshift bins in which to estimate the merger fraction, we ensure that the bins are chosen to match the bins in which the SMF are constrained (i.e. the SMF used to weight the merger fraction is the same across the bin).

To calculate the effective completeness weights for comparison requires integrating over the redshift dependent $w_1^{\mathrm{flux}}(z)$ or $w_2^{\mathrm{flux}}(z)$. When doing so we must also take into account the redshifts at which the primary and secondary galaxy are contributing to the total galaxy pair count and therefore the redshifts at which the completeness weights are being applied. As such, we define the pair-weighted flux completeness weights for a galaxy pair, $\left\langle w_n^{\mathrm{flux}} \right\rangle^{i,j}$, as

$$\left\langle w_n^{\mathrm{flux}} \right\rangle^{i,j} = \frac{\int \mathrm{PPF}^{i,j}(z) w_n^{\mathrm{flux,\,i}}(z) \mathrm{d}z}{\int \mathrm{PPF}^{i,j}(z) \mathrm{d}z}, \tag{3.19}$$

where n equals either 1 or 2, corresponding to the primary or secondary flux-weight respectively. Similarly, i and j are the primary and secondary galaxies in a galaxy pair, with $\mathrm{PPF}^{i,j}(z)$ the corresponding pair probability function.

To see how the the completeness weights change as a function of redshift and limiting depth (i.e. the variation between regions in GOODS South) we calculated the median completeness weights in each of the redshift bins used later in Section 3.4.2 and 3.4.3. The resulting completeness weights for each region of GOODS South are shown in Figure 3.5, assuming a mass selection of $\log_{10}(\mathrm{M}_{\star}/\mathrm{M}_{\odot}) > 9.5$ and minimum mass ratio of $\mu = \frac{1}{4}$ when calculating $\mathrm{PPF}^{i,j}(z)$. As $\log_{10}(\mathrm{M}_{\star}/\mathrm{M}_{\odot}) > 9.5$ is the lowest mass limit used in this work, the pair-weighted completeness weights shown in Figure 3.5 represent the lower or upper limits for the primary and secondary weights respectively.

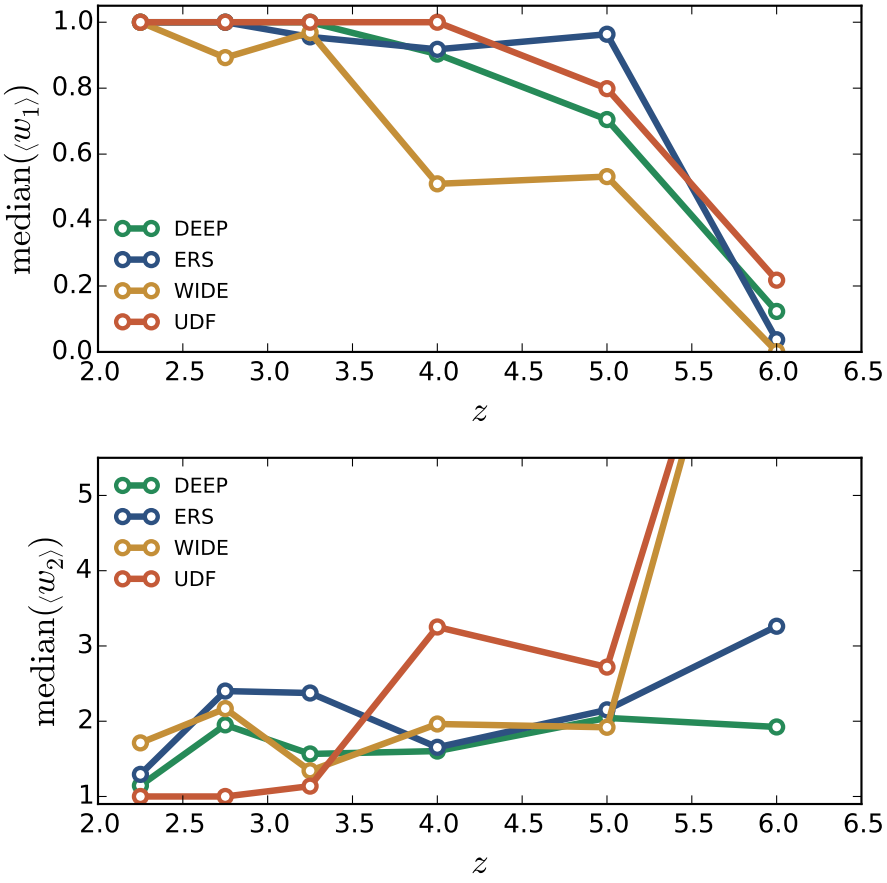

Figure 3.5: The median completeness weights as a function of redshift for each region of GOODS South, assuming a mass selection of $\log_{10}(M_\star/M_\odot) > 9.5$ and minimum mass ratio of $\mu = \frac{1}{4}$.

In addition to the median pair-weighted completeness weights, we also estimated the effects of the errors in the stellar mass function parametrizations as a function of redshift. We estimated the errors by randomly perturbing the Schechter function parameters in each redshift bin by their quoted errors and then re-calculating $\langle w_n^{\rm flux} \rangle$, repeating this process 32 times to give a distribution of pair-weighted completeness weights for each individual galaxy pair. In Figure 3.6 we show the average fractional standard deviation in each redshift bin for both the primary and secondary completeness weights.

Inspecting Figures 3.5 and 3.6, we find that up to $z \sim 4$, the completeness weights remain relatively small and have low errors due to the uncertainties in the observed stellar mass functions. However at $z \gtrsim 4$, the weights become increasingly large (median($\langle w_2^{\rm flux} \rangle$)) or have much greater uncertainty ($\sigma_{\langle w_1^{\rm flux} \rangle}$). These results suggest that for redshifts $z \geq 5$, the mass completeness corrections

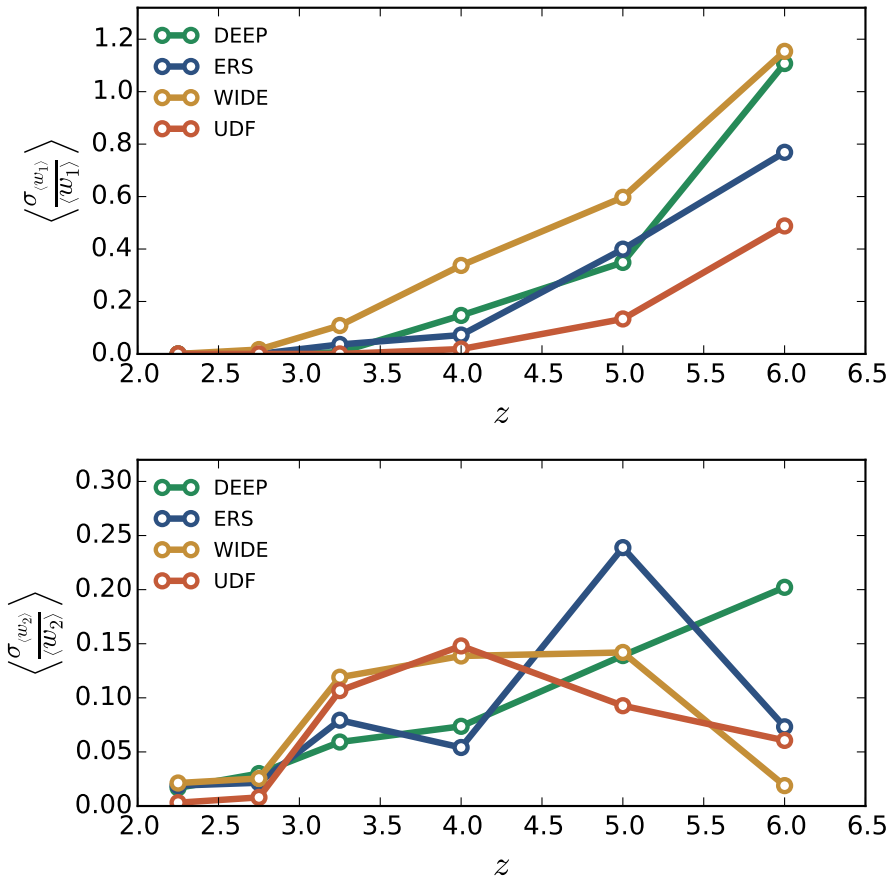

Figure 3.6: Effect of stellar mass function errors on w_1 and w_2.

become increasingly important, but also that they will be increasingly unreliable. As such, these uncertainties will likely place an upper limit on the redshifts at which we can estimate the major merger rate.

3.3.5.2 Image boundary and excluded regions

A second correction which must be taken into account is to the search area around primary galaxies that lie close to the boundaries of the survey region. Because of the fixed physical search distance, this correction is also a function of redshift so must be calculated for all redshifts within the range of interest.

In addition to the area lost at the survey boundaries, it is also necessary to correct for the potential search area lost due to the presence of large stars and other artefacts, around which no sources are included in the catalog (see Section 3.3.1).

We have taken both of these effects into account when correcting for the search

areas by creating a mask image based on the underlying photometry. Firstly, we define the image boundary based on the exposure map corresponding to the H_{160} photometry used for object detection. Next, for every source excluded from the sample catalog based its classification as a star or image artefact by our photometric or visual classification, the area corresponding to that object (from the photometry segmentation map) is set to zero in our mask image. Finally, areas of photometry which are labelled in the flag map (and excluded based on their corresponding catalog flags) are also set to zero.

To calculate the area around a primary galaxy that is excluded by these effects, we perform photometry on the mask image. Photometry is performed in annuli around each primary galaxy target, with inner and outer radii of $\theta_{\rm min}(z)$ and $\theta_{\rm max}(z)$ respectively. The area weight is then defined as

$$w_{\rm area}(z) = \frac{1}{f_{\rm area}(z)} \tag{3.20}$$

where $f_{\rm area}(z)$ is the sum of the normalised mask image within the annulus at a given redshift divided by the sum over the same area in an image with all values equal to unity. By measuring the area in this way we are able to automatically take into account the irregular survey shape and any small calculation errors from quantisation of areas due to finite pixel size.

Despite the relatively small survey area explored in this study (and hence a higher proportion of galaxies likely to lie near the image edge), the effect of the area weight on the estimated pair fractions is very small. To quantify this, we calculate the pair averaged area weights, $\langle w_{\rm area} \rangle$, following the same formalism as outlined for the mass completeness weights above:

$$\left\langle w^{i,j}_{\rm area} \right\rangle = \frac{\int {\rm PPF}^{i,j}(z) w^{i}_{\rm area}(z) {\rm dz}}{\int {\rm PPF}^{i,j}(z) {\rm dz}}, \tag{3.21}$$

where $w^{i}_{\rm area}(z)$ is the redshift dependent area weight for a primary galaxy i, and ${\rm PPF}^{i,j}(z)$ the corresponding pair-probability function for primary galaxy and a secondary galaxy j. Of the full sample of primary galaxies, less than 10% have average area weights greater than 1% (where a primary galaxy has multiple pairs, we take the average of $\langle w^{i,j}_{\rm area} \rangle$ over all secondary galaxies). Furthermore, only $\approx 2\%$ of primary galaxies have average weights $> 10\%$ (i.e. $\langle w^{i,j}_{\rm area} \rangle > 1.1$)

and only 0.15% have weights $> 50\%$. The effects of area weights on the final estimated merger fractions will therefore be minimal. Never the less, we include these corrections in all subsequent analysis.

3.3.5.3 The Odds sampling rate

Following LS15, we also apply a selection based on the photometric redshift quality, or odds $\mathcal{O}$ parameter. The odds parameter is defined by Benítez (2000) and Molino et al. (2014) as

$$\mathcal{O} = \int_{-K(1+z_{\rm p})}^{+K(1+z_{\rm p})} P(z)dz \tag{3.22}$$

where $z_{\rm p}$ is the redshift corresponding peak of the redshift PDF, $P(z)$ (or the PDF average or median). In Molino et al. (2014) $K = 0.0125$, based on the typical photometric redshift accuracy of their survey. However due to the high redshifts of interest and the broadband nature of the CANDELS survey (as opposed to the lower redshift narrow-band ALHAMBRA survey studied in Molino et al. (2014)) we assume a broader criteria of $K = 0.05$ based on difference in photometric redshift scatter between the two surveys ($\approx 4\times$).

The odds sampling rate (OSR) for galaxies with an apparent H_{160} magnitude of M is then defined as

$$\mathrm{OSR}(M) = \frac{\sum_i N_{i,\mathcal{O}\geq 0.3}}{\sum_i N_{i,\mathcal{O}\geq 0}}, \tag{3.23}$$

the ratio between the number of galaxies with $\mathcal{O} \geq 0.3$ and the total number of galaxies ($\mathcal{O} \geq 0$) with magnitude M (Molino et al., 2014).

We first calculate $\mathrm{OSR}(M)$ in bins with width $\Delta M = 0.5$ and interpolate these values to define the odds sampling rate for each galaxy based on its apparent H_{160} magnitude. From this value, the OSR weight for each individual galaxy, i, is then defined as

$$w_i^{\rm OSR} = \frac{1}{\mathrm{OSR}(M_i)}. \tag{3.24}$$

For both $w_1^{\rm OSR}$ and $w_2^{\rm OSR}$, the average value is ≈ 1.5 (again, weighted by the corresponding pair likelihoods) and the largest OSR weight is less than 1.8.

3.3.5.4 The combined weights

Taking all three of the above effects into account, the pair weights for each secondary galaxy found around a galaxy primary are given by

$$w_2(z) = w_1^{\rm area}(z) \times w_1^{\rm flux}(z) \times w_2^{\rm flux}(z) \times w_1^{\rm OSR} \times w_2^{\rm OSR}. \tag{3.25}$$

The weights applied to every primary galaxy in the sample are then given by

$$w_1 = w_1^{\rm flux}(z) \times w_1^{\rm OSR}. \tag{3.26}$$

These weights are then applied to the integrated pair-probability functions for each set of potential pairs to calculate the merger fraction. As discussed in the previous sections, the greatest contribution to the total weights primarily comes from the secondary galaxy completeness weights, $w_2^{\rm flux}(z)$, with additional non-negligible contributions from the primary completeness and the odds sampling rate weights. Furthermore, the largest error in the total weights results from the mass completeness weights.

In the implementation of the pair-count methodology used in this chapter, it is not currently possible to fully incorporate the individual completeness weight errors in the overall merger fraction uncertainties. However, in future studies incorporating the full CANDELS datasets where Poisson and cosmic variance errors will be significantly reduced, propagating the SMF uncertainty into the final of increasing importance. For the results presented later in this chapter, it is necessary to bear in mind that there may additional statistical errors in the measured pair-fraction up to $\sigma_x/x \lesssim 0.2$.

3.3.6 The merger fraction

For each galaxy, i, in the primary sample, the number of associated pairs, $N^i_{\rm pair}$, within the redshift range $z_{\rm min} < z < z_{\rm max}$ is given by

$$N^i_{\rm pair} = \sum_j \int_{z_{\rm min}}^{z_{\rm max}} w_2^j(z) \times {\rm PPF}_j(z) dz \tag{3.27}$$

where j indexes the number of potential close pairs found around the primary galaxy, ${\rm PPF}_j(z)$ the corresponding pair-probability function (Section 3.3.2) and

$w_2^j(z)$ its pair weight (Equation 3.25). The corresponding weighted primary galaxy contribution, N_1^i, within the redshift bin is

$$N_1^i = \sum_i \int_{z_{\min}}^{z_{\max}} w_1^i(z) \times P_i(z) \times S_1^i(z) dz \tag{3.28}$$

where $S_1^i(z)$ is the selection function for the primary galaxies given in Equation 3.8, $P_i(z)$ its normalised redshift probability distribution and w_1^i its weighting. In the case of a primary galaxy with stellar mass in the desired range with its redshift PDF contained entirely within the redshift range of interest, $N_1^i = w_1^i$ and hence always equal or greater than unity.

The estimated merger fraction $f_{\rm m}$ is defined as the number of pairs divided by the total number of galaxies. In the redshift range $z_{\min} < z < z_{\max}$, $f_{\rm m}$ is then given by

$$f_{\rm m} = \frac{\sum_i N_{\rm pair}^i}{\sum_i N_1^i} \tag{3.29}$$

where i is summed over all galaxies in the primary sample. In the case of a field consisting of different sub-fields with differing depths like GOODS South, this sum becomes

$$f_{\rm m} = \frac{\sum_k \sum_i N_{\rm pair}^{k,i}}{\sum_k \sum_i N_1^{k,i}} \tag{3.30}$$

where k is indexed over the number distinct regions within a field (in the case of GOODS South – Deep, Wide, ERS and UDF) and the flux-limited mass completeness used throughout the calculations is set by the corresponding H_{160} depth within each field.

3.4 The merger evolution at $z > 2$

For this work we select our initial sample of galaxies in each field based on the following criteria:

$$\int_2^\infty P(z)\ dz > 0.95, \tag{3.31}$$

ensuring that the bulk of the redshift probability distribution lies at high redshift and that any secondary redshift solutions are minor. The result of this criteria is to decrease the scatter ($\sigma_{\rm NMAD} = 0.03$) and bias (median$(z_{\rm phot} - z_{\rm spec}) = 0.01$)

and give a primary sample with very low outlier fraction. Specifically, for the definitions of outlier fraction in Molino et al. (2014), we find $\eta_1 = 0.7\%$ and $\eta_2 = 1.1\%$.

For this clean high-redshift sample, we then performed the PDF pair-count analysis in six redshift bins from $z = 2$ to $z = 6.5$ for stellar mass cuts of $\log_{10}(\mathrm{M}_\star/\mathrm{M}_\odot) > 9.5$ and $\log_{10}(\mathrm{M}_\star/\mathrm{M}_\odot) > 10$. We perform the pair searches in two annuli with projected separation $5 \leq r_\mathrm{p} \leq 20$ and $5 \leq r_\mathrm{p} \leq 30$. The minimum radius of 5 kpc is typically included in close pair analysis to prevent confusion of close sources due to the photometric or spectroscopic fibre resolution. Although the high-resolution HST photometry allows for reliable de-confusion at radii smaller than this (Laidler et al., 2007; Galametz et al., 2013), we adopt this radius for consistency with previous results.

The error on f_m is estimated using the common bootstrap technique of Efron (1979, 1981). The standard error, σ_{f_m}, is defined as

$$\sigma_{f_\mathrm{M}} = \sqrt{\frac{\sum_i^N \left(f_\mathrm{m}^i - \langle f_\mathrm{m} \rangle\right)^2}{(N-1)}} \tag{3.32}$$

where f_m^i is the estimated merger fraction for a randomly drawn sample of galaxies (with replacement) from the initial sample (for N independent realisations) and $\langle f_\mathrm{m} \rangle = \left(\sum_i f_\mathrm{m}^i\right)/N$. The results of this analysis are outlined in Section 3.4.2.

3.4.1 Merger fractions for semi-analytical models

To make a direct comparison with theoretical models we also perform the pair-count analysis on mock lightcones from the semi-analytical models (SAMs) of Lu et al. (2011, see also Lu et al. 2014). We treat the mock data as a 'perfect' spectroscopic survey and apply a pseudo-spectroscopic pair-count methodology for the same separation and mass criteria as used on the observational data, using a separation criteria of $\Delta v \leq 500$ km s^{-1} along the line-of-sight.

Although the field size of the lightcone is approximately 10× the size of the observed GOODS South field, the counts obtained are still subject to significant errors due to cosmic variance. To minimise the effects of cosmic variance, we

apply the analysis to 8 different realisations of the mock lightcone, taking the average and standard deviation of these values. We calculate the pair-counts for overlapping redshift bins with width $\Delta z = 0.5$, in steps of half this size. Due to volume limitations at low-redshift and the simulation time and resolution limits at high-redshift, we restrict the mock pair-count analysis to $0.5 \leq z \leq 5.75$.

3.4.1.1 Cosmic variance estimates from SAMs

The large field size of the SAMs and the multiple realisations of the lightcone (effectively simulating separate fields on the sky) also allows us to make well informed estimates of the cosmic variance (CV) for our observations. We estimate the CV error for the GOODS South field by repeatedly measuring the pair-counts in the mock lightcones using a field size equal to that of the CANDELS field (10×16 arcmin). The position of the sub-region being studied is selected randomly from five of the lightcones and centred at a random position within the larger lightcone field (the centre of the sub-region is chosen such that never extends outside the lightcone).

For each redshift bin, mass cut and separation studied for the real data we calculate the fractional CV error, $\left(\frac{\sigma_{f_\mathrm{m}}}{\langle f_\mathrm{m} \rangle}\right)_\mathrm{CV}$, based on 64 random fields. The total error, $\sigma_{f_\mathrm{m}}^\mathrm{Tot}$, on the observed merger counts is then

$$\sigma_{f_\mathrm{M}}^\mathrm{Tot} = f_\mathrm{m} \times \sqrt{\left(\frac{\sigma_{f_\mathrm{m}}}{f_\mathrm{m}}\right)_\mathrm{Obs}^2 + \left(\frac{\sigma_{f_\mathrm{m}}}{\langle f_\mathrm{m} \rangle}\right)_\mathrm{CV}^2} \tag{3.33}$$

where $\left(\frac{\sigma_{f_\mathrm{m}}}{f_\mathrm{m}}\right)_\mathrm{Obs}$ is the fractional bootstrap error calculated in Equation 3.32.

3.4.2 Evolution of the merger fraction

In Figure 3.7 we plot the estimated merger fractions for this work along with other comparable estimates from the literature and those predicted by the semi-analytic models of Lu et al. (2011). We also show the calculated values and their corresponding total errors (bootstrap plus cosmic variance) in Table 3.1.

Due to the wide range of criteria used for selecting close pairs in past observations

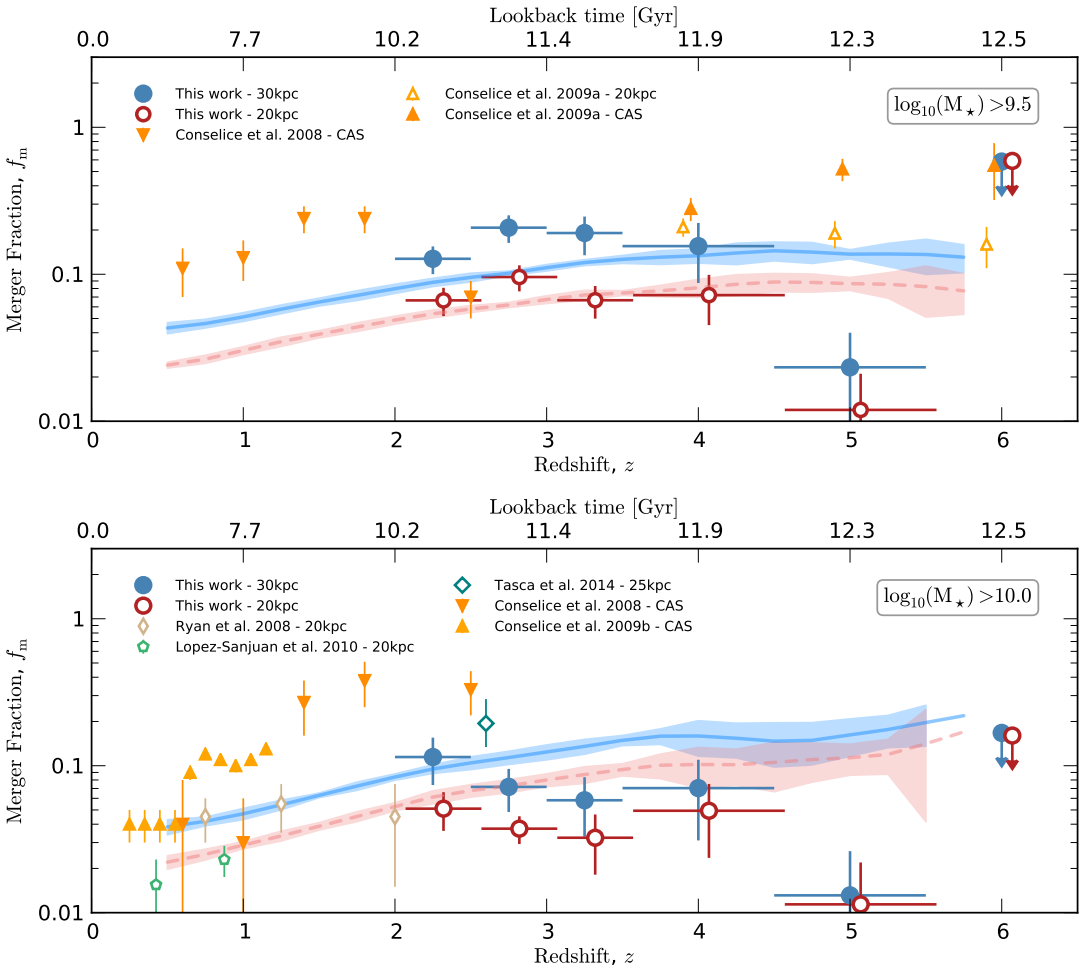

Figure 3.7: Estimated merger fraction as a function of redshift for galaxies with stellar mass $\log_{10}(M_\star/M_\odot) > 9.5$ (top) and $\log_{10}(M_\star/M_\odot) > 10$ (bottom). Also shown are the merger fractions from close pair statistics of Ryan et al. (2008), Conselice & Arnold (2009), López-Sanjuan et al. (2010) and Tasca et al. (2014) and the morphological estimates of Conselice et al. (2008), Conselice & Arnold (2009) and Conselice et al. (2009). The continuous blue and dashed red lines correspond to the model predictions of Lu et al. (2011, 2014), with the shaded regions representing the Poisson noise for the model number counts.

and the various timescales involved, making direct comparisons with previous estimates can be difficult. The majority of merger rate studies typically focus on the most massive galaxies, i.e. $\log_{10}(M_\star/M_\odot) > 11$. For studies at $z > 1$, such massive galaxies are above the typical flux or mass completeness limits and are bright enough for obtaining accurate spectroscopic redshift, they therefore represent the most robust samples studied to date (Bluck et al., 2009; Man et al., 2011).

We have therefore plotted only those literature results that represent comparable sample selections or methodology. For $\log_{10}(M_\star/M_\odot) \geq 10$ (bottom panel of Fig-

Table 3.1: Estimated merger fractions from PDF analysis, as plotted in Figure 3.7. Quoted errors include the bootstrapped errors on $f_{\rm m}$ and the estimated cosmic variance, as calculated in Section 3.4.1.1.

Merger fraction - $5 \leq r_{\rm p} \leq 20$

Redshift	$\log_{10}(M_\star/M_\odot) > 9.5$	$\log_{10}(M_\star/M_\odot) > 10$
$2.0 \leq z < 2.5$	0.07 ± 0.02	0.05 ± 0.02
$2.5 \leq z < 3.0$	0.10 ± 0.03	0.04 ± 0.02
$3.0 \leq z < 3.5$	0.07 ± 0.02	0.03 ± 0.02
$3.5 \leq z < 4.5$	0.07 ± 0.03	0.05 ± 0.04
$4.5 \leq z < 5.5$	0.01 ± 0.01	$0.01^{+0.02}_{-0.01}$
$5.5 \leq z < 6.5$	< 0.59	< 0.16

Merger fraction - $5 \leq r_{\rm p} \leq 30$

Redshift	$\log_{10}(M_\star/M_\odot) > 9.5$	$\log_{10}(M_\star/M_\odot) > 10$
$2.0 \leq z < 2.5$	0.13 ± 0.03	0.11 ± 0.04
$2.5 \leq z < 3.0$	0.21 ± 0.04	0.07 ± 0.04
$3.0 \leq z < 3.5$	0.19 ± 0.06	0.06 ± 0.04
$3.5 \leq z < 4.5$	0.16 ± 0.07	0.07 ± 0.04
$4.5 \leq z < 5.5$	0.02 ± 0.02	$0.01^{+0.02}_{-0.01}$
$5.5 \leq z < 6.5$	< 0.58	< 0.17

ure 3.7) we present the close pair results of Ryan et al. (2008) and López-Sanjuan et al. (2010) at $z \leq 2$ and Tasca et al. (2014) at $1.81 \leq z \leq 3.65$. Following LS15, since Ryan et al. (2008) and López-Sanjuan et al. (2010) both present the number of close companions $N_{\rm c}$ (i.e. twice the number of close pairs: two galaxies per pair), plotted in Figure 3.7 is $0.5N_{\rm c}$. Also shown are the morphological merger fraction estimates of Conselice et al. (2008) and Conselice et al. (2009) at $z \leq 2$. As shown in Lotz et al. (2008) and further discussed in Bluck et al. (2012), the morphological signatures of mergers are only sensitive to merger ratios of 1:4 or less so are likely probing the same kind of merging systems as is probed by the close pair analysis.

For the $\log_{10}(M_\star/M_\odot) \geq 9.5$ mass selection (top panel) we show the $9 \leq \log_{10}(M_\star/M_\odot) \leq 10$ morphology estimates of Conselice et al. (2008) and the morphology and pair-count merger rates of Conselice & Arnold (2009). Based on a flux limited Lyman break selection, the samples explored by Conselice & Arnold (2009) likely represent a lower mass range ($\log_{10}(M_\star/M_\odot) \gtrsim 9$) based on the typical rest-frame magnitude of dropouts in the UDF and the observed mass-to-light ratios at these redshifts Chapter 2. As such, these samples may therefore not represent a valid

comparison.

At $z \sim 2$ to 2.5, our results for close pair with projected separations of 20kpc are in good agreement with those of Ryan et al. (2008) for the same separation and mass limits. However, both results are significantly lower than the morphological estimates of Conselice et al. (2008) at this same redshift. Our results currently support the idea that the merger fraction for galaxies with $\log_{10}(M_\star/M_\odot) \geq 10$ peaks at $z \sim 2.5$ (Conselice, 2014), with an overall decline in the measured merger fraction above this redshift. However, the fact that the merger fraction declines so sharply at $z \sim 5$ is perhaps more likely due to the mass completeness limits applied. As illustrated in Figure 3.4, for fields with comparable depth to the GOODS Deep or ERS the mass completeness limit is $\log_{10}(M_\star/M_\odot) \approx 10$. Hence, galaxies which are close to this limit will have fewer companions that are above the completeness limits. The statistical corrections calculated in Section 3.3.5.1 rely on having a representative sample of selected companions to up-weight accordingly. Therefore at $z \sim 5$ and $z \sim 6$ the merger fraction estimates are dominated by the much rarer bright objects in the shallow fields and the very small area of the deeper UDF.

The sharp drop in merger fraction at $z \sim 5$ is even more pronounced for the lower mass cut of $\log_{10}(M_\star/M_\odot) \geq 9.5$, supporting our hypothesis that this drop is driven by issues of mass completeness. The inclusion of the four remaining CANDELS fields may help to reduce this effect by providing more statistically significant samples of galaxies with $\log_{10}(M_\star/M_\odot) \geq 10$. Furthermore, the increased area covered should provide the number statistics required to investigate the merger fraction at higher mass limits (e.g. $\log_{10}(M_\star/M_\odot) \geq 10.5$) to better quantify these completeness effects.

When related to the SAM predictions of Lu et al. (2011), our estimated merger fractions give rise to somewhat confusing comparisons. For $\log_{10}(M_\star/M_\odot) \geq 9.5$, the overall evolution and normalisation of the merger fraction at $z \sim 2$ to $z \sim 4$ are in reasonable agreement with the SAM predictions, especially for pairs selected at 20kpc separation. In contrast the evolution for our observed f_m at $\log_{10}(M_\star/M_\odot) \geq 10$ over this same redshift range is markedly different. Inter-

estingly, although the SAM models predict a peak in the merger fractions the redshift at which this occurs is significantly higher than that of earlier observations ($z \sim 2.5$; Conselice 2014).

The relatively poor agreement between the observed merger fractions and the results of SAMs for $\log_{10}(M_\star/M_\odot) \geq 10$ is similar to previous comparisons with models in this way (Bertone & Conselice, 2009; Jogee et al., 2009). Typically, SAMs are not necessarily tuned to reproduce observed merger rates at low-redshift (Lu et al., 2014). As such, it is not necessarily expected that their predicted merger rates match expectations. The observed disagreement is therefore necessarily not indicative of a fault in the observational pair counts.

3.4.3 Evolution of the merger rate

Since the merger fraction itself is a purely observational quantity and not a fundament physical property, it can make comparisons between different redshift bins and methodologies difficult. A more fundamental property of interest is therefore the merger rate, either as the average time between mergers per galaxy (Γ)[3] or the overall merger rate, i.e. (specifically the merger rate density, denoted $\mathcal{R}$ in this work).

In order to convert a merger fraction into a merger rate requires knowledge of the merger timescale, $\tau_{\rm m}$. The merger timescale can be derived either empirically (Conselice, 2009) or through simulations (Kitzbichler & White, 2008; Lotz et al., 2010a,b), with different morphology or pair criteria potentially probing different timescales within the merger process. Based on the simulations of Lotz et al. (2010a), we assume merger timescales of $\tau_{\rm m} = 0.29$ and $\tau_{\rm m} = 0.63$ for pairs with projected separation of ≤ 20 and ≤ 30 kpc respectively. These values are based on the average timescales for those separations and similar (baryonic) mass ratios of 1:3. For significantly higher mass ratios of 1:9, the average timescale increases only by $\approx 50\%$, we therefore assume that the relative difference between the 1:3 simulations of Lotz et al. (2010a) and the 1:4 ratio's used in this work is minimal. However, the error on the merger timescale for individual simulations can be

[3]Referred to in some literature as a merger rate per galaxy (Conselice, 2014).

between ≈ 0.15 and > 1 Gyr and the simulations span a range of $\Delta\tau_{\rm m} = 0.1$ and 0.38 Gyr for ≤ 20 and ≤ 30 kpc respectively. As is the case in all previous studies of the galaxy merger rate, the assumption of merger timescales represents a sizeable systematic uncertainty.

Regardless, the average time between mergers per galaxy is defined simply as

$$\Gamma(> {\rm M}_\star, z) = \frac{\tau_{\rm m}}{f_{\rm m}(> {\rm M}_\star, z)} \tag{3.34}$$

where $f_{\rm m}(> {\rm M}_\star, z)$ is the merger fraction at redshift z and masses greater than $\rm M_\star$ (Section 3.4.2) and $\tau_{\rm m}$ the corresponding merger timescale. Since the timescale is typically of the order of 0.15 to 2+ Gyr, Γ is therefore typically quoted in units of Gyr and represents the average timescale between mergers. In Table 3.2 we present $\Gamma(> {\rm M}_\star, z)$ for our estimates of the galaxy merger fraction and the merger timescales outlined above.

If the respective merger timescales for the differing separations (20 kpc and 30 kpc) are accurate, the corresponding merger rates should be the same. For the results of this work, we find that the estimated merger rates per galaxy at ≤ 20 kpc and ≤ 30 kpc projected separation are in very good agreement. The fact that the agreement is so good (albeit with very large errors) lends support to the estimated timescales from Lotz et al. (2010a).

Given the estimated time between mergers per galaxy, we can then estimate the relative contribution to the overall stellar mass growth which is a result of mergers. Based on a constant merger rate per galaxy of ≈ 4 Gyr, a galaxy with $\log_{10}({\rm M}_\star/{\rm M}_\odot) > 9.5$ will undergo ≈ 0.4 major mergers in the ≈ 1.7 Gyr between $z = 4$ and $z = 2$. The mass accumulated through major mergers ($\mu = 1/4$) will therefore only contribute an additional ≈ 10 to 40% of the stellar mass in place at $z \sim 4$. In contrast, from the observations of Chapter 2 we know that galaxies of comparable mass ($\log_{10}({\rm M}_\star/{\rm M}_\odot) = 9.7 \pm 0.3$) have average specific star-formation rates of ≈ 2.3 Gyr^{-1}. Therefore, over the same ≈ 1.7 Gyr timescale, the in-situ star-formation can increase the galaxy's stellar mass by $\approx 4\times$. The ratio between the growth by star-formation and growth through *major* mergers is of order $10\times$.

Admittedly, this simple calculation does not take into account the on-going star-

formation within the companion galaxy during this same period. For major mergers such as those probed in this study, the star-formation rates within the primary and secondary galaxies in a merging pair will be similar such that the star-formation within the secondary will also be significant. The star-formation rates of galaxies during this epoch are so high that over the assumed merger timescales, the stellar masses of the galaxies within a merger could increase their stellar mass by between $\sim$ 70% and $\sim$ 150% ($\tau_{\rm m}$ = 0.29 and $\tau_{\rm m}$ = 0.63 Gyr respectively).

The rough calculations above do however make two additional assumptions. Firstly, it assumes that the star-formation in both galaxies is not connected, i.e. the on-going star-formation is due to secular evolution. Secondly, that the star-formation duty cycles of both galaxies is long (at least comparable to the merger timescale). However, it is strongly suspected that gas-rich mergers are likely to trigger strong episodes of star-formation within the merging galaxies ('merger triggered starbursts': Hopkins et al. 2006, Cox et al. 2008). The star-formation within galaxies undergoing mergers at high redshift might therefore be significantly enchanced relative to average for galaxies of similar stellar masses. Because the method used in this chapter allows for the identification of galaxies with both high and low pair likelihoods, it is possible to then study the relative star-formation rate properties of those different galaxy populations. In future work we aim to constrain not just the merger rates of galaxies but also the effects those mergers have on star-formation in galaxies over cosmic history.

Although more informative than the merger fraction alone, the characteristic time between mergers does not take into account the relative abundances of the galaxies that are merging. We are therefore also interested in the comoving merger rate density, $\mathcal{R}$, defined following Lin et al. (2004) as

$$\mathcal{R}(> {\rm M}_\star, z) = f_{\rm m}(> {\rm M}_\star, z) n_{\rm c}({\rm M}_\star, z) C_{\rm m} \tau_{\rm m}^{-1}, \tag{3.35}$$

where $f_{\rm m}(> {\rm M}_\star, z)$ is the mass and redshift-dependent galaxy merger fraction as above, $n_{\rm c}(> {\rm M}_\star, z)$ the comoving number density for galaxies with stellar mass $> {\rm M}_\star$ and $C_{\rm m}$ the fraction of galaxies in close pairs that will merge in the timescale $\tau_{\rm m}$. The comoving number densities for galaxies with $\log_{10}({\rm M}_\star/{\rm M}_\odot) \geq$

Table 3.2: Average time between mergers for a galaxy in Gyr, Γ, for the merger fractions presented in Table 3.1. Assumed timescales are $\tau_{\rm m} = 0.29$ Gyr and $\tau_{\rm m} = 0.63$ Gyr for projected separations of $5 \leq r_{\rm p} \leq 20$ kpc and $5 \leq r_{\rm p} \leq 30$ kpc respectively, see text for details.

Γ [Gyr] - $5 \leq r_{\rm p} \leq 20$ kpc		
Redshift	$\log_{10}(M_\star/M_\odot) > 9.5$	$\log_{10}(M_\star/M_\odot) > 10$
$2.0 < z < 2.5$	4.4 ± 1.3	5.7 ± 2.2
$2.5 < z < 3.0$	3.0 ± 0.9	7.8 ± 3.1
$3.0 < z < 3.5$	4.4 ± 1.5	9.0 ± 5.4
$3.5 < z < 4.5$	4.0 ± 1.8	5.9 ± 4.2
$4.5 < z < 5.5$	24.3 ± 20.5	$25.5^{+37.3}_{-25.5}$
$5.5 < z < 6.5$	> 0.5	> 1.8

Γ [Gyr] - $5 \leq r_{\rm p} \leq 30$ kpc		
Redshift	$\log_{10}(M_\star/M_\odot) > 9.5$	$\log_{10}(M_\star/M_\odot) > 10$
$2.0 < z < 2.5$	5.0 ± 1.1	5.6 ± 2.0
$2.5 < z < 3.0$	3.1 ± 0.7	8.9 ± 2.9
$3.0 < z < 3.5$	3.4 ± 1.0	11.0 ± 4.8
$3.5 < z < 4.5$	4.1 ± 1.8	9.1 ± 5.1
$4.5 < z < 5.5$	27.5 ± 19.8	$48.8^{+64.0}_{-48.4}$
$5.5 < z < 6.5$	> 1.1	> 3.8

9.5 and $\log_{10}(M_\star/M_\odot) \geq 10$ are estimated from the same stellar mass function parametrisations used for the mass completeness weights. Specifically, those of Mortlock et al. (2014) at $z \leq 3$, Santini et al. (2012) at $3 < z < 3.5$ and from Chapter 2 at $z \geq 3.5$. Errors on the number densities are estimated by perturbing the Schechter function parameters based on their quoted errors and recalculating the integrated number density. This step is then repeated 1000 times and the lower and upper 1-σ errors are taken as the $16^{\rm th}$ and $84^{\rm th}$ percentiles.

In Figure 3.8 we show the resulting merger rate densities calculated following Equation 3.35. Plotted are the merger fractions estimated in this work and the model predictions of Lu et al. (2011) for which the comoving number densities have been calculated directly from the models (Lu, *priv. communication*). We also plot the merger rates quoted by López-Sanjuan et al. (2010) and the merger density values of Ryan et al. (2008) converted to merger rates using the same timescale ($\tau_{\rm m} = 0.29$) as used for the 20kpc estimates of this work. The estimated merger rates and corresponding errors are also shown in Table 3.3. It is worth noting that the large uncertainty at the high-mass end of the stellar mass function results in significantly larger errors for the merger rates than the corresponding

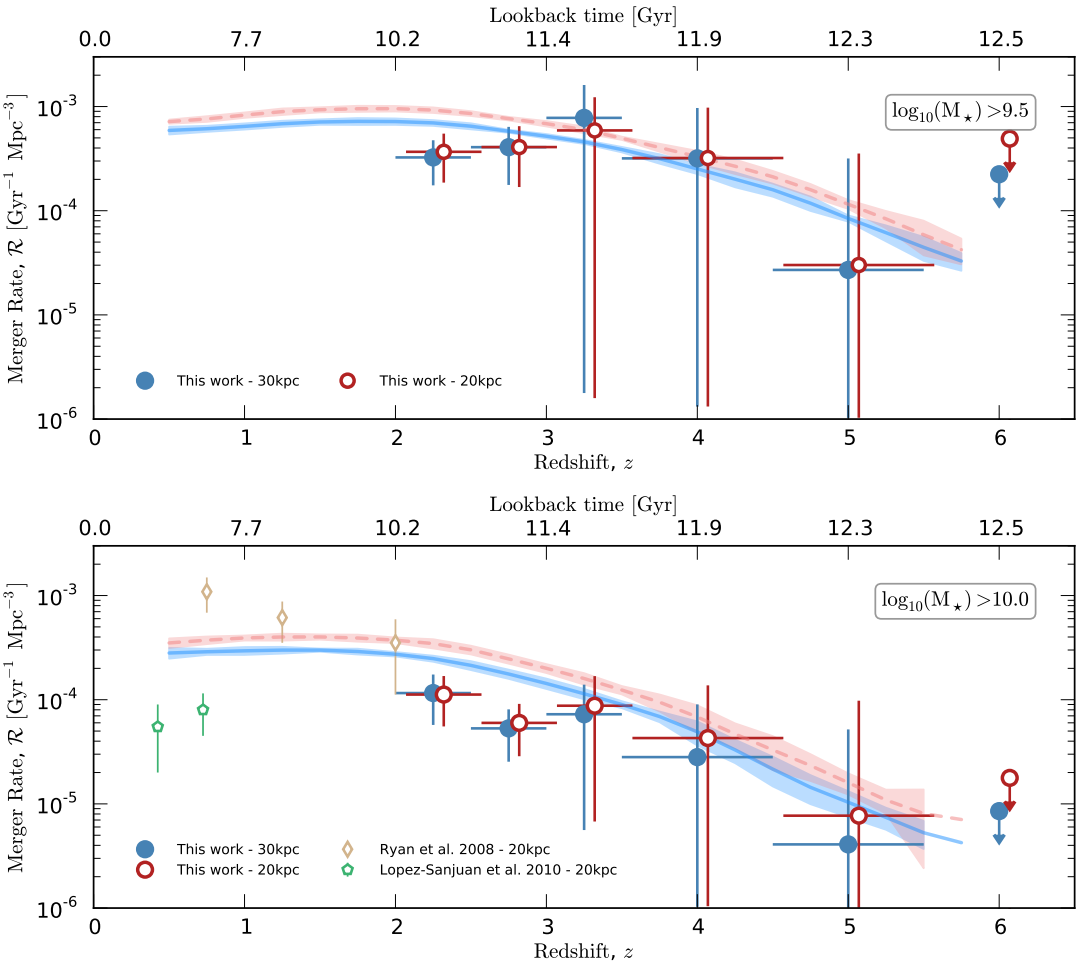

Figure 3.8: Estimated galaxy merger rates as a function of redshift for galaxies with stellar mass $\log_{10}(M_\star/M_\odot) > 9.5$ (top) and $\log_{10}(M_\star/M_\odot) > 10$ (bottom). The merger rates are calculated following Equation 3.35, assuming $\tau_m = 0.29$ and 0.64 Gyr for the 20 and 30kpc estimates respectively. Also shown are the merger rates from close pair statistics of Ryan et al. (2008) and López-Sanjuan et al. (2010). The continuous blue and dashed red lines correspond to the model predictions of Lu et al. (2011, 2014), with the shaded regions representing the Poisson noise for the model number counts.

estimates for the merger fraction.

For $\log_{10}(M_\star/M_\odot) > 10$, the merger rate gradually declines beyond $z \geq 2$, with the discrepancy between $z \sim 4$ and $z \sim 5$ less stark. For the merger rate of galaxies with $\log_{10}(M_\star/M_\odot) > 9.5$, over the whole redshift range studied in this work the merger rate also declines and is roughly consistent with the predictions of Lu et al. (2011). However, for both mass selections, when the mass completeness affected $z \sim 5$ observations are discounted the remaining observations are consistent with remaining constant between $2 \lesssim z \lesssim 4$. Given the large errors in the current observations, it is clearly difficult to draw any meaningful conclusions about the redshift evolution of the merger fraction at $z > 3$.

Table 3.3: Comoving merger rate, $\mathcal{R}$ in units of 10^{-4} Gyr^{-1} Mpc^{-3} for the merger fractions presented in Table 3.1. Assumed timescales are $\tau_{\rm m} = 0.29$ and 0.63 Gyr for projected separations of $5 \leq r_{\rm p} \leq 20$ kpc and $5 \leq r_{\rm p} \leq 30$ kpc respectively, see text for further details. Comoving number densities for the mass selected samples are calculated from the corresponding stellar mass functions as described in the text.

Merger rate, $\mathcal{R}$ [10^{-4} Gyr^{-1} Mpc^{-3}] - $5 \leq r_{\rm p} \leq 20$ kpc

Redshift	$\log_{10}(M_\star/M_\odot) > 9.5$	$\log_{10}(M_\star/M_\odot) > 10$
$2.0 < z < 2.5$	3.64 ± 1.83	3.22 ± 1.51
$2.5 < z < 3.0$	4.21 ± 2.28	4.20 ± 2.18
$3.0 < z < 3.5$	$5.36^{+6.36}_{-5.36}$	$7.07^{+8.30}_{-7.07}$
$3.5 < z < 4.5$	$3.18^{+6.61}_{-3.18}$	$3.15^{+6.55}_{-3.15}$
$4.5 < z < 5.5$	$0.28^{+4.07}_{-0.28}$	$0.25^{+3.65}_{-0.25}$
$5.5 < z < 6.5$	< 3.76	< 1.71

Merger rate, $\mathcal{R}$ [10^{-4} Gyr^{-1} Mpc^{-3}] - $5 \leq r_{\rm p} \leq 30$ kpc

Redshift	$\log_{10}(M_\star/M_\odot) > 9.5$	$\log_{10}(M_\star/M_\odot) > 10$
$2.0 < z < 2.5$	1.11 ± 0.55	1.15 ± 0.57
$2.5 < z < 3.0$	0.58 ± 0.31	0.52 ± 0.28
$3.0 < z < 3.5$	0.85 ± 0.83	0.70 ± 0.69
$3.5 < z < 4.5$	$0.43^{+1.03}_{-0.43}$	$0.28^{+0.68}_{-0.28}$
$4.5 < z < 5.5$	$0.07^{+0.82}_{-0.07}$	$0.04^{+0.43}_{-0.04}$
$5.5 < z < 6.5$	< 0.18	< 0.09

When compared to the literature values of Ryan et al. (2008) at $z \sim 2$, the merger rate density measured in this work is significantly lower at $z \sim 2.25$ (by a factor of $\approx 3\times$). Given the good agreement in the merger fractions and the identical assumed merger timescales, this discrepancy is likely due to a difference in the assumed comoving number densities. We have excluded the results of Conselice & Arnold (2009) at $z \geq 4$ in Figure 3.8 as the Lyman break selection used in that analysis make it difficult to retrospectively estimate accurate corresponding comoving number densities for the samples studied.

For the comoving merger rates predicted by the semi-analytic models, there is a small disagreement between the ≤ 20 kpc and ≤ 30 kpc close pair estimates with those for ≤ 20 kpc being $\approx 30\%$ higher. Given the large systematic uncertainty (and variation) in the merger timescales (Lotz et al., 2008, 2010b,a) this to be expected when a simplified average is used. A critical goal for future work is therefore to estimate the true merger rate within the models (i.e. directly from the merger trees) in order to test the origin of this difference and further explore the scatter and evolution of the predicted merger timescales at $z \geq 2$.

3.4.4 Minor mergers

The merger fraction and corresponding merger rate results presented in this section have been for major mergers only (defined as $\mu \geq 1/4$). This choice was primarily motivated by the expected limits on the mass completeness at the high redshift we aimed to probe, as the mass of secondary galaxies in mergers with mass ratios > 4 will typically be significantly below the mass completeness limits and thus excluded from our analysis. However, based on the estimated mass completeness levels at $z \leq 3$ in Figure 3.4, the deep CANDELS GOODS South data will clearly allow for merger fraction estimates for mass ratios up to ≥ 10 for mass selections $\log_{10}(\mathrm{M}_{\star}/\mathrm{M}_{\odot}) > 10$ and even higher for more massive samples. This wide dynamic range will should make it possible to measure the merger rate as a function of μ in future work, fully quantifying the relative contribution of mergers at different mass ratios over a crucial period in the evolution of galaxies (e.g. Bluck et al. 2012).

Based on the observed galaxy stellar mass function evolution, to first order we would expect the relative number of minor to major mergers to be greater at high redshift (for a galaxy of a given mass, the relative number of lower mass galaxies will be higher for steeper mass functions). The relative contribution of minor mergers to the stellar mass growth of massive galaxies should therefore also be greater at high redshift. For the most massive galaxies at $z \leq 3$, Ownsworth et al. (2014) estimated the inverse to be true; with the ratio of minor to major merger fuelled growth found to be *decreasing* with increasing redshift (see also Bluck et al. 2012). Even if minor mergers make only a minor contribution to the overall stellar mass growth of galaxies below $z = 3$, they are still expected to have a significant effect on the size growth of massive galaxies (Trujillo et al., 2011; Newman et al., 2012; McLure et al., 2012) during this period. Understanding how the relative contributions from different merger ratios change will provide extremely useful clues as to what processes are driving the evolution of the galaxy stellar mass function in this epoch.

3.5 Discussion

In the results presented in Section 3.4 we have shown that using the probabilistic redshift PDF pair-count method it is possible to obtain estimates of the merger fraction out to redshifts of $z \sim 4$ and potentially beyond. The major drawback based on these early results is down to the compounding effects of increasing mass incompleteness with redshift and the rapidly decreasing number density of massive galaxies at higher redshift (Duncan et al., 2014; Grazian et al., 2014).

Despite the large uncertainties, our results give us cause for optimism with regards to studying merger rates at $z \geq 2$ and into the first billion years of galaxy evolution. The inclusion of the additional 4 remaining CANDELS fields will help to reduce the existing uncertainties by significantly increasing the volume being probed and reducing the error from cosmic variance. Of particular interest will be the GOODS North field. Firstly, it will double the area of CANDELS DEEP data being studied, improving the small samples of the faint highest redshift galaxies. Secondly this field benefits from the very deep SHARDS narrowband survey (Pérez González et al., 2012), allowing for significantly improved photometric redshift accuracy. The additional larger WIDE fields of COSMOS, EGS and UDS will also be ideal for selecting the rarer high-mass galaxies at $z \sim 5$ and $z \sim 6$ required to improve the estimates available from GOODS South alone. Finally, the Frontier Fields parallels (Coe et al., 2015) will provide deep HST photometry for 6 additional blank fields with depths comparable to those of the Hubble Ultra-deep Field. These additional fields will be vital for further increasing the available samples of galaxies at $z \geq 5$.

If gas-rich major mergers play a critical role in driving AGN accretion and quasar activity (Springel et al., 2005; Hopkins et al., 2008a), linking the evolution of galaxy merger rates and AGN activity through cosmic history is clearly of key importance. Based on the declining merger rates calculated in this work, there is certainly no strong evidence against a correlation between the quasar or AGN luminosity density and the merger rate density. Given the preliminary nature of these results and the scarcity of directly comparable merger rate estimates at $z < 2$ (i.e. in mass selection) we are wary of trying to parametrise our results

for such a comparison. As discussed in Conselice (2014), parametrisations of the merger history at $z < 3$ can be systematically affected by the very low redshift ($z \sim 0$) anchor point.

However, such an analysis will soon be much more viable. In combination with a forthcoming study of galaxy merger fractions at $z < 3$ in the deep ground-based fields of UltraVISTA (McCracken et al., 2012), UDS (Lawrence et al., 2007) and VIDEO (Jarvis et al., 2012) (Mundy et al. *in prep*), the close pair merger analysis of CANDELS will make it possible to study the full assembly of massive galaxies over almost the complete cosmic history.

With the improved merger fraction estimates measured for the full CANDELS dataset, it is likely that the limiting uncertainty on the fundamental physical properties such as the merger rate density will actually be the merger timescales and the constraints on the true number densities of the samples of interest. As well as reducing the statistical uncertainties in the merger fraction estimates, the wealth of additional ground and space-based data available will be crucial in providing better constraints on the galaxy stellar mass function at high redshifts.

With the new generation of hydrodynamical simulations over cosmological volumes (e.g. Illustris, Vogelsberger et al. 2014; EAGLE, Schaye et al. 2014), it is also now possible to study the variation and evolution of merger timescales for large samples of mergers. Not only will representative sample of galaxy properties and environments provide key insights into the the systematic variation of merger timescales, the ability to perform identical analyses to synthetic images of these simulations (Torrey et al., 2015) will greatly improve our understanding of the systematics errors and biases involved.

3.6 Summary

In this chapter we have estimated the major merger fraction of galaxies at $z \geq 2$ in the CANDELS GOODS South field (Guo et al., 2013) by analysing the close pair statistics. The close pair method used is based on that presented by López-Sanjuan et al. (2015) and makes use of the full photometric redshift probability

distribution to account for line-of-sight separation in the absence of high-quality spectroscopic data.

The merger fractions based on close pairs were measured for projected separations of $5 \leq r_{\rm p} \leq 20$ kpc and $5 \leq r_{\rm p} \leq 30$ kpc. For a mass selection of $\log_{10}(\mathrm{M}_{\star}/\mathrm{M}_{\odot}) > 9.5$ and merger ratios of 1:4 or less ($\mu > 1/4$) the merger fraction is approximately constant between $z \approx 2.25$ and $z \sim 4$ with a potential peak at $z \approx 3$. Similarly, for a mass selection of $\log_{10}(\mathrm{M}_{\star}/\mathrm{M}_{\odot}) > 10$ the merger fraction is consistent with constant or in slight decline of this same redshift range. For both mass selections the observed merger fraction rapidly declines at $z \sim 5$, something which we believe is most likely due to the effects of the mass-completeness limit applied to the analysis. Future work over wider survey areas should produce more statistically significant high mass samples at these redshifts and allow us to better investigate the nature of this drop.

Assuming merger timescales from simulations of Lotz et al. (2010a), we estimate the average time between mergers per galaxy (Γ, in Gyr) and the comoving merger rate density ($\mathcal{R}$, Gyr^{-1} Mpc^{-3}) for our observed merger fractions. The estimated Γ at $2 \lesssim z \lesssim 4$ (where our merger fractions are reasonably well constrained) are consistent with a constant ≈ 4 Gyr for $\log_{10}(\mathrm{M}_{\star}/\mathrm{M}_{\odot}) > 9.5$ and ≈ 8 Gyr for $\log_{10}(\mathrm{M}_{\star}/\mathrm{M}_{\odot}) > 9.5$. Relative to the on-going star-formation within galaxies over this redshift range, this low merger rate means that the galaxy growth through star-formation is of order $10\times$ greater than the growth through major mergers.

For both mass selections, the estimated comoving merger rate density, $\mathcal{R}$, gradually declines at $z \geq 2$. However, due to the large uncertainties in the high-mass end of the galaxy stellar mass function (and hence the estimated number densities) the errors on $\mathcal{R}$ are too large to draw any meaningful conclusions with regards to the mechanisms of galaxy assembly.

Given the limited dataset on which we have tested the redshift PDF merger methodology, we are confident that many of the existing uncertainties can be greatly reduced with the inclusion and analysis of existing available data. With careful analysis, it should soon be possible to build an observational picture of the assembly history of mass galaxies.

Chapter 4

Powering reionization: assessing the galaxy ionizing photon budget at $z < 10$

4.1 Introduction

At the present day, the intergalactic and interstellar medium (IGM,ISM) are known to be predominantly ionized. However, following recombination at $z \approx 1100$, the baryon content of the Universe was mostly neutral. At some point in the history of the Universe, the IGM underwent a transition from this neutral phase to the ionized medium we see today, a period known as the epoch of reionization (EoR hereafter). The strongest constraints on when reionization occurred are set by observations of the Gunn-Peterson trough of distant quasars (Fan et al., 2006), which indicate that by $z \approx 5.5$, the Universe was mostly ionized (with neutral fractions $\sim 10^{-4}$).

Additionally, measurements of the total optical depth of electrons to the surface of last scattering implies that reionization should be occurring at higher redshift, towards $z \approx 10$, for models of instantaneous reionization (Hinshaw et al., 2013; Bennett et al., 2013). However, critical outstanding questions still remain. Firstly, when did the intergalactic hydrogen and helium complete reionization?

And secondly, what were the sources of ionizing photons that powered the reionization process? Was it predominantly powered by star-forming galaxies or by active galactic nuclei/quasars?

For hydrogen reionization – with its earlier completion – the rapid decline in the quasar luminosity function at high redshift (Willott et al., 2010; Fontanot et al., 2012, 2014) does suggest that star-forming galaxies are the most likely candidates for completing the bulk of reionization by $z \sim 6$. The contribution from faint AGN could still however make a significant contribution to the ionizing emissivity at $z > 4$ (Giallongo et al., 2015). Based on the optical depth constraints set by WMAP (Hinshaw et al., 2013) and either observed IGM emissivities at lower redshift (Kuhlen & Faucher-Giguère, 2012; Robertson et al., 2013; Becker & Bolton, 2013), or emissivities predicted by simulations (Ciardi et al., 2012), several studies have drawn the same conclusion that faint galaxies from below the current detection limits and/or an increasing ionizing 'efficiency' at higher redshift is required. Even with the lower optical depth measurement now favoured by the recent Planck analysis (Planck Collaboration et al., 2015), such assumptions are essentially still required to satisfy these criteria (Robertson et al., 2015).

One of the possible mechanisms for this increasing ionizing efficiency is an evolution in the fraction of the ionizing photons able to escape their host galaxy and ionize the surrounding IGM – known as the escape fraction ($f_{\rm esc}$). There have been several studies designed to understand this issue, but there are still large uncertainties in what the escape fraction for galaxies is and how it evolves with redshift and other galaxy properties. In a study of $z \sim 1.3$ galaxies, Siana et al. (2010) searched for Lyman-continuum photons from star forming galaxies, although no systems were detected. After correcting for the Lyman-break and IGM attenuation the limit placed on the escape fraction is $f_{\rm esc} < 0.02$ after stacking all sources. Bridge et al. (2010b) find an even lower limit of $f_{\rm esc} < 0.01$ using slitless spectroscopy at $z \sim 0.7$, although one AGN in their sample is detected. However, higher escape fractions of $\sim 5\%$ to $\sim 20 - 30\%$ have been measured for galaxies at $z \sim 3$ (Shapley et al., 2006; Iwata et al., 2009; Vanzella et al., 2010; Nestor et al., 2013), consistent with the relatively high $f_{\rm esc} \sim 0.2$ expected

from IGM recombination rates determined from Lyα forests (Bolton & Haehnelt, 2007). Furthermore, the average $f_{\rm esc}$ for galaxies at $z \sim 3$ may be significantly higher than the existing measurements due to the selection biases introduced by the Lyman-break technique (Cooke et al., 2014).

It is important to bear in mind that the property that is fundamental to studies of reionization is the total number of ionizing photons that are available to ionize the intergalactic medium surrounding galaxies. Hence, while the escape fraction is a critical parameter for reionization, it must be measured or constrained in conjunction with the underlying continuum emission to which it applies. For example, an increase in $f_{\rm esc}$ may not have an effect on reionization if it is accompanied by a reduction in the intrinsic number of ionizing photons being produced.

As shown in Robertson et al. (2013) (see also Leitherer et al. 1999), the number of ionizing photons produced per unit UV luminosity emitted (e.g. $L_{1500\text{Å}}$) can vary significantly as a function of the stellar population parameters such as age, metallicity and dust extinction. Thankfully, evolution or variation among the galaxy population in these parameters will not only influence the production of ionizing photons but will have an effect on other observable properties such as the UV continuum slope (β, Calzetti et al. 1994). With the advent of ultra-deep near-infrared imaging surveys such as the UDF12 (Koekemoer et al., 2013) and CANDELS (Grogin et al., 2011; Koekemoer et al., 2011) surveys, observations of the UV continuum slope extending deep into the epoch of reionization are now available. Furthermore, there is now strong evidence for an evolution in β as a function of both galaxy luminosity and redshift out to $z \sim 8$ (Bouwens et al., 2014; Rogers et al., 2014).

In this chapter we use the latest observations of β spanning the EoR combined with SED modelling, incorporating the physically motivated escape mechanisms to explore what constraints on the key emissivity coefficients are currently available. We also explore the consequences these constraints may have on the EoR for current observations of the star-formation rates in this epoch. In addition to the observations of in-situ star-formation through the UV luminosity functions, we also investigate whether recent measurements of the galaxy stellar mass func-

tion and stellar mass density at high redshift (Duncan et al., 2014; Grazian et al., 2014) can provide additional useful constraints on the star-formation rates during EoR (Stark et al., 2007; González et al., 2010).

In Section 4.2, we outline the physics and critical parameters required to link the evolution of the neutral hydrogen fraction to the production of ionizing photons. We also explore plausible physical mechanisms for the escape of Lyman continuum photons from galaxies, outlining the models explored throughout the chapter. We then review the current literature constraints on the UV continuum slope, β, both as a function of redshift and galaxy luminosity. Next, in Section 4.3, we explore how the escape fraction, dust extinction and other stellar population parameters affect the observed β and the coefficients relating ionizing photon production rates to observed star-formation rates and UV luminosities. In Section 4.4, we apply these coefficients to a range of existing observations, exploring the predicted ionizing emissivity throughout the epoch of reionization for both constant and redshift-dependent conversions. We then discuss how the varying assumptions and proposed relations would impact the ionizing photon budget consistent with current observations before outlining the future prospects for improving these constraints in Section 4.5. Finally, we summarise our findings and conclusions in Section 4.6.

Throughout this chapter, all magnitudes are quoted in the AB system (Oke & Gunn, 1983). We also assume a Λ-CDM cosmology with $H_0 = 70$ kms^{-1}Mpc^{-1}, $\Omega_m = 0.3$ and $\Omega_\Lambda = 0.7$. Quoted observables (e.g. luminosity density) are expressed as actual values assuming this cosmology. We note that luminosity and luminosity based properties such as stellar masses and star-formation rates scales as h^{-2}, whilst densities scale as h^3.

4.2 Linking reionization with observations

4.2.1 The ionizing emissivity

The currently accepted theoretical picture of the epoch of reionization, as initially described by Madau et al. (1999), outlines the competing physical processes of ionization of neutral hydrogen by Lyman continuum photons and recombination of free electrons and protons. The transition from a neutral Universe to a fully ionized one can be described by the differential equation:

$$\dot{Q}_{\rm HII} = \frac{\dot{N}_{\rm ion}}{\langle n_{\rm H} \rangle} - \frac{Q_{\rm HII}}{\langle t_{\rm rec} \rangle} \tag{4.1}$$

where $Q_{\rm HII}$ is the dimensionless filling factor of ionized hydrogen (such that $Q_{\rm HII} = 1$ for a completely ionized Universe) and $\dot{N}_{\rm ion}$ is the comoving ionizing photon production rate ($\rm s^{-1}$ $\rm Mpc^{-3}$) or ionizing emissivity. The comoving density of hydrogen atoms, $\langle n_{\rm H} \rangle$, and average recombination time $\langle t_{\rm rec} \rangle$ are redshift-dependent and are dependent on the primordial Helium abundance, IGM temperature and crucially the inhomogeneity of the IGM, parametrised as the clumping factor $C_{\rm HII} \equiv \langle n_{\rm H}^2 \rangle / \langle n_{\rm H} \rangle^2$(Pawlik et al., 2009). We refer the reader to Madau et al. (1999), Kuhlen & Faucher-Giguère (2012) and Robertson et al. (2010, 2013) for full details on these parameters and the assumptions associated.

In this chapter we will concentrate on $\dot{N}_{\rm ion}$ and the production of Lyman continuum photons by star-forming galaxies. The link between the observable properties of galaxies and the ionizing photon rate, $\dot{N}_{\rm ion}$ can be parametrised as

$$\dot{N}_{\rm ion} = f_{\rm esc} \xi_{\rm ion} \rho_{\rm UV} \tag{4.2}$$

following the notation of Robertson et al. (2013) (R13 hereafter), where $\rho_{\rm UV}$ is the observed UV (1500Å) luminosity density (in erg $\rm s^{-1}$ $\rm Hz^{-1}$ $\rm Mpc^{-3}$), $\xi_{\rm ion}$ the number of ionizing photons produced per unit UV luminosity ($\rm erg^{-1}$ Hz) and $f_{\rm esc}$ the fraction of those photons that escape a host galaxy into the surrounding IGM. Alternatively, $\dot{N}_{\rm ion}$ can be considered in terms of the star-formation rate density, $\rho_{\rm SFR}$ ($\rm M_\odot$ $\rm yr^{-1}$ $\rm Mpc^{-3}$),

$$\dot{N}_{\rm ion} = f_{\rm esc} \kappa_{\rm ion} \rho_{\rm SFR} \tag{4.3}$$

where $\kappa_{\rm ion}$ ($\rm s^{-1}$ $\rm M_{\odot}^{-1}$ yr) is the ionizing photon production-rate per unit star-formation (ζ_Q in the notation used in Robertson et al. (2010)). In addition to observing $\rho_{\rm UV}$ or $\rho_{\rm SFR}$ during the EoR, accurately knowing $f_{\rm esc}$, $\xi_{\rm ion}$ and $\kappa_{\rm ion}$ is therefore critical to estimating the total ionizing emissivity independent of how well we are able to measure the UV luminosity or star-formation rate densities.

As the production of *LyC* photons is dominated by young UV-bright stars, the rate of ionizing photons is therefore highly dependent on the age of the underlying stellar population and the recent star-formation within the galaxy population. Physically motivated values of $\xi_{\rm ion}$ (or its equivalent coefficient in other notation) can be estimated from stellar population models based on plausible assumptions on the properties of high-redshift galaxies (Bolton & Haehnelt, 2007; Ouchi et al., 2009; Kuhlen & Faucher-Giguère, 2012).

However, with observations of the UV continuum slope, β (Calzetti et al., 1994), now extending deep into the epoch of reionization, limited spectral information is now available for a large sample of galaxies. Despite the many degeneracies in β (see later discussion in Section 4.3), it is now possible to place some constraints on whether the assumptions made are plausible. In R13, values of $\xi_{\rm ion}$ are explored for a range of stellar population parameters relative to the β observations of Dunlop et al. (2013). Based on the range of values consistent with the observed values of $\beta \approx -2$, Robertson et al. choose a physically motivated value of $\log_{10} \xi_{\rm ion} = 25.2$.

Typically, a constant $f_{\rm esc}$ is applied to all galaxies in addition to the estimated or assumed values of $\xi_{\rm ion}/\kappa_{\rm ion}$ (Ouchi et al., 2009; Finkelstein et al., 2012; Robertson et al., 2013), motivated in part by our lack of understanding of the redshift or halo mass dependence of $f_{\rm esc}$. However, applying a constant $f_{\rm esc}$ does not take into account exactly how the Lyman continuum photons escape the galaxy, what effect the different escape mechanism might have on the observed galaxy colours, and how that might alter the assumed $\xi_{\rm ion}/\kappa_{\rm ion}$ based on β.

4.2.2 Mechanisms for Lyman continuum escape

In Zackrisson et al. (2013), detailed SSP and photo-dissociation models were used to explore how future observations of β and Hα equivalent-width with the James Webb Space Telescope (JWST) could be used to constrain the escape fraction for two different Lyman continuum escape mechanisms (see Fig. 8 of Zackrisson et al. (2013)). However, it may already be possible to rule out significant parts of the $f_{\rm esc}$ and dust extinction parameter space using current constraints on β and other galaxy properties. To estimate the existing constraints on $f_{\rm esc}$, $\xi_{\rm ion}$, $\kappa_{\rm ion}$ and their respective products, we combine the approaches of Zackrisson et al. (2013) and Robertson et al. (2010, 2013). To do this, we model β, $\xi_{\rm ion}$ and $\kappa_{\rm ion}$ as a function of $f_{\rm esc}$ for the two models of Zackrisson et al. (2013). The components and geometry of these two models are illustrated in Fig. 4.1.

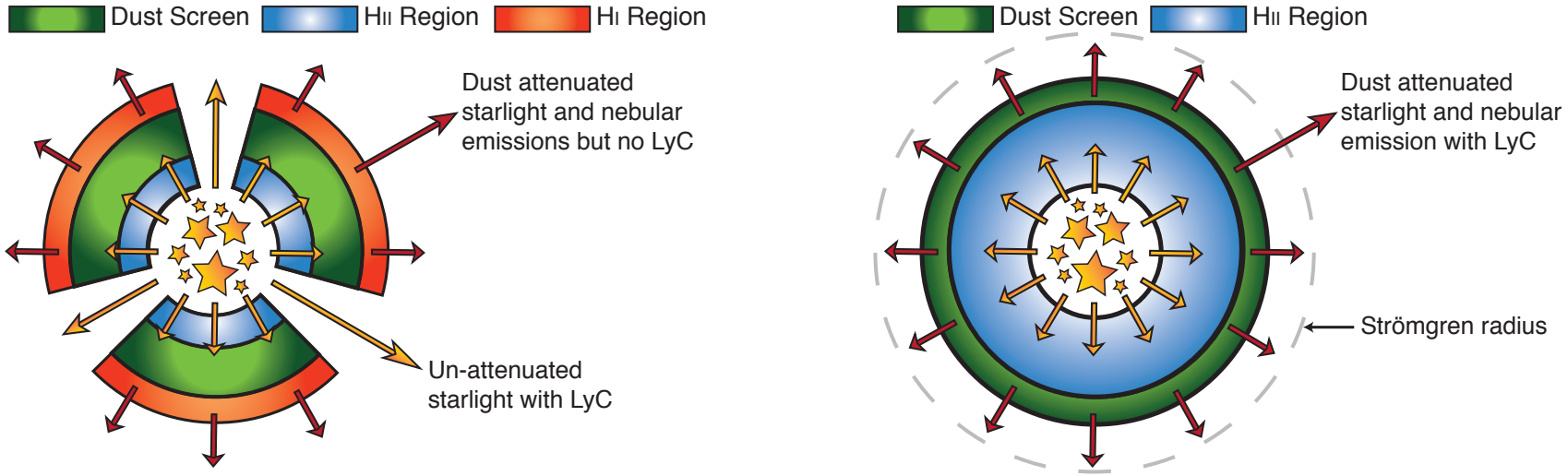

Figure 4.1: Schematic cartoon illustrations of the Lyman continuum escape mechanisms outlined in Section 4.2. For both models, the stars represent a central galaxy surrounded by a HII ionization region, dust is distributed in an outer dust-screen. Left: An ionization bounded nebula with holes (sometimes referred to as the 'picket fence model') in which LyC escapes through holes in the ISM. Right: a density bounded nebula where LyC is able to escape due to the incomplete Strömgren sphere formed when the galaxy depletes its supply of neutral hydrogen.

In the first model, model A hereafter (Fig. 4.1 left) and dubbed 'ionization bounded nebula with holes' by Zackrisson et al., Lyman continuum photons along with unattenuated starlight are able to escape through low-density holes in the neutral ISM. In this model, the escape fraction is determined by the total covering fraction of the neutral ISM. Under the assumption that these holes are small and evenly distributed, the observed galaxy SED (averaged across the galaxy as in the case of photometry) would then be a combination of the unattenuated starlight from holes and the dust reddened starlight and nebular emission from the HI enshrouded regions.

A second model, model B hereafter (Fig. 4.1 right) corresponds to the 'density-bounded nebula' of Zackrisson et al. (2013). This model could occur when the local supply of HI is exhausted before a complete Strömgren sphere[1] can form, allowing Lyman continuum photons to escape into the surrounding ISM. The fraction of LyC photons which can escape the nebular region is determined by the fraction of the full Strömgren radius at which the nebular region is truncated. The total escape fraction is then also dependent on the optical depth of the surrounding dust screen. Of these two mechanisms, the former (Model A: ionization bounded nebula with holes) is the model that most closely represents the physics predicted by full radiation hydrodynamical models of dwarf galaxies.

In Wise & Cen (2009), it was found that Lyman continuum radiation preferentially escaped through channels with low column densities, produced by radiative feedback from massive stars. The resulting distribution of LyC escape fraction within a galaxy is highly anisotropic and varies significantly between different orientations. Evidence for such an anisotropic escape mechanism has also been found recently by Zastrow et al. (2013), who find optically thin ionization cones through which LyC can escape in nearby dwarf starbursts. Similarly, Borthakur et al. (2014) find a potential high-redshift galaxy analog at $z \sim 0.2$ with evidence for LyC leakage through holes in the surrounding neutral gas with an escape

[1] A Strömgren sphere is a sphere of ionized hydrogen, HII, surrounding a young star (or cluster of stars in this scenario) that is ionizing the surrounding medium. The volume of the sphere is determined by the corresponding Strömgren radius, that radius at which the ionizing flux from the central star(s) is balanced by recombinations in the ionized gas (Strömgren, 1939).

fraction as high as $f_{\rm esc} \approx 0.2$ (21%).

However, this value represents the optimum case in which there is no dust in or around the low-density channels (corresponding to Model A). For the same system, when Borthakur et al. (2014) include dust in the low-density channels, the corresponding total LyC escape fraction is reduced to $\approx 1\%$. The two models explored in this work represent the two extremes of how dust extinction will effect the escaping Lyman continuum for toy models such as these, the dust-included estimates of Borthakur et al. (2014) therefore represent a system which lies somewhere between Models A and B.

A potential third mechanism for Lyman continuum escape was posited by Conroy & Kratter (2012), whereby 'runaway' OB stars which have traveled outside the galaxy centre can contribute a significant amount to the LyC emitted into the surrounding IGM. For high-redshift galaxies with significantly smaller radii than local galaxies, massive stars with large velocities could venture up to 1 kpc away from their initial origin into regions with low column density. Conroy & Kratter (2012) estimate that these stars could in fact contribute $50-90\%$ of the escaping ionizing radiation. In contrast, recent work by Kimm & Cen (2014) finds that when runaway stars are included into their models of Lyman continuum escape, the time average escape fraction only increases by $\sim 20\%$. Given the additional complications in modelling the relevant observational properties and their relatively small effect, we neglect the contribution of runaway stars in the subsequent analysis.

In Section 4.3, we describe how we model both the observable (β) and unobservable ($\xi_{\rm ion}$,$\kappa_{\rm ion}$) properties for both model A and model B. But first, we examine the existing observations on the evolution of β into the epoch of reionization.

4.2.3 Observed UV Continuum Slopes

In Fig. 4.2, we show a compilation of recent results in the literature on the observed UV slope, β, as a function of both redshift and rest-frame UV magnitude, $M_{\rm UV}$ (Dunlop et al., 2011, 2013; Wilkins et al., 2011; Finkelstein et al., 2011;

Table 4.1: Bayesian Information Criterion (BIC) for the assumption of either a colour-magnitude relation or a constant β, ΔBIC is defined as $\mathrm{BIC_{const}} - \mathrm{BIC_{slope}}$. For each dataset, we also show the best-fit model parameters and corresponding 1-σ errors for the model with lowest BIC.

Redshift	$\mathrm{BIC_{slope}}$	$\mathrm{BIC_{const}}$	ΔBIC
$z \sim 7$	35.2 [a]	45.0	9.8
$z \sim 8$	5.8	4.2 [b]	-1.6

[a] $\beta(M_{\mathrm{UV}}) = -2.05 \pm 0.04 - 0.13 \pm 0.04 \times (M_{\mathrm{UV}} + 19.5)$
[b] $\beta = -2.00 \pm 0.11$

Bouwens et al., 2014; Duncan et al., 2014; Rogers et al., 2014). Disagreement between past observations on the existence or steepness of a color-magnitude relation (cf. Dunlop et al. (2011) and Bouwens et al. (2011a)) have recently been reconciled by Bouwens et al. (2014) after addressing systematics in the selection and photometry between different studies. Bouwens et al. (2014) find a clear colour-magnitude relation (CMR) with bluer UV-slopes at lower luminosities, the relation is also found to evolve with bluer β's at high redshift (blue circles in Fig. 4.2). The existence of a strong colour-magnitude relation has also been confirmed by Rogers et al. (2014) at $z \sim 5$ for a sample of even greater dynamic range (pink diamonds in Fig. 4.2), measuring a CMR slope and intercept within error of the measured $z \sim 5$ values of Bouwens et al. (2014).

While the evidence for a colour-magnitude relation at $z \leq 6$ is quite strong, during the crucial period of reionization at $z \sim 7$ the limited dynamic range and samples sizes of existing observations means that similar conclusions are less obvious. Given the importance of this period in reionization and also the importance the assumption of a colour-magnitude relation has on the conclusions of this study, it is pertinent to critically assess which model is statistically favoured by the existing observations. To assess the statistical evidence for a colour-magnitude relation at $z \sim 7$, we calculate the Bayesian information criterion (BIC, Schwarz 1978), defined as

$$BIC = -2 \ln \mathcal{L}_{\mathrm{max}} + k \ln N, \tag{4.4}$$

where $\mathcal{L}_{\mathrm{max}}$ is the maximised value of the likelihood function for the model in question ($-2 \ln \mathcal{L}_{\mathrm{max}} \equiv \chi^2_{\mathrm{min}}$ under the assumption of gaussian errors), k the number of parameters in said model and N the number of data-points being fitted. Values of ΔBIC greater than 2 are positive evidence against the model with higher

BIC, whilst values greater than 6 (10) are strong (very strong) evidence against. The model fits were performed using the MCMC implementation of Foreman-Mackey et al. (2013) assuming a flat-prior. The resulting BIC for the constant β and linear $M_{\rm UV}$-dependent models are shown in Table 4.1. For the $z \sim 7$ observations, a color-magnitude relation is strongly favoured over a constant β with a best-fit model of $-2.05 \pm 0.04 - 0.13 \pm 0.04(M_{\rm UV} + 19.5)$. At $z \sim 8$, while the assumption of a constant β provides a better fit ($\beta = -2.00 \pm 0.11$), no model is strongly preferred over the other.

Past studies into the ionizing emissivity during the EoR have often used a fixed average $\beta = -2$ to motivate or constrain $\xi_{\rm ion}$, e.g. Bolton & Haehnelt (2007), Ouchi et al. (2009), Robertson et al. (2010, 2013) and Kuhlen & Faucher-Giguère (2012). Although we now find good evidence for a colour-magnitude relation during this epoch, it does not necessarily make the assumption of a constant β invalid, as we must take into account the colours of the galaxies that dominate the SFR or luminosity density. To estimate an average β which takes into account the corresponding number densities and galaxy luminosities, we calculate $\langle\beta\rangle_{\rho_{\rm UV}}$, the average β weighted by the contribution to the total UV luminosity density:

$$\langle\beta\rangle_{\rho_{\rm UV}} = \frac{\int_{L_{\rm min}}^{\infty} L_{\rm UV}(m) \times \phi(m) \times \langle\beta\rangle\,(m)}{\int_{L_{\rm min}}^{\infty} L_{\rm UV}(m) \times \phi(m)} \tag{4.5}$$

where $L_{\rm UV}(m)$, $\phi(m)$ and $\langle\beta\rangle\,(m)$ are the luminosity, number density and average β at the rest-frame UV magnitude, m, respectively. We choose a lower limit of $L_{\rm UV} \equiv M_{\rm UV} = -17$, corresponding to the approximate limiting magnitude of the deepest surveys at $z \geq 6$. For the discrete bins in which $\langle\beta\rangle\,(m)$ is calculated, $\langle\beta\rangle_m$, this becomes a sum over the bins of absolute magnitude, k, brighter than our lower limit $M_{\rm UV} = -17$:

$$\langle\beta\rangle_{\rho_{\rm UV}} = \frac{\sum_k L_{{\rm UV},k} \times \phi_k \times \langle\beta\rangle_k}{\sum_k L_{{\rm UV},k} \times \phi_k.} \tag{4.6}$$

The number density for a given rest-frame magnitude bin, ϕ_k, is calculated from the best-fitting UV luminosity functions of Bouwens et al. (2015b) at the corresponding redshift. We use the same luminosity function at each redshift for all of the observations for consistency. We note that given the relatively good agreement between estimates given their errors, the use of differing luminosity function estimates would have minimal effect on the calculated values.

Table 4.2: Bayesian Information Criterion (BIC) for the assumption of a redshift-dependent or constant $\langle\beta\rangle_{\rho_{\rm UV}}$, ΔBIC is defined as $\mathrm{BIC}_{\rm const} - \mathrm{BIC}_z$. For each dataset, we also show the best-fit model parameters and corresponding 1-σ errors for the model with lowest BIC.

Redshift range	BIC_z	$\mathrm{BIC}_{\rm const}$	ΔBIC
$4 \lesssim z \lesssim 8$	44.0 [a]	76.9	32.8
$5 \lesssim z \lesssim 8$	41.0 [b]	46.2	5.2

[a] $\langle\beta\rangle_{\rho_{\rm UV}}(z) = -1.59 \pm 0.05 - 0.07 \pm 0.01 \times z$.
[b] $\langle\beta\rangle_{\rho_{\rm UV}}(z) = -1.61 \pm 0.12 - 0.07 \pm 0.02 \times z$.

We estimate errors on $\langle\beta\rangle_{\rho_{\rm UV}}$ through a simple Monte Carlo simulation, whereby $\langle\beta\rangle_m$ and the best-fitting Schechter (1976) parameters used to calculate ϕ_m are perturbed by the quoted errors (making use of the full covariance measured by Bouwens et al. 2015b), this is repeated 10^4 times. $\langle\beta\rangle_{\rho_{\rm UV}}$ and error are then taken as the median and 1σ range of the resulting distribution.

Fig. 4.3 shows the calculated $\langle\beta\rangle_{\rho_{\rm UV}}$ and corresponding errors for each of the samples shown in Fig. 4.2. Overall, we can see that $\beta \approx -2$ is still a valid choice for a fiducial value of β during the epoch of reionization ($z > 6$) based on all of the existing observations. However, for several of the sets of observations there is evidence for a potential evolution at $z < 7$ (Wilkins et al., 2011; Finkelstein et al., 2012; Bouwens et al., 2014; Duncan et al., 2014).

To determine whether there is statistical evidence for a redshift evolution in $\langle\beta\rangle_{\rho_{\rm UV}}$, we again calculate the corresponding Bayesian information criteria to assess the relative merits of each model, assuming a simple linear evolution for the redshift-dependent model. The resulting BIC and ΔBIC are listed in Table 4.2. Based on the observations in the redshift range $4 \lesssim z \lesssim 8$, there is very strong evidence for a redshift-dependent $\langle\beta\rangle_{\rho_{\rm UV}}$ over one that is constant. Because the model fits may be dominated by the $z \sim 4$ observations and their significantly smaller errors, we also calculate the fits using only the $5 \lesssim z \lesssim 8$ data. At $z \gtrsim 5$, the collective observations do still favour redshift evolution, but the statistical significance is notably reduced.

Throughout this work we choose to use the β observations of Bouwens et al. (2014) for both β vs $M_{\rm UV}$ and $\langle\beta\rangle_{\rm UV}$ as the basis of our analysis. This choice is motivated by the fact that these observations represent the largest samples

studied (both in number and dynamic range) and due to the careful minimisation of the potential systematic errors are likely the least-biased observations. For this set of observations, there is strong evidence for evolution in $\langle\beta\rangle_{\rm UV}$ at $z < 7$. Specifically, from $z \sim 4$ to $z \sim 7$, $\langle\beta\rangle_{\rm UV}$ steepens considerably from -1.9 ± 0.02 to -2.21 ± 0.14. Parametrising the Bouwens et al. (2014) observations with a simple linear relation, we find:

$$\langle\beta\rangle_{\rho_{\rm UV}}(z) = -1.52 \pm 0.11 - (0.09 \pm 0.02) \times z. \tag{4.7}$$

Based on this fit we predict a $\langle\beta\rangle_{\rho_{\rm UV}} = -2.24$ for $z \sim 8$. Whilst this is significantly bluer than that based on the existing observations at $z \sim 8$, it is comparable to the average β measured for fainter galaxies in the lower redshift samples and represents a reasonable extrapolation. We note that at $z \approx 8$, the $\langle\beta\rangle_{\rho_{\rm UV}}$ changes significantly depending on the choice of average due to the significantly smaller samples observable and large scatter in the faintest bin. For example, using the bi-weight means recommended by Bouwens et al. (2014), $\langle\beta\rangle_{\rho_{\rm UV}} = -1.74$ based on their observations. Re-calculating using the inverse-weighted means of this same sample gives $\langle\beta\rangle_{\rho_{\rm UV}} = -2.1$, in better agreement with the observed trend at $z < 8$.

While there is now good agreement on the existence and slope of the colour-magnitude relation between independent studies (cf. Bouwens et al. 2014 and Rogers et al. 2014), what is less well understood is the intrinsic scatter in the CMR and whether it is luminosity dependent. Currently, the most extensive study of the intrinsic scatter is that of Rogers et al. (2014), who found that the intrinsic scatter in β is significantly larger for bright galaxies. They also find an apparent lower limit (25th percentile) of $\beta = -2.1$ that varies little with galaxy luminosity whilst the corresponding 75th percentiles increase significantly from fainter to brighter galaxies. Such a scenario implies that galaxies with $\beta \leq -2.5$ should be extremely rare at high-redshift, even though such galaxies are observed locally and at intermediate redshifts (Stark et al., 2014). Without a better understanding of the causes of the intrinsic scatter in β and the underlying stellar populations it is difficult to predict the expected numbers of such galaxies during this epoch.

Rogers et al. interpret the intrinsic scatter as consistent with two simple scenarios: 1) the scatter is due to galaxy orientation, or 2) that brighter galaxies have more stochastic star-formation histories and the β variation is a result of observing galaxies at different points in the duty cycle of star-formation. However, this second scenario is contrary to the theoretical predictions of Dayal et al. (2013), whereby fainter low-mass galaxies have more stochastic star-formation histories due to the greater effect of feedback shutting down star-formation in low-mass haloes.

After the discovery that high-redshift galaxies exhibit significant UV emission lines by Stark et al. (2015) (specifically CIII] at 1909Å), it is worth asking if the presence of such far-UV emission lines can systematically affect measurements of the UV slope to the same degree which optical emission lines can affect age estimates and stellar masses. In Stark et al. (2014), the authors find that the fitting of β is not affected by the presence of UV emission lines in a sample of young low-mass galaxies at $z \sim 2$. The same is true for galaxies out to $z \lesssim 6$, where β is typically measured by fitting a power-law to three or more filters (Bouwens et al., 2014). However, at $z \geq 7$ where β must be measured using a single colour, the effect of UV emission line contamination in one of the filters is more significant. For a CIII] equivalent width of 13.5Å (the highest observed in the Stark et al. (2014) sample at $z \sim 2$) could result in a measured β which is too red by $\Delta\beta \approx 0.18$ relative to the intrinsic slope based on the method outlined in Section 4.3.

Given the limited samples of $z \gtrsim 6$ galaxies with UV emission line detections, fully quantifying the effects of the emission line contamination on β observations is not possible at this time. As such, in this work we do not include UV emission lines in our simulated SEDs or attempt to correct for their effects on the observed βs in Fig. 4.3. We do caution that despite the significant improvement on β measurements at high redshift, there may still be unquantified systematics when interpreting the UV slope during the EoR.

4.3 Modelling β, ξ_{ion} and κ_{ion}

To model the apparent β's and corresponding emissivity coefficients for our two Lyman continuum escape models, we make use of composite stellar population models from Bruzual & Charlot (2003) (BC03). Using a stellar population synthesis code, we are able to calculate the full spectral energy distribution for a stellar population of the desired age, star-formation history, metallicity and dust extinction. Our code allows for any single-parameter star-formation history (e.g. exponential decline, power-law, truncated or 'delayed' star-formation models), and a range of dust extinction models. The models also allow for the inclusion of nebular emission (both line and continuum emission) proportional to the LyC photon rate, full details of which can be found in Chapter 2.

For each resulting SED with known star-formation rate (SFR), we calculate the UV luminosity by convolving the SED with a top-hat filter of width 100Å centred around 1500Å, as is standard practice for such studies (e.g. Finkelstein et al. 2012, McLure et al. 2013). To measure β, each SED is redshifted to $z \sim 7$ and convolved with the WFC3 F125W and F160W filter responses (hereafter J_{125} and H_{160} respectively). We then calculate β as:

$$\beta = 4.43(J_{125} - H_{160}) - 2. \tag{4.8}$$

as in Dunlop et al. (2013). This method is directly comparable to how the majority of the high redshift observations were made and should allow for direct comparison when interpreting the observations with these models. Using comparable colours at $z \sim 5$ and $z \sim 6$ or different combinations of filters has minimal systematic effect on the calculated values of β (see Dunlop et al. 2011 and Appendix of Bouwens et al. 2011d).

The LyC flux from these models is calculated before and after the applied absorption by gas (for nebular emission) and dust. We are therefore able to calculate the total escape fraction of LyC photons for a given stellar population. Using these values, it is therefore relatively straight-forward to link the observed β distribution of high-redshift galaxies with the distribution of predicted $\kappa_{\rm ion}$ or $L_{\rm UV}$ per unit SFR and the corresponding $f_{esc,tot}$.

For the ionization-bounded nebula with holes model (Model A), the 'observed' SED is a weighted (proportional to $f_{\rm esc}$) sum of the un-attenuated starlight escaping through holes and the attenuated starlight and nebular emission from the H II and dust enclosed region. The two SED components are weighted proportional to the covering fraction ($\equiv 1 - f_{\rm esc}$) of the H II and dust region. The resulting observable quantities are effectively the average over all possible viewing angles, as would be expected for a large sample of randomly aligned galaxies.

For Model B, the density-bounded nebula, Lyman continuum emission from the underlying stellar spectrum is partially absorbed by the surrounding truncated Strömgren sphere with an escape fraction $f_{esc,neb}$. The remaining Lyman continuum photons along with the UV-optical starlight and nebular emission are then attenuated by the surrounding dust shell according to the chosen dust attenuation law. The total escape fraction for this model is therefore

$$f_{\rm esc} = 10^{0.4 \times A(LyC)} f_{\rm esc,neb} \tag{4.9}$$

where $A(LyC)$ is the magnitude of dust extinction for Lyman continuum photons and is highly dependent on the choice of attenuation curve (see Section 4.3.1.6).

4.3.1 Modelling assumptions: current constraints on stellar populations at $z > 3$

Although there are now good constraints on both the UV luminosity function and UV continuum slope at high redshift, both of these values suffer strong degeneracies with respect to many stellar population parameters. As such, constraints on $f_{\rm esc}$, $\xi_{\rm ion}$ and $\kappa_{\rm ion}$ still requires some assumptions or plausible limits set on the range of some parameters. In this section we outline the existing constraints on the relevant stellar population properties at high-redshift, discuss what assumptions we make in our subsequent analysis, and explore the systematic effects of variations in these assumptions.

4.3.1.1 Star-formation history

Typically, star formation histories are parameterised as exponential models,

$$\rho_{\rm SFR}(t) \propto \exp(-\frac{t-t_{\rm f}}{\tau}), \tag{4.10}$$

where τ is the characteristic timescale and can be negative or positive (for increasing or decreasing SFH respectively). Or, alternatively as a power-law, following

$$\rho_{\rm SFR}(t) \propto (t-t_{\rm f})^{\alpha}. \tag{4.11}$$

The star-formation history (SFH) of high-redshift galaxies, $SFR(t)$, is still very poorly constrained due to the limited rest-frame wavelengths available for SED fitting or spectroscopy. For large samples of both intermediate- and high- redshift galaxies, it has been found that rising SFHs produce better SED fits to the observed photometry (Maraston et al., 2010; Lee et al., 2014). However, reliably constraining the characteristic timescales, τ or α, for individual galaxies at $z > 2$ is not possible for all but the brightest sources.

Using a comoving number density selected sample of galaxies at high redshift, Papovich et al. (2011) found that the average star formation history between $3 < z < 8$ is best fit by a power-law with $\alpha = 1.7 \pm 0.2$ or an exponentially rising history with $\tau = 420$ Myr. Recently, for the deep observations of the CANDELS GOODS South field, Salmon et al. (2015) applied an improved version of this method (incorporating the predicted effects of merger rates on the comoving sample) and found a shallower power-law with $\alpha = 1.4 \pm 0.1$ produced the closest match.

In Fig. 4.4, we show that all three of these models ($\alpha = 1.4/1.7$ and $\tau = -450$Myr) can provide a good fit to the observed evolution in the cosmic star-formation rate density at $z > 3$ (Age of the Universe $\lesssim 2$ Gyr) through a simple scaling alone. However, the power-law fit with $\alpha = 1.4$ provides the best fit to not only to the evolution of the SFR-density at ages < 2 Gyr, but also to the SFR density at later epochs. A smoothly rising star-formation is also favoured by hydrodynamic models such as Finlator et al. (2011) and Dayal et al. (2013), although the star-formation histories of individual galaxies are likely to be more varied or stochastic

(Dayal et al., 2013; Kimm & Cen, 2014). Furthermore, there is also growing evidence of galaxy populations with older populations and possibly quiescent populations (Nayyeri et al., 2014; Spitler et al., 2014) suggesting some galaxies form very rapidly at high-redshift before becoming quenched. The assumption of a single parametrised SFH is clearly not ideal, however our choice of a rising power-law SFH with $\alpha = 1.4$ is at least well motivated by observations and a more physical choice than a constant or exponentially declining SFH.

4.3.1.2 Initial mass function

Interpretation of extragalactic observations through modelling and SED fitting is typically done assuming a universal bi-modal Milky Way-like initial mass function (IMF) such as Kroupa (2001)/Chabrier (2003) or the unimodal Salpeter (1955) IMF. However, there is now growing evidence for systematic variation in the IMF of both nearby (van Dokkum & Conroy, 2010; Treu et al., 2010; Cappellari et al., 2012; Conroy & van Dokkum, 2012; Ferreras et al., 2013) and distant (Martín-Navarro et al., 2014) early-type galaxies.

Under a hierarchical model of galaxy evolution with downsizing, the bright galaxies in overdense regions observed at $z > 3$ are likely to eventually form into the massive early-type galaxies in which these variations can be found. Variation in the slope of the IMF would have a significant effect on many of the critical observable properties at high redshift such as stellar masses and mass-to-UV-light ratios. However, given the lack of theoretical understanding as to how the IMF should vary with physical conditions, incorporating the effects of a varying IMF at high-redshift is beyond the scope of this work. Throughout the following analysis we use the Chabrier (2003) IMF as our primary assumption, but also consider the systematic effect of a steeper IMF such as Salpeter (1955) on the inferred values or observables in Appendix A.

The Chabrier (2003) IMF implemented in the models of Bruzual & Charlot (2003) (and therefore this work) takes the functional form:

$$\phi(\log m) \propto \begin{cases} \exp\left[-\frac{(\log m - \log m_c)^2}{2\sigma^2}\right], & \text{for m} \leq 1\text{M}_\odot, \\ m^{-1.3}, & \text{for m} > 1\text{M}_\odot, \end{cases} \tag{4.12}$$

where $\phi(m)$dm is defined as the number of stars born in the mass range m to $m + \mathrm{dm}$ and $m_c = 0.08\mathrm{M}_\odot$ and $\sigma = 0.69$. The Salpeter (1955) IMF takes the simpler form of $\phi(\log m) \propto m^{-1.35}$, over the full range of masses. Crucially, for both forms of the IMF, lower and upper mass cut-offs of 0.1 and 100 $\mathrm{M}_\odot$ respectively are applied.

The exact mass of the upper mass limit imposed in the stellar population models could have a potentially significant effect on the ionizing emissivity of stellar populations at all redshifts. It is particularly important for reionization because $\approx 100\%$ of the ionizing radiation emitted by composite stellar populations comes from the small number of stars with masses > 20 $\mathrm{M}_\odot$ (see Figure 5 of Conroy 2013 for illustration). More recent estimates of the physical upper mass-limit for massive stars place it at 150 $\mathrm{M}_\odot$ (Zinnecker & Yorke, 2007). There is therefore potentially a significant ionizing population that is not currently accounted for in stellar population models. Estimates of the full effect this would have on the ionizing emissivity are not currently possible due to the model limitations. However, this systematic uncertainty should be considered when interpreting the results presented in later this chapter.

An additional factor which must also be considered is the expectation that as observations reach ever higher redshifts, we will eventually encounter an earlier (and possibly first) generation of metal-free primordial stars[2]. The differing physical processes which govern the formation of the first generation of stars are expected to give rise to a markedly different IMF to that of subsequent generations of stars (Bromm et al., 2002; Bromm, 2013; Crosby et al., 2013) and the stars themselves will be much more efficient at producing ionizing photons (Schaerer, 2002). However, the complete lack of observational constraints on models for these stellar populations means it is not currently possible to make meaningful predictions for primordial stars in this study.

[2]Often referred to by the increasingly confusing term 'Population-III' stars

4.3.1.3 Metallicity

Current spectroscopic constrains on galaxy metallicities at $z \geq 3$ indicate moderately sub-solar stellar and gas-phase metallicities (Shapley et al., 2003; Maiolino et al., 2008b; Laskar et al., 2011; Jones et al., 2012; Sommariva et al., 2012). In addition, Troncoso et al. (2014), present measurements for 40 galaxies at $3 < z < 5$ for which the observed metallicities are consistent with a downward evolution in the mass-metallicity relation (with increasing redshift).

Measurements of galaxy metallicities at higher redshift ($z > 6$) are even fewer due to the lack of high-resolution rest-frame optical spectroscopy normally required to constrain metallicity. However, thanks to a clear detection of the CIII] emission line (1909Å) and strong photometric constraints, Stark et al. (2015) are able to measure a metallicity of $\approx 1/20$th solar metallicity for a lensed galaxy at $z = 6.029$. Given these observations and the metallicities available in the Bruzual & Charlot (2003) models, we assume a fiducial metallicity of $\approx 1/5$th solar metallicity ($Z = 0.004 = 0.2Z_{\odot}$).

4.3.1.4 Age

For the rising star-formation history used throughout this work, there is a weak evolution of β as a function of age ($\Delta\beta \approx 0.13$ between $t \approx 100$ Myr and ≈ 1 Gyr) whereby older stellar populations have redder UV continuum slopes. However, at very young ages, the contribution of nebular continuum emission in the UV continuum can also significantly redden the apparent β compared to the much steeper underlying intrinsic UV slope (Robertson et al., 2010). This results in a degeneracy with respect to β between young and old populations. For example, for identical observed (stellar + nebular continuum) UV-slopes, $\xi_{\rm ion}$ (and $\kappa_{\rm ion}$) for a young stellar population can be a factor of up ~ 0.5 (0.2) dex higher. Given this degeneracy, additional constraints from other parts of the electromagnetic spectrum are required to make a well informed choice of stellar population age.

Due to the observational restrictions on high-resolution rest-frame optical spectroscopy, measurement of stellar population ages for high-z galaxies is limited to

photometric fitting and colour analysis. At $z \sim 4$, where the Balmer break can be constrained through deep *Spitzer* IRAC photometry, estimates of the average stellar population ages vary significantly from $\sim 200 - 400$ Myr (Lee et al., 2011) to $\sim$ 1 Gyr (Oesch et al., 2013) (dependent on assumptions of star-formation history).

For galaxies closer to the epoch of reionization, constraints on the Balmer/D(4000) breaks become poorer due to the fewer bands available to measure the continuum above the break, a problem that is exacerbated by the additional degeneracy of strong nebular emission lines redshifted into those filters (Schaerer & de Barros, 2009, 2010). The effect of incorporating the effects of emission lines on SED fits at $z \geq 4$ is that on average the best-fitting ages and stellar masses are lowered. This reduction in best-fit age is because the rest-frame optical colours can often be well fit by either a strong Balmer break or by a significantly younger stellar population with very high equivalent width Hα or OIII emission.

Recent observations of galaxies at high-redshift with constraints on the UV emission-line strengths (Lyα or otherwise) have found that single-component star-formation histories are unable to adequately fit both the strong line emission and the photometry at longer wavelengths (Rodriguez Espinosa et al., 2014; Stark et al., 2015). For example, to match both the observed photometry at rest-frame optical wavelengths and the high-equivalent width UV emission lines of a lensed galaxy at $z = 6.02$, Stark et al. (2015) require two stellar populations. In combination with a 'young' 10 Myr old starburst component, the older stellar component is best fitted with an age since the onset of star-formation of $\approx$ 500 Myr.

Based on the observations discussed above and the median best-fit ages found by Curtis-Lake et al. (2013), the star-formation history outlined in Section 4.3.1.1 is consistent with the existing limited constraints. At $z \sim 7$, the redshift of strongest interest to current studies of reionization, the assumed onset of star-formation at $z = 12$ gives rise to a stellar population age (since the onset of star-formation) of $\sim$ 390 Myr.

4.3.1.5 Nebular continuum and line emission

If nebular line emission is "ubiquitous" at high-redshift as an increasing number of studies claim (e.g. Shim et al. (2011); Stark et al. (2013); Smit et al. (2014)), the accompanying nebular continuum emission should also have a strong effect on the observed SEDs of high-redshift galaxies (Reines et al., 2009). In this work, we include both nebular continuum and optical line emission using the prescription outlined in Chapter 2 (and equivalent to the methods described in Ono et al. (2010); Schaerer & de Barros (2010); McLure et al. (2011)).

Whilst the strength of nebular emission in this model is directly proportional to the number of ionizing photons produced by the underlying stellar population, additionally both the strength and spectral shape of the nebular continuum emission are also dependent on the continuum emission coefficient, $\gamma_{\nu}^{(total)}$, given by

$$\gamma_{\nu}^{(total)} = \gamma_{\nu}^{(HI)} + \gamma_{\nu}^{(2q)} + \gamma_{\nu}^{(HeI)}\frac{n(He^{+})}{n(H^{+})} + \gamma_{\nu}^{(HeII)}\frac{n(He^{++})}{n(H^{+})} \tag{4.13}$$

where $\gamma_{\nu}^{(HI)}$, $\gamma_{\nu}^{(HeI)}$, $\gamma_{\nu}^{(HeII)}$ and $\gamma_{\nu}^{(2q)}$ are the continuum emission coefficients for free-free and free-bound emission by Hydrogen, neutral Helium, singly ionized Helium and two-photon emission for Hydrogen respectively (Krueger et al., 1995). As in Chapter 2, the assumed continuum coefficients are taken from Osterbrock & Ferland (2006), assuming an electron temperature $T = 10^4$ K and electron density $n_e = 10^2$ cm^{-3} and abundance ratios of $y^{+} \equiv \frac{n(He^{+})}{n(H^{+})} = 0.1$ and $y^{++} \equiv \frac{n(He^{++})}{n(H^{+})} = 0$ (Krueger et al., 1995; Ono et al., 2010).

Although the exact ISM conditions and abundances of high-redshift HII regions is not well known, singly and doubly ionised helium abundances for nearby low-metallicity galaxies have been found to be $y^{+} \approx 0.08$ and $y^{++} \approx 0.001$ (Dinerstein & Shields, 1986; Izotov et al., 1994; Hagele et al., 2006). We estimate that for the age, metallicity and dust values chosen for our fiducial model (see Table 4.3), variations of $\Delta y^{+} = 0.05$ corresponds to $\Delta\beta = 0.004$, while values of y^{++} as large as 3% (Izotov et al., 2013) would redden the observed UV slope by $\Delta\beta = +0.003$. In this case, because the nebular continuum emission is dominated by the stellar continuum at these wavelengths for our assumption, the effects of variation in the HII region properties is negligible and our interpretation of the observed UV

slopes should not be affected by our assumed nebular emission properties.

4.3.1.6 Dust Extinction

In Bouwens et al. (2009), it is argued that the most likely physical explanation for variation in the observed βs between galaxies is through the variation in dust content. Large changes in metallicity and ages are required to produce significant variation in β (see later discussion in Section 4.3.2), however as previously discussed in this section, such large variations are not observed in the galaxy population in either age or metallicity at $z > 3$ based on current observations. For the fiducial model in our subsequent analysis, we allow the magnitude of dust extinction (A_V) to vary along with $f_{\rm esc}$, but we must also choose a dust attenuation law to apply.

Direct measurements of dust and gas at extreme redshifts are now possible thanks to the sub-mm facilities of ALMA. However, the current number of high redshift observations is still very small. Ouchi et al. (2013) and Ota et al. (2014) observe Lyman alpha emitters (LAEs) at $z \sim 7$, finding only modest dust extinction ($E(B-V) = 0.15$). Recent work by Schaerer et al. (2015) extends the analysis to a larger sample of five galaxies, finding a range in dust extinction of $0.1 < A_V < 0.8$. While the dust attenuation in these objects is consistent with normal extragalactic attenuation curves such as (Calzetti et al., 2000) or the SMC extinction curve (e.g. Pei (1992)), the results are not strong enough to constrain or distinguish between these models. Similarly, for broadband SED fits of high-redshift objects, neither a starburst or SMC-like attenuation curve is strongly favoured (Salmon et al., 2015). Based on these factors, we assume the starburst dust attenuation curve of Calzetti et al. (2000) in order to make consistent comparisons with the SED fitting of Chapter 2 and Meurer et al. (1999) dust corrections to UV star-formation rates (e.g. Bouwens et al. (2011a); Smit et al. (2012)).

In addition, due to the lack of constraints on the dust attenuation strengths at wavelengths less than 1200Å we must also assume a plausible extrapolation below these wavelengths. For our fiducial model, we simply extrapolate linearly based on the slope of the attenuation curve at $1200 - 1250$Å, in line with similar works

on the escape fraction of galaxies (Siana et al., 2007). In addition, we also assume a second model in which the extreme-UV and Lyman continuum extinction follows the functional form of the component of the Pei (1992) SMC extinction model at $\lambda \leq 1000$Å, whereby the relative absorption begins to decrease below 800Å. The systematic effect of choosing this second assumption along with a third assumption of an SMC extinction curve are outlined in Table A.1.

As shown in Fig. 4.1, we assume a simple foreground dust screen (Calzetti et al., 1994) and that dust destruction is minimal and/or balanced by grain production (Zafar & Watson, 2013; Rowlands et al., 2014); effectively that dust for a given model is fixed with relation to the stellar population age. The assumption of a different dust geometry, such as one with clouds dispersed throughout the ISM, would require a greater amount of dust to achieve the same optical depth and could also have a significant effect on the extinction of nebular emission relative to that of the stellar continuum (Zackrisson et al., 2013).

4.3.1.7 Differing SSP models: the effects of stellar rotation and binarity

The choice of Bruzual & Charlot (2003) stellar population synthesis (SPS) models in this work was motivated by the more direct comparison which can be made between this analysis and the stellar mass, luminosity and colour measurements based on the same models, e.g. Finkelstein et al. (2011); Duncan et al. (2014). However, several other SPS models are available and in common usage, e.g. Starburst99 (Leitherer et al., 1999), Maraston (2005) and FSPS (Conroy et al., 2009a,b).

Due to differences in assumptions/treatment of various ingredients such as horizontal branch morphology or thermally-pulsating asymptotic giant branch (TP-AGB) stars, the SEDs produced for the same input galaxy properties (such as age and metallicity) can vary significantly. The full systematic effects of the different assumptions and models for galaxies at high-redshift is not well quantified and adequately doing so is beyond the scope of this work. We do however caution that these systematics could significantly affect the inferred ionizing photons rates of

galaxies during the EoR. In particular, it has been suggested that rotation of massive stars could have a significant effect on the UV spectra and production rate of ionizing photons (Vazquez et al., 2007).

In Leitherer et al. (2014), the effects of the new stellar models including stellar rotation (Ekström et al., 2012) are incorporated into the Starburst99 SPS models. The resulting SEDs are changed drastically with an increase in the ionizing photon rate of up to a factor of five for the most extreme model of rotation.

A second, equally significant effect comes from the inclusion of binary physics in stellar population synthesis models. It is now believed that the majority of massive stars exist in binaries (Sana et al., 2012, 2013; Aldoretta et al., 2015) while the majority of stellar population models (including all of the aforementioned SPS models) are for single stars. The BPASS code of Eldridge & Stanway (2009, 2011)) incorporates the physics of binary rotation on massive stars to explore the effects on the predicted stellar population features, observing similar effects to the addition of rotation in single star models; an increased fraction of red supergiants that go on to form bluer UV bright Wolf-Rayet stars.

We note that for the same assumed stellar populations parameters (age, metallicity, SFH, dust), the use of either of these models would result in SEDs with bluer UV continuum slopes and an increased LyC production rate. However, the full ramifications of how these models may change the interpretation of SEDs, stellar masses and βs for the observations of high-redshift galaxies is beyond the scope of this work.

4.3.2 Observed UV slopes as a function of $f_{\rm esc}$ and dust extinction

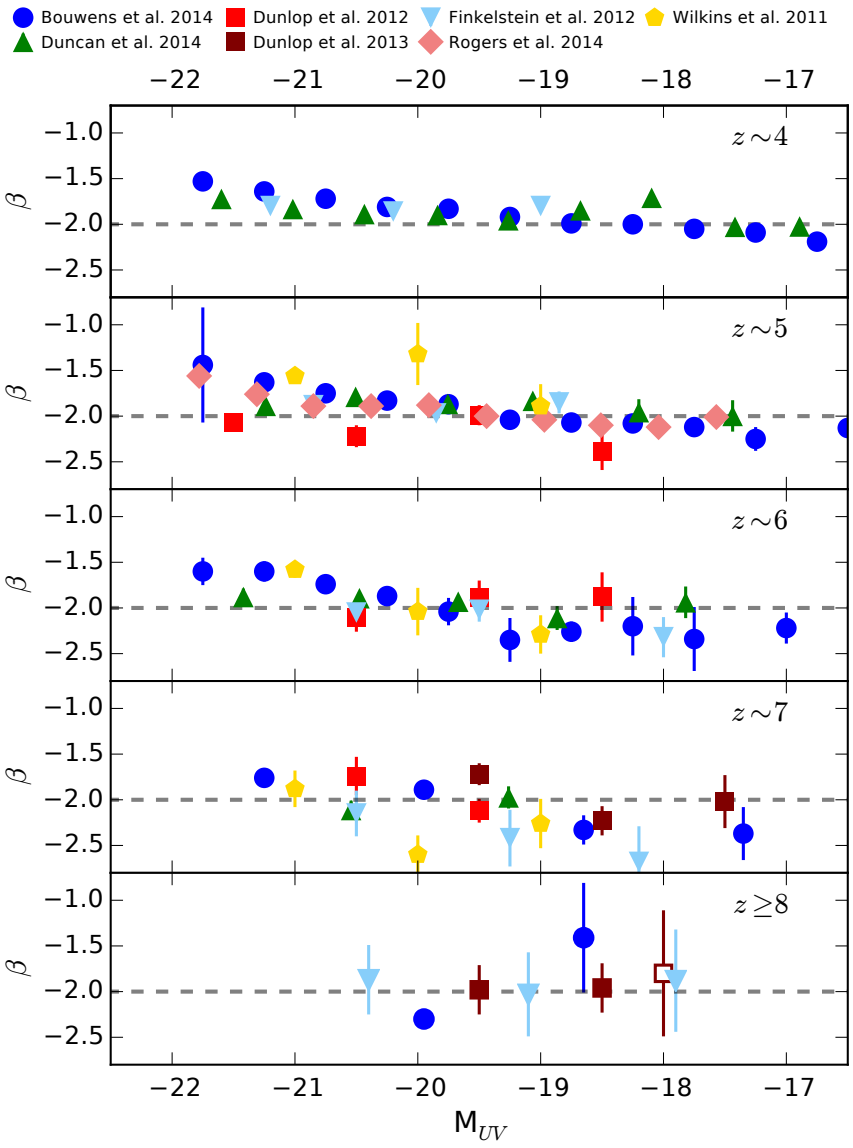

Figure 4.2: Observed average values of the UV continuum slopes β as a function of rest-frame UV magnitude, $M_{\rm UV}$, as of May 2015. Presented are results from Wilkins et al. (2011), Dunlop et al. (2011, 2013), Finkelstein et al. (2011), Bouwens et al. (2014), Rogers et al. (2014) and Chapter 2 of this thesis at redshifts $z \sim 4$, 5, 6, 7 and $8-9$. In the bottom panel, filled symbols show the average for $8 \sim 7$ samples while the open symbol shows the averages for $z \geq 9$ (see respective papers for sample details and redshift ranges).

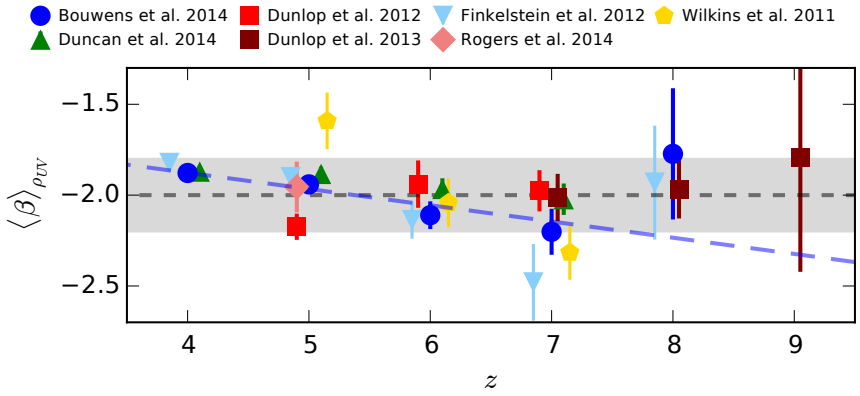

Figure 4.3: Luminosity-weighted average β, $\langle\beta\rangle_{\rho_{\rm UV}}$, as a function of redshift for the $M_{\rm UV} - \beta$ observations shown in Fig. 4.2. The grey shaded region covers the range $-2.2 < \beta < -1.8$ and the blue long-dashed line shows our parametrisation of $\langle\beta\rangle_{\rho_{\rm UV}}$ vs z based on the observations of Bouwens et al. (2014) (see Equation 4.7).

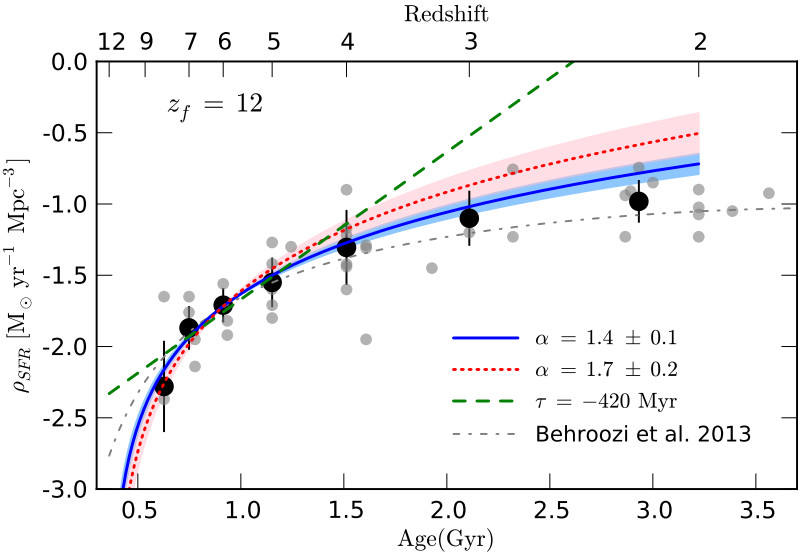

Figure 4.4: Power-law (blue continuous: Salmon et al. 2015, red dotted: Papovich et al. 2011) and exponential (green dashed: Papovich et al. 2011) fits to the median observed SFR-densities at $z > 4$ for 3 different star formation histories. The grey datapoints are taken from the compilation of SFR-density observations in Behroozi et al. (2013) with additional points from recent observations (Smit et al., 2012; Bouwens et al., 2015b; Duncan et al., 2014). For the power-law fits, the shaded red and blue regions correspond to the 1-σ errors on the slope of the power-law, α, quoted in the respective papers. The grey dot-dashed line shows the best-fit to the median star-formation rates across the the full cosmic history for the functional form outlined in Behroozi et al. (2013). All of the models assume an initial onset of star-formation at $z_f = 12$.

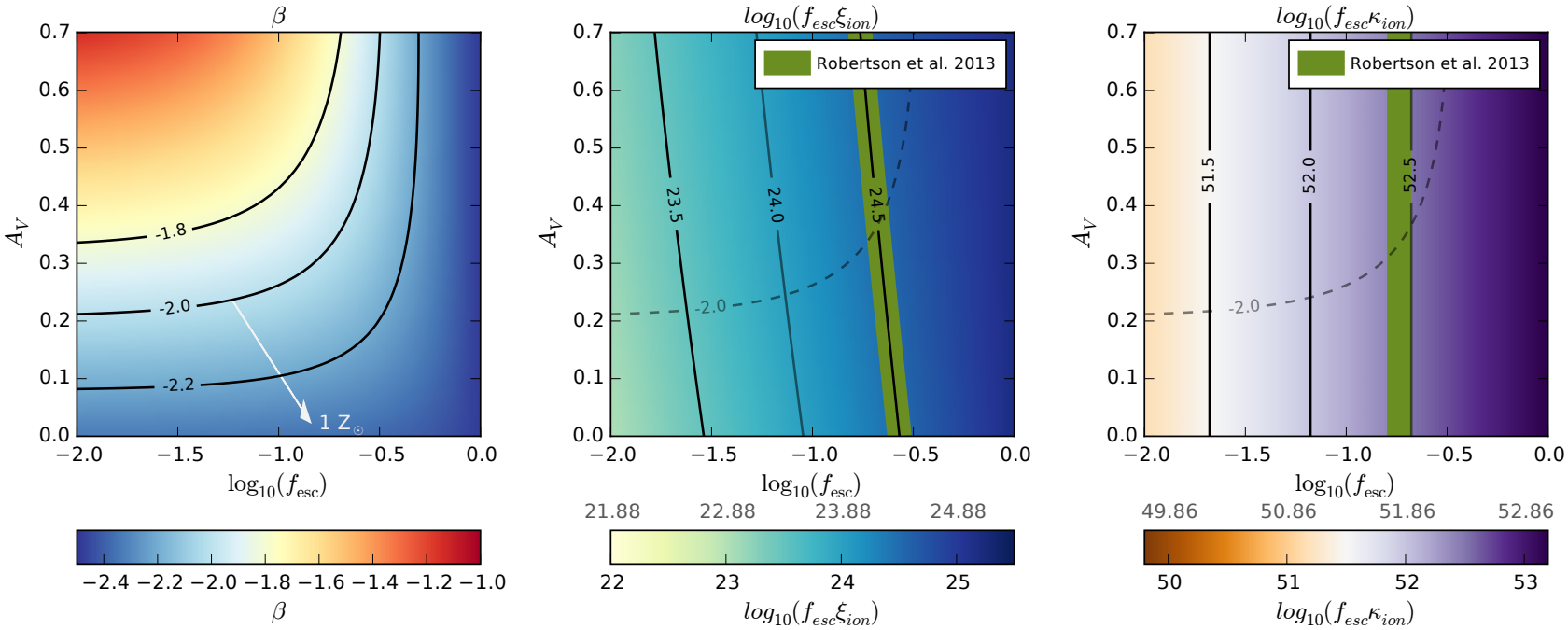

Figure 4.5: Left: UV continuum slope β as a function of total escape fraction, $f_{\rm esc}$, and dust extinction, A_V, for the *ionization bounded nebula with holes* continuum escape model (Model A, Fig. 4.1 left) with stellar population properties as outlined in Section 4.3.1. The contours indicate lines of constant β around the observed average β, and the light grey arrow indicates how those contours move for a stellar population with solar metallicity. Middle and right: $\log_{10} f_{\rm esc}\xi_{\rm ion}$ and $\log_{10} f_{\rm esc}\kappa_{\rm ion}$ as a function of escape fraction and dust extinction respectively for the same continuum escape model. Solid contours represent lines of constant $f_{\rm esc}\xi_{\rm ion}$ and $f_{\rm esc}\kappa_{\rm ion}$ whilst the dashed contour shows where $\beta = -2$ is located for reference. The green labelled contour shows the assumed $f_{\rm esc}\xi_{\rm ion} = 24.5$ value of R13 and the equivalent in $f_{\rm esc}\kappa_{\rm ion}$ (see text for details). For the colour scales below the centre and right panels, the lower black tick labels correspond to the scale for the fiducial model ($Z = 0.2Z_\odot$) whilst the grey upper tick label indicate how $f_{\rm esc}\xi_{\rm ion}$ and $f_{\rm esc}\kappa_{\rm ion}$ change for stellar populations with solar metallicity.

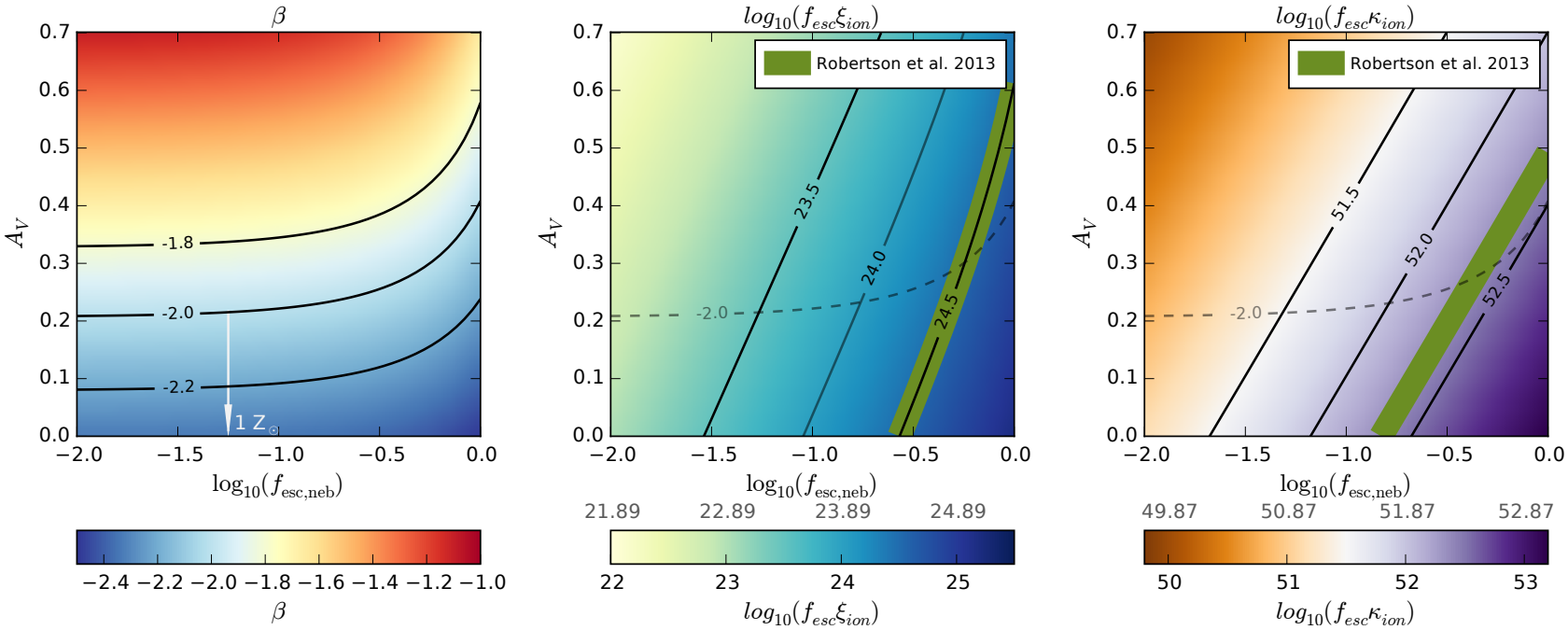

Figure 4.6: Left: UV continuum slope β as a function of HII region escape fraction, $f_{\rm esc}$, and dust extinction, A_V, for the *density-bounded nebula* continuum escape model (Model B, Fig. 4.1 right) with stellar population properties as outlined in Section 4.3.1. The contours indicate lines of constant β around the observed average β, and the light grey arrow indicates how those contours move for a stellar population with solar metallicity. Centre and right: $\log_{10} f_{\rm esc}\xi_{\rm ion}$ and $\log_{10} f_{\rm esc}\kappa_{\rm ion}$ (where $f_{\rm esc}$ is the total dust attenuated escape fraction) as a function of escape fraction and dust extinction respectively for the same continuum escape model. Solid contours represent lines of constant $f_{\rm esc}\xi_{\rm ion}$ and $f_{\rm esc}\kappa_{\rm ion}$ whilst the dashed contour shows where $\beta = -2$ is located for reference. The green labelled contour shows the assumed $f_{\rm esc}\xi_{\rm ion} = 24.5$ value of R13 and the equivalent in $f_{\rm esc}\kappa_{\rm ion}$ (see text for details). For the colour scales below the centre and right panels, the lower black tick labels correspond to the scale for the fiducial model ($Z = 0.2Z_{\odot}$) whilst the grey upper tick label indicate how $f_{\rm esc}\xi_{\rm ion}$ and $f_{\rm esc}\kappa_{\rm ion}$ change for stellar populations with solar metallicity.

The galaxy properties with the largest uncertainties and expected variation are the optical depth of the dust attenuation (or extinction magnitude A_V) and the property we wish to constrain photometrically, the escape fraction of ionizing photons $f_{\rm esc}$. For the assumptions of our fiducial model (Table 4.3), we want to explore the possible range of these two properties which are consistent with the observed UV slopes (as calculated for each model following Eq. 4.8) and what constraints can then be placed on the ionizing emissivity coefficients $f_{\rm esc}\xi_{\rm ion}$ or $f_{\rm esc}\kappa_{\rm ion}$.

In the left panels of Fig. 4.5 and Fig. 4.6, we show how β varies as a function of the dust extinction magnitude and escape fraction for each of the continuum escape mechanisms respectively (Section 4.2/Fig. 4.1). For both models, β is relatively constant as a function of $f_{\rm esc}$ at low values of escape fraction ($f_{\rm esc} < 0.1$). At larger escape fractions, the two mechanisms produce different UV slopes. For Model A, as $f_{\rm esc}$ increases to $\sim 10\%$ (covering fraction $\approx 90\%$) the unattenuated stellar continuum begins to dominate the overall colours as $f_{\rm esc}$ increases and by $f_{\rm esc} \gtrsim 30\%$ the observed average β is determined only by the unattenuated light, irrespective of the magnitude of the dust extinction in the covered fraction. This effect is also illustrated in a different way in Figure 9 of Zackrisson et al. (2013), whereby the same amount of dust extinction in the covered/high-density regions has a decreasing effect on the observed β as the escape fraction increases. This result means that if Lyman continuum is escaping through holes in the ISM and is un-attenuated by dust, it is possible to set constraints on the maximum escape fraction possible that is still consistent with the UV slopes observed.

For Model B, β remains constant with $f_{esc,neb}$ at a fixed dust extinction until $f_{\rm esc} \approx 30\%$. Beyond this, the reduction in nebular continuum emission from the high escape fraction begins to make the observed βs bluer for the same magnitude of dust extinction.

For both escape mechanisms, a UV slope of $\beta \approx -2$ is achievable with only moderate amounts of dust extinction required ($A_V \approx 0.4$ and 0.25 for models A and B respectively at $f_{\rm esc} \approx 0.2$). When metallicity is increased to $Z = Z_\odot$, the isochromes (of constant β) are shifted downwards such that $\beta \approx -2$ requires

negligible dust attenuation (cf. Robertson et al. 2013). In Section 4.3.4 we further explore the effects of varying metallicity on the apparent β and corresponding emissivity coefficients. However, first we wish to examine the range of ξ_{ion} and κ_{ion} which correspond to the values of $f_{\rm esc}$ and A_V consistent with $\beta \approx -2$ found here.

4.3.3 ξ_{ion} and κ_{ion} as a function of $f_{\rm esc}$ and dust extinction

In the centre and right panels of Figures 4.5 and 4.6 we show $\log_{10} f_{\rm esc}\xi_{\rm ion}$ and $\log_{10} f_{\rm esc}\kappa_{\rm ion}$ as a function of $f_{\rm esc}$ and the extinction magnitude of dust in the covered regions (A_V).

For dust model A, the ionization-bounded nebula with holes, there is very little dependence of the ionizing photon rate per unit UV luminosity on the magnitude of dust extinction in the covered fraction (centre panel). Because the increase dust extinction magnitude around the high column density areas only affects the UV/optical component, the increasing dust extinction results in higher values of $\log_{10} f_{\rm esc}\xi_{\rm ion}$ due to the increased absorption of the UV light in the dust covered regions. For this dust model, the corresponding ionizing photon rate per unit SFR ($f_{\rm esc}\kappa_{\rm ion}$) has zero evolution as a function of dust extinction in this geometry.

The assumed $\log_{10} f_{\rm esc}\xi_{\rm ion} = 24.5$ of R13 is consistent with $\beta = -2$ for this model, with an escape fraction of $f_{\rm esc} = 0.16$ and moderate dust extinction ($A_V = 0.31$). Given the low escape fractions that are still consistent with blue β slopes, a value of $\log_{10} f_{\rm esc}\xi_{\rm ion} = 24.5$ does represent a relatively optimistic assumption on the ionizing efficiency of galaxies. However, it is still ≈ 0.2 dex lower than the largest $f_{\rm esc}$ still consistent with a UV slope of $\beta = -2$.

In contrast to model A, because the dust in the density-bounded nebula (model B) is assumed to cover all angles, increases in the dust extinction magnitude results in significantly smaller $\log_{10} f_{\rm esc}\xi_{\rm ion}/\log_{10} f_{\rm esc}\kappa_{\rm ion}$ for the same fixed $f_{\rm esc}$. This can be seen clearly in the centre and right panels of Fig. 4.6.

Despite this, an assumed value of $\log_{10} f_{\rm esc}\xi_{\rm ion} = 24.5$ is still consistent with $\beta = -2$ for this model. However, it requires a higher escape fraction ($f_{\rm esc} = 0.42$)

Table 4.3: Summary of the stellar population assumptions for our fiducial $\beta = -2$ model.

Star-formation history	$SFR \propto t^{1.4}$ [a]	
Initial Mass Function	Chabrier (2003)	
Dust attenuation curve	Calzetti et al. (2000)	
Metallicity	$Z = 0.2Z_{\odot}$	
Nebular Emission	Continuum included[b]	
Age	390 Myr[c]	
	Model A	*Model B*
Dust attenuation magnitude A_V	0.31	0.27
Escape fraction $f_{esc,neb}$	0.16	0.42
$\log_{10} f_{\rm esc}\xi_{\rm ion}$	24.5[d]	24.5
$\log_{10} f_{\rm esc}\kappa_{\rm ion}$	52.39	52.34

[a] Salmon et al. (2015)
[b] $T = 10^4$ K, $n_e = 10^2$ cm^{-3}, $y^+ = 0.1$ and $y^{++} = 0$
[c] Age at $z \sim 7$ since onset of star-formation at $z \sim 12$.
[d] The assumed $\log_{10} f_{\rm esc}\xi_{\rm ion}$ of R13

and lower dust extinction ($A_V = 0.27$) to achieve this for the same underlying stellar population. The maximum $f_{esc,neb} = 1$ is still consistent with the fiducial UV slope, but the increased dust required to match $\beta = -2$ means that the total LyC escape fraction is reduced and that the corresponding maximum $\log_{10} f_{\rm esc}\xi_{\rm ion}$ is only marginally higher than the assumptions of (Kuhlen & Faucher-Giguère, 2012) or (R13).

For the assumed stellar population properties in our reference model, the UV continuum slope of the intrinsic dust-free stellar population is $\beta = -2.55$ excluding the contribution of nebular continuum emission. This value is significantly bluer than the dust-free β assumed by the Meurer et al. (1999) relation commonly used to correct UV star-formation rates for dust absorption. It is however in better agreement with the dust-free β's estimated recently for observed galaxies at $z \geq 3$ (Castellano et al., 2014; de Barros et al., 2014) and the theoretical predictions of Dayal & Ferrara (2012).

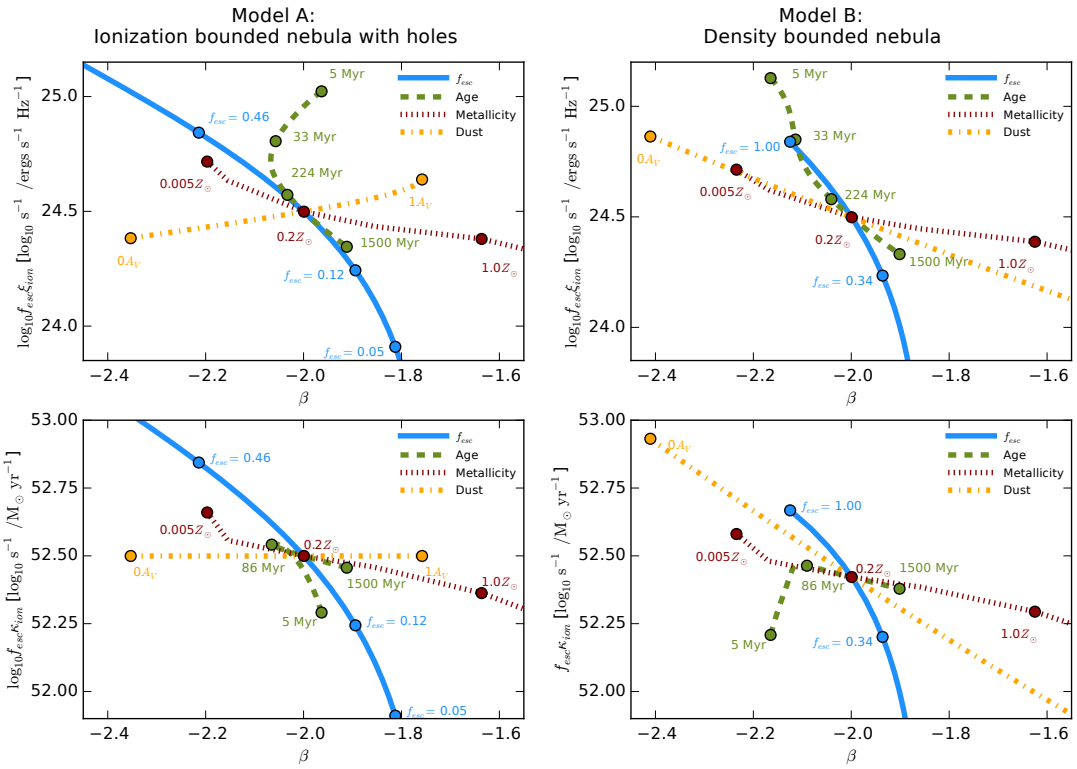

Figure 4.7: Evolution of $\log_{10} f_{\rm esc}\xi_{\rm ion}$ (top panels) and $\log_{10} f_{\rm esc}\kappa_{\rm ion}$ (bottom panels) vs β as a function of changes in the stellar population age (green dashed), metallicity (red dotted), dust extinction (yellow dot-dashed) and escape fraction (blue continuous) with the remaining parameters fixed to the fiducial values listed in Table 4.3. Values are plotted for both the ionization bounded nebula with holes (Model A; left panels) and density-bounded nebula (Model B; right panels). Some individual points are labelled for both Lyman continuum escape models to illustrate the range and differences in evolution between each model. Note that the small difference in β between Model A and Model B for the case of zero-dust ($0A_V$) is due to the difference in nebular emission contribution for the two models; $f_{esc,neb} = 0.16$ and $f_{esc,neb} = 0.42$ for models A and B respectively.

4.3.4 Effect of different stellar population properties on ξ_{ion} and κ_{ion} vs β

Given the strong evidence for both luminosity and redshift-dependent βs, we wish to explore whether evolution in each of the stellar population parameters can account for the observed range of βs and estimate what effect such evolution would have on the inferred values of $f_{\rm esc}\xi_{\rm ion}$ and $f_{\rm esc}\kappa_{\rm ion}$. At $z > 6$, the the average β for the brightest and faintest galaxies by $\Delta\beta \approx 0.6$ (Fig. 4.2). As a function of redshift, the evolution in β is less dramatic, with average slopes (at a fixed luminosity) reddening by $\Delta\beta \approx 0.1$ in the ~ 400 million years between $z \sim 7$ and $z \sim 5$.

In the left panel of Fig. 4.7, we show how β and $f_{\rm esc}\xi_{\rm ion}$ or $f_{\rm esc}\kappa_{\rm ion}$ vary as a func-

tion of each model parameter for the ionization-bounded nebula model (Model A) with the remaining parameters kept fixed at our fiducial $\beta = -2$ model (Table 4.3). The corresponding values for the density-bounded nebula model (Model B) are shown in the right-hand panel of Fig. 4.7. How $f_{\rm esc}\xi_{\rm ion}$ and $f_{\rm esc}\kappa_{\rm ion}$ vary with respect to β for changes in the different parameters differs significantly:

- *Dust:* As has already been seen in Fig. 4.5, β varies strongly as a function of dust attenuation strength for the ionization-bounded nebula model. There is however minimal variation in $f_{\rm esc}\xi_{\rm ion}$ or $f_{\rm esc}\kappa_{\rm ion}$ with respect to that large change in β. The inferred $f_{\rm esc}\xi_{\rm ion}$ or $f_{\rm esc}\kappa_{\rm ion}$ can justifiably be considered constant as a function of redshift for this escape model if it is assumed that evolution in the dust extinction is responsible for the observed evolution of β.

  For model B, the density-bounded nebula, the large evolution in β is coupled to a significant evolution in the inferred emissivity coefficients. For a change in the UV slope of $\Delta\beta \approx 0.2$, there is a corresponding evolution in $f_{\rm esc}\xi_{\rm ion}$ and$f_{\rm esc}\kappa_{\rm ion}$ of ≈ 0.19 and 0.25 dex respectively.

- *Metallicity:* Between extremely sub-solar ($Z = 0.005\ Z_{\odot}$) and super-solar ($Z > 1\ Z_{\odot}$) metallicities, the variation in β is large enough to account for the wide range of observed average β's for both Lyman escape mechanisms. In this regard, metallicity evolution is a plausible mechanism to explain the apparent variation in β. However, such a wide variation in metallicities is not supported by current observations (see Section 4.3.1.3).

  Both $f_{\rm esc}\xi_{\rm ion}$ and $f_{\rm esc}\kappa_{\rm ion}$ vary by a factor of ~ 2 across the full metallicity range modelled in this work, with bluer low-metallicity stellar populations producing more Lyman continuum photons per unit SFR/UV luminosity.

- *Age:* Due to the strong nebular continuum contribution to the overall spectra at young ages, evolution in the stellar population age results in a more complicated β-emissivity relation. When nebular emission is included the continuum emission reddens the slope at very young ages before turning over at $t \approx 100$ Myr and reddening with age towards ages of $t = 1$ Gyr and

greater. For both LyC escape models, younger stellar populations results in a higher number of ionizing photons per unit UV luminosity.

For Model A, the effect of reddening by nebular emission at young ages is more pronounced due to the lower nebular region escape fraction ($f_{esc,neb} = 0.21$) in our fiducial model. The result of this reddening is that for the same $\beta = -2$, the corresponding $\log_{10} f_{\rm esc}\xi_{\rm ion}$ can be either ≈ 24.5 or ≈ 25.0. This effect represents a potentially huge degeneracy if the ages of galaxy stellar populations are not well constrained.

Between $z \sim 7$ and $z \sim 4$, the evolution in stellar population age can only account for a reddening of $\Delta\beta \approx 0.1$, less than the evolution in both the normalisation of the colour-magnitude relation and in $\langle\beta\rangle_{\rho_{\rm UV}}$. Similarly, it worth noting that at $z \sim 7$, the assumption of a later onset for star-formation (e.g. $z \sim 9$, Planck Collaboration et al. (2015)) results in a ~ 0.14 dex increase in the intrinsic $\xi_{\rm ion}$ and a change in the UV slope of $\Delta\beta \approx -0.065$.

- $f_{\rm esc}$*:* For both models of LyC escape, variation in $f_{\rm esc}$ has a strong evolution in $f_{\rm esc}\xi_{\rm ion}$ or$f_{\rm esc}\kappa_{\rm ion}$ with respect to changes in β. However, for Model B (density-bounded nebula) the range of β covered by the range of $f_{esc,neb}$ ($0 \leq f_{esc,neb} \leq 1$) is only ≈ 0.2 dex, significantly less than the range of colours reached by variation in the other stellar population parameters.

4.4 Estimated galaxy emissivity during reionization

Using our improved understanding of the ionizing efficiencies of galaxies during the EoR, we can now estimate the total ionizing emissivity $\dot{N}_{\rm ion}$ of the galaxy population at high redshift following the prescription outlined in Equations 4.2 and 4.3. We quantify $\rho_{\rm UV}$ and $\rho_{\rm SFR}$ using the latest available observations of the galaxy population extending deep in the epoch of reionization.

4.4.1 Observations

Thanks to the deep and wide near-infrared observations of the CANDELS survey (Grogin et al., 2011; Koekemoer et al., 2011) and the extremely deep but narrow UDF12 survey (Koekemoer et al., 2013), there now exist direct constraints on the observed luminosity function deep into the epoch of reionization. In this chapter, we will make use of the UV luminosity functions calculated by McLure et al. (2013) and Schenker et al. (2013a) at $z = 7 - 9$ as part of the UDF12 survey along with the recent results of Bouwens et al. (2015b) and (Finkelstein, 2014) at $z \geq 4$ and the latest results from lensing clusters at $z > 8$ (Oesch et al., 2014; McLeod et al., 2014).

A second, complimentary constraint on the amount of star-formation at high redshift is the stellar mass function and the integrated stellar mass density observed in subsequent epochs. As the time integral of all past star-formation, the stellar mass density can in principal be used to constrain the past star-formation rate if the star-formation history is known (Stark et al., 2007). A potential advantage of using the star-formation rate density in this manner is that by being able to probe further down the mass function, it may be possible to indirectly measure more star-formation than is directly observable at higher redshifts. Or to outline in other terms, if the total stellar mass density of all galaxies can be well known at $z \sim 4$ or $z \sim 5$, strict upper limits can be placed on the amount of unobserved (e.g. below the limiting depth of $z \sim 8$ observations) or obscured star-formation at $z > 6$.

At its simplest, the relation between a star-formation history, $S(t)$, and the resulting stellar mass M_* (or stellar mass density ρ_*) is given by

$$M_*(t_z) = (1 - \epsilon_z) \times \int_{t_f}^{t_z} S(t)\ dt \tag{4.14}$$

where t_f and t_z are the age of the Universe at the onset of star-formation and observed redshift respectively and ϵ_z is the fraction of mass returned to the ISM at the observed redshift. For a parametrised star-formation history, $F(t)$, which is normalised such that $\int_{t_f}^{t_z} F(t)\ dt = 1\mathrm{M}_\odot(\mathrm{Mpc}^{-3})$, we can substitute $S(t) = C_{obs,z} \times F(t)$. The normalisation, $C_{obs,z}$, accounts for the normalisation of the

star-formation history required to match the observed stellar mass (or stellar mass density) at the redshift z.

From recent observations of the stellar-mass density at $z > 4$, such as those from the stellar mass functions presented in Chapter 2 and Grazian et al. (2014), it is then straight-forward to calculate the corresponding $C_{obs,z}$ and the inferred star-formation history ($C_{obs,z} \times F(t)$) for any assumed parametrisation. Motivated by the discussion of star-formation histories in Section 4.3.1, we assume a normalised star-formation history which is $F(t) \propto t^{1.4}$ (Salmon et al., 2015), as is done for the modelled β values.

Using our stellar population models, we calculate ϵ for the star-formation history and metallicity used in this work at any desired redshift. We find that for a Chabrier (2003) IMF, ϵ_z varies from $\epsilon_z \approx 0.29$ at $z = 8$ to $\epsilon_z \approx 0.35$ at $z = 4$ (for a Salpeter IMF and constant SFH at ~ 10 Gyr old, we calculate $\epsilon = 0.279$ in agreement with the figure stated in R13).

4.4.2 $\dot{N}_{\rm ion}$ for constant $f_{\rm esc}\xi_{\rm ion}$ and $f_{\rm esc}\kappa_{\rm ion}$

In Fig. 4.8, we show the estimated ionizing emissivity as a function of redshift for UV luminosity function observations of Bouwens et al. (2015b); Finkelstein (2014); Oesch et al. (2014) and McLeod et al. (2014), assuming our fiducial constant $\log_{10} f_{\rm esc}\xi_{\rm ion} = 24.5$ (Table 4.3, as assumed in Robertson et al., 2013). The integrated luminosity density and corresponding confidence intervals for each UV LF observation are estimated by drawing a set of LF parameters from the corresponding MCMC chain or likelihood distribution obtained in their fitting. This is repeated 10^4 times to give a distribution from which we plot the median and 68% confidence interval. The luminosity functions of Bouwens et al. (2015b) and Finkelstein (2014) span a large redshift range from $z \sim 4$ to $z \sim 8$ and predominantly make use of the same imaging data (including the ultra deep UDF12 observations, Koekemoer et al. 2013) but use different reductions of said data and differing selection and detection criteria, we refer the reader to the respective papers for more details.

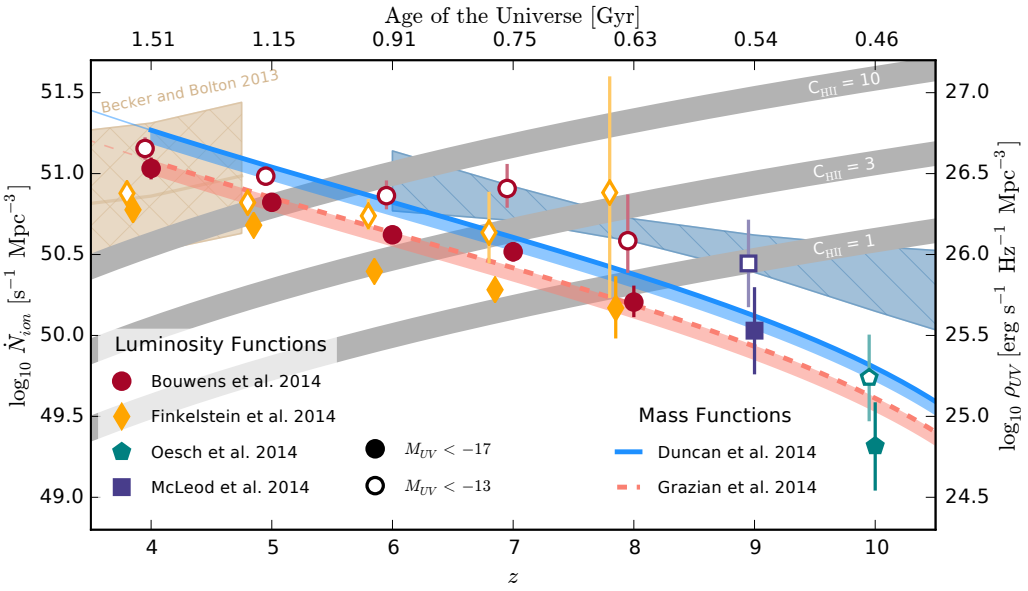

Figure 4.8: Ionizing emissivity $\dot{N}_{\rm ion}$ predicted for a fixed $f_{\rm esc}\xi_{\rm ion}$ for the UV luminosity function observations of Bouwens et al. (2015b), Oesch et al. (2014), Finkelstein (2014) and McLeod et al. (2014). Filled symbols are for luminosity functions integrated down to $M_{\rm UV} = -17$ (typical limiting depth of while open symbols correspond to a UV luminosity density integrated down to a constant $M_{\rm UV} = -13$ for all redshifts. Also shown are the ionizing emissivities inferred by the $z \sim 4$ stellar mass density observations of Chapter 2 (solid blue line) and Grazian et al. (2014) (dashed pink line) for the power-law star-formation history outlined in Section 4.3.1. For the stellar mass function predictions, the thick solid and dashed line correspond to a constant $\log_{10} f_{\rm esc}\kappa_{\rm ion} = 52.39$ (Lyman escape model A) while the filled region shows the systematic offset when assuming $\log_{10} f_{\rm esc}\kappa_{\rm ion} = 52.34$ for Lyman escape model B, see the text for details. We show the IGM emissivity measurements and corresponding total errors of Becker & Bolton (2013) (tan line and cross-hatched region respectively) and the ionizing background constraints of Bouwens et al. (2015a) (blue-gray diagonal-hatched region). The ionizing emissivity required to maintain reionization as a function of redshift and clumping factors ($C_{\rm HII}$) of one, three and ten are shown by the wide grey regions (Madau et al. 1999, also see Equation 18 of Bolton & Haehnelt 2007).

Also shown are the current constraints at $z \sim 10$ based on the luminosity function from Oesch et al. (2014). Due to the small number of sources available at $z \sim 10$ and the very large uncertainty in their redshift, the luminosity function is not well constrained at these redshifts. Fits using the Schechter (1976) parametrisation realistically allows only one free parameter to be varied while the remainder are fixed to their $z \sim 8$ values (we plot the $\dot{N}_{\rm ion}$ predicted for the luminosity function parameters where ϕ_* is allowed to vary). Despite the large uncertainty, we include these values to illustrate the early suggestions of Oesch et al. (2014) and other works (Zheng et al., 2012; Coe et al., 2012) that the luminosity function (and hence the inferred underlying star-formation rate density) begins to fall more rapidly at $z \geq 9$ than extrapolations from lower redshift naively suggest. However, more recent analysis by McLeod et al. (2014) of

existing Frontier Fields data is in better agreement with the predicted luminosity density at $z \approx 9$. Completed observations of all six Frontier Fields clusters should provide significantly improved constraints at $z > 9$ (Coe et al., 2015), although the large cosmic variance of samples due to the volume effects of strong lensing will limit the constraints that can be placed at the highest redshifts (Robertson et al., 2014).

For all redshift samples plotted in Fig. 4.8, filled symbols correspond to the UV luminosity density integrated to $M_{\rm UV} = -17$ and $M_{\rm UV} = -13$ respectively. The predicted $\dot{N}_{\rm ion}$ for the UV luminosity functions of Schenker et al. (2013a) and McLure et al. (2013) (not shown in Fig. 4.8) effectively reproduce the UV luminosity density constraints outlined in R13 and lie between those predicted by Bouwens et al. (2015b) and Finkelstein (2014). The more recent works of Bouwens et al. (2015b) and Finkelstein (2014) show a greater disagreement between both themselves and previous works. This is a concern as it means that the choice of luminosity function (and hence the underlying selection/methodology) could have a significant effect on the conclusions drawn on galaxies' ability to complete or maintain reionization by the desired redshift.

At $z \sim 6$, the UV luminosity density from galaxies brighter than the limiting depth observed by Bouwens et al. (2015b) is large enough to maintain reionization for a clumping factor of three. This is in contrast to the previous LF of Bouwens et al. (2012) and the results of Finkelstein (2014) which require a contribution from galaxies fainter than $M_{\rm UV} = -17$ (approximately the observational limits) to produce the $\dot{N}_{\rm ion}$ needed to maintain reionization. At $z \sim 8$, the large uncertainties (and fitting degeneracies) in both the faint-end slope and characteristic luminosity of the luminosity function means that both of the luminosity density (and hence $\dot{N}_{\rm ion}$) assuming a constant $f_{\rm esc}\xi_{\rm ion}$) estimates included in this work agree within their 1σ errors. For the redshift-dependent ionizing emissivity inferred by Bouwens et al. (2015a, assuming $C_{\rm HII} = 3$), faint galaxies down to at least $M_{\rm UV} = -13$ are required for all redshifts at $z \geq 6$ based on the current UV luminosity density constraints and the fiducial $f_{\rm esc}\xi_{\rm ion} = 24.5$.

To convert the star-formation rates inferred by the stellar mass densities observed

by Chapter 2 and Grazian et al. (2014) to a $\dot{N}_{\rm ion}$ directly comparable with the LF estimates, we choose the $f_{\rm esc}\kappa_{\rm ion}$ at the $log_{10}f_{\rm esc} - A_V$ values where $\beta = -2$ and $\log_{10} f_{\rm esc}\xi_{\rm ion} = 24.5$. For the ionization-bounded nebula with holes model, the corresponding $\log_{10} f_{\rm esc}\kappa_{\rm ion} = 52.39$, whilst for the density-bounded nebula $\log_{10} f_{\rm esc}\kappa_{\rm ion} = 52.34$.

The ionizing photon rate predicted by the $z \sim 4$ stellar mass functions of Chapter 2 and Grazian et al. (2014) for stellar masses greater than $10^{8.55}{\rm M}_{\odot}$ (the estimated lower limit from Chapter 2 for which stellar masses can be reliably measured at $z \sim 4$) are shown as the blue and pink lines plotted in Fig. 4.8. Plotted as thick solid and dashed lines are the $\dot{N}_{\rm ion}$ assuming $\log_{10} f_{\rm esc}\kappa_{\rm ion} = 52.39$ with the corresponding shaded area illustrating the systematic offset for $\log_{10} f_{\rm esc}\kappa_{\rm ion} = 52.34$.

The UV luminosity density at $z > 4$ implied by the SMD observations of Grazian et al. (2014) (for $M > 10^{8.55}{\rm M}_{\odot}$) are in good agreement with the UV LF estimates of Finkelstein (2014) when integrated down to $M_{\rm UV} = -17$ ($\approx$ observation limits). However, when integrating the stellar mass function down to significantly lower masses such as $> 10^{7}{\rm M}_{\odot}$, the shallower low-mass slope of (Grazian et al., 2014) results in a negligible increase in the total stellar mass density (≈ 0.07 dex). This is potentially inconsistent with the star-formation (and resulting stellar mass density) implied at $z > 6$ when galaxies from below the current observations limits of the luminosity functions are taken into account (open plotted symbols).

The higher stellar mass density observed in Chapter 2 results in $\dot{N}_{\rm ion}$ most consistent with those inferred by the Bouwens et al. (2015b) luminosity density ($M_{\rm UV} > -17$). Overall, there is reasonable agreement between the implied star-formation rates of the luminosity and stellar mass functions. However, both estimates have comparable systematic differences between different sets of observations.

Since the observational limit for the stellar mass function is currently limited by the reliability of stellar mass estimates for galaxies rather than their detection, better stellar mass estimates alone (through either deeper IRAC data or more informative fitting priors) could extend the observational limit for current high

redshift galaxy samples. Improved constraints on the stellar mass functions at $z \leq 6$ are therefore a viable way of improving the constraints on SFR density and ionizing emissivity of faint galaxies at higher redshifts.

4.4.3 $\dot{N}_{\rm ion}$ for evolving $f_{\rm esc}\xi_{\rm ion}$

To estimate what effect a β dependent $f_{\rm esc}\xi_{\rm ion}$ or $f_{\rm esc}\kappa_{\rm ion}$ would have on the predicted $\dot{N}_{\rm ion}$, we assume two separate $f_{\rm esc}\xi_{\rm ion}(\beta)$ relations based on the predicted evolution of $f_{\rm esc}\xi_{\rm ion}$ and $f_{\rm esc}\kappa_{\rm ion}$ vs β shown in Fig. 4.7. The first relation, *'ModelB_dust'*, is based on the relatively shallow evolution of $f_{\rm esc}\xi_{\rm ion}$ and $f_{\rm esc}\kappa_{\rm ion}$ vs β as a function of dust extinction for the density-bounded nebula model (Model B). Over the dynamic range in β, the *ModelB_dust* model evolves ≈ 0.5dex from $\log_{10} f_{\rm esc}\xi_{\rm ion}(\beta = -2.3) \approx 24.75$ to $\log_{10} f_{\rm esc}\xi_{\rm ion}(\beta = -1.7) \approx 24.25$.

The second relation, *ModelA_fesc*, follows the $f_{\rm esc}\xi_{\rm ion}$ or $f_{\rm esc}\kappa_{\rm ion}$ vs β evolution as a function of $f_{\rm esc}$ for the ionization-bounded nebula model (Model A). This model evolves from $\log_{10} f_{\rm esc}\xi_{\rm ion} \approx 25$ at $\beta = -2.3$ to effectively zero ionizing photons per unit luminosity/star-formation at $\beta = -1.8$. Due to the lack of constraints on β for galaxies all the way down to $M_{\rm UV} = -13$, we set a lower limit on how steep the UV slope can become. This limit is chosen to match the UV slope for the dust-free, $f_{\rm esc} = 1$ scenario for fiducial model and has a slope of $\beta = -2.55$. We choose these two relations (three including the constant assumption above) because they correspond to the most likely mechanisms through which β or the LyC escape fraction are expected to evolve.

Firstly, the constant (equivalent to *'ModelA_dust'*) and *'ModelB_dust'* models cover the assumption that evolution in the dust content of galaxies is responsible for the observed evolution in β and any corresponding evolution in the ionizing efficiency of galaxies ($f_{\rm esc}\xi_{\rm ion}$ or $f_{\rm esc}\kappa_{\rm ion}$). Secondly, the *'ModelA_fesc'* model corresponds to an evolution in $f_{\rm esc}$ alone and for the ionization-bounded nebula with holes model, represents the steepest evolution of $f_{\rm esc}\xi_{\rm ion}$ ($/f_{\rm esc}\kappa_{\rm ion}$) with respect to β of any of the parameters. While there is no obvious physical mechanism for such evolution at high-redshift, using this model we can at least link an inferred $f_{\rm esc}$ redshift evolution such as that from the Kuhlen & Faucher-Giguère (2012)

and R13 to a corresponding evolution in β and vice-versa. In these works, the evolving escape fraction is parametrised as:

$$f_{\rm esc}(z) = f_0 \times \left(\frac{1+z}{5}\right)^{\gamma} \tag{4.15}$$

where $f_0 = 0.054$ and $\gamma = 2.4$ (R13) and are constrained by the observed IGM emissivity values of Faucher-Giguère et al. (2008) at $z \leq 4$ and the WMAP total integrated optical depth measurements of Hinshaw et al. (2013) at higher redshift. For the subsequent analysis we also show how the total ionizing emissivity would change following this evolution of $f_{\rm esc}$ (assuming a constant $\xi_{\rm ion} = 25.2$ in line with R13).

It is important to note here that the more recent measurements of the IGM emissivity at $z \sim 4$ by Becker & Bolton (2013) are a factor ~ 2 greater than those of Faucher-Giguère et al. (2008) at the same redshift. As such, the assumed values may under-estimate the zero-point f_0 and over-estimate the slope of the $f_{\rm esc}$ evolution compared to those fitted to the IGM emissivities of Becker & Bolton (2013). However, we include this result to illustrate the effects that forcing consistency with IGM and optical depth measurements has on total ionizing emissivity for comparable underlying UV luminosity/star-formation rate density measurements relative to the assumption of a constant conversion.

For the star-formation history assumed throughout this work, both of these models should in principle also take into account the reddening of the intrinsic UV slope due to age evolution (see Section 4.3.4). However, we neglect this contribution in the following analysis for two reasons. Firstly, the effect of age evolution on the observed β is small in comparison to that of $f_{\rm esc}$ or dust for these models. Secondly, the vector relating β and $f_{\rm esc}\xi_{\rm ion}$ for increasing age is either almost parallel to or slightly steeper than those for $f_{\rm esc}$ and dust respectively. As such, the effects on the inferred $f_{\rm esc}\xi_{\rm ion}$ will be negligible.

4.4.3.1 Evolving luminosity-averaged $f_{\rm esc}\xi_{\rm ion}$

To explore how a β-dependent coefficient would change the inferred emissivities, we first calculate a constant $f_{\rm esc}\xi_{\rm ion}$ for each redshift based on the luminosity

weighted $\langle\beta\rangle_{\rm UV}$. The $z\sim4$ to $z\sim7$ $\langle\beta\rangle_{\rm UV}$ used are those from Bouwens et al. (2014), with the $z\sim8$ value based on the fit outlined in Equation 4.7.

For clarity, we plot the resulting predicted emissivities only for the UV luminosity densities predicted by Bouwens et al. (2015b) luminosity function parametrisations, these are shown in Fig. 4.9 for both the *ModelB_dust* and *ModelA_fesc* (top and bottom panels respectively) $f_{\rm esc}\xi_{\rm ion}(\beta)$ relations. The shaded regions around the solid green and blue lines (top and bottom panels respectively) represent the uncertainty on $f_{\rm esc}\xi_{\rm ion}$ due to the statistical uncertainty in $\langle\beta\rangle_{\rm UV}$. The full statistical uncertainties include the luminosity density errors illustrated in Fig. 4.8 and are included in Appendix Table 4.3.

By assuming a β-dependent coefficient, the estimated $\dot{N}_{\rm ion}$ evolution changes shape to a much shallower evolution with redshift. For our *ModelB_dust* β relation, the decline in $\dot{N}_{\rm ion}$ from $z=4$ to $z=8$ is reduced by ≈0.25 dex when the luminosity function is integrated down to the limit of $M_{\rm UV}<-13$. The effect is even stronger for the *ModelA_fesc* β evolution, with the $\dot{N}_{\rm ion}$ actually increasing over this redshift. The larger $f_{\rm esc}\xi_{\rm ion}$ inferred by the increasingly blue UV slopes at high redshift are able to balance the rapid decrease in UV luminosity density.

A key effect of the increasing ionizing efficiency with increasing redshifts is that for both $f_{\rm esc}\xi_{\rm ion}(\beta)$ relations explored here, the observable galaxy population at $z\sim7$ is now capable of maintaining reionization for a clumping factor of $C_{\rm HII}=3$. This is in contrast to the result inferred when assuming a constant $f_{\rm esc}\xi_{\rm ion}$.

However, we know the brightest galaxies are in fact also the reddest and that any of our predicted $f_{\rm esc}\xi_{\rm ion}(\beta)$ relations imply they are therefore the least efficient at producing ionizing photons. The application of an average $f_{\rm esc}\xi_{\rm ion}$ (even one weighted by the relative contributions to the luminosity density) may give a misleading impression of the relative contribution the brightest galaxies make to the ionizing background during the EoR. A more accurate picture can be obtained by applying a luminosity-dependent β relation (e.g. $f_{\rm esc}\xi_{\rm ion}(M_{\rm UV})$) to the observed luminosity function and integrating the ionizing emissivity, $\dot{N}_{\rm ion}$, from this.

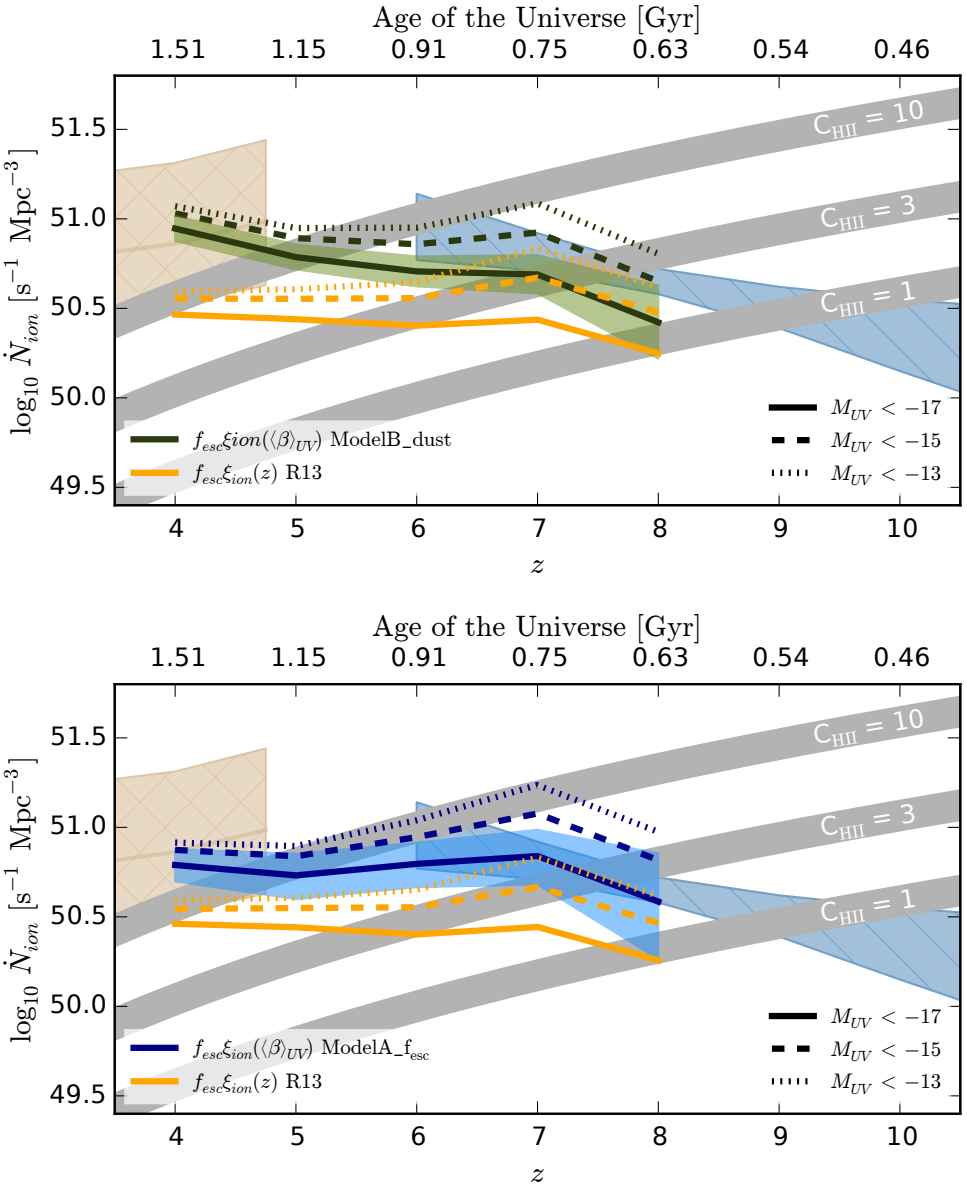

Figure 4.9: Ionizing emissivity, $\dot{N}_{\rm ion}$, predicted by the luminosity functions measured by Bouwens et al. (2015b) for an evolving $f_{\rm esc}\xi_{\rm ion}$ as a function of redshift, based on the luminosity-weighted average β. See text for details on the assumed $f_{\rm esc}\xi_{\rm ion}$ as a function of $\langle\beta\rangle_{\rm UV}$ for the *ModelB_dust* (top - green) and *ModelA_fesc* (bottom - blue) models. In both panels, the thick solid and dashed lines correspond to the UV luminosity density integrated down to the observational limit and a constant $M_{\rm UV} = -13$ respectively. The yellow lines indicate the emissivity predicted for redshift-dependent $f_{\rm esc}$ as inferred by R13, see Equation 4.15. As in Figure 4.8, we show the IGM emissivity measurements and corresponding total errors of Becker & Bolton (2013) (tan line and cross-hatched region respectively) and the ionizing background constraints of Bouwens et al. (2015a) (blue-gray diagonal-hatched region).

4.4.3.2 Luminosity-dependent $f_{\rm esc}\xi_{\rm ion}$

Using the observed $\beta(M_{\rm UV})$ relations of Bouwens et al. (2014) (Fig. 4.3) and our models for $f_{\rm esc}\xi_{\rm ion}(\beta)$, we next calculate $\dot{N}_{\rm ion}$ as a function of both the changing luminosity function and the evolving colour-magnitude relation. Fig. 4.10 shows the evolution of $\dot{N}_{\rm ion}$ based on these assumptions, again for the Bouwens et al. (2015b) luminosity function parametrisations. For both the *ModelB_dust* and *ModelA_fesc* relations, the emissivity of galaxies above the limiting depths of the observations are reduced due to the fact that the brighter galaxies have significantly redder observed βs.

For the *ModelA_fesc* β evolution and the *ModelB_dust* relation at high redshift, the difference between the $\dot{N}_{\rm ion}$ for $M_{\rm UV} < -17$ and $M_{\rm UV} < -13$ is quite significant. This is due to the observed steepening of the colour-magnitude relation (Section 4.2.3) at higher redshifts results in a larger $f_{\rm esc}\xi_{\rm ion}$ evolution between the brightest and faintest galaxies in the luminosity function. When integrating the UV luminosity function from fainter magnitudes, the number of ionizing photons produced per unit UV luminosity density significantly increases. At lower redshifts, the sharp decline in $f_{\rm esc}\xi_{\rm ion}$ for redder galaxies in *ModelA_fesc* means that the brightest galaxies can potentially contribute very little to the total ionizing emissivity.

The total galaxy ionizing emissivity ($M_{\rm UV} < -13$) for both models of β evolution is high enough to maintain reionization (for a clumping factor of $C_{\rm HII} \lesssim 3$) at all redshifts. In fact, only galaxies down to a rest-frame magnitude of $M_{\rm UV} = -15$ are required to match these rates. Furthermore, despite the increased $\dot{N}_{\rm ion}$ predicted at $z > 5$ both models are in good agreement with the observed IGM emissivities of Becker & Bolton (2013) at lower redshifts when the luminosity functions are integrated down to a limit of $M_{\rm UV} < -13$. Including galaxies such faint galaxies does however result in a potential over-production of ionizing photons at $z > 6$ based on the emissivity estimates of Bouwens et al. (2015a). Given that we have shown that significantly lower values of $f_{\rm esc}$ are still consistent with the observed colours (as stated in Section 4.3.2), an overproduction for the optimistic models assumed does not necessarily present an immediate problem.

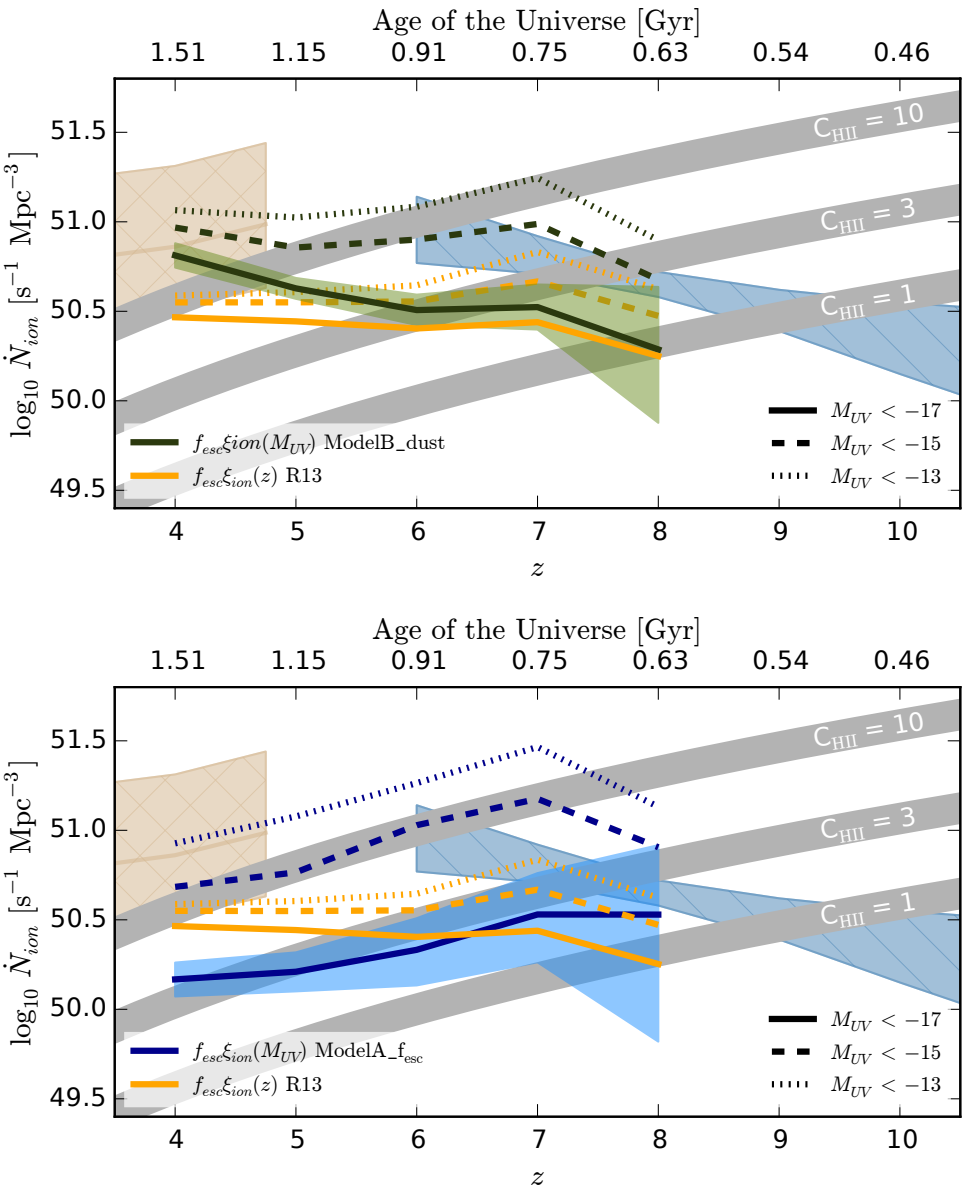

Figure 4.10: Ionizing emissivity, $\dot{N}_{\rm ion}$, predicted by the luminosity functions measured by Bouwens et al. (2015b) for a luminosity dependent $f_{\rm esc}\xi_{\rm ion}$. See text for details on the assumed $f_{\rm esc}\xi_{\rm ion}$ as a function of $\beta(M_{\rm UV})$ for the *ModelB_dust*(top) and *ModelA_fesc* (bottom) models. In both panels, the thick solid, dashed and dotted lines correspond to the UV luminosity density integrated down to $M_{\rm UV} = -17$, -15 and -13 respectively. The yellow lines indicate the emissivity predicted for redshift-dependent $f_{\rm esc}$ as inferred by R13, see Equation 4.15. As in Figure 4.8, we show the IGM emissivity measurements and corresponding total errors of Becker & Bolton (2013) (tan line and cross-hatched region respectively) and the ionizing background constraints of Bouwens et al. (2015a) (blue-gray diagonal-hatched region).

From these results we can see that changes in the ionizing efficiency of galaxies during EoR that are still consistent with the evolving UV continuum slopes have significantly less effect on the predicted total ionizing emissivity ($M_{\rm UV} < -13$) at $z \sim 4$ than at higher redshifts based on the current observations. This result has a crucial outcome with regards to current numerical models for the epoch of reionization, as it allows for a wider range of reionization histories which are still consistent with both the observed UV luminosity/SFR-density and lower redshift IGM emissivity estimates.

4.5 Discussion and future prospects

In several previous studies of the reionization history of the Universe the conclusion has been drawn that at earlier times in the epoch of reionization, galaxies must have been more efficient at ionizing the surrounding IGM than similar galaxies at lower redshift (Becker & Bolton, 2013; Kuhlen & Faucher-Giguère, 2012; Robertson et al., 2013). Based on the constraints on galaxy stellar populations and escape fractions explored in Section 4.3 and their application to the existing observations in Section 4.4, it is not yet possible to establish that one particular galaxy property is evolving to cause such an increase in ionizing efficiency.

Nevertheless, what we find in this work is that evolution in galaxy properties, such as dust extinction and escape fraction (or some combination of these and others), which are consistent with the observed colour evolution of high-redshift galaxies can readily account for any increase in the ionizing efficiency required by other constraints such as the total optical depth. Ongoing and future observations of both local and distant galaxies will be able to provide much tighter constraints on the evolving galaxy properties.

If the observed β evolution is a result of dust alone, as is assumed by Bouwens et al. (2011d) and other works, the inferred evolution in $f_{\rm esc}\xi_{\rm ion}$ as a function of β is highly dependent on the assumed model of Lyman continuum escape and hence the underlying geometry of dust and gas. For example, if the channels through which LyC photons escape are dust-free (as in Model A), the effect of the dust

evolution will have negligible effect on the emissivity of galaxies as a function of β (as discussed in Section 4.3.4). Real galaxies will of course be significantly more complicated (and messy) than the simple toy models adopted in this work, as such the channels through which LyC escape may also contain significant quantities of dust. We find that if we modify Model A such that the dust screen is extended to include the low-density channels, the resulting model is indistinguishable from Model B (density-bounded nebula) with regards to β as a function of $f_{\rm esc}$ or A_V. Such a model closely matches that observed by Borthakur et al. (2014) (see also Heckman et al. 2011) for a local analog of galaxies during the EoR and represents our best model for LyC escape.

For any of the plausible causes for the luminosity and redshift evolution of β (dust, metallicity, escape fraction), the models explored in this work infer that fainter/low-mass galaxies are emitting more ionizing photons per unit star-formation into the IGM than their higher mass counterparts. Currently, simulations of galaxies at high redshift draw somewhat differing conclusions on the mass/luminosity dependence of the escape fraction. Based on a combination of theoretical models and the existing limited observations, Gnedin et al. (2008) find that angular averaged escape fraction increases with higher star-formation rates and galaxy masses, the inverse of what we predict based on β alone. However, in isolation from the model predictions, the observational data explored by Gnedin et al. (2008) does not place any strong constaints on the luminosity dependence of $f_{\rm esc}$ (Giallongo et al., 2002; Fernández-Soto et al., 2003; Shapley et al., 2006).

Subsequent simulations predict the opposite luminosity dependence, in better agreement with the colour evolution predictions of this work (Razoumov & Sommer-Larsen, 2010; Yajima et al., 2010). Recent work exploring the escape fraction of both typical (Kimm & Cen, 2014) and dwarf (Wise et al., 2014) galaxies at $z \geq 7$ find that the instantaneous escape fraction (measured at the virial radius in these simulations) is inversely proportional to the halo mass. However, as discussed by Kimm & Cen (2014), the average instantaneous escape fraction may be somewhat misleading due to the bursty nature of star-formation in their models and the delay between the peak SFR and maximum escape fraction for an episode of

star-formation. They find that the time-averaged escape fraction weighted by the overall LyC photon production rate remains roughly constant for size haloes. Improved measurements on the stellar or halo mass dependence of $f_{\rm esc}$ are therefore clearly crucial.

Although direct measurements of the LyC escape fraction for galaxies during EoR will never be possible due to the effects of IGM absorption along the line of sight, measurements of the escape fraction as a function of stellar mass and luminosity (or SFR) at $z \lesssim 3$ should soon be possible due to the deep UV imaging of new surveys such as the UVUDF (Teplitz et al., 2013) and the forthcoming GOODS UV Legacy Survey (PI: Oesch, GO13872). The wealth of ancillary data available in these fields (both photometric and spectroscopic) should make it possible to tightly constrain $f_{\rm esc}$, $\xi_{\rm ion}$ or $\kappa_{\rm ion}$, and β for either individual galaxies or samples stacked by galaxy properties. Measuring β vs $f_{\rm esc}\xi_{\rm ion}$ at $2 \lesssim z \lesssim 3$ would significantly reduce systematic errors in the inferred $\dot{N}_{\rm ion}$ during the EoR from incorrect or poorly informed assumptions on $f_{\rm esc}\xi_{\rm ion}$.

Given the large degeneracies in β with respect to the various stellar population parameters, understanding β vs $f_{\rm esc}\xi_{\rm ion}$ both at $z \sim 3$ and during the EoR will require an improved understanding of what is responsible for the observed β evolution. With ALMA observations of statistically significant samples of galaxies at high-redshift, it should be possible to make strong constraints on not just the strength and attenuation curve of the dust extinction, but also the location and geometry of the dust relative to the gas and star-formation within galaxies (De Breuck et al., 2014).

With the new generation of near-infrared sensitive spectrographs allowing precision spectroscopic measurement of metallicities and dust out to $z > 3$ (e.g. MOSFIRE: Kriek et al. (2015)), it will be possible to place much more accurate priors on the expected ages, metallicities and star-formation histories for galaxies during the EoR. Finally, as with many outstanding problems in astrophysics, the launch of the James Webb Space Telescope will address many of the systematic and statistical uncertainties which limit current observations. Crucially, JWST should be able to probe much fainter galaxy populations, potentially down to

rest-frame magnitudes of $M_{\rm UV} = -15$ and below. Based on the findings in this chapter, such observations might even mean we are finally able to observe the full galaxy population responsible for powering reionization.

To date, extrapolation of the observed luminosity functions down to absolute magnitudes of $M_{\rm UV} = -13$ or fainter has been required to produce sufficient UV luminosity density (and hence ionizing emissivity) to accomplish reionization by $z \sim 6$. However, the integrated luminosity density for luminosity functions with faint-end slopes < -2 tends towards infinity. There must therefore be some physically imposed minimum galaxy luminosity (or stellar mass) below which star-formation cannot occur (truncating the luminosity function) or a deviation from the steep power-law slope observed at brighter magnitudes. The suppression of star-formation by supernova or radiative feedback is expected to produce such a turnover or flattening of the UV luminosity function, although the luminosity or halo-mass at which this turnover occurs is still unknown.

In hydrodynamic simulations, Duffy et al. (2014) find that extrapolation of the observed UV luminosity function is valid at least until the resolution limits of their survey. Similarly, the separate simulation by Wise et al. (2014) is able to produce significantly fainter dwarf galaxies ($M_{\rm UV} \gtrsim -6$) and also find that the luminosity functions begins to flatten at $M_{\rm UV} = -12$. Studies based on the fossil record of local group dwarf galaxies currently show some agreement with such predictions, with dwarf galaxies down to very faint magnitudes at $z \sim 5$ (Weisz et al., 2014), or breaks in power-law at $M_{\rm UV} \approx -14$ to -12 (Boylan-Kolchin et al., 2014, 2015). A key conclusion of this chapter is that even with a conservatively high break in the shape of the luminosity function of $M_{\rm UV} \lesssim -14$, the total ionizing emissivity of galaxies at $z \sim 7$ and 8 could still be high enough to complete or maintain reionization.

4.6 Summary

In this work, we explore in-depth the ionizing photon budget of galaxies during the epoch of reionization based solely on the observed galaxy properties. For

the latest observational constraints on the star-formation rate and UV luminosity density at $z > 4$, we assess the ionizing emissivity consistent with new constraints on the rest-frame UV colours of galaxies at these redshifts.

Using a comprehensive set of SED models for two plausible Lyman continuum escape mechanisms – previously outlined in Zackrisson et al. (2013) – we explore in detail the relationship between the UV continuum slope β and the number of ionizing photons produced per unit UV luminosity or star-formation ($\xi_{\rm ion}$ and $\kappa_{\rm ion}$ respectively). We find that the ionizing efficiencies assumed by several previous works ($\log_{10} f_{\rm esc}\xi_{\rm ion} = 24.5 - 24.6$: Robertson et al. (2013); Kuhlen & Faucher-Giguère (2012)) are still consistent with the current β observations during the EoR. However, for both of the LyC escape models explored here, this assumption is close to the maximum efficiency which is still consistent with the fiducial UV slope typically considered at these redshifts ($\beta = -2$). Based on our SED modelling, escape fractions or ionizing efficiency that are 1 dex lower than typically assumed are still consistent with the observed galaxy colours.

Applying the fiducial $\log_{10} f_{\rm esc}\xi_{\rm ion} = 24.5$ to the the latest observations of the luminosity and mass functions at $z \geq 4$, we find that at $z \sim 6$, the observed population can produce enough ionizing photons to maintain reionization assuming a clumping factor $C_{\rm HII} = 3$. At earlier times, we confirm previous results that found that galaxies from below our current observation limits are required to produce enough ionizing photons to maintain reionization at $z \sim 7$ and beyond (Robertson et al., 2010, 2013; Kuhlen & Faucher-Giguère, 2012; Finkelstein et al., 2012).

Motivated by increasing evidence for a luminosity dependence of the UV continuum slope (Bouwens et al., 2014; Rogers et al., 2014) and evidence for evolution in this relation with redshift (Bouwens et al., 2014), we explore the effects of assuming an ionizing efficiency that is not constant but varies with the observed β. The two galaxy properties that are able to plausibly account for the required range of observed β's, dust extinction and $f_{\rm esc}$, both predict an ionizing efficiency that increases for increasingly blue UV continuum slopes. While the other galaxy properties such as age and metallicity predict similar trends, current observations

do not support a large enough variation to account for the required range of observed UV slopes.

We find that when assuming an ionizing efficiency based on the luminosity-weighted average β, the currently observable galaxy population alone is now able to maintain reionization at $z \sim 7$ (assuming $C_{\rm HII} = 3$). Despite this increase in efficiency at early times, the predicted $\dot{N}_{\rm ion}$ at $z < 5$ remain consistent with measurements based on the IGM (Becker & Bolton, 2013).

Assuming instead that the ionizing efficiency of galaxies is dependent on their luminosity, the observed $M_{\rm UV} - \beta$ relations and our SED models can result in significant changes in the inferred ionizing photon budget. Since our models suggest that redder (brighter) galaxies have lower $f_{\rm esc}\xi_{\rm ion}$ than their blue (faint) counterparts, the inferred ionizing photon budget for the currently observable galaxy population may be significantly reduced, especially at lower redshifts. However, because of the increasing importance of faint galaxies (which have higher inferred $f_{\rm esc}\xi_{\rm ion}$), only galaxies down to $M_{\rm UV} \approx -15$ may be required to produce the required ionizing photons.

Our conclusion is that the inferred ability of galaxies to complete or maintain reionization is highly dependent on the stellar population assumptions used to predict their ionizing efficiencies. Crucially though, the models explored in this study can potentially allow for a wide range of reionization histories whilst remaining consistent with the observed colour evolution and luminosity (or star-formation rate) density during this epoch. Future work on constraining both the colour and luminosity dependence of $f_{\rm esc}$ at lower redshifts as well as measuring the ages and dust content of galaxies during the EoR will be vital in understanding the precise ionizing emissivity of galaxies throughout this epoch.

Chapter 5

Conclusions and Future Prospects

In the introduction to this thesis I highlighted some of the outstanding questions in astronomy and the study of galaxy evolution. This thesis aimed to address two key issues at high redshift, firstly how and when galaxies assembled their stellar mass at high redshift. And secondly what role galaxies played in the epoch of reionization, specifically whether they are the sources responsible for powering the reionization of the intergalactic medium.

In the following chapter I will outline what new conclusions can be drawn from the results of this thesis on these particular issues. I will also discuss the future prospects for solving these questions and the work which can be done to build upon the results of this thesis.

5.1 Finding and studying high redshift galaxies

In Section 1.2.1 of the thesis introduction, we outlined the evolution in recent years of the methods and techniques used to find and study galaxies at increasingly high redshifts. Chief among these methods for finding galaxies at $z > 3$ are Lyman break galaxies (LBG) and photometric redshift analysis. Motivated by an apparent discrepancy between the observed colours of galaxies selected by these

methods, in Chapter 2 we performed extensive tests on the use of photometric redshift selection at high redshift. We find that the large spread of colours for galaxies selected by photometric redshifts can be explained purely by the photometric scatter of faint galaxies (with the predicted intrinsic colours) out of the traditional colour criteria.

In addition, we conclude that photometric redshift selection can be much less sensitive to photometric scatter than Lyman break criteria for the same redshift range. Furthermore, it can also correctly identify high-redshift sources which would otherwise fail LBG selection criteria.

5.2 The growth of stellar mass in the early universe

In Chapter 2 we investigate the evolution of the galaxy stellar mass function (SMF) and star-formation rates at $z \geq 4$ in the CANDELS GOODS South field. Our new observations of the stellar mass function exhibit steep low-mass slopes, steeper than previously observed at these redshifts but in greater agreement with the theoretical predictions of semi-analytic and hydrodynamical models. Comparing the redshift evolution of the observed mass functions with those of the semi-analytic models illustrates their potential for constraining the physics of galaxy feedback in future analyses.

Our observed mass functions represent the first direct construction of the galaxy stellar mass function at $z \sim 6$ and $z \sim 7$. However, the large errors at these redshifts (due to the small number counts and large stellar mass errors) illustrates the need for both additional wide-area ground-based data and further ultra deep (and potentially lensed) observations to better constrain the high and low mass ends of the SMF respectively.

The steeper low-mass slopes measured in this work results in higher estimates of the stellar mass density than previously observed, even accounting for the effect of reduced stellar mass estimates due to the effects of nebular emission on

SED fitting. For the high redshift samples studied in Chapter 2, the observed stellar mass-to-UV luminosity ratios show minimal luminosity dependence and are consistent with a constant mass-to-light ratio at all redshifts. We also find that the overall normalisation of the mass-to-light distribution increases with redshift.

In addition to measuring the galaxy stellar masses, we also investigate the star-formation properties for our high-redshift galaxy samples. For a fixed stellar mass (5×10^9 $M_\odot$), the average specific star-formation rate (sSFR) rises strongly with redshift, confirming recent observations and showing good agreement with the theoretical prediction that the sSFR is proportional to the specific accretion rates of neutral gas onto dark matter halos at early times. In combination with other recent studies, this result lays to rest the previous tension between theory and observation.

The star-formation rate densities observed in Chapter 2 are higher than previously measured at $z > 3$, we find that this difference is most likely due to the differing treatment of dust extinction when correcting its effects. These differences highlight the large systematic uncertainties that still strongly affect the estimation of star-formation rates from the rest-frame ultra-violet emission of galaxies. In Section 5.4 of this chapter, we explore these systematic effects further and discuss how they could soon be addressed.

Another route through which galaxies can grow is via mergers with other galaxies in their local environment. However, due to the difficulty in estimating the merger rates of galaxies at $z \geq 3$, very few observational constraints on galaxy mergers have been made at these redshifts. In Chapter 3, we attempt to build on the existing merger constraints at high redshift by trialling a new method for measuring mergers in photometric surveys.

We apply a modified version of a recently published method for estimating the close pair statistics of galaxies to the CANDELS GOODS South field, studying the merger fraction at $z \geq 2$. In the redshift range of $2 \lesssim z \lesssim 4$, we find that for galaxies with $\log_{10}(M_\star/M_\odot) > 9.5$ and merger ratios of 1:4 or less, the average timescale between major mergers (Γ) is roughly constant at ≈ 4 Gyr,

while for higher mass galaxies ($\log_{10}(M_\star/M_\odot) > 10$) the average is $\approx$ 7 to 10 Gyr over this same redshift range. Given these merger rates we conclude that in the few billion years preceding the peak in cosmic star-formation rate history, star-formation is the dominant mechanism of mass growth by approximately an order of magnitude.

We find that the method used in Chapter 3 produces robust results at the redshifts where there are good number statistics for galaxies above the completeness limits. However due to the compounding effects of mass completeness and decreasing number counts at high redshift (as measured in Chapter 2), the dataset used for this study is not sufficiently large enough to produce good results at $z \sim 5$ and $z \sim 6$. With the inclusion of the four remaining CANDELS fields in this analysis we are confident that robust estimates of the merger rate at $z \geq 5$ will soon be possible.

5.3 The contribution of galaxies to reionization

The epoch of reionization was the last major phase change of the Universe and represents one of the current frontiers of extragalactic astronomy. Of particular interest is the question of what sources powered this reionization process and whether star-forming galaxies are responsible. In Chapter 4 we explore in detail the current constraints on the ionizing photon emissivity of galaxies during the epoch of reionization. As current observations strongly support a luminosity and redshift dependence for the UV continuum slope (β) during this period, we use extensive SED modelling to understand the effects of such evolution on the inferred ionizing emissivity.

A key conclusion of this chapter is that for evolution in any major galaxy property (e.g. age, metallicity, dust attenuation), as galaxies become bluer their ionizing efficiency increases. Or in other terms, any evolution in a property that makes a galaxy bluer, increases its ionizing efficiency. Since current observations strongly support a colour-magnitude relation where brighter galaxies are redder, this result has a significant effect on the inferred total ionizing emissivity at $z > 6$ and the

potential for galaxies to power reionization. When assuming an ionizing efficiency that is dependent on the luminosity-weighted average β, the galaxy population that is brighter than current detection limits can produce enough ionizing photons to maintain reionization at $z \sim 7$.

The effect of the observed β evolution on the ionizing emissivity is even more pronounced when the luminosity dependence is fully taken into account. Assuming an ionizing efficiency which is luminosity dependent increases the importance of faint galaxies due to the fact they are bluer, and hence more efficient at producing ionizing photons. While the predicted ionizing emissivity for the currently observed bright galaxies is reduced (due to their redder β), the increased efficiency of fainter galaxies means that only galaxies as faint as $M_{UV} \approx -15$ may be required to complete reionization at all redshifts. Galaxies as faint as this should be easily detected by the James Webb Space Telescope. We conclude that based on the existing colour constraints and observed star-formation densities, star-forming galaxies can easily produce enough ionizing photons to power the reionization of hydrogen.

The model predictions of Chapter 4 relate the observable properties to the fundamental but un-observable ionizing photon rates, and can therefore provide crucial testable predictions for the latest faint UV surveys. With mass, luminosity and colour dependent constraints on f_{esc} at $2 \lesssim z \lesssim 3$, surveys such as the UVUDF (Teplitz et al., 2013) and GOODS UV Legacy Survey (PI: Oesch) will allow for significantly improved estimates of the ionizing emissivity during the epoch of reionization.

5.4 Future prospects

One of the key conclusions we draw from the results of this thesis is that the key limitation in solving the outstanding questions in galaxy evolution at $z > 3$ is not the availability of suitable data, but actually the systematic uncertainties in some of the methods and assumptions used to analyse it. With the full five CANDELS HST fields now completed and the ongoing Frontier Fields survey

providing even deeper observations over narrower areas, the potential available sample sizes are large enough to provide excellent number statistics at $z > 3$. Furthermore, as shown by Bowler et al. (2012, 2013), deep ground-based surveys can provide vital constraints on the rarest and brightest sources not typically measured by the smaller HST fields. The addition of contiguous *Spitzer* data (SPLASH, PI: Capak) means that similar analysis can also be extended to the high-mass end of stellar mass function at $z \sim 4$ and above.

As outlined in the introduction and illustrated by the results of this thesis, the spectral energy distributions (SEDs) of galaxies are an important tool for understanding galaxy evolution at high redshift. However, the information we can learn is limited not just by the quality of the data but also by our understanding and suitability of the ingredients that we put into the SED fitting.

The assumption of either a dust extinction curve (e.g. Milky Way or SMC-like) or an empirical attenuation curve (such as Calzetti et al. (2000) or Charlot & Fall (2000)) is a critical component in measuring and understanding the intrinsic SEDs of large galaxy samples. However, dust is arguably the least understood baryonic component of galaxies, especially at $z > 1$ where the observations of Herschel and ALMA are still only just beginning to be fully exploited.

Although a universal attenuation law is widely assumed when fitting the SED of galaxies, it is well known that the attenuation law is not universal (Buat et al., 2012; Kriek & Conroy, 2013). The assumption of a universal attenuation law to fit galaxy samples in which it systematically varies will bias estimates of the galaxy and stellar population properties we are trying to measure through SED fitting. Additionally, such variations will result in strong biases on the measurements of the UV continuum slope β at high-redshift, leading to significantly biased estimates for dust-corrected star-formation rates. Measuring and understanding how the dust attenuation curve varies is essential to improving our physical understanding of the evolution of galaxies both at the epoch of peak star-formation and during their early formation at higher redshifts.

Using the latest generation of deep narrow-band (Pérez González et al., 2012) and grism surveys (Brammer et al., 2012) combined with rest-frame far-infrared

data (e.g. GOODS Herschel; Elbaz et al. (2011), or ALMA observations), it is now possible to fully quantify the systematic variation in dust attenuation curve at $1 \lesssim z \lesssim 4$ for the first time. For both bright individual galaxies and stacked samples of faint galaxies, it will be possible to measure the variation as a function of not just a galaxys stellar mass, luminosity and spectral type but also its morphology (both parametric and non-parametric). In addition to providing more reliable estimates of star-formation rates and SFR densities such as those calculated in Chapter 2, a better understanding of dust attenuation is also vital in constraining the ionizing emissivity of galaxies during the epoch of reionization (see Chapter 4).

As well as the wealth of deep photometric data (CANDELS, Frontier Fields, UltraVISTA) that have yet to be utilised in full, the latest generation of spectroscopic instruments and surveys offer the potential for a much deeper understanding of galaxy properties at $z \sim 3$ and beyond. Rest-frame optical spectroscopy from surveys such as MOSDEF (Kriek et al., 2015) can potentially put tight constraints on the ages and metallicities of galaxies at $z \sim 3$. Similarly, the massively multiplexed spectroscopy of MUSE (Bacon et al., 2015) offers the potential for spatially resolved studies of Lyman-α emission out to redshifts of $z \sim 6$. As well as helping to unravel the physical processes of galaxy formation at these redshifts, such observations will also serve as crucial priors for the study of galaxies deep into the epoch of reionization.

At longer wavelengths, the Atacama Large Millimetre Array (ALMA) has already shown in early science results that not only can it detect the gas and dust in distant galaxies, but actually study in detail the kinematics and structures of $z \sim 5$ galaxies (De Breuck et al., 2014). The ALMA Deep Field (PI: Dunlop), a survey of the *Hubble* Ultra Deep Field at a wavelength of 1.3mm is already underway and potentially offers constraints on the dust properties of galaxies at to $z \sim 6$. At even longer wavelengths, the deep blank field surveys with LOFAR will allow the study of bright radio galaxies out to $z > 5$ and even offer a new method for selecting high-redshift galaxies through their 21-cm forest. The era of *truly* multi-wavelength studies of galaxies as far back as the epoch of reionization

has most certainly begun.

Appendices

Appendix A

Reionization Data Tables

In this appendix we present the estimated $\rho_{\rm UV}$ and $\dot{N}_{\rm ion}$ at $4 \leq z \leq 8$ for the range of assumptions outlined in Section 4.4. we list the calculated properties for integration limits $M_{\rm UV}$ = -17, -15 and -13 respectively. In Table A.1 we list the values based on the luminosity function parametrisations of Bouwens et al. (2015b) and are plotted in Figures 4.8, 4.9 and 4.10. In Table A.2, we list the corresponding values for the luminosity function parametrisations of Finkelstein (2014). For both sets of values, we include errors based on the uncertainties in the luminosity function parameters and the random errors in the weighted average of β or the best-fit $\beta - M_{\rm UV}$ slope parameters (Bouwens et al., 2014) as appropriate. When assuming an SMC-like dust attenuation (Pei, 1992), to match the fiducial $\beta = -2$ and $\log_{10} f_{\rm esc}\xi_{\rm ion} = 24.5$ for LyC escape Model B, we find $f_{\rm esc} = 0.28$ and $A_V = 0.08$ are required.

Table A.1: Calculated values of $\rho_{\rm UV}$ and $\dot{N}_{\rm ion}$ for the different integration limits and efficiency assumptions explored in the paper, based on the luminosity function parametrisations of Bouwens et al. (2015b). For each calculated value, we include statistical errors from the uncertainties in the Schechter (1976) parameters and β observations. Also shown are the effects of some of the assumptions made in Section 4.3.1 and their corresponding systematic changes to the estimated values.

	Limit ($M_{\rm UV}$)	$z\sim4$	$z\sim5$	$z\sim6$	$z\sim7$	$z\sim8$
$\log_{10}\rho_{\rm UV}$	-17	$26.53^{+0.07}_{-0.07}$	$26.32^{+0.05}_{-0.05}$	$26.12^{+0.06}_{-0.06}$	$26.02^{+0.06}_{-0.06}$	$25.71^{+0.10}_{-0.09}$
(erg s^{-1} Hz^{-1} Mpc^{-3})	-15	$26.62^{+0.07}_{-0.07}$	$26.43^{+0.06}_{-0.06}$	$26.27^{+0.07}_{-0.07}$	$26.25^{+0.10}_{-0.08}$	$25.93^{+0.18}_{-0.14}$
	-13	$26.66^{+0.07}_{-0.07}$	$26.48^{+0.06}_{-0.06}$	$26.36^{+0.09}_{-0.08}$	$26.41^{+0.15}_{-0.12}$	$26.09^{+0.29}_{-0.20}$
		$\log_{10} f_{\rm esc}\xi_{\rm ion} = 24.5$				
$\log_{10}\dot{N}_{\rm ion}$	-17	$51.03^{+0.07}_{-0.07}$	$50.82^{+0.05}_{-0.05}$	$50.62^{+0.06}_{-0.06}$	$50.52^{+0.06}_{-0.06}$	$50.21^{+0.10}_{-0.09}$
(s^{-1} Mpc^{-3})	-15	$51.12^{+0.07}_{-0.07}$	$50.93^{+0.06}_{-0.06}$	$50.77^{+0.07}_{-0.07}$	$50.75^{+0.10}_{-0.08}$	$50.43^{+0.18}_{-0.14}$
	-13	$51.16^{+0.07}_{-0.07}$	$50.98^{+0.06}_{-0.06}$	$50.86^{+0.09}_{-0.08}$	$50.91^{+0.15}_{-0.12}$	$50.59^{+0.29}_{-0.20}$
		$\log_{10} f_{\rm esc}\xi_{\rm ion} \propto \langle\beta\rangle_{\rho_{\rm UV}}(z)$				
				$Model B\_Dust$		
$\log_{10}\dot{N}_{\rm ion}$	-17	$50.95^{+0.07}_{-0.07}$	$50.79^{+0.07}_{-0.07}$	$50.71^{+0.08}_{-0.08}$	$50.69^{+0.11}_{-0.11}$	$50.42^{+0.21}_{-0.20}$
(s^{-1} Mpc^{-3})	-15	$51.03^{+0.07}_{-0.07}$	$50.89^{+0.07}_{-0.07}$	$50.86^{+0.10}_{-0.09}$	$50.92^{+0.13}_{-0.12}$	$50.65^{+0.25}_{-0.23}$
	-13	$51.07^{+0.07}_{-0.07}$	$50.95^{+0.08}_{-0.07}$	$50.95^{+0.11}_{-0.10}$	$51.09^{+0.17}_{-0.15}$	$50.80^{+0.33}_{-0.27}$
				$Model A\_f_{\rm esc}$		
$\log_{10}\dot{N}_{\rm ion}$	-17	$50.79^{+0.09}_{-0.09}$	$50.74^{+0.12}_{-0.14}$	$50.80^{+0.12}_{-0.13}$	$50.84^{+0.14}_{-0.16}$	$50.58^{+0.27}_{-0.32}$
(s^{-1} Mpc^{-3})	-15	$50.87^{+0.09}_{-0.09}$	$50.84^{+0.12}_{-0.14}$	$50.95^{+0.13}_{-0.14}$	$51.08^{+0.16}_{-0.17}$	$50.82^{+0.30}_{-0.34}$
	-13	$50.91^{+0.09}_{-0.09}$	$50.90^{+0.12}_{-0.14}$	$51.04^{+0.14}_{-0.15}$	$51.24^{+0.20}_{-0.19}$	$50.98^{+0.37}_{-0.37}$
		$\log_{10} f_{\rm esc}\xi_{\rm ion}(M_{\rm UV})$				
				$Model B\_Dust$		
$\log_{10}\dot{N}_{\rm ion}$	-17	$50.81^{+0.07}_{-0.07}$	$50.63^{+0.06}_{-0.06}$	$50.51^{+0.09}_{-0.08}$	$50.52^{+0.13}_{-0.13}$	$50.29^{+0.35}_{-0.41}$
(s^{-1} Mpc^{-3})	-15	$50.97^{+0.07}_{-0.07}$	$50.86^{+0.07}_{-0.07}$	$50.90^{+0.11}_{-0.10}$	$50.99^{+0.14}_{-0.14}$	$50.68^{+0.28}_{-0.43}$
	-13	$51.07^{+0.07}_{-0.07}$	$51.02^{+0.08}_{-0.08}$	$51.08^{+0.14}_{-0.12}$	$51.25^{+0.19}_{-0.17}$	$50.90^{+0.35}_{-0.37}$
				$Model A\_f_{\rm esc}$		
$\log_{10}\dot{N}_{\rm ion}$	-17	$50.17^{+0.09}_{-0.10}$	$50.21^{+0.10}_{-0.11}$	$50.33^{+0.18}_{-0.20}$	$50.53^{+0.23}_{-0.27}$	$50.51^{+0.41}_{-0.72}$
(s^{-1} Mpc^{-3})	-15	$50.68^{+0.08}_{-0.08}$	$50.76^{+0.10}_{-0.10}$	$51.03^{+0.14}_{-0.15}$	$51.18^{+0.17}_{-0.19}$	$50.89^{+0.32}_{-0.69}$
	-13	$50.93^{+0.10}_{-0.10}$	$51.08^{+0.11}_{-0.12}$	$51.27^{+0.16}_{-0.16}$	$51.47^{+0.21}_{-0.20}$	$51.14^{+0.36}_{-0.51}$

Systematic Uncertainties

Salpeter IMF		$\Delta log_{10}\kappa_{\rm ion} = -0.19$
Dust: Calzetti w/ SMC-like extrapolation	Model A: $\Delta log_{10}\xi_{\rm ion} = 0$	Model B: $\Delta log_{10}\xi_{\rm ion} = +0.10$ (For fiducial values)
Dust: SMC (Pei, 1992)	Model A: $\Delta log_{10}\xi_{\rm ion} = 0$	Model B: $\Delta log_{10}\xi_{\rm ion} = +0.18$ (For fiducial $f_{\rm esc} = 0.42$, $A_V = 0.08$, $\beta = -2$)

Table A.2: Calculated values of $\rho_{\rm UV}$ and $\dot{N}_{\rm ion}$ for the different integration limits and efficiency assumptions explored in the paper, based on the luminosity function parametrisations of Finkelstein (2014). For each calculated value, we include statistical errors from the uncertainties in the Schechter (1976) parameters and β observations. Also shown are the effects of some of the assumptions made in Section 4.3.1 and their corresponding systematic changes to the estimated values.

	Limit ($M_{\rm UV}$)	$z\sim4$	$z\sim5$	$z\sim6$	$z\sim7$	$z\sim8$
$\log_{10}\rho_{\rm UV}$	-17	$26.28^{+0.01}_{-0.01}$	$26.18^{+0.01}_{-0.01}$	$25.90^{+0.02}_{-0.02}$	$25.78^{+0.06}_{-0.06}$	$25.67^{+0.20}_{-0.19}$
(erg s^{-1} Hz^{-1} Mpc^{-3})	-15	$26.35^{+0.02}_{-0.02}$	$26.28^{+0.02}_{-0.02}$	$26.10^{+0.06}_{-0.05}$	$25.99^{+0.15}_{-0.13}$	$26.05^{+0.44}_{-0.41}$
	-13	$26.38^{+0.02}_{-0.02}$	$26.32^{+0.03}_{-0.02}$	$26.24^{+0.10}_{-0.09}$	$26.14^{+0.25}_{-0.19}$	$26.38^{+0.72}_{-0.65}$
		$\log_{10} f_{\rm esc}\xi_{\rm ion} = 24.5$				
$\log_{10}\dot{N}_{\rm ion}$	-17	$50.78^{+0.01}_{-0.01}$	$50.68^{+0.01}_{-0.01}$	$50.40^{+0.02}_{-0.02}$	$50.28^{+0.06}_{-0.06}$	$50.17^{+0.20}_{-0.19}$
(s^{-1} Mpc^{-3})	-15	$50.85^{+0.02}_{-0.02}$	$50.78^{+0.02}_{-0.02}$	$50.60^{+0.06}_{-0.05}$	$50.49^{+0.15}_{-0.13}$	$50.55^{+0.44}_{-0.41}$
	-13	$50.88^{+0.02}_{-0.02}$	$50.82^{+0.03}_{-0.02}$	$50.74^{+0.10}_{-0.09}$	$50.64^{+0.25}_{-0.19}$	$50.88^{+0.72}_{-0.65}$
		$\log_{10} f_{\rm esc}\xi_{\rm ion} \propto \langle\beta\rangle_{\rho_{\rm UV}}(z)$				
				$ModelB\_Dust$		
$\log_{10}\dot{N}_{\rm ion}$	-17	$50.69^{+0.02}_{-0.02}$	$50.65^{+0.04}_{-0.04}$	$50.48^{+0.07}_{-0.07}$	$50.46^{+0.11}_{-0.10}$	$50.38^{+0.26}_{-0.25}$
(s^{-1} Mpc^{-3})	-15	$50.76^{+0.02}_{-0.02}$	$50.74^{+0.05}_{-0.05}$	$50.69^{+0.09}_{-0.08}$	$50.67^{+0.17}_{-0.15}$	$50.77^{+0.47}_{-0.44}$
	-13	$50.79^{+0.03}_{-0.03}$	$50.79^{+0.05}_{-0.05}$	$50.83^{+0.12}_{-0.11}$	$50.82^{+0.26}_{-0.22}$	$51.11^{+0.76}_{-0.66}$
				$ModelA\_f_{\rm esc}$		
$\log_{10}\dot{N}_{\rm ion}$	-17	$50.54^{+0.06}_{-0.06}$	$50.60^{+0.10}_{-0.12}$	$50.57^{+0.11}_{-0.12}$	$50.61^{+0.14}_{-0.16}$	$50.53^{+0.32}_{-0.35}$
(s^{-1} Mpc^{-3})	-15	$50.61^{+0.06}_{-0.06}$	$50.69^{+0.10}_{-0.13}$	$50.77^{+0.12}_{-0.13}$	$50.82^{+0.19}_{-0.19}$	$50.92^{+0.51}_{-0.50}$
	-13	$50.64^{+0.06}_{-0.06}$	$50.74^{+0.11}_{-0.12}$	$50.92^{+0.15}_{-0.15}$	$50.97^{+0.27}_{-0.24}$	$51.24^{+0.78}_{-0.69}$
		$\log_{10} f_{\rm esc}\xi_{\rm ion}(M_{\rm UV})$				
				$ModelB\_Dust$		
$\log_{10}\dot{N}_{\rm ion}$	-17	$50.55^{+0.02}_{-0.02}$	$50.50^{+0.03}_{-0.03}$	$50.31^{+0.07}_{-0.07}$	$50.27^{+0.14}_{-0.14}$	$50.29^{+0.38}_{-0.45}$
(s^{-1} Mpc^{-3})	-15	$50.69^{+0.03}_{-0.03}$	$50.70^{+0.04}_{-0.04}$	$50.78^{+0.11}_{-0.11}$	$50.71^{+0.22}_{-0.21}$	$50.82^{+0.55}_{-0.57}$
	-13	$50.77^{+0.04}_{-0.04}$	$50.84^{+0.06}_{-0.06}$	$51.03^{+0.15}_{-0.14}$	$50.95^{+0.32}_{-0.29}$	$51.24^{+0.79}_{-0.76}$
				$ModelA\_f_{\rm esc}$		
$\log_{10}\dot{N}_{\rm ion}$	-17	$49.88^{+0.08}_{-0.08}$	$50.08^{+0.09}_{-0.11}$	$50.18^{+0.17}_{-0.18}$	$50.26^{+0.25}_{-0.30}$	$50.51^{+0.43}_{-0.68}$
(s^{-1} Mpc^{-3})	-15	$50.36^{+0.07}_{-0.07}$	$50.59^{+0.09}_{-0.08}$	$50.95^{+0.14}_{-0.15}$	$50.89^{+0.27}_{-0.28}$	$51.04^{+0.58}_{-0.73}$
	-13	$50.58^{+0.09}_{-0.09}$	$50.86^{+0.10}_{-0.10}$	$51.25^{+0.17}_{-0.15}$	$51.17^{+0.34}_{-0.33}$	$51.51^{+0.78}_{-0.85}$

Systematic Uncertainties

Salpeter IMF		$\Delta log_{10}\kappa_{\rm ion} = -0.19$
Dust: Calzetti w/ SMC-like extrapolation	Model A: $\Delta log_{10}\xi_{\rm ion} = 0$	Model B: $\Delta log_{10}\xi_{\rm ion} = +0.10$ (For fiducial values)
Dust: SMC (Pei, 1992)	Model A: $\Delta log_{10}\xi_{\rm ion} = 0$	Model B: $\Delta log_{10}\xi_{\rm ion} = +0.18$ (For fiducial $f_{\rm esc} = 0.42$, $A_V = 0.08$, $\beta = -2$)

Bibliography

Aldoretta E. J., et al., 2015, The Astronomical Journal, 149, 26

Anders P., Alvensleben U. F. v., 2003, A&A, 401, 1063

Ashby M. L. N., et al., 2013, ApJ, 769, 80

Atek H., et al., 2011, ApJ, 743, 121

Avni Y., Bahcall J. N., 1980, ApJ, 235, 694

Bacon R., et al., 2015, A&A, 575, A75

Balestra I., et al., 2010, A&A, 512, A12

Becker G. D., Bolton J. S., 2013, MNRAS, 436, 1023

Beckwith S. V. W., et al., 2006, The Astronomical Journal, 132, 1729

Behroozi P. S., Wechsler R. H., Conroy C., 2013, ApJ, 770, 57

Bell E. F., Phleps S., Somerville R. S., Wolf C., Borch A., Meisenheimer K., 2006, ApJ, 652, 270

Benítez N., 2000, ApJ, 536, 571

Bennett C. L., et al., 2013, ApJS, 208, 20

Benson A. J., Bower R. G., Frenk C. S., Lacey C. G., Baugh C. M., Cole S., 2003, ApJ, 599, 38

Bertone S., Conselice C. J., 2009, MNRAS, 396, 2345

Bluck A. F. L., Conselice C. J., Bouwens R. J., Daddi E., Dickinson M., Papovich C., Yan H., 2009, MNRAS: Letters, 394, L51

Bluck A. F. L., Conselice C. J., Buitrago F., Grützbauch R., Hoyos C., Mortlock A., Bauer A. E., 2012, ApJ, 747, 34

Bolton J. S., Haehnelt M. G., 2007, MNRAS, 382, 325

Bolzonella M., Miralles J. M., Pello R., 2000, A&A, 363, 476

Borthakur S., Heckman T. M., Leitherer C., Overzier R. A., 2014, Science, 346, 216

Bouwens R. J., et al., 2004, ApJ, 616, L79

Bouwens R. J., Illingworth G. D., Franx M., Ford H., 2007, ApJ, 670, 928

Bouwens R. J., et al., 2009, ApJ, 705, 936

Bouwens R. J., et al., 2010, ApJ, 709, L133

Bouwens R. J., et al., 2011a, U V -CONTINUUM SLOPES AT Z 4 7 FROM THE HUDF09+ERS+CANDELS OBSERVATIONS: DISCOVERY OF A WELL-DEFINED U V -COLOR MAGNITUDE RELATIONSHIP FOR Z 4 STAR-FORMING GALAXIES

Bouwens R. J., et al., 2011b, Nature, 469, 504

Bouwens R. J., et al., 2011c, ApJ, 737, 90

Bouwens R. J., et al., 2011d, ApJ, 1109, 994

Bouwens R. J., et al., 2012, ApJ, 752, L5

Bouwens R. J., et al., 2014, ApJ, 793, 115

Bouwens R. J., Illingworth G. D., Oesch P. A., Caruana J., Holwerda B., Smit R., Wilkins S., 2015a, eprint arXiv:1503.08228

Bouwens R. J., et al., 2015b, ApJ, 803, 34

Bower R. G., Benson A. J., Malbon R., Helly J. C., Frenk C. S., Baugh C. M., Cole S., Lacey C. G., 2006, MNRAS, 370, 645

Bowler R. A., et al., 2012, MNRAS, 426, 2772

Bowler R. A. A., et al., 2013

Boylan-Kolchin M., Bullock J. S., Garrison-Kimmel S., 2014, MNRAS: Letters, 443, L44

Boylan-Kolchin M., Weisz D. R., Johnson B. D., Bullock J. S., Conroy C., Fitts A., 2015, eprint arXiv:1504.06621

Brammer G. B., van Dokkum P. G., Coppi P., 2008, ApJ, 686, 1503

Brammer G. B., et al., 2012, ApJS, 200, 13

Brammer G. B., van Dokkum P. G., Illingworth G. D., Bouwens R. J., Labbé I., Franx M., Momcheva I., Oesch P. A., 2013, ApJ, 765, L2

Bridge C. R., Carlberg R. G., Sullivan M., 2010a, ApJ, 709, 1067

Bridge C. R., et al., 2010b, ApJ, 720, 465

Bromm V., 2013, Rep. Prog. Phys., 76, 112901

Bromm V., Coppi P. S., Larson R. B., 2002, ApJ, 564, 23

Bruzual G., Charlot S., 2003, MNRAS, 344, 1000

Buat V., et al., 2012, A&A, 545, A141

Bundy K., Fukugita M., Ellis R. S., Targett T. A., Belli S., Kodama T., 2009, ApJ, 697, 1369

Bunker A. J., Stanway E. R., Ellis R. S., McMahon R. G., McCarthy P. J., 2003, MNRAS, 342, L47

Bunker A. J., et al., 2010, MNRAS, 409, 855

Burles S., Nollett K. M., Turner M. S., 2001, ApJ, 552, L1

Caballero J. A., Burgasser A. J., Klement R., 2008, A&A, 488, 181

Calzetti D., Kinney A. L., Storchi-Bergmann T., 1994, ApJ, 429, 582

Calzetti D., Armus L., Bohlin R. C., Kinney A. L., Koornneef J., Storchi-Bergmann T., 2000, ApJ, 533, 682

Capak P., et al., 2004, The Astronomical Journal, 127, 180

Cappellari M., et al., 2012, Nature, 484, 485

Caputi K. I., Cirasuolo M., Dunlop J. S., McLure R. J., Farrah D., Almaini O., 2011, MNRAS, 413, 162

Castellano M., et al., 2010, A&A, 524, 28

Castellano M., et al., 2014, A&A, 566, A19

Chabrier G., 2003, PUBL ASTRON SOC PAC, 115, 763

Charlot S., Fall S. M., 2000, ApJ, 539, 718

Ciardi B., Bolton J. S., Maselli A., Graziani L., 2012, MNRAS, 423, 558

Cirasuolo M., et al., 2007, MNRAS, 380, 585

Coe D., et al., 2012, ApJ, 762, 32

Coe D., Bradley L., Zitrin A., 2015, ApJ, 800, 84

Collister A. A., Lahav O., 2004, PUBL ASTRON SOC PAC, 116, 345

Conroy C., 2013, ANNU REV ASTRON ASTR, 51, 393

Conroy C., Kratter K. M., 2012, ApJ, 755, 123

Conroy C., van Dokkum P. G., 2012, ApJ, 760, 71

Conroy C., Gunn J. E., White M., 2009a, ApJ, 699, 486

Conroy C., White M., Gunn J. E., 2009b, ApJ, 708, 58

Conselice C. J., 2009, MNRAS: Letters, 399, L16

Conselice C. J., 2014, ANNU REV ASTRON ASTR, 52, 291

Conselice C. J., Arnold J., 2009, MNRAS, 397, 208

Conselice C. J., Bershady M. A., Dickinson M., Papovich C., 2003, The Astronomical Journal, 126, 1183

Conselice C. J., Rajgor S., Myers R., 2008, MNRAS, 386, 909

Conselice C. J., Yang C., Bluck A. F. L., 2009, MNRAS, 394, 1956

Conselice C. J., et al., 2011, MNRAS, 413, 80

Cooke J., Ryan-Weber E. V., Garel T., Díaz C. G., 2014, MNRAS, 441, 837

Cowie L. L., Hu E. M., 1998, The Astronomical Journal, 115, 1319

Cowie L. L., Songaila A., Hu E. M., Cohen J. G., 1996, The Astronomical Journal, 112, 839

Cox T. J., Jonsson P., Somerville R. S., Primack J. R., Dekel A., 2008, MNRAS, 384, 386

Crosby B. D., O'Shea B. W., Smith B. D., Turk M. J., Hahn O., 2013, ApJ, 773, 108

Croton D. J., et al., 2006, MNRAS, 365, 11

Curtis-Lake E., et al., 2013, MNRAS, 429, 302

Daddi E., et al., 2007, ApJ, 670, 156

Dahlen T., Mobasher B., Somerville R. S., Moustakas L. A., Dickinson M., Ferguson H. C., Giavalisco M., 2005, ApJ, 631, 126

Dahlen T., et al., 2010, ApJ, 724, 425

Dahlen T., et al., 2013, ApJ, 775, 93

Davé R., Katz N., Oppenheimer B. D., Kollmeier J. A., Weinberg D. H., 2013, MNRAS, 434, 2645

Dayal P., Ferrara A., 2012, MNRAS, 421, 2568

Dayal P., Dunlop J. S., Maio U., Ciardi B., 2013, MNRAS, 434, 1486

De Breuck C., et al., 2014, A&A, 565, A59

De Lucia G., Springel V., White S. D. M., Croton D., Kauffmann G., 2006, MNRAS, 366, 499

Dekel A., Zolotov A., Tweed D., Cacciato M., Ceverino D., Primack J. R., 2013, MNRAS, 435, 999

Dickinson M., et al., 2004, ApJ, 600, L99

Dinerstein H. L., Shields G. A., 1986, ApJ, 311, 45

Duffy A. R., Wyithe J. S. B., Mutch S. J., Poole G. B., 2014, MNRAS, 443, 3435

Duncan K., et al., 2014, MNRAS, 444, 2960

Dunlop J. S., 2013, The First Galaxies, 396, 223

Dunlop J. S., Cirasuolo M., McLure R. J., 2007, MNRAS, 376, 1054

Dunlop J. S., McLure R. J., Robertson B. E., Ellis R. S., Stark D. P., Cirasuolo M., de Ravel L., 2011, MNRAS, 420, 901

Dunlop J. S., et al., 2013, MNRAS, 432, 3520

Eales S., 1993, ApJ, 404, 51

Efron B., 1979, The annals of statistics

Efron B., 1981, Biometrika, 68, 589

Ekström S., et al., 2012, A&A, 537, A146

Elbaz D., et al., 2011, A&A, 533, A119

Eldridge J. J., Stanway E. R., 2009, MNRAS, 400, 1019

Eldridge J. J., Stanway E. R., 2011, MNRAS, 419, 479

Erb D. K., Steidel C. C., Shapley A. E., Pettini M., Reddy N. A., Adelberger K. L., 2006, ApJ, 647, 128

Erb D. K., Pettini M., Shapley A. E., Steidel C. C., Law D. R., Reddy N. A., 2010, ApJ, 719, 1168

Fan X., Carilli C. L., Keating B., 2006, ANNU REV ASTRON ASTR, 44, 415

Faucher-Giguère C.-A., Lidz A., Hernquist L., Zaldarriaga M., 2008, ApJ, 682, L9

Fazio G. G., et al., 2004, ApJS, 154, 10

Ferguson H. C., et al., 2004, ApJ, 600, L107

Fernandez E., Shull J. M., 2011, ApJ, 731, 20

Fernández-Soto A., Lanzetta K. M., Chen H. W., 2003, MNRAS, 342, 1215

Ferreras I., Barbera F. L., Rosa I. G. d. l., Vazdekis A., Carvalho R. R. d., Falcon-Barroso J., Ricciardelli E., 2013, MNRAS: Letters, 429, L15

Finkelstein S. L., 2014, eprint arXiv:1410.5439

Finkelstein S. L., Papovich C., Giavalisco M., Reddy N. A., Ferguson H. C., Koekemoer A. M., Dickinson M., 2010, ApJ, 719, 1250

Finkelstein S. L., et al., 2011, ApJ, 1110, 3785

Finkelstein S. L., et al., 2012, ApJ, 758, 93

Finlator K., Oppenheimer B. D., Davé R., 2011, MNRAS, 410, 1703

Fioc M., Rocca-Volmerange B., 1997, A&A, 326, 950

Fontana A., Poli F., Menci N., Nonino M., Giallongo E., Cristiani S., D'Odorico S., 2003, ApJ, 587, 544

Fontanot F., Cristiani S., Vanzella E., 2012, MNRAS, 425, 1413

Fontanot F., Cristiani S., Pfrommer C., Cupani G., Vanzella E., 2014, MNRAS, 438, 2097

Foreman-Mackey D., Hogg D. W., Lang D., Goodman J., 2013, PUBL ASTRON SOC PAC, 125, 306

Förster Schreiber N. M., et al., 2009, ApJ, 706, 1364

Franx M., et al., 2003, ApJ, 587, L79

Galametz A., et al., 2013, ApJS, 206, 10

Giallongo E., Cristiani S., D'Odorico S., Fontana A., 2002, ApJ, 568, L9

Giallongo E., et al., 2015, A&A, 578, A83

Giavalisco M., et al., 2004a, ApJ, 600, L93

Giavalisco M., et al., 2004b, ApJ, 600, L103

Gnedin N. Y., Kravtsov A. V., Chen H. W., 2008, ApJ, 672, 765

González V., Labbé I., Bouwens R. J., Illingworth G. D., Franx M., Kriek M., Brammer G. B., 2010, ApJ, 713, 115

González V., Labbé I., Bouwens R. J., Illingworth G. D., Franx M., Kriek M., 2011, ApJ, 735, L34

González V., Bouwens R. J., Labbé I., Illingworth G. D., Oesch P. A., Franx M., Magee D., 2012, arXiv, p. 148

González V., Bouwens R. J., Illingworth G. D., Labbé I., Oesch P. A., Franx M., Magee D., 2014, ApJ, 781, 34

Grazian A., et al., 2011, A&A, 532, 33

Grazian A., et al., 2014, eprint arXiv:1412.0532

Grogin N. A., et al., 2011, ApJS, 197, 35

Guhathakurta P., Tyson J. A., Majewski S. R., 1990, ApJ, 357, L9

Guo Y., et al., 2013, ApJS, 207, 24

Hagele G. F., Perez-Montero E., Diaz A. I., Terlevich E., Terlevich R., 2006, MNRAS, 372, 293

Haislip J. B., et al., 2006, Nature, 440, 181

Hathi N. P., Jansen R. A., Windhorst R. A., Cohen S. H., Keel W. C., Corbin M. R., Ryan Jr R. E., 2007, The Astronomical Journal, 135, 156

Hathi N. P., Malhotra S., Rhoads J. E., 2008, ApJ, 673, 686

Hauser M. G., Dwek E., 2001, ANNU REV ASTRON ASTR, 39, 249

Heckman T. M., et al., 2011, ApJ, 730, 5

Henriques B. M. B., White S. D. M., Lemson G., Thomas P. A., Guo Q., Marleau G.-D., Overzier R. A., 2012, MNRAS, 421, 2904

Henriques B. M. B., White S. D. M., Thomas P. A., Angulo R. E., Guo Q., Lemson G., Springel V., 2013, MNRAS, 431, 3373

Henriques B. M. B., White S. D. M., Thomas P. A., Angulo R., Guo Q., Lemson G., Springel V., Overzier R., 2015, MNRAS, 451, 2663

Hildebrandt H., Wolf C., Benitez N., 2008, A&A, 480, 703

Hinshaw G., et al., 2013, ApJS, 208, 19

Hopkins A. M., 2004, ApJ, 615, 209

Hopkins A. M., Beacom J. F., 2006, ApJ, 651, 142

Hopkins P. F., Hernquist L., Cox T. J., Di Matteo T., Robertson B., Springel V., 2006, ApJS, 163, 1

Hopkins P. F., Hernquist L., Cox T. J., Keres D., 2008a, ApJS, 175, 356

Hopkins P. F., Cox T. J., Keres D., Hernquist L., 2008b, ApJS, 175, 390

Hopkins P. F., et al., 2010, ApJ, 724, 915

Hu E. M., 1998, The Young Universe: Galaxy Formation and Evolution at Intermediate and High Redshift, 146, 148

Hu E. M., McMahon R. G., 1996, Nature, 382, 231

Huang K.-H., Ferguson H. C., Ravindranath S., Su J., 2013, ApJ, 765, 68

Hubble E. P., 1926, ApJ, 64, 321

Ilbert O., et al., 2005, A&A, 439, 863

Ilbert O., et al., 2013, A&A, 556, A55

Iwata I., et al., 2009, ApJ, 692, 1287

Izotov Y. I., Thuan T. X., Lipovetsky V. A., 1994, ApJ, 435, 647

Izotov Y. I., Stasińska G., Guseva N. G., 2013, A&A, 558, A57

Jarvis M. J., et al., 2012, MNRAS, 428, 1281

Jogee S., et al., 2009, ApJ, 697, 1971

Jones T., Stark D. P., Ellis R. S., 2012, ApJ, 751, 51

Kartaltepe J. S., et al., 2007, ApJS, 172, 320

Kawai N., et al., 2006, Nature, 440, 184

Kennicutt Jr R. C., 1998, ApJ, 498, 541

Kimm T., Cen R., 2014, ApJ, 788, 121

Kitzbichler M. G., White S. D. M., 2008, MNRAS, 391, 1489

Koekemoer A. M., et al., 2011, ApJS, 197, 36

Koekemoer A. M., et al., 2013, ApJS, 209, 3

Kriek M., Conroy C., 2013, ApJ, 775, L16

Kriek M., et al., 2010, ApJ, 722, L64

Kriek M., et al., 2015, ApJS, 218, 15

Kroupa P., 2001, MNRAS, 322, 231

Krueger H., Fritze-v Alvensleben U., Loose H.-H., 1995, A&A, 303, 41

Kuhlen M., Faucher-Giguère C.-A., 2012, MNRAS, 423, 862

Kurk J., et al., 2012, A&A, 549, A63

Labbé I., et al., 2010, ApJ, 716, L103

Laidler V. G., et al., 2007, PUBL ASTRON SOC PAC, 119, 1325

Laskar T., Berger E., Chary R.-R., 2011, ApJ, 739, 1

Lawrence A., et al., 2007, MNRAS, 379, 1599

Le Fèvre O., et al., 2000, MNRAS, 311, 565

Le Fèvre O., et al., 2004, A&A, 428, 1043

Lee S.-K., Ferguson H. C., Somerville R. S., Wiklind T., Giavalisco M., 2010, ApJ, 725, 1644

Lee K.-S., et al., 2011, ApJ, 733, 99

Lee K.-S., et al., 2012, ApJ, 752, 66

Lee S.-K., Ferguson H. C., Somerville R. S., Giavalisco M., Wiklind T., Dahlen T., 2014, ApJ, 783, 81

Leitherer C., et al., 1999, ApJS, 123, 3

Leitherer C., Ekström S., Meynet G., Schaerer D., Agienko K. B., Levesque E. M., 2014, ApJS, 212, 14

Lin L., et al., 2004, ApJ, 617, L9

López-Sanjuan C., Balcells M., Pérez-González P. G., Barro G., Gallego J., Zamorano J., 2010, A&A, 518, A20

López-Sanjuan C., et al., 2015, A&A, 576, A53

Lorenzoni S., Bunker A. J., Wilkins S. M., Stanway E. R., Jarvis M. J., Caruana J., 2011, MNRAS, 414, 1455

Lotz J. M., Jonsson P., Cox T. J., Primack J. R., 2008, MNRAS, 391, 1137

Lotz J. M., Jonsson P., Cox T. J., Primack J. R., 2010a, MNRAS, 404, 575

Lotz J. M., Jonsson P., Cox T. J., Primack J. R., 2010b, MNRAS, 404, 590

Lotz J. M., Jonsson P., Cox T. J., Croton D., Primack J. R., Somerville R. S., Stewart K., 2011, ApJ, 742, 103

Lu Y., Mo H. J., Weinberg M. D., Katz N., 2011, MNRAS, 416, 1949

Lu Y., et al., 2014, ApJ, 795, 123

Madau P., 1995, ApJ, 441, 18

Madau P., Ferguson H. C., Dickinson M. E., Giavalisco M., Steidel C. C., Fruchter A., 1996, MNRAS, 283, 1388

Madau P., Pozzetti L., Dickinson M., 1998, ApJ, 498, 106

Madau P., Haardt F., Rees M. J., 1999, ApJ, 514, 648

Maiolino R., et al., 2008a, Formation and Evolution of Galaxy Disks ASP Conference Series, 396, 409

Maiolino R., et al., 2008b, A&A, 488, 463

Man A. W. S., Toft S., Zirm A. W., Wuyts S., van der Wel A., 2011, ApJ, 744, 85

Maraston C., 2005, MNRAS, 362, 799

Maraston C., Pforr J., Renzini A., Daddi E., Dickinson M., Cimatti A., Tonini C., 2010, MNRAS, 407, 830

Marchesini D., van Dokkum P. G., Förster Schreiber N. M., Franx M., Labbé I., Wuyts S., 2009, ApJ, 701, 1765

Martín-Navarro I., et al., 2014

McCracken H. J., et al., 2012, A&A, 544, A156

McLeod D. J., McLure R. J., Dunlop J. S., Robertson B. E., Ellis R. S., Targett T. T., 2014, eprint arXiv:1412.1472

McLure R. J., et al., 2006, MNRAS, 372, 357

McLure R. J., Cirasuolo M., Dunlop J. S., Foucaud S., Almaini O., 2009, MNRAS, 395, 2196

McLure R. J., Dunlop J. S., Cirasuolo M., Koekemoer A. M., Sabbi E., Stark D. P., Targett T. A., Ellis R. S., 2010, MNRAS, 403, 960

McLure R. J., et al., 2011, MNRAS, 418, 2074

McLure R. J., et al., 2012, MNRAS, 428, 1088

McLure R. J., et al., 2013, MNRAS, 432, 2696

Meier D. L., 1976, ApJ, 203, L103

Meurer G. R., Heckman T. M., Calzetti D., 1999, ApJ, 521, 64

Molino A., et al., 2014, MNRAS, 441, 2891

Mortlock A., et al., 2013, MNRAS, 433, 1185

Mortlock A., et al., 2014, MNRAS, 447, 2

Moster B. P., Somerville R. S., Newman J. A., Rix H.-W., 2011, ApJ, 731, 113

Muzzin A., et al., 2013, ApJ, 777, 18

Nayyeri H., et al., 2014, ApJ, 794, 68

Neistein E., Dekel A., 2007, MNRAS, 383, 615

Nestor D. B., Shapley A. E., Kornei K. A., Steidel C. C., Siana B., 2013, ApJ, 765, 47

Newman J. A., Davis M., 2002, ApJ, 564, 567

Newman A. B., Ellis R. S., Bundy K., Treu T., 2012, ApJ, 746, 162

Nonino M., et al., 2009, ApJS, 183, 244

Oesch P. A., et al., 2009, ApJ, 709, L16

Oesch P. A., et al., 2010, The Astrophysical Journal Letters, 709, L21

Oesch P. A., et al., 2012, ApJ, 759, 135

Oesch P. A., et al., 2013, ApJ, 772, 136

Oesch P. A., et al., 2014, ApJ, 786, 108

Oke J. B., Gunn J. E., 1983, ApJ, 266, 713

Ono Y., Shimasaku K., Dunlop J., Farrah D., McLure R., Okamura S., 2010, ApJ, 724, 1524

Osterbrock D. E., Ferland G. J., 2006, Astrophysics of Gaseous Nebulae and Active Galactic Nuclei. University Science Books

Ota K., et al., 2014, ApJ, 792, 34

Ouchi M., et al., 2009, ApJ, 706, 1136

Ouchi M., et al., 2013, ApJ, 778, 102

Ownsworth J. R., Conselice C. J., Mortlock A., Hartley W. G., Almaini O., Duncan K., Mundy C. J., 2014, MNRAS, 445, 2198

Pacifici C., Charlot S., Blaizot J., Brinchmann J., 2012, MNRAS, 421, 2002

Papovich C., Finkelstein S. L., Ferguson H. C., Lotz J. M., Giavalisco M., 2011, MNRAS, 412, 1123

Partridge R. B., Peebles P. J. E., 1967, ApJ, 147, 868

Patton D. R., Carlberg R. G., Marzke R. O., Pritchet C. J., da Costa L. N., Pellegrini P. S., 2000, ApJ, 536, 153

Pawlik A. H., Schaye J., van Scherpenzeel E., 2009, MNRAS, 394, 1812

Pei Y. C., 1992, ApJ, 395, 130

Peng Y.-j., et al., 2010, ApJ, 721, 193

Penzias A. A., Wilson R. W., 1965, ApJ, 142, 419

Pérez González P. G., et al., 2008, ApJ, 675, 234

Pérez González P. G., et al., 2012, ApJ, 762, 46

Pirzkal N., et al., 2009, ApJ, 695, 1591

Pirzkal N., Rothberg B., Nilsson K. K., Finkelstein S., Koekemoer A., Malhotra S., Rhoads J., 2012, ApJ, 748, 122

Pirzkal N., Rothberg B., Ryan R., Coe D., Malhotra S., Rhoads J., Noeske K., 2013

Planck Collaboration et al., 2015, arXiv, p. 1589

Popesso P., et al., 2009, A&A, 494, 443

Pozzetti L., et al., 2010, A&A, 523, A13

Ravindranath S., et al., 2006, ApJ, 652, 963

Razoumov A. O., Sommer-Larsen J., 2010, ApJ, 710, 1239

Reddy N. A., Steidel C. C., 2009, ApJ, 692, 778

Reddy N. A., Pettini M., Steidel C. C., Shapley A. E., Erb D. K., Law D. R., 2012, ApJ, 754, 25

Reines A. E., Nidever D. L., Whelan D. G., Johnson K. E., 2009, ApJ, 708, 26

Retzlaff J., Rosati P., Dickinson M., Vandame B., Rité C., Nonino M., Cesarsky C., the GOODS team 2010, A&A, 511, A50

Rhoads J. E., et al., 2009, ApJ, 697, 942

Robertson B. E., Ellis R. S., Dunlop J. S., McLure R. J., Stark D. P., 2010, Nature, 468, 49

Robertson B. E., et al., 2013, ApJ, 768, 71

Robertson B. E., Ellis R. S., Dunlop J. S., McLure R. J., Stark D. P., McLeod D., 2014, The Astrophysical Journal Letters, 796, L27

Robertson B. E., Ellis R. S., Furlanetto S. R., Dunlop J. S., 2015, The Astrophysical Journal Letters, 802, L19

Robson I., Priddey R. S., Isaak K. G., McMahon R. G., 2004, MNRAS, 351, L29

Rodriguez Espinosa J. M., et al., 2014, MNRAS: Letters, 444, L68

Rogers A. B., McLure R. J., Dunlop J. S., 2013, MNRAS, 429, 2456

Rogers A. B., et al., 2014, MNRAS, 440, 3714

Rowlands K., Gomez H. L., Dunne L., Aragon-Salamanca A., Dye S., Maddox S., da Cunha E., Werf P. v. d., 2014, MNRAS, 441, 1040

Ryan Jr R. E., Cohen S. H., Windhorst R. A., Silk J., 2008, ApJ, 678, 751

Salmon B., et al., 2015, ApJ, 799, 183

Salpeter E. E., 1955, ApJ, 121, 161

Sana H., et al., 2012, Science, 337, 444

Sana H., et al., 2013, A&A, 550, A107

Santini P., et al., 2012, A&A, 538, A33

Schaerer D., 2002, A&A, 382, 28

Schaerer D., de Barros S., 2009, A&A, 502, 423

Schaerer D., de Barros S., 2010, A&A, 515, 73

Schaerer D., de Barros S., Sklias P., 2013, A&A, 549, 4

Schaerer D., Boone F., Zamojski M., Staguhn J., Dessauges-Zavadsky M., Finkelstein S., Combes F., 2015, A&A, 574, A19

Schawinski K., et al., 2014, MNRAS, 440, 889

Schaye J., et al., 2014, MNRAS, 446, 521

Schechter P., 1976, ApJ, 203, 297

Schenker M. A., et al., 2013a, ApJ, 768, 196

Schenker M. A., Ellis R. S., Konidaris N. P., Stark D. P., 2013b, ApJ, 777, 67

Schmidt M., 1965, ApJ, 141, 1295

Schmidt M., 1968, ApJ, 151, 394

Schwarz G., 1978, The annals of statistics, 6, 461

Shapley A. E., Steidel C., Pettini M., 2003, ApJ

Shapley A. E., Steidel C. C., Pettini M., Adelberger K. L., Erb D. K., 2006, ApJ, 651, 688

Shim H., Chary R.-R., Dickinson M., Lin L., Spinrad H., Stern D., Yan C.-H., 2011, ApJ, 738, 69

Siana B., et al., 2007, ApJ, 668, 62

Siana B., et al., 2010, ApJ, 723, 241

Smit R., Bouwens R. J., Franx M., Illingworth G. D., Labbé I., Oesch P. A., van Dokkum P. G., 2012, ApJ, 756, 14

Smit R., et al., 2014, ApJ, 784, 58

Smolčić V., et al., 2015, A&A, 576, A127

Somerville R. S., Davé R., 2014, eprint arXiv:1412.2712

Somerville R. S., Hopkins P. F., Cox T. J., Robertson B. E., Hernquist L., 2008, MNRAS, 391, 481

Somerville R. S., Gilmore R. C., Primack J. R., Domínguez A., 2012, MNRAS, 423, 1992

Sommariva V., Mannucci F., Cresci G., Maiolino R., Marconi A., Nagao T., Baroni A., Grazian A., 2012, A&A, 539, 136

Spitler L. R., et al., 2014, ApJ, 787, L36

Springel V., Di Matteo T., Hernquist L., 2005, MNRAS, 361, 776

Stanway E. R., Bunker A. J., McMahon R. G., 2003, MNRAS, 342, 439

Stanway E. R., et al., 2004a, ApJ, 604, L13

Stanway E. R., Bunker A. J., McMahon R. G., Ellis R. S., Treu T., McCarthy P. J., 2004b, ApJ, 607, 704

Stanway E. R., Bremer M. N., Lehnert M. D., Eldridge J. J., 2008, MNRAS, 384, 348

Stark D. P., Bunker A. J., Ellis R. S., Eyles L. P., Lacy M., 2007, ApJ, 659, 84

Stark D. P., Ellis R. S., Bunker A., Bundy K., Targett T., Benson A., Lacy M., 2009, ApJ, 697, 1493

Stark D. P., Schenker M. A., Ellis R., Robertson B., McLure R., Dunlop J., 2013, ApJ, 763, 129

Stark D. P., et al., 2014, MNRAS, 445, 3200

Stark D. P., et al., 2015, MNRAS, 450, 1846

Steidel C. C., Hamilton D., 1992, Astronomical Journal (ISSN 0004-6256), 104, 941

Steidel C. C., Pettini M., Hamilton D., 1995, The Astronomical Journal, 110, 2519

Steidel C. C., Giavalisco M., Dickinson M., Adelberger K. L., 1996, The Astronomical Journal, 112, 352

Steidel C. C., Adelberger K. L., Giavalisco M., Dickinson M., Pettini M., 1999, ApJ, 519, 1

Strömgren B., 1939, ApJ, 89, 526

Strukov I. A., Brukhanov A. A., Skulachev D. P., Sazhin M. V., 1992, MNRAS, 258, 37P

Tanvir N. R., et al., 2009, Nature, 461, 1254

Targett T. A., et al., 2013, MNRAS, 432, 2012

Tasca L. A. M., et al., 2014, A&A, 565, A10

Teplitz H. I., et al., 2013, The Astronomical Journal, 146, 159

Thompson R. I., 2003, ApJ, 596, 748

Thompson R. I., Weymann R. J., Storrie Lombardi L. J., 2001, ApJ, 546, 694

Torrey P., et al., 2015, MNRAS, 447, 2753

Treu T., Auger M. W., Koopmans L. V. E., Gavazzi R., Marshall P. J., Bolton A. S., 2010, ApJ, 709, 1195

Troncoso P., et al., 2014, A&A, 563, A58

Trujillo I., Ferreras I., de la Rosa I. G., 2011, MNRAS, 415, 3903

Vanzella E., et al., 2008, A&A, 478, 83

Vanzella E., et al., 2009, ApJ, 695, 1163

Vanzella E., Siana B., Cristiani S., Nonino M., 2010, MNRAS, 404, 1672

Vazquez G. A., Leitherer C., Schaerer D., Meynet G., Maeder A., 2007, ApJ, 663, 995

Vogelsberger M., et al., 2014, MNRAS, 444, 1518

Walter F., et al., 2003, Nature, 424, 406

Weinmann S. M., Neistein E., Dekel A., 2011, MNRAS, 417, 2737

Weisz D. R., Johnson B. D., Conroy C., 2014, ApJ, 794, L3

Wiklind T., et al., 2014, ApJ, 785, 111

Wilkins S. M., Bunker A. J., Stanway E., Lorenzoni S., Caruana J., 2011, MNRAS, 417, 717

Wilkins S. M., Matteo T. D., Croft R., Khandai N., Feng Y., Bunker A., Coulton W., 2013, MNRAS, 429, 2098

Wilkins S. M., Stanway E. R., Bremer M. N., 2014, MNRAS, 439, 1038

Willott C. J., et al., 2010, The Astronomical Journal, 139, 906

Windhorst R. A., et al., 2011, ApJS, 193, 27

Wise J. H., Cen R., 2009, ApJ, 693, 984

Wise J. H., Demchenko V. G., Halicek M. T., Norman M. L., Turk M. J., Abel T., Smith B. D., 2014, MNRAS, 442, 2560

Wuyts S., van Dokkum P. G., Franx M., Schreiber N. M. F., Illingworth G. D., Labbé I., Rudnick G., 2009, ApJ, 706, 885

Yajima H., Choi J.-H., Nagamine K., 2010, MNRAS, 412, 411

Yan H., et al., 2012, ApJ, 761, 177

Zackrisson E., Inoue A. K., Jensen H., 2013, ApJ, 777, 39

Zafar T., Watson D., 2013, A&A, 560, A26

Zastrow J., Oey M. S., Veilleux S., McDonald M., 2013, ApJ, 779, 76

Zheng W., et al., 2012, Nature, 489, 406

Zinnecker H., Yorke H. W., 2007, ANNU REV ASTRON ASTR, 45, 481

de Barros S., Schaerer D., Stark D. P., 2014, A&A, 563, A81

de Vaucouleurs G., 1959, Handbuch der Physik, 53, 275

van Dokkum P. G., 2001, PUBL ASTRON SOC PAC, 113, 1420

van Dokkum P. G., Conroy C., 2010, Nature, 468, 940

van Dokkum P. G., et al., 2003, ApJ, 587, L83

van der Wel A., et al., 2011, ApJ, 742, 111